Imperial College London
Department of Bioengineering

Non-invasive neural interfacing for wearable electromyographic systems

Irene Mendez Guerra
Supervision: Prof. Dario Farina, Dr. Deren Y. Barsakcioglu, Dr. Dan Wetmore

Submitted in part fulfilment of the requirements for the degree of Doctor of Philosophy in Bioengineering at Imperial College London
February 2024, London, United Kingdom

Copyright Declaration

The copyright of this thesis rests with the author. Unless otherwise indicated, its contents are licensed under a Creative Commons Attribution-Non Commercial 4.0 International Licence (CC BY-NC).

Under this licence, you may copy and redistribute the material in any medium or format. You may also create and distribute modified versions of the work. This is on the condition that: you credit the author and do not use it, or any derivative works, for a commercial purpose.

When reusing or sharing this work, ensure you make the licence terms clear to others by naming the licence and linking to the licence text. Where a work has been adapted, you should indicate that the work has been changed and describe those changes.

Please seek permission from the copyright holder for uses of this work that are not included in this licence or permitted under UK Copyright Law.

Declaration of Originality

I declare that the work introduced in this thesis is my own, except where explicitly stated otherwise. Portions of the research were carried out in collaboration with other researchers, which are duly noted where applicable.

Acknowledgements

To my beloved grandparents and parents

This thesis has only been possible thanks to brilliant and wonderful people that have accompanied me during this wild PhD journey.

First, I would like to express my sincere gratitude to my PhD supervisor, Prof. Dario Farina. Throughout this journey, your guidance and support have been instrumental in shaping my research and academic growth. Being able to learn so much from you is an experience that I am very grateful for.

Thank you, Dr. Deren Y. Barsakcioglu for your unwavering support and mentorship throughout these years as my postdoc supervisor. Your expertise, dedication, and unbreakable optimism always reminded me that at the end, everything will be alright.

Thank you, Dr. Dan Wetmore for all your support and encouragement during the PhD, and for playing a crucial role in making this industrial partnership an incredible journey. I would also like to extend my gratitude to the CTRL-Labs, now Meta, team for funding this research. I am deeply honoured and humbled by the trust you have placed in my work. Talking about Meta is impossible not to thank the Motor Augmentation group. Thank you for welcoming to your team and fascinating work during my internship, it was an amazing experience.

Back in London, I would like to thank the EPSRC for also funding this research through the CDT of Neurotechnology. It has been an honour being part of this CDT and Imperial during this journey. Thank you, Dr. Kate Hobson, for being the heart of the CDT of Neurotechnology and supporting us every step of the way. Also, thank you, my incredible CDT cohort, for the very fond memories of our start together.

I would also like to extend my heartfelt gratitude to my past and present mentors for guiding me through even the most challenging times. Thank you, Dr. Ernest N. Kamavuako, for your mentorship and encouragement in the early days of my research journey in Aalborg and the opportunity to come to Imperial. Thank you, Dr. Ivan Vujaklija, for your contagious passion for science and for being a mentor and friend in the distance. Also thank you, Dr. Simon Avrillion, for your inspiring view on research, infectious humour, and guidance with the fellowship world.

Thank you to the brilliant Farina lab, past and present members, for not being just colleagues but friends, and sparkling this PhD journey with incredible moments together. Particularly, to the fantastic girls in Il Sogno di Bacco, I truly believe in our plan B.

This journey wouldn't have been the same without my wonderful close friends Chiara, Amparo, Hristo, Miko, Mario, Jenna, Diana, Nacho, Julia, Viktorija and Natasha. Thank you for the treasured time together and for being my emergency kit of sunshine, happiness, and rainbows. I would also like to thank my great friends in Spain for all their support in the distance and the fantastic experiences together.

Wholehartedly thank you, Tao, mi amor, for bearing with me throughout this journey. I wouldn't have made it without your infinite support and emanating happiness. Thank you for our adventures together that have kept me sane and dreaming during the last five years. I am looking forward to many more, and now, excitingly, without the PhD in our way!

Finalmente, gracias a mi familia, especialmente a mis padres y abuelos, por ser mis mejores (y nada objetivos) fans. Muchísimas gracias por vuestro apoyo incondicional y por siempre creer en mí. Este PhD no habría sido posible sin todo vuestro esfuerzo durante años para que yo pudiera estar aquí hoy. Esto es para vosotros.

Abstract

In our ever-growing digital world, our interaction with technology is constantly evolving, pursuing more intuitive and immersive experiences. This has led to the exploration of neural interfaces, a technology initially developed for rehabilitation purposes, for general consumer electronics. Neural interfaces promise a seamless interaction with technology by translating how our nervous system encodes intentions and movements. These interfaces can be established at various points along the neural pathway, with varying degrees of invasiveness. Unlike in clinical applications, non-invasive technologies are essential to address ethical concerns in widespread consumer use.

One promising approach to meet these requirements involves detecting neural signals non-invasively at the terminal layer of the nervous system, where they are transformed into muscle forces and actions. This is achieved through surface electromyography (EMG) signals, which capture muscle electrical potentials. However, for advanced control paradigms, it's essential to identify individual motor neuron activity rather than collective muscle signals. Recent breakthroughs in decoding algorithms have made this possible, offering great potential for non-invasive wearable interfaces. However, current decoding algorithms have not been applied to the wrist, a prime location for wearable devices that shows unique electrical properties. In addition, these algorithms are designed for static conditions rather than natural dynamic movements.

In this thesis, I address these challenges to develop an accurate, robust, non-invasive neural interface for the wrist, suitable for consumer wearables. Here I validate that motor neuron activity can be decoded from EMG signals recorded at the wrist, demonstrating its ability to accurately predict finger gestures in real-time. I also investigate how joint movements affect the decoding of motor neuron activity and introduce online learning metrics to adapt to dynamic conditions. These advancements enhance our understanding of non-invasive motor neuron interfacing at the wrist, bringing us closer to achieving seamless, intuitive human-computer interaction for general consumer applications.

Contents

Copyright Declaration **1**

Declaration of Originality **2**

Acknowledgements **3**

Abstract **5**

List of Figures **9**

List of Tables **10**

List of Abbreviations **12**

Motivations **14**

1 Introduction **16**

1.1 Neuromuscular system 16

1.1.1 Motor neurons 16

1.1.2 Neuromechanical transduction 18

1.1.3 Muscle and tendon anatomy at the forearm and wrist 20

1.1.4 Force modulation 24

1.1.4.1 Sarcomere length 24

1.1.4.2 Contraction speed 25

1.1.4.3 Recruitment: the size principle 25

1.1.4.4 Rate coding 26

1.2 Electromyography 27

1.2.1 Electromyography generative model 27

1.2.2 Electromyography decomposition 29

1.2.2.1 Requirements and ambiguities 29

1.2.2.2 Algorithm 30

1.2.2.3 Validation 35

1.2.2.4 Reliability and robustness 36

1.2.2.5 Real-time implementation 37

1.2.2.6 Limitations 37

1.3 Recordings at the muscle-tendon interface: the end-of-fibre effect 38

1.3.1 Leading and trailing dipole model of the intracellular action potential . . 39

1.3.2 Far-field potentials and the end-of-fibre effect . . . 40
1.3.3 End-of-fibre effect at the motor unit action potential level . . . 43
1.4 Non-invasive human-computer interaction based on motor neuron activity . . . 44
1.5 Aims and thesis outline . . . 48

2 Decoding motor neuron activity from the wrist non-invasively 49
2.1 Introduction . . . 49
2.2 Methods . . . 52
2.2.1 Offline experiment . . . 52
2.2.1.1 Experimental setup . . . 52
2.2.1.2 Decomposition of far-field potentials . . . 53
2.2.1.3 Physiological analysis . . . 54
2.2.1.4 Finger command classification . . . 54
2.2.1.5 Statistical analyses . . . 55
2.2.2 Real-time experiment . . . 56
2.3 Results . . . 57
2.3.1 Physiological analysis . . . 57
2.3.2 Finger command prediction (offline) . . . 60
2.3.3 Real-time control . . . 64
2.4 Discussion . . . 64

3 Decoding motor neuron activity during dynamic contractions 70
3.1 Introduction . . . 71
3.2 Methods . . . 73
3.2.1 Neuromuscular model simulations . . . 73
3.2.2 Experimental data . . . 74
3.2.3 Decomposition adaptation . . . 76
3.2.3.1 Whitening adaptation . . . 77
3.2.3.2 Adaptation of separation vectors adaptation . . . 79
3.2.3.3 Adaptation of spike detection . . . 80
3.2.4 Motor unit action potential tracking . . . 81
3.2.5 Decomposition adaptation evaluation . . . 83
3.2.6 Statistics . . . 84
3.3 Results . . . 84
3.3.1 Decomposition adaptation in simulations . . . 84
3.3.2 Experimental motor unit action potential tracking . . . 87
3.3.3 Decomposition adaptation in experimental data . . . 91
3.4 Discussion . . . 94
3.4.1 Effect of dynamics in the decomposition model . . . 96
3.4.2 Motor neuron identification performance during dynamics . . . 97
3.4.3 Translational potential, limitations, and future directions . . . 98
3.5 Conclusions . . . 100

4 Conclusions and future work **101**
4.1 Summary . . . 101
4.2 Strengths and limitations . . . 102
4.2.1 Detection of motor neuron non-invasively from the wrist . . . 102
4.2.2 Control based on motor neuron activity . . . 103
4.2.3 Decomposition during dynamic contractions . . . 104
4.3 Future perspectives . . . 105
4.4 Final remarks . . . 108

Appendices **109**
A1 Isokinetic wrist platform . . . 109
A1.1 Design . . . 109
A1.2 Electrical components . . . 113
A1.2.1 Computer . . . 113
A1.2.2 External screen . . . 114
A1.2.3 DC motor . . . 114
A1.2.4 DC motor controller . . . 114
A1.2.5 DC power supply . . . 114
A1.2.6 Emergency stop button board . . . 114
A1.2.7 Inductive proximity sensors . . . 116
A1.2.8 ArduinoUno board . . . 116
A1.2.9 Force load cells and dedicated DAQs . . . 116
A1.3 Software . . . 118
A1.3.1 Software prerequisites . . . 118
A1.3.2 Motor calibration . . . 119
A1.3.3 Data Acquisition Procedure . . . 119
A1.3.4 Calibrate force sensors . . . 120
A1.3.5 Recordings with force only . . . 121
A1.3.6 Recordings with the motor . . . 121
A1.4 Emergency stop procedure . . . 122
A2 Copyright licenses and permissions . . . 123

List of Figures

1.1 Neuromuscular system anatomy . . . 17
1.2 Muscle anatomy . . . 18
1.3 Cross-bridge cycle . . . 19
1.4 Muscles of the forearm . . . 21
1.5 Mid and distal transverse sections of the forearm . . . 22
1.6 Force relationship with sarcomere length and velocity . . . 24
1.7 Intracellular action potential in time and space . . . 39
1.8 Intracellular action potential, ion concentrations, current flow, and extracellular potential . . . 40
1.9 Current and isopotential lines of a dipole in (semi-)finite volume conductors . . . 41
1.10 Multiple dipole model of intracellular action potentials with end-of-fibre effect . . . 42
1.11 End-of-fibre effect at the motor unit action potential level . . . 44
1.12 Spatial filters attenuate end-of-fibre effects . . . 45

2.1 Interfacing motor neurons in the spinal cord non-invasively from the wrist . . . 52
2.2 Decoded far-field potentials from the wrist interface . . . 58
2.3 Retracing far-field potentials from the wrist to the forearm . . . 59
2.4 Offline finger classification performance at the wrist . . . 61
2.5 2D spatial distribution of the normalised amplitude of the EMG signals at the wrist. 62
2.6 Real-time finger classification performance at the wrist . . . 63
2.7 Feature space for the wrist electromyography signals and decomposed motor neuron firings from the online task training . . . 64

3.1 Experimental setup . . . 75
3.2 Proposed dynamic decomposition adaptation pipeline . . . 76
3.3 Whitening learning rate optimisation for simulated and experimental data . . . 78
3.4 MUAP tracking approach . . . 81
3.5 Dynamic neuromechanical simulations . . . 85
3.6 Detection of MN firings during simulated dynamics . . . 86
3.7 Decomposition adaptation performance in simulations . . . 87
3.8 Tracked experimental MUAPs across angles from the wrist and forearm . . . 88
3.9 Decomposition calibration for MUAP tracking across angles and properties . . . 89
3.10 Kullback-Liebler divergence error with respect to the calibration . . . 90
3.11 Detection of MN firings during experimental dynamic contractions from the wrist 92
3.12 Decomposition adaptation performance in experimental data . . . 93

A1.1 IsoKin-Wrist setup 109
A1.2 Dimensions of the isokinetic wrist system (bottom part) 110
A1.3 Dimensions of the isokinetic wrist system (top part) 111
A1.4 Dimensions of the isokinetic wrist system (hand platform) 112
A1.5 IsoKin-Wrist connection setup 113
A1.6 IsoKin-Wrist v1 Lite 119
A1.7 IsoKin-Wrist v1 Lite 120
A2.1 Proof of permission for Figure 1.3 124
A2.2 Proof of permissions for Figures 1.5, Figures 1.6, 1.7, 1.8, 1.10, 1.11, 1.12 125
A2.3 Confirmation of publication and licensing rights for Figure 1.1 126
A2.4 Confirmation of publication and licensing rights for Figure 1.2 127

List of Tables

1.1 Forearm muscles with innervation and function 23

A1.1 DOGA Brushed Geared DC motor (319.4862.30.00) specifications 114
A1.2 DC motor controller (BasicMicro RoboClaw 2x15A) specifications 115
A1.3 Emergency stop button voltage and current ranges 116
A1.4 Inductive proximity sensors (LJ12A3-4-Z/BX, Heschen) specifications 116
A1.5 Phidgets 5Kg load cells specifications 117
A1.6 PhidgetBridge 4-Input DAQ specifications 118
A2.1 A summary of the sources and copyright license of items included in the thesis. . 123

List of Abbreviations

ACh acetylcholine. 18, 20, 39

ADP adenosin diphosphate. 19, 20

AI artificial intelligence. 73, 107

ANOVA analysis of variance. 55, 56, 58, 60–62

ATP adenosin triphosphate. 18–20

CBSS convolutive blind source separation. 29–32, 34–37, 74

CKC convolutive kernel compensation. 29, 31, 34–37

CNS central nervous system. 16, 20, 27

CoV coefficient of variation. 34, 36, 58, 82–85, 89, 90, 96

DR discharge rate. 58, 82, 84, 85, 89, 96

EMG electromyography. 5, 9, 15, 16, 20, 27–30, 32–34, 36, 43–48, 50–68, 70–76, 94, 99–103, 106, 113

EPSP excitatory postsynaptic potential. 17, 18, 20

fastICA fast independent component analysis. 29, 31–34, 36

FDS flexor digitorum superficialis. 73, 74

FN false negative. 35, 36, 83, 92, 99

FP false positive. 35, 36, 83, 92, 99

IAP intracellular action potential. 18, 19, 38–40, 42, 43

ICA independent component analysis. 29, 33

IPSP inhibitory postsynaptic potential. 17

IPT innervated pulse train. 34, 35, 92

MN motor neuron. 8, 16–18, 20, 25–30, 33–38, 44–68, 70–74, 76, 77, 80, 82–94, 96–98, 100–108

MU motor unit. 20, 25, 27, 43

MUAP motor unit action potential. 7, 9, 20, 27, 28, 30, 34, 37, 38, 43–46, 48, 50–54, 59, 66, 71–74, 76, 81–85, 87–90, 92, 94–98, 100, 103–105, 107

MVC maximum voluntary contraction. 53, 55, 60, 75

NMSE normalised mean squared error. 81–87, 89–96, 98, 104, 107

PCA principal component analysis. 55

Pi inorganic phosphate. 19, 20

PNR pulse to noise tatio. 35, 36, 54–56, 58, 60, 66, 82–87, 89–91, 93, 96, 98, 99, 106

RoA rate of agreement. 35–37, 65, 73, 84–87, 91–94, 96–100, 102, 103

SFAP single fibre action potential. 19, 20, 40, 42, 43

SIL silhouette measure. 35, 36, 106

TP true positive. 35, 83, 92

Motivation

As we navigate through an increasingly digital world, the way we interact with technology is paramount, not just in shaping our conception of it but also in defining its functionality and user-friendliness. Traditional input methods, such as buttons, joysticks, keyboards, or touchscreens are designed to be physically actuated to perform a predefined task. While extremely effective in many scenarios, their compelling operation in emerging virtual and augmented realities remains to be seen. These physical interfaces tend to interrupt the sense of immersion in virtual reality and obtrude augmentative interactions, highlighting the demand for new control paradigms that more naturally mirror our movements and gestures. This pursuit has led to the exploration of neural interfaces for wearable consumer electronics.

Neural interfaces - initially conceived for rehabilitation applications - leverage knowledge of how the nervous system prepares, generates, and controls movement to ultimately develop seamless, intuitive, and information-rich interaction paradigms (Schwartz et al. 2006; Sorrell et al. 2021). Briefly, movement intent originates at various regions in the brain that account for factors such as context, experience, and motivation. The resulting motor planning is transformed into motor commands that are conveyed down the spinal cord and refined with feedback from sensory neurons for coordination. This neural code is propagated through the peripheral nervous system to activate muscles for movement. Therefore, neural interfaces to decode actions can be established at multiple levels in this neural pathway with different degrees of invasiveness depending on the application and/or lesion (Farina et al. 2023; Jackson et al. 2012; Lorach et al. 2023; Sorrell et al. 2021; Tonin et al. 2021).

Yet, the information bandwidth of neural interfaces increases with the level of invasiveness (Martini et al. 2020). For instance, over the last decades, invasive brain-computer interfaces have shown remarkable progress in the control prostheses (Collinger et al. 2013; Hochberg et al. 2006), exoskeletons (Benabid et al. 2019), and even the restoration of movement when paired with electrical stimulation (Bouton et al. 2016; Lorach et al. 2023) in proof of concept clinical studies. However, for general consumer applications the need of non-invasive technologies is crucial to address ethical concerns and attract the general public (Yuste et al. 2017).

An alternative approach to meet these requirements involves the detection of the neural code at the terminal layer of the nervous system where it is converted into muscle forces and actions (Holobar et al. 2021). Here, the electrical signals of spinal motor neurons are amplified by their innervated muscle fibres, triggering a chain of reactions that transform neural electrical signals into mechanical actions. Electrodes on top of the skin capture the overall muscle electrical

potential, the so-called surface electromyography (EMG) signal (Farina et al. 2016b). For this reason, EMG signals have been widely used to predict movement and force (Ahmadizadeh et al. 2021). However, enhanced control paradigms require the identification of the underlying motor neuron activity, rather than their collective and distorted ensemble (Farina et al. 2014b, 2023; Holobar et al. 2021). Recently, advanced decoding algorithms have made this possible by levering the strength of the motor neuron and muscle fibres connection (Ruff 2003; Wood et al. 2001), as well as properties of their electrical signals (Farina et al. 2016a). Hence, the identification of individual motor neuron activity from surface EMG signals (the so-called EMG decomposition) shows great promise for the development of non-invasive wearable interfaces for general consumer applications (Holobar et al. 2021).

Nevertheless, several challenges remain. For instance, the potential for motor neuron interaction at the wrist, a key site for wearable devices, is relatively unexplored. The wrist's suitability for wearable technology, due to the familiarity with wristwatches, is clear (Cho 2019; Fang et al. 2016). However, the applicability of existing EMG decomposition models to the wrist requires further investigation. While previous studies have predominately targeted muscle bellies for non-invasive motor neuron detection (Martinez-Valdes et al. 2023), electrodes at the wrist cover muscles' termination into tendons, which show distinct electrical properties (Dimitrova et al. 2006; Dumitru et al. 1991; Merletti et al. 2019; Stegeman et al. 1997). Additionally, most decomposition algorithms are designed for static conditions, where both force and joint position are fixed (Farina et al. 2016a), which contrasts sharply with the dynamics of natural movements. Consequently, the robustness of EMG decomposition to varying conditions is crucial for effective long-term human-computer interaction (Formento et al. 2021).

In this thesis, I aimed to develop a robust, non-invasive neural interface at the wrist, suitable for general consumer wearable systems. First, I validated the EMG decomposition model under the unique electrical characteristics of the muscle-tendon interface at the wrist, showcasing that the detected activity could accurately predict individual and combined finger presses in real-time. Thereafter, I characterised the modulation joint movement induced in the decomposition model. Leveraging these insights, I introduced online learning metrics to compensate these changes and reliably identify motor neuron activity under dynamic conditions. Taken together, these advancements expand our understanding and stability of non-invasive motor neuron interfacing at the most distal end of the neuromuscular system, bringing us closer to realising our vision of seamless, intuitive human-computer interaction for general consumer applications.

Chapter 1

Introduction

This chapter offers a broad overview of the fundamental concepts and prior research that served as basis to the original work presented in Chapters 2-3, which include their own specific introductions. Section 1.5 outlines the objectives and structure of the following chapters.

1.1 Neuromuscular system

Human movement requires the coordinated activation of multiple regions in the nervous system to transform motion intentions into actions. These commands, fine-tuned by multimodal sensory feedback, are delivered to the musculoskeletal system for their execution. This section, introduces the anatomy and physiology of the neuromuscular system that serves as basis for the decoding of neural motor commands (neural code) from electromyography (EMG) signals. In particular, it describes how the neural code is translated into force and movement (neuromechanical transduction) and the factors that influence this process.

1.1.1 Motor neurons

The central nervous system (CNS) orchestrates movement by translating action intent into motor commands that activate skeletal muscles. These converge to alpha motor neuron (MN) originating at the brain stem and ventral horn of the spinal cord, projecting out their axons to innervate muscle fibres (Enoka et al. 2016) (Figure 1.1). Notably, they provide a direct link between the CNS and skeletal muscles, constituting the final common pathway (Hounsgaard 2017).

Alpha MNs integrate inputs from supraspinal centres, spinal interneurons, and peripheral afferents to drive muscle contraction (Hounsgaard 2017). These set of descending connections, motor efferents, sensory afferents, and spinal interneurons form the spinal circuits. Some include important sensory feedback loops that regulate muscle contraction such as the Ia afferent group activated by the muscle spindle (proprioceptor sensitive to changes in muscle length), and the Ib afferent group driven by the increase in tendon tension with the excitation of the Golgi tendon organs (Moritani et al. 2004).

Most of the synaptic inputs MNs receive are ionotropic, which are driven by the binding of a neurotransmitter to ligand-gated channels in their dendrites' membrane. The main excitatory

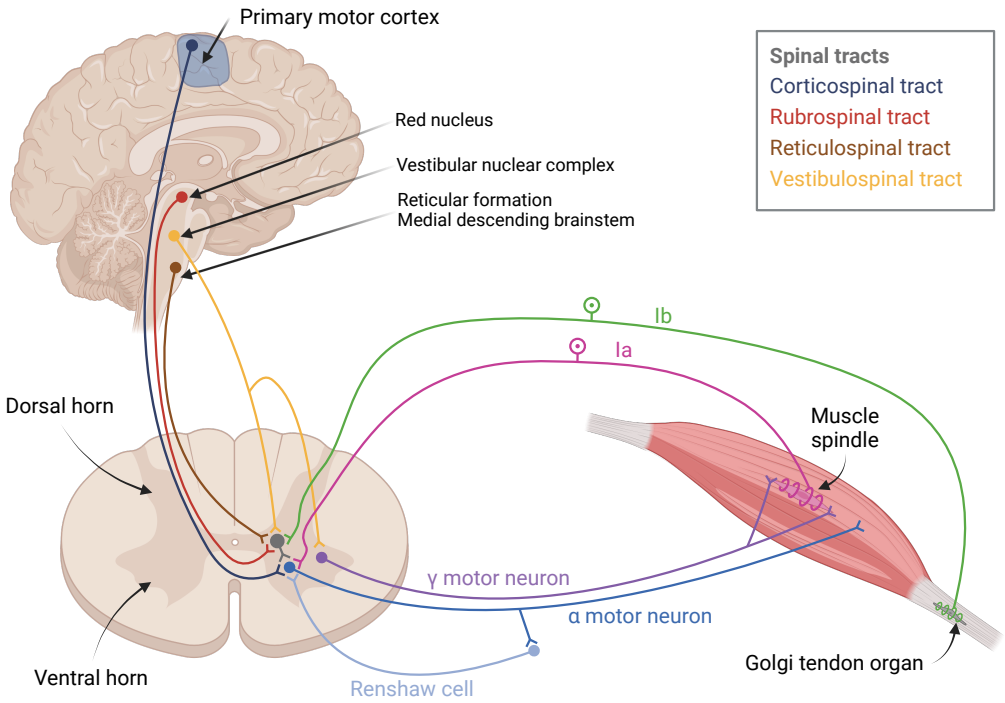

Figure 1.1: Neuromuscular system anatomy. Projections of the main cortico-spinal tracts (colour-coded) related to motion, and their spinal circuits innervating interneurons (grey), as well as alpha (blue) and gamma (purpule) motor neurons. Sensory feedback is integrated into the circuit via the Ia afferent detecting muscle length from the muscle spindle, and Ib afferent sensitive to muscle tension from the Golgi tendon organ. Created with BioRender.com

neurotransmitter is glutamate, while glycine and GABA produce inhibitory responses (Enoka et al. 2016). These bindings result in excitatory and inhibitory postsynaptic potentials (EPSP and IPSP, respectively) that either depolarise the membrane towards 0 mV or hyperpolarise it below their resting potential at approximately -70 mV (Enoka et al. 2016). An action potential is only triggered at the axon hillock (densely populated with voltage-gated Na^+ channels) if the spatio-temporal summation of these inputs surpasses the MN's excitatory threshold ($\sim$ -50 mV, Heckman et al. 2004). The overall communication process is highly regulated by neuromodulatory inputs whose neurotransmitters, such as serotonin and noradrenaline, bind metabolic receptors in the membrane of the MN. This, in turn, initiates second messenger reactions inside the MN that conditions its excitability to ionotropic inputs (Hounsgaard 2017).

When the excitatory potential threshold is reached, voltage-gated Na^+ channels open, producing an influx of Na^+ into the intracellular space that depolarises the membrane. This initiates a self-amplifying cycle, resulting in a significant surge in the membrane potential. Concurrently, this heightened potential prompts the influx of Ca^{2+} through the activation of voltage-gated Ca^{2+} channels (Heckman et al. 2012). The subsequent repolarisation phase is produced by the inactivation of Na^+ channels and the delayed opening of voltage-gated K^+ channels, which release K^+ to the extracellular space. This phase is known as the absolute refractory period of the MN, which is characterised by the inability to produce a subsequent action potential due to the inactive

state of the Na^+ channels. When they reset, the relative refractory period begins. Here, the combined K^+ efflux of different types of K^+ channels (including Ca^{2+} mediated), hyperpolarises the membrane potential below its resting state (Heckman et al. 2012). Consequently, during this phase, a larger stimulus would be needed to drive the potential above the excitation threshold and activate the voltage-gated Na^+ channels again. Finally, Na^+-K^+ and Ca^{2+} pumps restore the equilibrium concentrations of intracellular and extracellular ions consuming chemical energy (adenosin triphosphate, ATP) (Koester et al. 2021). Hence, the action potential is actively propagated along the axon to its terminal endings without amplitude decay. This process is accelerated by the myelin sheaths insulating MNs' axons, which produce saltatory conduction at the nodes of Ranvier (Koester et al. 2021).

1.1.2 Neuromechanical transduction

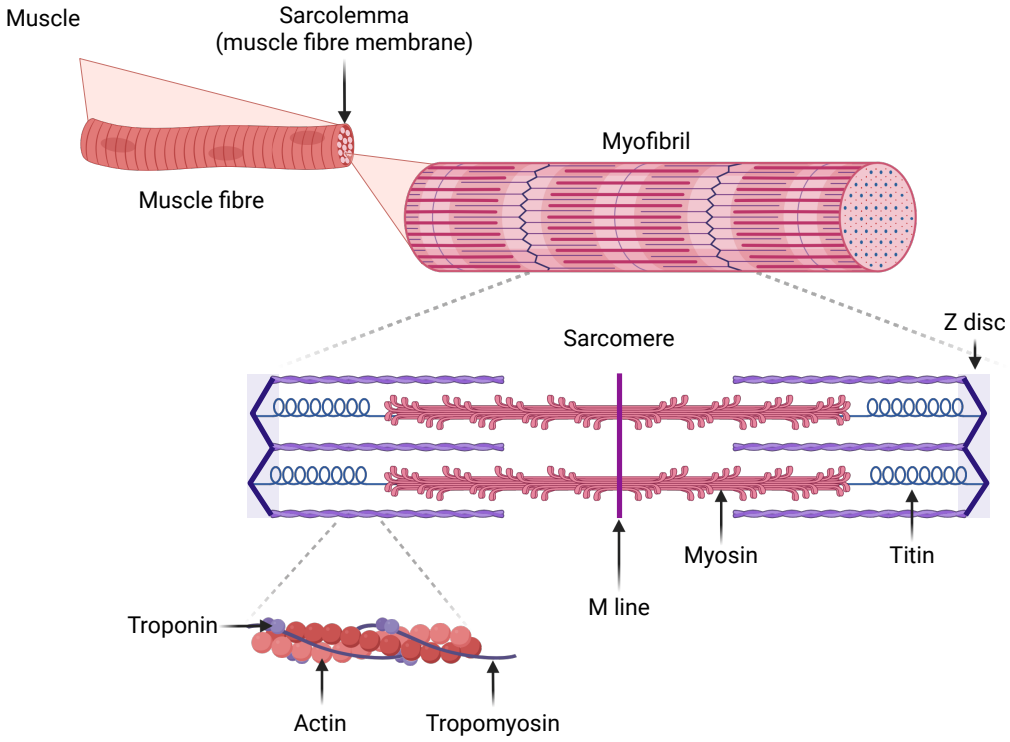

Figure 1.2: Muscle anatomy. Created with BioRender.com.

MN axons terminate at the neuromuscular junctions (also known as end-plates), where they innervate multiple muscle fibres. In here, the neuromechanical transduction of motor commands into force and movement is initiated. When a propagating action potential reaches the MN axon terminal, it activates voltage-gated Ca^{2+} channels in the MN. The influx of Ca^{2+} into the cytoplasm prompts the release of the acetylcholine (ACh) neurotransmitter into the synaptic cleft via excocytosis of synaptic vesicles. The binding of acetylcholine (ACh) to the receptors in the muscle fibre membrane (sarcolemma, Figure 1.2) causes a subsequent EPSP. This potential is normally large enough to trigger the activation of voltage-gated Na^+ channels, that produce an action potential along the sarcolemma. The former follows a monophasic profile when measured inside the sarcoplasm with respect to the extracellular space and is known as the intracellular

action potential (IAP) (Dumitru 2000). The corresponding extracellular potential constitutes the single fibre action potential (SFAP) (Dimitrova et al. 2006).

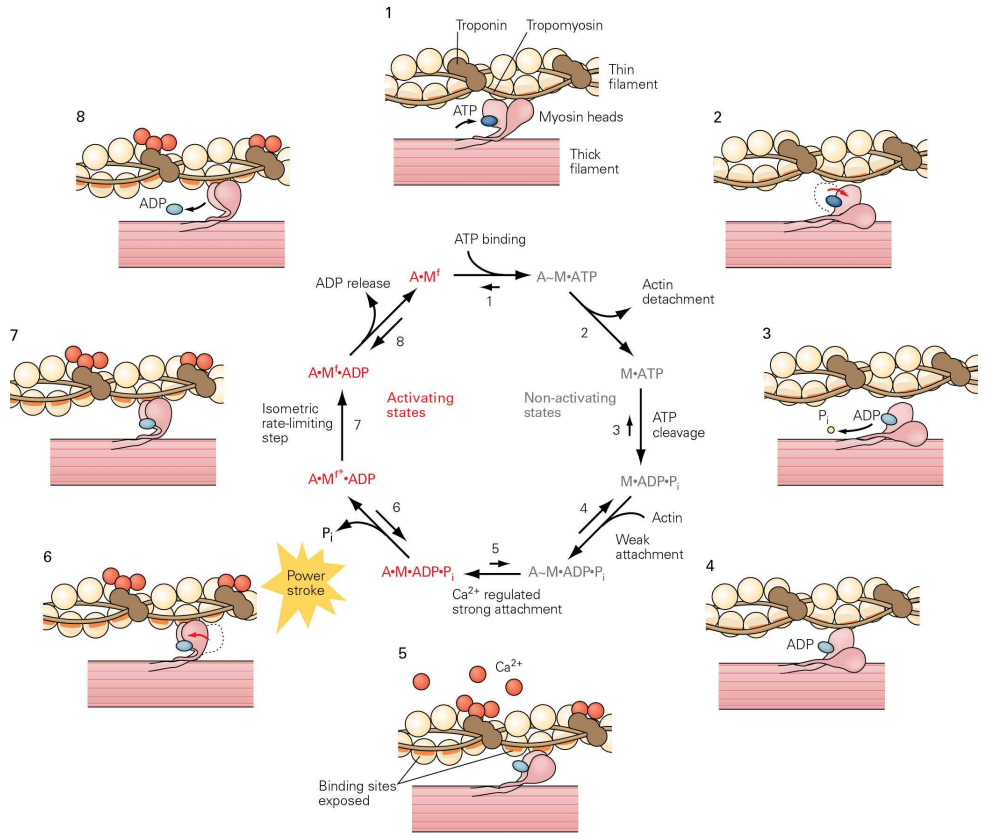

Figure 1.3: Cross-bridge cycle. The cycle starts in (1), where ATP binds the myosin heads, causing it to detach from actin (2). The hydrolisation of ATP (3) results in a weak bound between the myosin head and actin (4). The binding of Ca^{2+} (released from the propagation of an IAP) to troponin triggers the displacement of tropmyosin and the exposure of the myosin binding sites in the actin filament (5). In the power stroke (6), a cross-bridge is formed by the attachment of the two heads of myosin to the actin filament, which releases Pi. This process pulls the actin filaments in the sarcomere closer to each other generating 2 pN of structural force (7). The cycle ends (8) by the release of adenosin diphosphate (ADP). Reproduced from Enoka et al. 2012 with permission.

The propagation of this IAP through the sarcolemma and t-tubes results in the release of Ca^{2+} from the sarcoplasmic reticulum into the sarcoplasm, initiating the excitation contraction-coupling (Enoka et al. 2016). Myofibrils are comprised by the sequential arrangement of sarcomeres, which are the most basic organisation of muscle contractile proteins. Sarcomeres contain thick filaments (formed by multiple myosin filaments anchored to the sarcomere by titin proteins) and thin filaments (made of actin, tropomyosin, and troponin arranged in an helix). During the relaxed state, the majority of myosin heads are attached to adenosin diphosphate (ADP) and inorganic phosphate (Pi) from previous ATP hydrolysis (Powers et al. 2021). This is the start of the cross-bridge cycle (Huxley et al. 1954) (Figure 1.3). Briefly, the binding of Ca^{2+} to troponin causes the movement of tropomyosin, exposing myosin binding sites in the actin filament. When this myosin-actin attachment or cross-bridge occurs, it causes a power stroke that releases Pi. This process pulls the actin filaments in the sarcomere closer to each other resulting in force

production. The resulting mechanical force is transmitted to the skeletal system via the tendons. After the power stroke, ADP detaches from the myosin heads initiating the brief rigour state. Finally, myosin detaches from actin by the attachment of ATP, and enters the resting state by its hydrolysation into ADP and Pi. . The cross-bridge cycle is repeated while Ca^{2+} and ATP are available. Yet, Ca^{2+} pumps quickly reduce the intracellular Ca^{2+} concentration, requiring multiple action potentials to generate peak force.

The large amplitude of the ACh-driven EPSP ($\sim$ 75 mV, Fischbach et al. 2021) coupled with the low action potential threshold at the end-plate of the muscle fibre ($\sim$ -55 mV, due to the high density of Na^{+} voltage-gated channels, Fischbach et al. 2021), contribute to the safety factor of the neuromuscular junction (Ruff 2003; Wood et al. 2001). Due to the strength of this action potential transmission at the neuromuscular junction, MNs and its innervated muscle fibres are commonly thought of as a single functional entity, the motor unit (MU) (Clarac et al. 2011; Liddell et al. 1925; Sherrington 1925). Hence, the motor unit action potential (MUAP) is the summation of all SFAPs innervated by the same MN. Importantly, MUAPs represent amplified and delayed ($\sim$ 1 ms, Katz et al. 1997) potentials with a one-to-one correspondence with MN firings (Enoka et al. 2016). Thanks to this muscle fibre amplification, electrodes on top of the skin can detect the spatio-temporal summation of neighbouring MUAPs, attenuated by the tissue in between (i.e. the EMG signal, Enoka et al. 2016; Farina et al. 2016b). Advanced decoding algorithms enable the identification of the underlying individual MN firings from EMG signals (see Section 1.2), establishing a non-invasive neural interface with the output of the CNS. Importantly, the delay between the muscle fibre action potential and force generation ($\sim$200 ms of neuromechanical delay, Del Vecchio et al. 2018) gives the upper bound of acceptable decoder execution time, beyond which users perceive actions as lagged (Farrell et al. 2007).

1.1.3 Muscle and tendon anatomy at the forearm and wrist

In this thesis, recording electrodes were placed around the circumference of the wrist and thickest part of the forearm (see Chapters 2-3). Figure 1.4 depicts the muscles and tendons present at both locations, while Table 1.1 summarises their innervation and mechanical function. Electrodes on top of the skin primarily record the activity of the underlying superficial muscles. This way, electrodes on the thickest part of the forearm (Figure 1.5.B) were more subjected to the activity of the flexor carpi radialis, palmaris longus, flexor digitorum superficialis, flexor carpi ulnaris, flexor digitorum profundus, extensor carpi ulnaris, extensor digiti minimi, extensor digitorum, extensor carpi radialis brevis and longus, and the brachioradialis muscle. In contrast, the distal transverse section of Figure 1.5.C shows a dramatic change in anatomy as most muscles converge into tendons close to the wrist. In here, deeper muscles in the forearm such as the flexor digitorum superficialis and flexor policis longus become more accessible. While the more superficial layout of the tendons with respect to their bellies promotes the detection of their associated potentials, the significantly lower cross-sectional area can reduce the discrimination power of the decoding algorithms (Holobar et al. 2009).

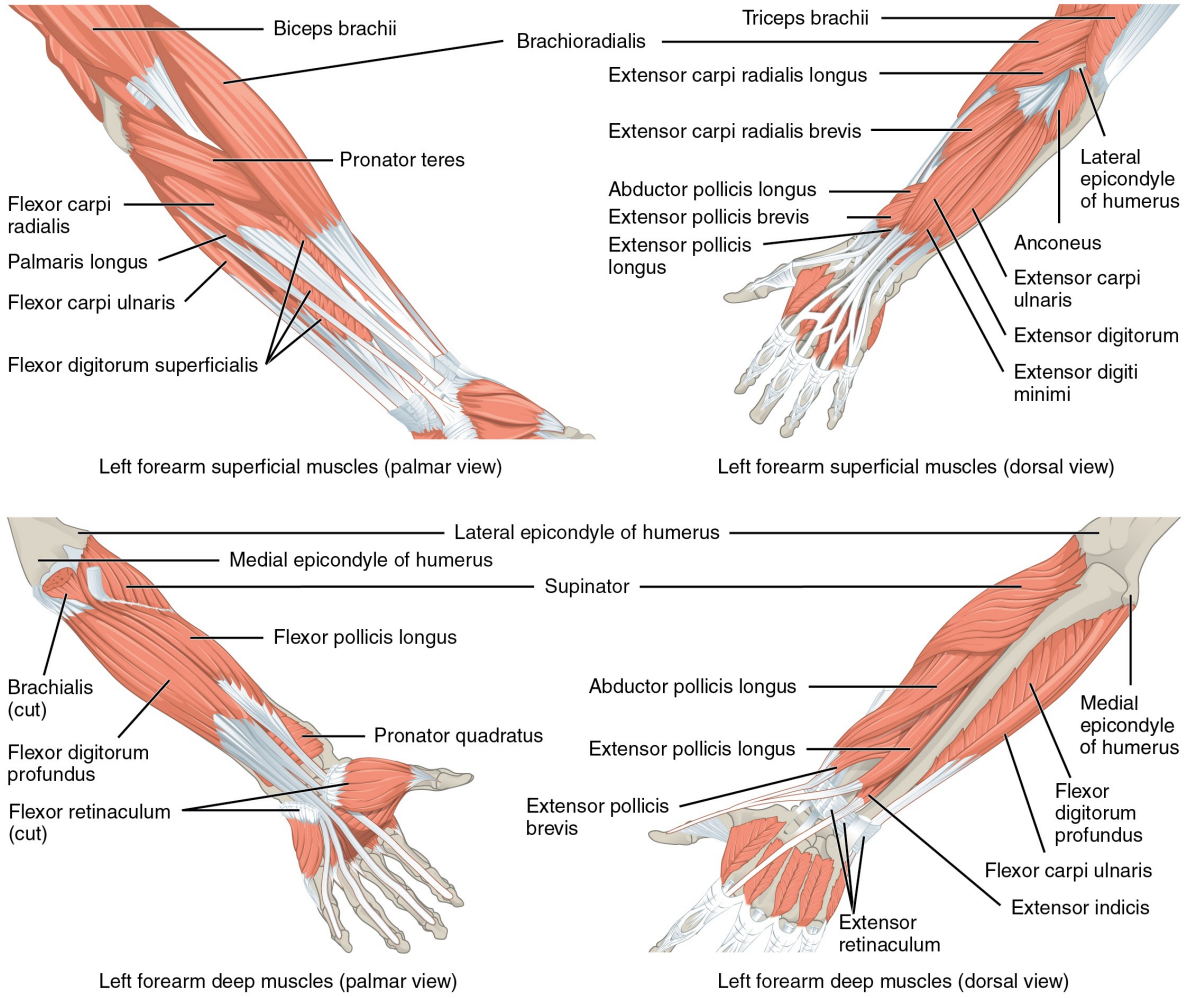

Figure 1.4: Muscles of the forearm. Superficial (top) and deep (bottom) muscles at the forearm from a palmar (left) and dorsal view (right) perspectives. Reproduced from Betts et al. 2022 with permission.

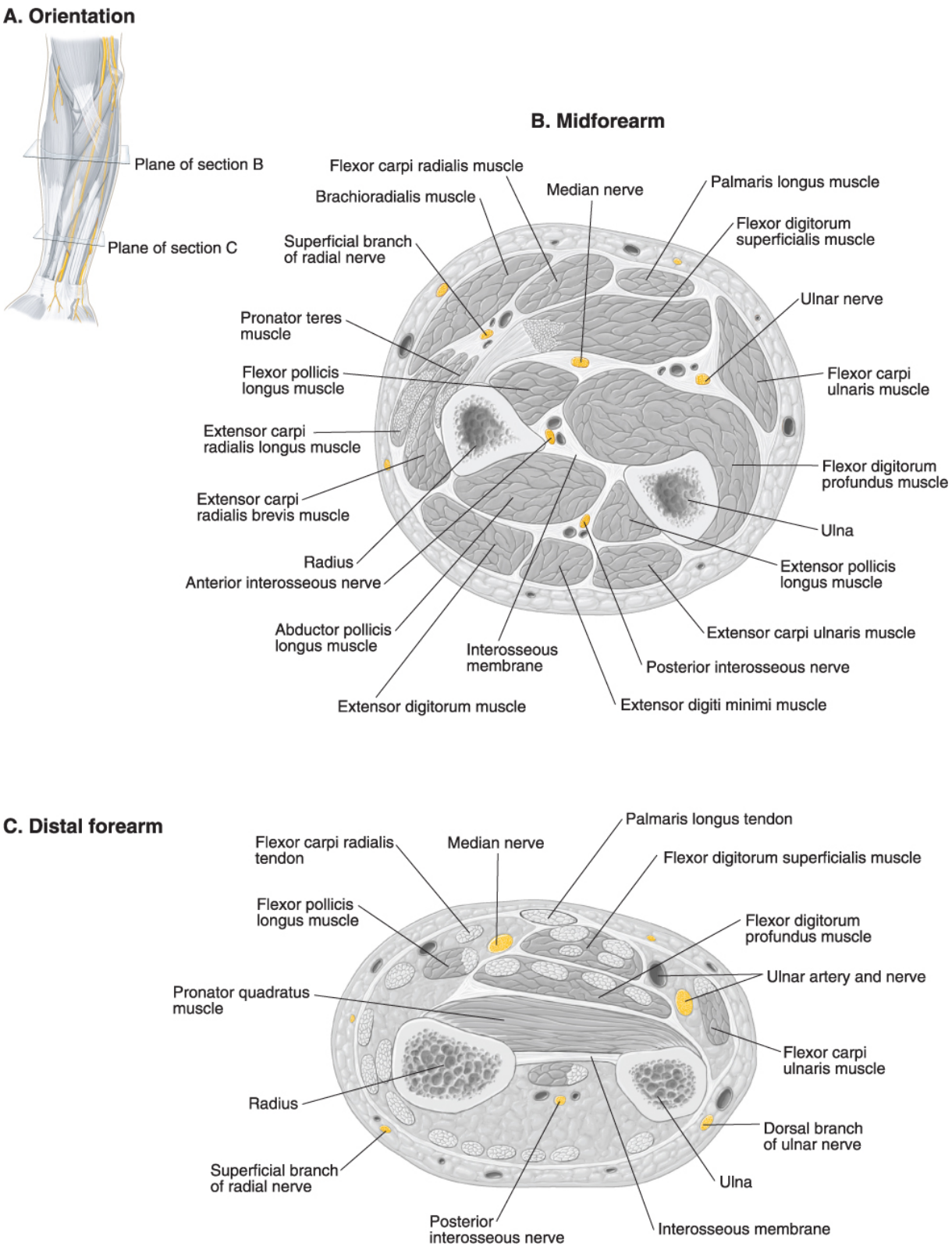

Figure 1.5: Mid and distal transverse sections of the forearm. Reproduced from Gest 2020 with permission.

Table 1.1: Forearm muscles with innervation and function

Muscle	Innervation	Action
Anconeus	Radial nerve	Extends forearm
Brachioradialis	Radial nerve	Flexes the elbow, assists in pronation and supination
Extensor carpi radialis longus	Radial nerve	Extends the wrist; abducts the hand
Extensor carpi radialis brevis	Radial nerve	Extends the wrist; abducts the hand
Extensor carpi ulnaris	Radial nerve	Extends the wrist; adducts the hand
Extensor digiti minimi	Radial nerve	Extends the metacarpophalangeal, proximal interphalangeal, and distal interphalangeal joints of the 5th digit
Extensor indicis	Radial nerve	Extends the index finger at the metacarpophalangeal, proximal interphalangeal, and distal interphalangeal joints
Extensor digitorum	Radial nerve	Extends the metacarpophalangeal, proximal interphalangeal, and distal interphalangeal joints of the 2nd–5th digits; extends wrist
Abductor pollicis longus	Radial nerve	Abducts the thumb at carpometacarpal joint
Extensor pollicis brevis	Radial nerve	Extends the thumb at the metacarpophalangeal joint
Extensor pollicis longus	Radial nerve	Extends the thumb at the interphalangeal joint
Supinator	Radial nerve	Supinates the forearm
Pronator quadratus	Median nerve	Pronates the forearm
Pronator teres	Median nerve	Pronates the forearm
Flexor carpi radialis	Median nerve	Flexes the wrist, abducts the hand
Palmaris longus	Median nerve	Flexes hand (at wrist) and tightens palmar aponeurosis
Flexor pollicis longus	Median nerve	Flexes the metacarpophalangeal and interphalangeal joints of the thumb
Flexor digitorum superficialis	Median nerve	Flexes the metacarpophalangeal and proximal interphalangeal joints
Flexor digitorum profundus	Median nerve (medial half acting on 1st-2nd digits) and Ulnar nerve (lateral half acting on 4th-5th digits)	Flexes the metacarpophalangeal, proximal interphalangeal, and distal interphalangeal joints
Flexor carpi ulnaris	Ulnar nerve	Flexes wrist, adducts hand

1.1.4 Force modulation

At a given time, the force produced by a muscle is proportional to the number of cross-bridges in a power stroke phase, and the force they generate. Four mechanisms, related to the state and transmission of the neural code, as well as the dynamics of the muscle contraction, modulate the force generation process. While they are described here independently for clarity, it is important to note that these processes occur concurrently.

1.1.4.1 Sarcomere length

Sarcomere length, and hence muscle length, determines the relative distance between actin and myosin filaments, conditioning the number of cross-bridges that can be formed and thus, the exerted force. This relationship is non-linear (Figure 1.6.a), with force peaking at moderate lengths and progressively decreasing with sarcomere shortening and lengthening. The reduced force at shorter lengths is caused by the overlap between thin filaments, which occludes potential binding sites. In contrast, sarcomere stretching pulls the thin filaments further apart reducing the potential contacts between myosin and actin. This effect tends to be less severe than binding site occlusion, as the forces produced during lengthening are typically larger than during shortening.

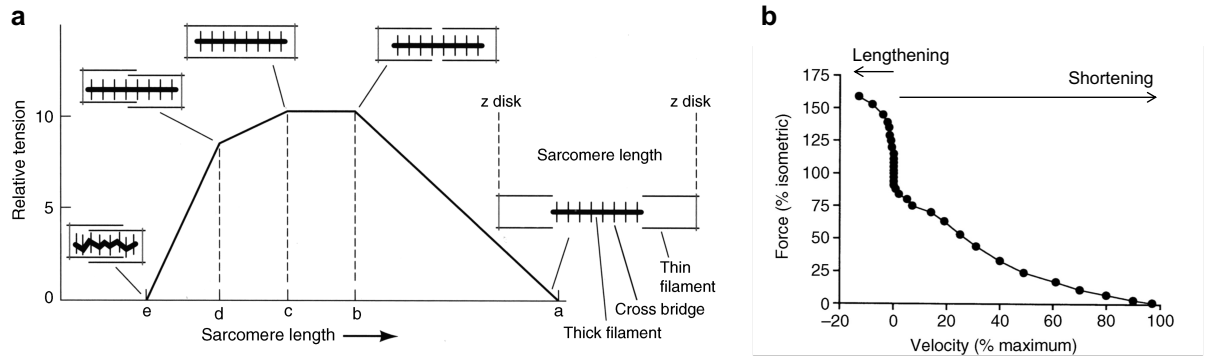

Figure 1.6: Force relationship with sarcomere length and velocity. (a) Sarcomere tension (force) with respect to its length. The relative position between the actin and myosin filaments conditions the number of cross-bridges and thus, the force. (b) Force velocity relationship during lengthening and shortening. Fast shortening contractions hinder the ability to form cross-bridges, reducing the force. In contrast, faster lengthening movements result in the contraction of titin increasing the force in the sarcomere. Adapted from Enoka et al. 2016 with permission.

Yet, measuring the sarcomere length in vivo can be challenging, and thus, their length is often inferred from the muscle-tendon unit. Typically, during concentric contractions, muscle fascicles contract, elongating the corresponding tendons (Kawakami et al. 1998). B-mode real-time ultrasound systems paired with force sensors and/or computer simulations enable the characterisation of the length changes of the muscle fascicles and tendons, as well as their force profile during dynamics (Fukashiro et al. 2006; Kawakami et al. 2006). In this regard, analyses on the gastrocnemius have shown that its fascicles can shorten up to 70% of their initial length during maximal isometric plantarflexion (Kawakami et al. 1998). In contrast, the fascicle length during peak concentric isometric force was $\sim$ 95% for the flexor digitorum superficialis and flexor carpi radialis (Hauraix et al. 2018), and $\sim$ 90% for the extensor carpi radialis (Goislard de Monsabert et al. 2020) with respect to their fascicle length at rest. In absolute terms, these values correspond

to a change in length of $\sim$ 1 cm and $\sim$ 1.5 cm for the flexor digitorum superficialis and flexor carpi radialis, respectively (Hauraix et al. 2018).

1.1.4.2 Contraction speed

While the previous section referred to the influence of sarcomere length at a given time, the dynamics of these length changes also modulate force production. Similarly to the sarcomere length, the relationship between force and velocity is non-linear and differs between shortening and lengthening contractions (Figure 1.6.b). During fast shortening contractions the efficiency of the cross-bridge formation decreases due to the fast efflux of Ca^{2+}, resulting in lower forces with respect to the neutral static position. In contrast, force increases and plateaus with speed during lengthening contractions. This effect is driven by the stretch of titin, increasing the tension in the sarcomere. The plateau is caused by the limited stretch of titin proteins driven by temporal attachments to actin filaments facilitated by Ca^{2+}.

In addition, contraction speed also affects the muscle-tendon interaction, affecting force production (Kawakami et al. 2006). For instance, countermovements or rebound actions are common in ballistic contractions, such as jumping, and are characterised by the stretch-shortening cycle (Komi 2003). The later refers to the pre-stretch (eccentric phase or countermovement) of the muscle-tendon unit subsequently followed by a quick shortening contraction (concentric phase). During the eccentric phase of this cycle, tendons elongate whereas the length of the fascicles remains almost constant. Subsequently, a concentric contraction is followed due to the fast recoil of the tendons. The later is referred as catapult action (Hof et al. 1983), where the tendons release their stored elastic energy. Hence, during the stretch-shortening cycle, the fascicles behave quasi-isometrically, taking advantage of the force-velocity relationship to produce high force (Fukashiro et al. 2006), while the speed of the contraction is driven by the dynamics of the tendons. The opposite occurs when the same action is performed without the countermovement (i.e. the length of the tendon remains constant, while the fascicles contract) (Fukashiro et al. 2006; Kawakami et al. 2006).

1.1.4.3 Recruitment: the size principle

MUs are recruited in an order manner, progressively increasing the exerted force (Henneman 1957). This effect is driven by the relative sizes of the MNs within a pool, and is known as Henneman's size principle (Henneman 1985). Based on Ohm's law, the excitability of a MN is proportional to their input synaptic current divided by their conductivity. MNs with more dendrites and a larger soma have greater conductivity, since they can accommodate more ion channels in their larger surface area, and experience reduced internal resistance due to their larger volumes. Hence, larger postsynaptic potentials are observed in smaller MNs for a given presynaptic current, favouring an orderly recruitment based on the excitation input.

These conductivity properties coupled with the higher force levels seen with recruitment, indicate that the MN and muscle unit sizes are related. In fact, it has been shown that the number of fibres in a muscle unit (innervation number) exponentially increases within the pool

when sorted based on recruitment. Taken together, these findings indicate that most MNs innervate smaller and weaker muscle units, with only few large and strong ones (Duchateau et al. 2022; Enoka 2019). Hence, in experimental recordings, the exerted force is used as a proxy for neural excitation. In fact, the force at which MNs start reliably discharging is known as recruitment threshold. Similarly, the derecruitment threshold corresponds to the force level at which a MN discharged last.

While electrical stimulation breaks the recruitment order, some studies have also reported a non-electrically induced disruption in human MNs (Basmajian 1963; Desmedt et al. 1981; Formento et al. 2021). Emerging conceptual frameworks suggest that these behaviours are associated to the distribution of common synaptic inputs (Farina et al. 2015; Negro et al. 2016b) across MN pools, which are driven by function rather than anatomical constraints (Hug et al. 2023). According to this, recruitment order would be preserved within each functional pool (Hug et al. 2023). Yet, the specific mechanisms governing this functional arrangement are not fully understood. Notably, the size principle dictates the order of recruitment, but its threshold value is not fixed. For instance, recruitment thresholds decrease during fast force demanding contractions to compensate the neuromechanical delay (Desmedt et al. 1979, 1978).

1.1.4.4 Rate coding

The action potential discharge rate of a MN also positively modulates the force. The associated frequent depolarisation of the muscle membrane causes a higher density of Ca^{2+} in the sarcomere, increasing the likelihood of a cross-bridge formation by attaching to troponin and exposing the actin binding sites. Yet, MNs discharge rates exhibit different behaviours depending on the task and dominating type of synaptic input (ionotropic vs neuromodulatory), and are influenced by factors such as age or training (Heckman et al. 2012).

Isometric contractions, which control for muscle length, have been widely used to study the interplay between recruitment and rate coding, among other physiological properties. The aforementioned processes happen concurrently, but their effects differ between force generation and reduction (Heckman et al. 2012). For instance, while MNs are orderly recruited, their derecruitment threshold is variable (Heckman et al. 2012) and their discharge rate tends to be lower during derecruitment than recruitment (De Luca et al. 1982a; Oya et al. 2009). This effect has been linked to neuromodulatory persistent inward currents (Oya et al. 2009) and longer action potential hyperpolarisation phases after continued activation (De Luca et al. 1982a; Oya et al. 2009; Wienecke et al. 2009).

During slow and moderate force increases in isometric contractions, the gain in peak discharge rate is inversely proportional to the recruitment order (Person et al. 1972; Westgaard et al. 2001). However, this trend is reversed at forces close to the maximum level (Moritz et al. 2005; Oya et al. 2009). Yet, the magnitude of the discharge rate also depends on the speed of force production. For instance, while peak discharge rates range between 30-50 pulses per second (pps) in isometric contractions (Enoka et al. 2016), these values more than double during ballistic

isometric contractions (Desmedt et al. 1979; Van Cutsem et al. 2005).

Sustained (fatiguing) isometric contractions alter these discharge patterns by concurrently decreasing the discharge rate of already active MNs while recruiting additional ones (Carpentier et al. 2001), or irregular firing patterns (Bawa et al. 2009). These effects are not regarded as intentional control strategies of the CNS but rather as a byproduct of fluctuations in the strength of ionotropic and neuromodulatory inputs (Bawa et al. 2009; Westad et al. 2003). In addition, these erratic behaviours are confounding factors for neural interfaces that tend to be avoided with shorter contractions and resting periods in the experimental protocols.

Finally, discharge rate is also modulated by changes in muscle fibre length due to the asymmetric force production during shortening and lengthening (Figure 1.6.a). While these effects are present in isometric contractions (Griffiths 1991; Ito et al. 1998), they are more evident in dynamic joint movements. The reduced force capacity during shortening contractions results in higher modulation with larger discharge rates and the temporal recruitment of new units (Pasquet et al. 2006). In contrast, during lengthening lower discharge rates have been observed (Duchateau et al. 2008). This effect has been consistent under different load scenarios (Heckman et al. 2012).

1.2 Electromyography

EMG is the technique that records the aggregated potential generated by active MUs. These signals can be acquired non-invasively using surface electrodes on top of the skin (Merletti et al. 2016) or invasively via intramuscular electrodes (Adrian et al. 1929; Basmajian et al. 1962; Muceli et al. 2022). Importantly, the properties of the recorded signals are influenced by anatomical and detection system factors (Farina et al. 2002a, 2016b). For instance, the tissue in between the fibres and the recording electrodes behaves as a volume conductor, attenuating the amplitude (Roeleveld et al. 1997) and decreasing the bandwidth (Farina et al. 1999) of the underlying potentials. Since this effect increases with the relative distance between the sources and the electrodes, intramuscular EMG recordings are less affected by it (Merletti et al. 2008). While other aspects such as the muscle fibre length, electrode montage, or position with respect to the muscle also affect the characteristics of the EMG signals (Farina et al. 2002a, 2008, 2016b), these are discussed in Section 1.3 in the context of EMG recordings over the muscle-tendon interface. Instead this section focuses on the models that facilitate the extraction of neural information from EMG signals. Specifically, the following subsections introduce the EMG generative model and its decomposition into MN firings through blind source separation, with an emphasis on surface recordings.

1.2.1 EMG generative model

EMG signals represent the spatiotemporal summation of the underlying MUAPs (De Luca 1979), which are modelled as finite impulse response filters that are active at the time of each MN firing (Farina et al. 2016a; Holobar et al. 2007b). Mathematically, this is expressed as:

$$x_i(k) = \sum_{l=0}^{L-1} \sum_{j=1}^{N} h_{ij}(l) s_j(k-l) + n_i(k) \tag{1.1}$$

where x_i represents the EMG signals of the ith channel (M in total), k is the discrete time, h_{ij} is the jth MUAP (N in total) recorded at the ith channel, L corresponds to the MUAP duration, $s_j = \sum_r \delta(k - \varphi_{jr})$ is the jth MN spike train with discharge times at φ_{jr}, and n_i is the additive noise at channel i. Therefore, Equation 1.1 describes a multiple input - multiple output system, with M observations of the convolutive mixture of N sources. Equation 1.1 can be simplified as:

$$\mathbf{x}(k) = \sum_{l=0}^{L-1} \mathbf{H}(l)\mathbf{s}(k-l) + \mathbf{n}(k) \tag{1.2}$$

where $\mathbf{x}(k) = [x_1, x_2, ..., x_M]^T$ is the matrix of concatenated EMG observations, $\mathbf{s}(k) = [s_1, s_2, ..., x_N]^T$ is the concatenated MN spike trains, and $\mathbf{H}(l)$ is the lth sample of the MUAPs observed across all channels and MNs ($M \times N$).

To further simplify the inversion problem, the convolutive mixture of Equation 1.2 can be unravelled into an instantaneous one by appending to each variable their respective $R-1$ delayed versions (Holobar et al. 2007b, 2001a), resulting in:

$$\tilde{x_j}(k) = [x_j(k), x_j(k-1), ..., x_j(k-R)], \quad j = 1, 2, ..., M \tag{1.3}$$

$$\tilde{n_j}(k) = [n_j(k), n_j(k-1), ..., n_j(k-R)], \quad j = 1, 2, ..., M \tag{1.4}$$

$$\tilde{s_i}(k) = [s_i(k), s_i(k-1), ..., s_i(k-L-R+1)], \quad i = 1, 2, ..., N \tag{1.5}$$

$$\tilde{h_{ij}} = \begin{bmatrix} h_{ij}[0] & h_{ij}[1] & \cdots & h_{ij}[L-1] & 0 & \cdots & 0 \\ 0 & h_{ij}[0] & \cdots & h_{ij}[L-2] & h_{ij}[L-1] & \cdots & 0 \\ \vdots & \vdots & \ddots & \vdots & \vdots & \ddots & \vdots \\ 0 & 0 & \cdots & h_{ij}[0] & h_{ij}[1] & \cdots & h_{ij}[L-1] \end{bmatrix} \tag{1.6}$$

for each channel and source. This can then be rewritten into matrix form as:

$$\tilde{\mathbf{x}}(k) = [\tilde{x}_1(k), \tilde{x}_2(k), ..., \tilde{x}_M(k)]^T \tag{1.7}$$

$$\tilde{\mathbf{n}}(k) = [\tilde{n}_1(k), \tilde{n}_2(k), ..., \tilde{n}_M(k)]^T \tag{1.8}$$

$$\tilde{\mathbf{s}}(k) = [\tilde{s}_1(k), \tilde{s}_2(k), ..., \tilde{s}_N(k)]^T \tag{1.9}$$

$$\tilde{\mathbf{H}} = \begin{bmatrix} \tilde{h}_{11} & \cdots & \tilde{h}_{1n} \\ \vdots & \ddots & \vdots \\ \tilde{h}_{m1} & \cdots & \tilde{h}_{mn} \end{bmatrix} \tag{1.10}$$

where $\tilde{\mathbf{x}}(k)$ and $\tilde{\mathbf{n}}(k)$ have dimensions $MR \times K$, $\tilde{\mathbf{s}}(k)$ is of size $N(L+R-1) \times K$ and $\tilde{\mathbf{H}}$, $MR \times N(L+R-1)$. This results into the instantaneous mixture of:

$$\tilde{\mathbf{x}}(k) = \tilde{\mathbf{H}}\tilde{\mathbf{s}}(k) + \tilde{\mathbf{n}}(k) \tag{1.11}$$

1.2.2 EMG decomposition

EMG decomposition refers to the pseudo-inversion of Equation 1.2 to identify the underlying MN firings from an observed set of EMG signals, which in the absence of noise is formulated as:

$$\tilde{\mathbf{s}}(k) = \tilde{\mathbf{A}}\tilde{\mathbf{x}}(k) \tag{1.12}$$

where $\tilde{\mathbf{A}}$ correspond to the separating matrix or pseudo-inverse of $\tilde{\mathbf{H}}$, and $\tilde{\mathbf{s}}(k)$ are the estimated sources.

While many approaches have been proposed for the identification of the underlying MN firings such as template matching (De Luca et al. 2006; Nawab et al. 2010), or deep learning methods (Clarke et al. 2021; Wen et al. 2021), this section focuses on blind source separation approaches, which offer methods to disentangle the linear mixture presented in Equation 1.11 under a small set of assumptions. Although multiple algorithms have been proposed in the literature such as the convolutive kernel compensation (CKC, Holobar et al. 2004, 2007a,b), the fast independent component analysis (fastICA) framework (Chen et al. 2016b), and the convolutive blind source separation algorithm (CBSS, Negro et al. 2016a); common steps can be found across modalities. This section provides an overview of the separation from an independent component analysis (ICA) perspective, with an emphasis on CBSS as it was the algorithm used in the original work presented in Chapters 2-3.

1.2.2.1 Requirements and ambiguities

The main two assumptions of ICA (Hyvärinen et al. 2001e) are that 1) sources are statistically independent which can be expressed in terms of their joint probability density function:

$$p(s_1, s_2, ..., s_N) = p_1(s_1)p_2(s_2)...p_N(s_N) \tag{1.13}$$

where $p_j(s_j)$ is the marginal distribution of the jth source; and that 2) they follow a non-gaussian distribution (with at most one gaussian source in the mixture, Thomas et al. 2006). In addition the number of observations should be greater or equal to the number of sources (Hyvärinen et al. 2001e). From these limited set of assumptions, ICA can extract the underlying sources up to a scaling and permutation factors (Hyvärinen et al. 2001e).

One of the most common formulations of ICA uses the maximisation of the non-gaussianity of the sources (measured by higher-order statistics such as the skewness or kurtosis, or the negentropy) to solve the inverse problem (Hyvärinen et al. 2001b). The rationale of this approach leverages the central limit theorem, by which the sum of two independent random variables tends to follow a more gaussian distribution than the original marginal ones. Therefore, non-gaussianity can be used as a proxy for independence. This heuristic formulation is preferred from an EMG

decomposition perspective due to the specific properties of the MN spike trains (Farina et al. 2016a), rather the equivalent maximum likelihood estimation (Hyvärinen et al. 2001c) of the independent components or the minimisation of the their mutual information (Hyvärinen et al. 2001d). While MN spikes trains in Equation 1.11 are highly sparse (supergaussian distribution with positive kurtosis), they are not fully statistically independent due to the presence of common inputs and their concatenated delayed versions. Still, due to the sparsity of the spike trains and the effect of the MNs refractory period, the discharge times of different MNs are uncorrelated or weakly correlated with only few overlapping spikes (Farina et al. 2016a). Furthermore, the effect of the MUAP length (L) and extension factor (R) on the spike trains' cross-correlation between the original and delayed version is minimal if $L + R - 1 < T_j$ where T_j is the average interspike interval of the jth MN (Farina et al. 2016a). Notably, the extension factor is further constrained by $MR \geq N(L + R)$ to account for the ratio between the unextended observations (M) and active sources (N). In practice, both conditions are met when using high-density EMG electrodes (typically $\geq$64 electrodes) by setting $R = 1000/M$ (Negro et al. 2016a). This results in an extension factor $R \leq 16$ samples, which is lower than the interspike interval of fastest MNs ($\sim$57 samples for 35 pps maximum discharge rate sampled at 2000 Hz sampling frequency).

Therefore, EMG decomposition maximises the sparsity of the sources (as a type of non-gaussianity), under the constraint that the identified sources must be weakly correlated (rather than independent) and have a unique MUAP representation different from that of other MNs (Farina et al. 2016a; Negro et al. 2016a).

1.2.2.2 Algorithm

EMG decomposition is divided in three processes: 1) whitening where the extended EMG signals are uncorrelated, 2) iterative computation of the separation vectors (sources are estimated one at a time) and 3) spike detection to identify the timings of the action potential firings. At this point it is assumed that signals have zero mean so a preconditioning step includes centring the observed EMG signals $x(k) = x(k) - E\{x(k)\}$ before applying the extension factor.

1.2.2.2.1 Whitening To simplify the separation problem, the centred and extended EMG signals ($\tilde{\mathbf{x}}(k)$) are whitened, such that the signals are uncorrelated and with covariance matrix equal to the identity. This process can be expressed as:

$$\tilde{\mathbf{z}}(k) = \mathbf{V}\tilde{\mathbf{x}}(k) \text{ such that } \mathbf{R}_z = E\{\tilde{\mathbf{z}}(k)\tilde{\mathbf{z}}^\top(k)\} = I \tag{1.14}$$

where $\tilde{\mathbf{z}}(k)$ are the extended and whitened EMG signals, $\mathbf{V}$ is the whitening matrix, $\mathbf{R}_z$ is the covariance matrix of the whitened signals, and I is the identity matrix. In CBSS, whitening matrix (V) is typically computed via eigenvalue decomposition (Negro et al. 2016a) or singular value decomposition (Barsakcioglu et al. 2021). In the former, V is computed as:

$$\mathbf{V} = \mathbf{U}\mathbf{D}^{-1/2}\mathbf{U}^\top \tag{1.15}$$

where $\mathbf{U}$ and $\mathbf{D}$ are the eigenvectors and eigenvalues, respectively, of the covariance matrix $\mathbf{R}_z = \mathbf{U}\mathbf{D}\mathbf{U}^\top$. Alternatively, singular value decomposition is a generalisation of the previous approach, where V is calculated as:

$$\mathbf{V} = \mathbf{U}_1\mathbf{D}^{-1/2}\mathbf{U}_2^\top \tag{1.16}$$

where $\mathbf{R}_z = \mathbf{U}_1\mathbf{D}\mathbf{U}_2^\top$, with $\mathbf{U}_1$ and $\mathbf{U}_2$ representing orthonormal bases, and $\mathbf{D}$ the diagonal matrix with the singular values of $\mathbf{R}_z$. In both cases, this step is regularised by an estimate of the noise variance in the signals equivalent to half of the lowest eigen or singular values (Belouchrani et al. 1997).

Finally, in CKC the inverse of the covariance is used $\mathbf{V} = \mathbf{R}_x^{-1}$ instead (Holobar et al. 2004, 2007a).

1.2.2.2.2 Separation vectors Whitening constrains the mixing matrix to an orthogonal space, reducing the number of parameters of the separation matrix to approximately half (Hyvärinen et al. 2001e). Therefore, the estimated sources ($\tilde{\mathbf{s}}(k)$) can be computed as:

$$\tilde{\mathbf{s}}(k) = \tilde{\mathbf{A}}\tilde{\mathbf{x}}(k) = \mathbf{B}\mathbf{V}\tilde{\mathbf{x}}(k) = \mathbf{B}\tilde{\mathbf{z}}(k) \tag{1.17}$$

where $\mathbf{B}$ represents the orthogonal separating matrix. The computation of $\mathbf{B}$ is done by extraction where each separation vector $\mathbf{b}_j$ is computed separately. In CBSS, the separation vectors are computed by maximising estimates of the negentropy using fastICA due to its fast convergence.

Briefly, negentropy ($J(\mathbf{s})$) is a measure of differential entropy ($H(\mathbf{s})$):

$$J(\mathbf{s}) = H(\mathbf{s}_{gauss}) - H(\mathbf{s}) \tag{1.18}$$

$$H(\mathbf{s}) = -\int p_{\boldsymbol{s}}(\boldsymbol{\xi}) \log p_{\boldsymbol{s}}(\boldsymbol{\xi}) d\boldsymbol{\xi} \tag{1.19}$$

where $p_{\boldsymbol{s}}$ is the probability density function of $\boldsymbol{s}$, and $\mathbf{s}_{gauss}$ represents a gaussian random variable with the same correlation (and covariance) as $\mathbf{s}$. Importantly, the entropy of a variable following a gaussian distribution has the largest entropy among all other possible distributions with equal variance. Therefore, the negentropy is a measure of non-gausssianity, that is only zero for gaussian variables and positive otherwise. However, computing the negentropy following Equation 1.18 can be unfeasible as it requires prior knowledge of the probability density function, which is not always available. Instead, the negentropy can be approximated using higher-order cumulants (Hyvärinen et al. 2001b, pages 113-115) resulting in:

$$J(\boldsymbol{s}) \approx \frac{1}{12}E\{\boldsymbol{s}^3\}^2 + \frac{1}{48}\text{kurt}(\boldsymbol{s})^2 \tag{1.20}$$

where $\boldsymbol{s}$ is assumed to be zero mean and unit variance. Yet, the use of high-order polynomial functions is prone to errors due to outliers, and so, non-quadratic approximations of $\boldsymbol{s}^3$ and $\boldsymbol{s}^4$ (derived from the kurtosis) are used instead, yielding into:

$$J(\boldsymbol{s}) \approx k_1 \left[E\{G_1(\boldsymbol{s})\}\right]^2 + k_2 \left[E\{G_2(\boldsymbol{s})\} - E\{G_2(\boldsymbol{\nu})\}\right]^2 \tag{1.21}$$

where ν is a standard gaussian, k_1 and k_2 positive constants, and G_1 and G_2 represent non-quadratic odd and even functions, respectively. Therefore, in Equation 1.21 the first term is an estimate of the square of the skewness (related to the symmetry of the underlying distribution), while the second one is an estimate of the square of the kurtosis. In practice, only one contrast function tends to be used depending on the properties of the sources. In EMG decomposition, common choices of the contrast functions include (Caillet et al. 2023; Negro et al. 2016a):

$$G_1(\boldsymbol{s}) = \frac{1}{3}\boldsymbol{s}^3 \tag{1.22}$$

$$G_2(\boldsymbol{s}) = \log\cosh(\boldsymbol{s}) \tag{1.23}$$

While Equation 1.22 is a higher-order polynomial directly proportional to the skewness, it has shown fast convergence in EMG decomposition due to the spiking nature of the sources (Negro et al. 2016a). CBSS uses these cost functions with fastICA to update the separation vectors ($\mathbf{b}$) in the direction that maximises the non-gaussianity of the sources. The convergence of fastICA is cubic (or at least quadratic, see Appendix A in Hyvarinen 1999) as it can be derived as an application of the Newton's method on the gradient of the optimisation function to accelerate convergence.

First, the optimisation problem is formulated with an additional constraint to ensure that the variance of the sources is constant and equal to one (i.e. $E\{(\mathbf{b}^\top\tilde{\mathbf{z}})^2\} = \|\mathbf{b}\|^2 = 1$). Using the Lagrange conditions this results in:

$$\mathcal{L}(\mathbf{b}, \lambda) = -E\{G(\mathbf{b}^\top\tilde{\mathbf{z}})\} + \lambda\left[\|\mathbf{b}\|^2 - 1\right] \tag{1.24}$$

where $\mathcal{L}$ is the loss function (to minimise, and as such, note the negative sign in front of the contrast function), and λ is the Lagrange multiplier. Applying Newton's method to the previous Equation 1.24 results in the following update rule:

$$\mathbf{b}' \leftarrow \mathbf{b} - \left[\frac{\partial^2\mathcal{L}(\mathbf{b}, \lambda)}{\partial\mathbf{b}^2}\right]^{-1} \frac{\partial\mathcal{L}(\mathbf{b}, \lambda)}{\partial\mathbf{b}} \tag{1.25}$$

where the new parameter value $\mathbf{b}'$ is in the direction of the steepest decrease in $\mathcal{L}(\mathbf{b}, \lambda)$. Hence, taking the first- and second-order derivatives of the loss function in Equation 1.24 yields:

$$\frac{\partial\mathcal{L}(\mathbf{b}, \lambda)}{\partial\mathbf{b}} = -E\{\tilde{\mathbf{z}}g(\mathbf{b}^\top\tilde{\mathbf{z}})\} + 2\lambda\|\mathbf{b}\|\frac{\mathbf{b}}{\|\mathbf{b}\|} \tag{1.26}$$

$$= -E\{\tilde{\mathbf{z}}g(\mathbf{b}^\top\tilde{\mathbf{z}})\} + \beta\mathbf{b} \tag{1.27}$$

$$\frac{\partial^2 \mathcal{L}(\mathbf{b}, \lambda)}{\partial \mathbf{b}^2} = -E\{\tilde{\mathbf{z}}\tilde{\mathbf{z}}^\top g'(\mathbf{b}^\top \tilde{\mathbf{z}})\} + \beta \mathbf{I} \tag{1.28}$$

$$\approx -E\{\tilde{\mathbf{z}}\tilde{\mathbf{z}}^\top\} E\{g'(\mathbf{b}^\top \tilde{\mathbf{z}})\} + \beta \mathbf{I} \tag{1.29}$$

$$= -E\{g'(\mathbf{b}^\top \tilde{\mathbf{z}})\}\mathbf{I} + \beta \mathbf{I} \tag{1.30}$$

where $\beta = 2\lambda$, g is the first-order derivative of the contrast function G ($g_1(\boldsymbol{s}) = \boldsymbol{s}^2$ and $g_2(\boldsymbol{s}) = \tanh(\boldsymbol{s})$ for the contrast functions in Equations 1.22-1.23, respectively), and g' is the second-order derivative of the contrast function G ($g_1'(\boldsymbol{s}) = 2\boldsymbol{s}$ and $g_2'(\boldsymbol{s}) = \text{sech}^2(\boldsymbol{s})$ for the contrast functions in Equations 1.22-1.23, respectively). Note that the approximation in Equation 1.29 is possible because the observations are prewhitened. This is crucial since it makes the second-order derivative of the loss a diagonal matrix, and hence, makes its inversion tractable during the update rule in Equation 1.25. Yet, further simplifications can be carried out by inserting Equations 1.27 and 1.30 in Equation 1.25 resulting in:

$$\mathbf{b} \leftarrow \mathbf{b} + \frac{E\{\tilde{\mathbf{z}} g(\mathbf{b}^\top \tilde{\mathbf{z}})\} - \beta \mathbf{b}}{\beta - E\{g'(\mathbf{b}^\top \tilde{\mathbf{z}})\}} \tag{1.31}$$

after some algebraic manipulation and omitting $\mathbf{I}$ for simplicity. Multiplying both sides by $\beta - E\{g'(\mathbf{b}^\top \tilde{\mathbf{z}})\}$ leads to the following fastICA update rule (Hyvarinen 1999):

$$\mathbf{b} \leftarrow E\{\tilde{\mathbf{z}} g(\mathbf{b}^\top \tilde{\mathbf{z}})\} - E\{g'(\mathbf{b}^\top \tilde{\mathbf{z}})\}\mathbf{b} \tag{1.32}$$

Note that the scaling factor $\beta - E\{g'(\mathbf{b}^\top \tilde{\mathbf{z}})\}$ on the new parameter $\mathbf{b}$ is disregarded since the separation vectors are normalised after each iteration. While Equation 1.32 iteratively finds the solution for a single separation vector, it does not guarantee the orthogonality of a set of separation vectors when more than one source is estimated. To ensure this, after each iteration of Equation 1.32, Gram-Schmidt deflationary orthogonalisation is applied (Hyvarinen 1999):

$$\mathbf{b}_i \leftarrow \mathbf{b}_i - \sum_{p=1}^{i-1} (\mathbf{b}_i^\top \mathbf{b}_p)\mathbf{b}_p \tag{1.33}$$

where $\mathbf{b}_i$ is the current separation vector, and $\mathbf{b}_p$ represents the set of previously identified separation vectors. This step is followed by the separation vector normalisation:

$$\mathbf{b}_i \leftarrow \frac{\mathbf{b}_i}{\|\mathbf{b}_i\|} \tag{1.34}$$

This orthonormalisation process avoids the repeated convergence over the same separation vector. Furthermore, it also makes fastICA akin to projection pursuit when finding the most nongaussian projections (rather than independent components) of the data (Hyvärinen et al. 2001b, pages 197-198). While the original ICA model assumes the independence of the sources, no such assumption is made in projection pursuit. Hence, in the EMG decomposition model where the independence of the MN firings is not guaranteed, fastICA returns the projection pursuit directions with maximum nongaussianity.

In the fastICA framework proposed by Chen et al. 2016b the separation vectors are computed as described in Equation 1.32. However, Gram-Schmidt deflationary orthogonalisation is replaced by the symmetric counterpart:

$$\mathbf{B} \leftarrow (\mathbf{B}\mathbf{B}^\top)^{-1/2}\mathbf{B} \tag{1.35}$$

and coupled with a peel-off strategy to avoid finding repeated separation vectors. The latter involves the estimation of the MUAP waveforms for the identified spike trains. This is attained by spike-triggered averaging the EMG signals over time windows (typically 25-40 ms corresponding to the length of the MUAP, Chen et al. 2016b) centred around the timing of each firing. Thereafter, the computed MUAPs are convolved by their respective spike train and their contribution is subtracted from the EMG signals.

In the CKC algorithm, particularly in its updated gradient version (Holobar et al. 2007a), the separation vectors are computed by taking the natural gradient over the skewness contrast function of Equation 1.22, resulting in:

$$\mathbf{b} \leftarrow \mathbf{b} - \eta E\{\tilde{\mathbf{z}} g(\mathbf{b}^\top \tilde{\mathbf{z}})\} \tag{1.36}$$

where η represents the learning rate of the update rule. While Equations 1.32 and 1.36 share some similarities, the convergence of fastICA is faster than that of the natural gradient (Hyvärinen et al. 2001c, pages 208-211).

Regardless of the approach, the computation of the separation vectors is an iterative process that is exited if either the convergence tolerance or the maximum number of iterations are reached.

1.2.2.2.3 Spike detection To detect the MN firing times from the obtained projected vectors ($\mathbf{b}^\top \tilde{\mathbf{z}}$), also referred as innervated pulse trains (IPTs) in the literature (Holobar et al. 2007a; Negro et al. 2016a), a k-means clustering algorithm is used in CBSS to separate the spike peaks from the baseline (two clusters) for each MN estimate (Negro et al. 2016a). Then, the MN firing times are computed as the timings of the values within the cluster with the largest centroid.

Other approaches include the progressive inclusion of the highest spikes when computing a given separation vector (see the so-called probabilistic separation of superimposed pulse trains in Holobar et al. 2007a,b), or the valley-seeking clustering approach proposed by Chen et al. 2018 for the fastICA framework to separate the spikes of different MNs in a mixed source.

1.2.2.2.4 Reinforcement In CBSS, there is a second iterative process to improve the quality of the detected MN firings, where the separation vectors and estimated MN firings times are iteratively updated until the coefficient of variation (CoV, ratio between the standard deviation and the mean) of the interspike intervals is minimised. The rationale of this criteria is based on the fact that under isometric contractions at constant force, MNs fire at a constant rate and therefore, their CoV should be low. In fact, it has been shown that values of CoV $> 30\%$

are associated with low decomposition accuracy (Holobar et al. 2010). At each iteration the separation vectors are updated as:

$$\mathbf{b}_j \leftarrow \frac{1}{R_j}\sum_{r=1}^{R_j}\tilde{\mathbf{z}}(\varphi_{jr}) \tag{1.37}$$

where R_j corresponds to the total number of spikes detected for source j, and φ_{jr} are the firings times computed as described in the previous section. This process is analogous to the original formulation of the CKC algorithm (Holobar et al. 2007b) that estimates the MN firings from the cross-correlation (second-order method) between the sources and the observations after whitening.

Finally, the amplitude of the detected spikes vs baseline is also evaluated as a proxy for decomposition accuracy. For instance, CBSS uses the silhouette measure (SIL - measured in normalised units, n.u.):

$$SIL = \frac{d_{spikes} - d_{base}}{\max(d_{spikes}, d_{base})} \tag{1.38}$$

where d_{spikes} and d_{base} represent the point-to-centroid distances for the spikes and baseline clusters, respectively. Typically, only the IPTs that have SIL > 0.9 are kept for further analyses (Negro et al. 2016a).

On the other hand, in CKC, the pulse to noise ratio (PNR - measured in decibels, dB) is used instead (Holobar et al. 2014):

$$PNR = 10\log\frac{E\{\mathbf{s}^2(k)|\mathbf{s}(k) \in c_{spikes}\}}{E\{\mathbf{s}^2(k)|\mathbf{s}(k) \in c_{base}\}} \tag{1.39}$$

where $\mathbf{s} = \mathbf{b}^\top\tilde{\mathbf{z}}$ are the IPTs, and c_{spikes} and c_{base} represent the spikes and baseline classes respectively. In this case only estimates with PNR > 30 dB are kept, since those values have been associated with $> 90\%$ sensitivity and $< 2\%$ false alarm rates (Holobar et al. 2014).

1.2.2.3 Validation

To assess the performance of any decomposition algorithm, its estimated MN firings are compared to a reference one. The most common metric for performance evaluation is the rate of agreement (RoA - measured in percentage) between the estimated and reference firings:

$$RoA = \frac{TP}{TP + FP + FN} \cdot 100\% \tag{1.40}$$

where TP represents the true positive (i.e. correctly identified spikes present in the estimated and reference trains), FP are the false positive (i.e. spikes detected only in the estimated train), and FN stands for the false negative (i.e. spikes in the reference that were missed in the estimate).

Other popular metrics include:

$$\text{precision} = \frac{TP}{TP + FP} \cdot 100\% \tag{1.41}$$

$$\text{sensitivity} = \frac{TP}{TP + FN} \cdot 100\% \tag{1.42}$$

$$\text{false alarm rate} = \frac{FP}{FP + FN} \cdot 100\% \tag{1.43}$$

While the ground truth MN firings are not often available in practice, these metrics have been extensively used in controlled conditions to extensively validate the presented decomposition model and algorithms. One approach relies on simulations, which often couple a model of MN recruitment, firing, and force generation (Fuglevand et al. 1993), with a computational model of the propagation of the action potentials over the volume conductor Farina et al. 2004. Although this simulations are arguably an oversimplification of the actual physiology, they enable the systematic evaluation of the effect of noise in the model (Holobar et al. 2014, 2007a,b).

Another approach, dubbed the two-source validation, uses two independent decomposition approaches on the same dataset and compares their outputs. The rationale is that if two independent methods converge towards the same solution, is highly likely that the commonly detected spikes are true MN firings. Chen et al. 2016a followed this strategy to compare the CKC algorithm and the fastICA framework, showing an average of ∼11 common MNs with ∼98% RoA between the two methods when decomposing experimental surface recordings.

Finally, the gold-standard approach involves the concurrent recording of surface and intramuscular EMG signals. In this case, decomposition performance over the surface recordings is compared against matched MNs detected from the intramuscular electrodes. Holobar et al. 2010 used this approach to validate the CKC algorithm showing $\geq 84\%$ RoA between the estimated and reference spike trains across different muscles and excitation levels. Similarly, Negro et al. 2016a showed that CBSS provided $> 90\%$ RoA with respect to the intramuscular MNs across multiple excitation levels for the first dorsal interosseous muscle.

In physiological studies, where the ground truth is not available, the PNR, SIL, and CoV are commonly used as proxies for decomposition accuracy. In addition, the decomposition output is visually inspected and manually edited (Enoka 2019). This process typically involves the recalculation of the separation vectors after visually inspecting for FP and FN (Del Vecchio et al. 2020a). Crucially, the final result after manual validation is highly consistent across trained operators (Hug et al. 2021).

1.2.2.4 Reliability and robustness

The calibrated decomposition parameters can reliably identify MNs across repetitions within the same session (Martinez-Valdes et al. 2016) enabling the generation of large data sets to study MNs behaviour. In terms of long term performance, decomposition algorithms enable the reliable identification of MNs across sessions ($\sim 40\%$ of the total MNs were identified over two sessions,

with half of those tracked across three different sessions, Martinez-Valdes et al. 2017), even as far apart as a month (Del Vecchio et al. 2019a). In these cases, tracking or matching MNs across sessions is based on the 2D correlation between their corresponding MUAPs (computed via spike-triggered averaging), where assignment is performed if the MUAPs similarities exceed a predefined threshold (Del Vecchio et al. 2019a; Martinez-Valdes et al. 2016, 2017). Hence, this process compares the spatial representation of the identified MUAPs when a direct comparison of the firings is not possible. However, this approach relies on precise electrode placement across sessions.

1.2.2.5 Real-time implementation

Importantly, the identification of MN firings as described in Subsection 1.2.2.2 requires tens of seconds of data due to the sparsity of the firings (Glaser et al. 2013). When coupled with the iterative calculation of the separation vectors, this yields execution times lasting a few minutes (Holobar et al. 2009). Consequently, the decomposition algorithm requires an initial calibration phase before its implementation in real-time for neural interfacing. This idea was presented in the seminal work of Glaser et al. 2013, who tackled the computational complexity by first initialising (calibrating) the CKC algorithm over few seconds of data (∼3 s), and then updating the whitening (inverse of the covariance) and separation vectors over new batches of data. Their approach resulted in ∼90% RoA with the offline version with an execution time of ∼70 ms per ∼120 ms batches (60 channels, 10 extension factor, for an average of 4 MNs, with an Intel Core 2 Quad, 2.66 GHz and 4 Gb), which was below the threshold defined by the neuromechanical delay (∼200 ms, Del Vecchio et al. 2018). Importantly, Glaser et al. 2013 also found that longer calibration segments resulted in a larger number of identified MNs.

Based on this, Barsakcioglu et al. 2021, 2018 proposed the direct application of the decomposition parameters previously computed by CBSS from an extended calibration phase (>40 s) to new batches of data to further reduce the execution time. Their approach resulted in >90% RoA with the corresponding offline version across different muscles, and between MNs concurrently detected from surface and intramuscular recordings (Barsakcioglu et al. 2021). Notably, this was accomplished with a maximum latency of ∼4 ms per ∼120 ms batches (192 channels, 5 extension factor, with an Intel Core i7, 4.5 GHz and 16 Gb), significantly reducing the execution time and enabling more complex postprocessing for real-time neural interfacing. This strategy was also applied to the CKC algorithm for its real-time implementation (Chen et al. 2020c).

1.2.2.6 Limitations

While decomposition algorithms have unveiled novel prospects in electrophysiology and motor control, it is pertinent to acknowledge and address existing limitations.

First, the decomposition model of Equation 1.12 assumes that the mixing model is static, i.e. that the MUAP representations of the underlying MNs are constant in the recording. Hence, conditions that alter the MUAP waveforms are challenging for decomposition algorithms. For instance, muscle fatigue characterised by a reduction in sarcolemma excitability leads to a decline

in action potential amplitude and conduction velocity (Dimitrova et al. 2003; Enoka et al. 1992). Similarly, changes in muscle and surrounding volume conductor geometries induced by muscle fibre shortening and lengthening during dynamic contractions, also alter the recorded MUAPs (Merletti et al. 2001). This elucidates why almost all non-invasive studies of MNs have been performed under isometric conditions (Farina et al. 2016a). At the beginning of this work, only the approach proposed by Glaser et al. 2013 offered a strategy to accommodate to such dynamics by updating the decomposition parameters based on new batches of data. Yet, this method could not identify newly recruited MNs. Since then, other decomposition approaches have emerged to tackle MN identification during dynamic contractions (Chen et al. 2020a; Glaser et al. 2019; Kramberger et al. 2021; Yeung et al. 2024). More details on this topic can be found in Chapter 3.

Second, decomposition algorithms tend to identify MNs whose MUAPs exhibit higher amplitudes, either by innervating a high number of fibres (such as MNs recruited at higher excitation levels) (Holobar et al. 2009) or due to their more superficial territories closer to the recording sites (Holobar et al. 2010). To compensate for this effect, Francic et al. 2021 proposed the transfer of the separation vectors from low to higher excitation levels (albeit efficiency depends on the muscle anatomy). Alternatively, Caillet et al. 2022a developed a framework to expand the detected MN pool by combining experimentally identified MNs firings with a realistic MN pool model (based on leaky integrate-and-fire MNs) for which the mathematical relationships between the electrophysiological parameters are known (Caillet et al. 2022b).

Finally, blind source separation algorithms require a high number of channels to avoid a severely undetermined system (more sources than observations) and to enhance the spatial resolution of the system to differentiate similar MUAPs (Farina et al. 2016a, 2008). Recently, Caillet et al. 2023 showed that the density of the electrode grid (up to 2mm), its size, and the number of electrodes (up to 256) consistently increased the number of identified MNs (even across different excitation levels). Importantly, this approach identified a larger number of early recruited MNs, also compensating the previous decomposition bias.

1.3 Recordings at the muscle-tendon interface: the end-of-fibre effect

While muscle bellies have been traditionally targeted for non-invasive MN identification (Martinez-Valdes et al. 2023), electrodes at the wrist cover the muscle-tendon interface. Here, the extinction of the IAP causes a non-propagating component in the MUAP that is known as end-of-fibre effect (Dumitru 2000; Farina et al. 2002b; Stegeman et al. 1987). This section covers the biophysical principles that explain this phenomenon. Particularly, the following subsections introduce the leading and trailing dipole model of the IAP that facilitates the understanding of this effect, borrowing notions from electromagnetism theory. The last subsection describes the properties of the end-of-fibre effect at the MUAP level.

1.3.1 Leading and trailing dipole model of the IAP

As described in Section 1.1.2, when sufficient amounts of ACh at the neuromuscular junction bind the receptors at the sarcolemma, they activate voltage-gated channels causing the influx of Na^+ into the sarcoplasm. This produces an IAP ($\sim$ 2 ms, Rodriguez-Falces 2015) that depolarises a portion ($\sim$ 10 mm, Rodriguez-Falces 2015) of the sarcolemma. Notably, due to the location of the neuromuscular junction in the muscle fibre, two mirrored IAPs are generated, propagating in opposite directions from the end-plates to the tendon endings (Figure 1.7).

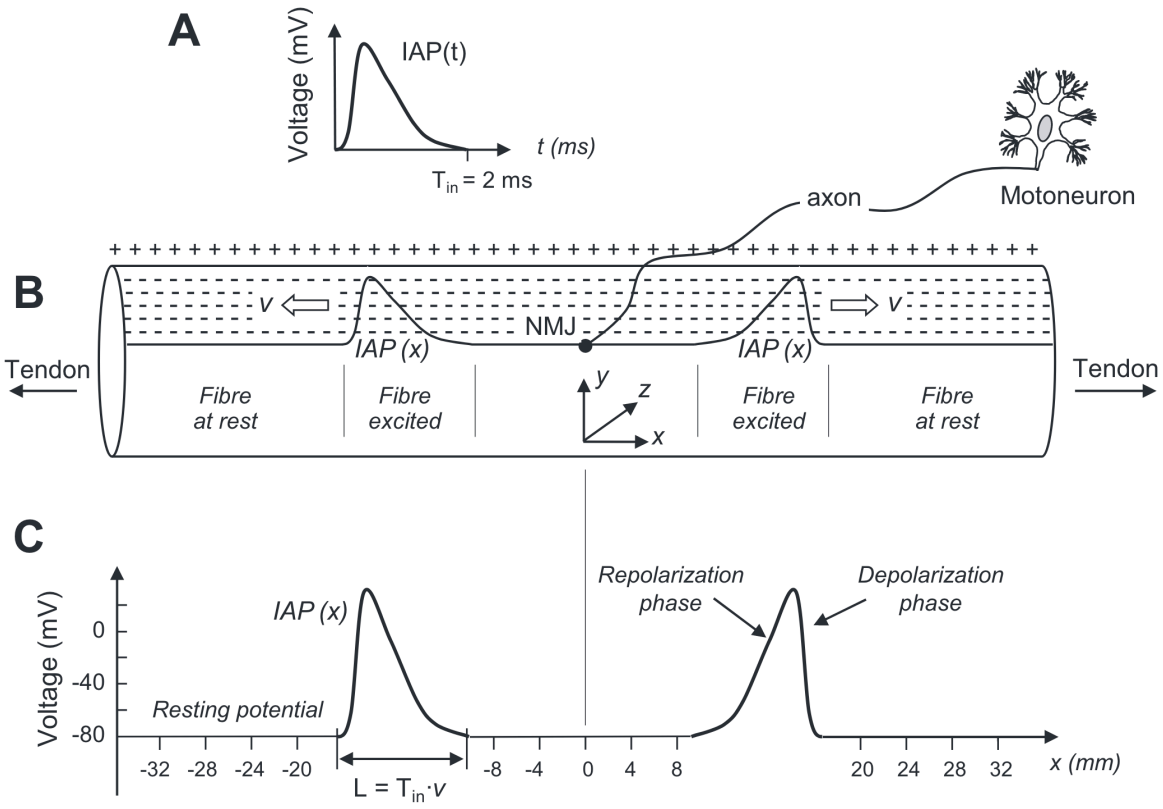

Figure 1.7: Intracellular action potential (IAP) in time and space. (a) Temporal profile of the IAP. (b) Depiction of the spatial propagation of two mirrored IAP in opposite directions from the neuromuscular junction to the tendon endings at velocity (v). (c) Equivalent spatial profile of the IAP at the time of (b). Reproduced from Rodriguez-Falces 2015 with permission.

The positive ionic influx of Na^+ over an area can be modelled as a current density that flows from the extracellular space (positively charged) into the sarcoplasm (negatively charged). Once inside, the current propagates axially through the fibre until it is drawn back to the extracellular space by the delayed K^+ efflux during the repolarisation phase. This flow is closed by the subsequent propagation of the IAP, that drives the current back into the sarcoplasm. Figure 1.8.a-c shows the temporal profile of an IAP (with the Na^+ and K^+ conductances), their respective concentrations in the muscle fibre, and their associated current flows.

In electromagnetism, the regions current flows from and to are known as current sources and sinks, which are assigned with 'positive' and 'negative' voltages, respectively. Based on this, the

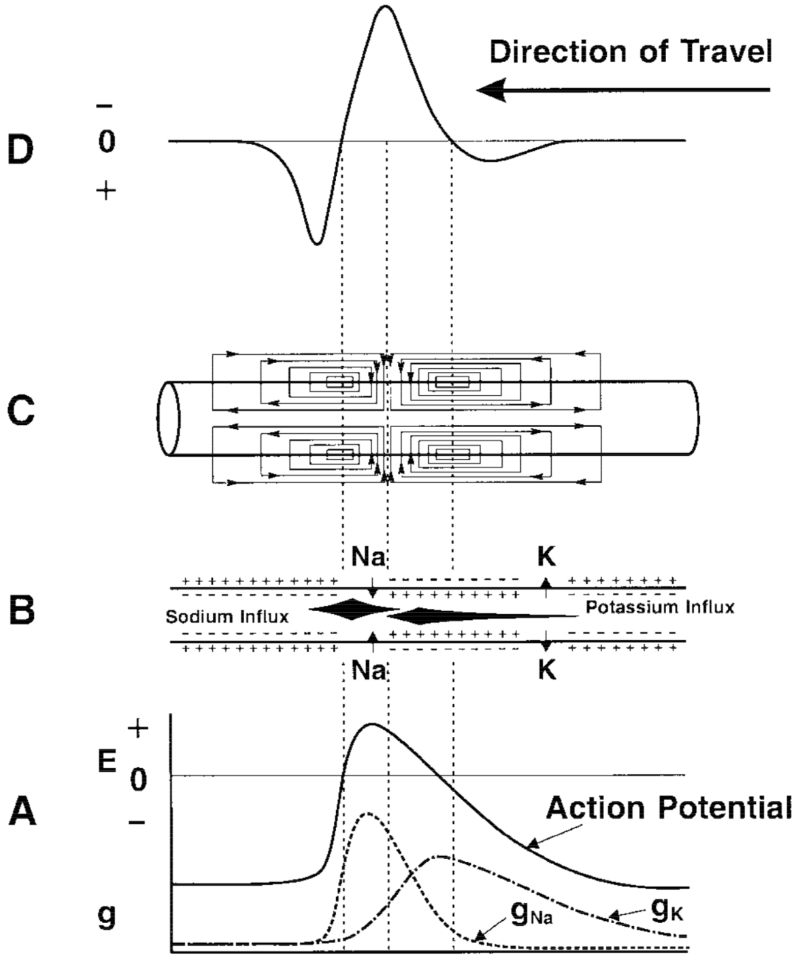

Figure 1.8: Intracellular action potential (IAP), ion concentrations, current flow, and extracellular potential. (a) Temporal profile of an IAP with the Na^+ and K^+ conductance. (b) Spatial propagation of the depolarised zone in the muscle fibre along wit the concentrations of Na^+ and K^+. (c) Generated ionic current flow into the muscle fibre through the sink and out through the source. (d) Corresponding extracellular potential (source-sink-source potential with positive values facing downwards for convention). Reproduced from Dumitru 2000 with permission.

corresponding extracellular potential (SFAP) follows a 'source-sink-source' profile (Figure 1.8.d) with two positive potentials (facing downward for convention) separated by a negative phase corresponding to the current sink (Dumitru 2000). By separating the sink into two distinct negative regions, the resulting potential can be modelled as the one generated by two consecutive dipoles (expressed as $+-$) with opposite polarity, i.e. a quadrupole (represented as $+--+$) or tripole when combining the negative phases ($+-+$) (Nunez et al. 2006). This is known as the leading and trailing dipole model, based on the direction of propagation (Dumitru et al. 1993).

1.3.2 Far-field potentials and the end-of-fibre effect

Notably, the properties of electric dipoles, particularly at finite volume conductors, elucidate some of the characteristics of the recorded SFAPs. In the context of an electric dipole placed in a finite volume conductor, Stegeman et al. 1997 defined far-field potentials as those who exhibit

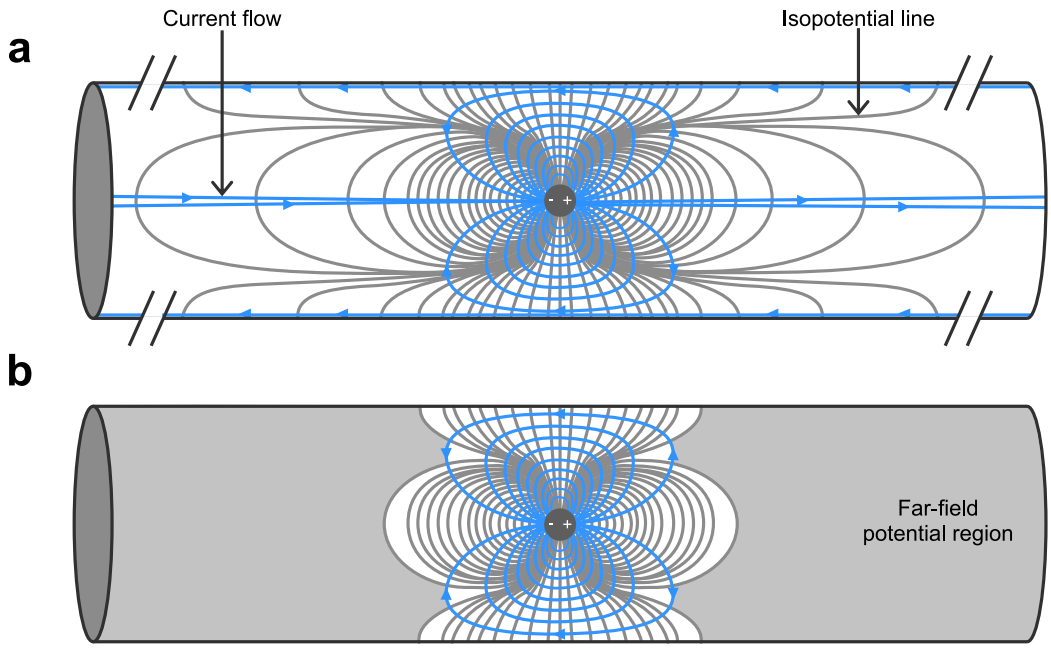

Figure 1.9: Current (blue) and isopotential (grey) lines of a dipole in (semi-)finite volume conductors. (a) Dipole current source in a cylinder of infinite length. While the radius of the cylinder constrains the current flow radially, its infinite length allows the current to flow axially from the positive pole through the central axis, returning close to the walls back to the negative pole. The infinite decrease in current with distance from the poles generates a voltage gradient across the length of the cylinder that prevents the appearance of a far-field region. (b) Same as in (a) but in a cylinder of finite length. In this case, the constrained length limits the asymptotical decrease in current, which translates in a region with nearly constant nonzero potential (grey-shaded area) corresponding to the far-field potential. Representation inspired from Stegeman et al. 1997.

constant amplitude, polarity, morphology and latency at large distances from the dipolar source, regardless of the specific recording location. In contrast, in the near-field potential region, the distance to the source could alter those four properties (Stegeman et al. 1997). To showcase this effects, Figure 1.9 depicts the current flow and isopotential lines of a dipole in a cylinder of infinite (a) and finite (b) lengths. In Figure 1.9.a the walls of the cylinder constrain the radial but not the axial current flow. This results in current being drawn through the central axis of the positive pole, progressively splitting and returning next to the cylinder walls back to the negative pole. Notably, the current density progressively decreases with the distance from the source, generating a voltage gradient along the length of the cylinder that also decreases with the distance to the source (more separated isopotential lines). In contrast in Figure 1.9.b, the limited length of the cylinder constrains the current decay, generating a region of almost constant nonzero potential (shaded area in Figure 1.9.b) corresponding to the far-field potential.

Therefore, according to the leading and trailing dipole model described above, both dipoles exhibit a far-field potential region due to the finite volume conductor (in this case the muscle fibre). However, since the dipoles are oriented with opposite polarities, their far-field potentials cancel each other (under the assumption of equal electrical dipole moments) or become negligible with respect to the near-field potential components (in case of asymmetry in their electrical

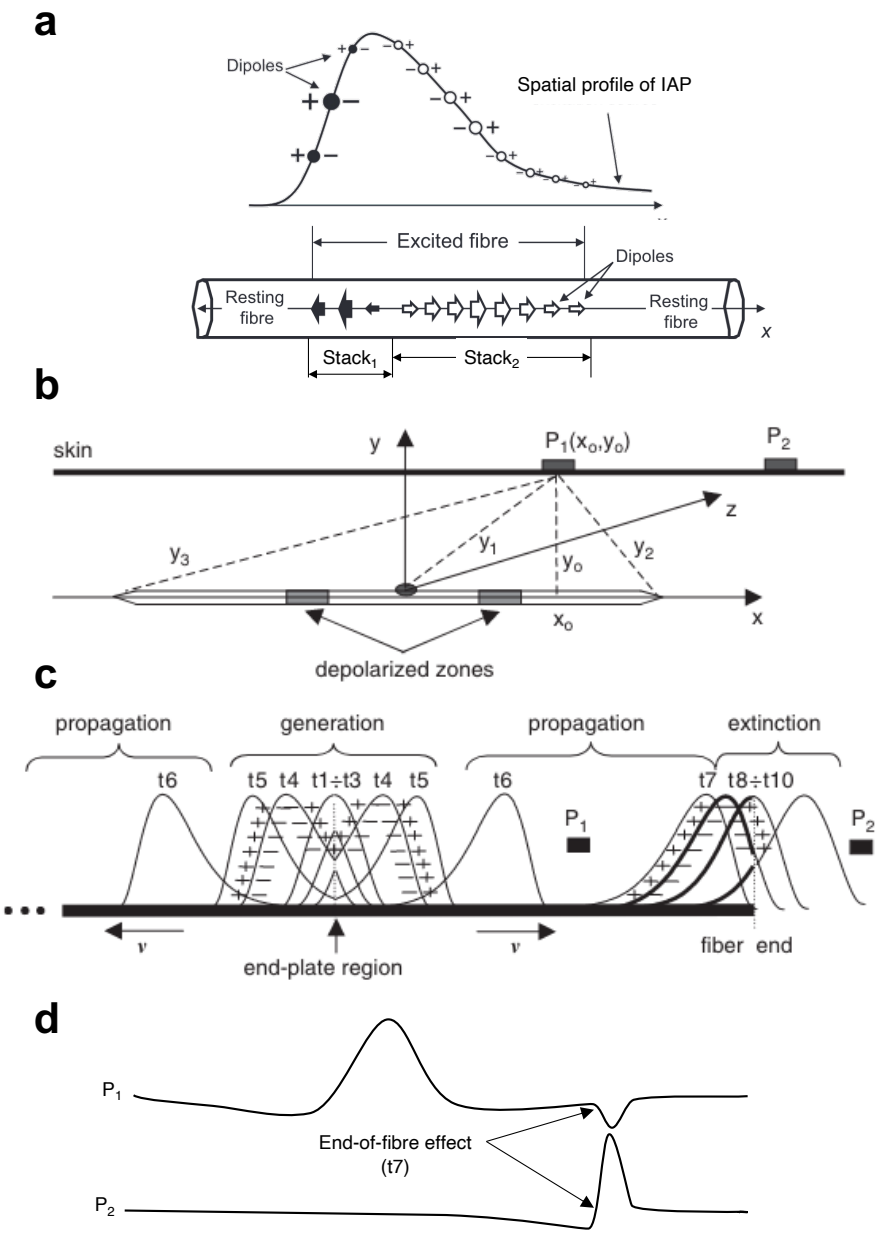

Figure 1.10: Multiple dipole model of IAPs with end-of-fibre effect. (a) Approximation of the IAP as a set of point dipoles whose electric dipole moment is proportional to the first spatial derivative of the IAP (represented in the size of the dipole). (b) Surface recording (on top of the skin) from two electrodes P1 (within the length of the fibre) and P2 (after the muscle-tendon interface). (c) Propagation of the estimated IAP along the fibre. (d) SFAPs recorded at P1 and P2 from a single active fibre showing a non-propagating component at the time the IAP reaches the musculo-tendon junction (t7). This corresponds to the end-of-fibre effect. Note that the sign of the potential (positive downwards for convention) depends on the dipole polarity seen by the electrode. (a) reproduced from Rodriguez-Falces 2015 with permission and (b-d) modified from Dimitrova et al. 2006 with permission.

dipole moments) (Stegeman et al. 1997). Therefore, the SFAP is only constituted by the tripole's near-field potentials as the IAP generates and propagates to the tendon endings. However, the sequential extinction of the dipoles in the tripole, causes an imbalance in the dipole's moments that translates in lower cancellation and the appearance of a non-propagating potential at the muscle-tendon interface (Stegeman et al. 1997). This is know as the end-of-fibre effect (Farina

et al. 2002b).

Nevertheless, the approximation of an IAP as two single point dipoles is an oversimplification of its actual electrical behaviour (Rodriguez-Falces 2015). Dimitrova et al. 2006 extended this concept based on the work of Helmholtz 1853 and Wilson et al. 1933, by approximating the spatial profile of the IAP as a series of point dipoles whose electric dipole moment is proportional to the first spatial derivative of the IAP. Hence, the latter model substitutes the two point dipoles with opposite polarities by two opposing stacks of dipoles that sample the potential of the IAP in space. This approach better captures the asymmetry of the IAP due to the faster depolarisation than repolarisation phase (Bean et al. 2021).

Under this model, the end-of-fibre effect is explained as the emergence of a stationary dipole at the muscle-tendon interface whose electric dipole moment varies in time according to the propagation and extinction of the IAP (Dimitrova et al. 2006; Rodriguez-Falces et al. 2022). These changes in the dipole moment also influence the associated extracellular potential (Figure 1.10). This is the same mechanism that accounts for the far-field components produced by inhomogeneities in the volume conductor that alter the propagation of the signal (Stegeman et al. 1987). Hence, the term 'far-field component' in this context does not relate to the dipole potential per se, but rather reflects the fact that these components (due to the end of the fibre or other conductor inhomogeneities) are non-decaying non-propagating components with respect to the recording site (Stegeman et al. 1997).

Furthermore, Farina et al. 2001a developed a general spatiotemporal formulation for a current density source travelling along the fibre that indirectly introduces the effect of the end-plate and muscle-tendon interface as a piece-wise window that modulates the first spatial derivative of the IAP. Importantly, this formulation does not rely on approximations of the current density source (Farina et al. 2001a) and is well-suited for EMG simulations (Farina et al. 2001a, 2004; Maksymenko et al. 2023).

1.3.3 End-of-fibre effect at the MUAP level

Since MUs are comprised of multiple muscle fibres, their associated MUAPs are generated as the spatiotemporal sum of their corresponding SFAPs (Figure 1.11.a), conditioned by the properties of the volume conductor, detection system, and anatomy (Farina et al. 2002a, 2008, 2016b). Yet, the previously described non-propagating components also emerge at the MUAP level, along with propagating ones (Figure 1.11.b). Notably, the end-of-fibre effects do not share the same morphology with their corresponding propagating components (Farina et al. 2002b; Stegeman et al. 1987). For instance, their amplitude is inversely proportional to the degree of tendon spread within the motor unit (Figure 1.11.a) (Merletti et al. 2019). Furthermore, in short fibres the amplitude of the end-of-fibre components tends to be larger than that of their propagating counterparts (Farina et al. 2016b).

These properties make the end-of-fibre effect the principal source of crosstalk in EMG (Farina

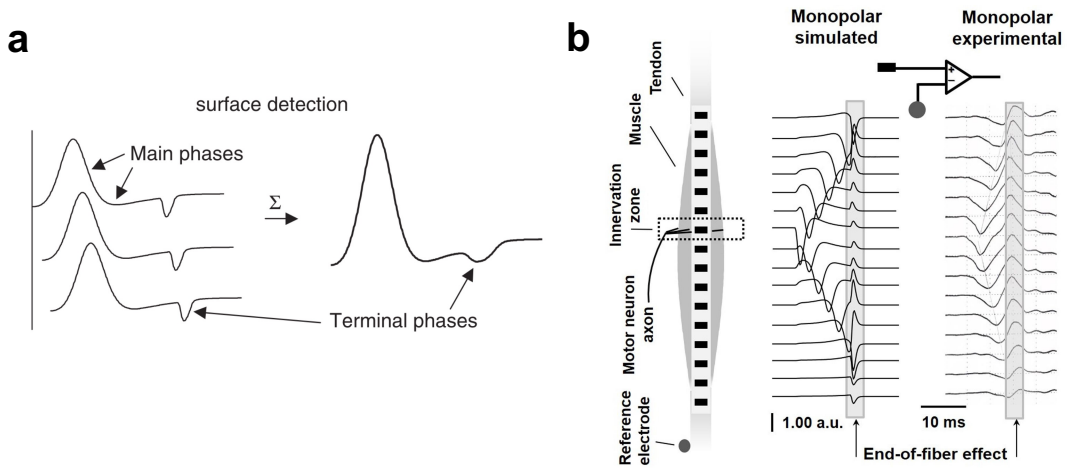

Figure 1.11: End-of-fibre effect at the motor unit action potential (MUAP) level. (a) MUAP (right) generation from asynchronous single fibre action potentials (left) due to fibre length and innervation point differences withing the motor unit. Note how the imperfect alignment results in a smoother end-of-fibre effect (terminal phase). (b) Examples of simulated and experimentally recorded MUAPs with propagating (misaligned waveforms) end-of-fibre components (shaded in grey). Reproduced from Dimitrova et al. 2006 (a) and Merletti et al. 2019 (b) with permission.

et al. 2002b). The latter refers to the signals recorded over a specific muscle that originated from a different nearby muscle (Winter et al. 1994). This confounding factor only emerges in surface recordings, where the relative distance between the electrodes and sources is comparable for the targeted and surrounding muscles (Farina et al. 2016b). Although Farina et al. 2002b showed that crosstalk signals produced by end-of-fibre effects have high-frequency temporal components with low spatial bandwidth (non-propagating), Dimitrova et al. 2002 demonstrated that these components cannot be compensated by temporal filtering. Instead, spatial filters (linear combinations between the recorded signals at different locations), such as the double differential configuration, are the most effective technique for suppressing these effects (Farina et al. 2002a) (Figure 1.12). On the other hand, the monopolar montage provides the highest sensitivity to end-of-fibre components (Farina et al. 2002a) (Figure 1.12), at the expense of lower discriminative power across MUAPs (Farina et al. 2008).

1.4 Non-invasive human-computer interaction based on MN activity

Decoding MN activity from surface EMG signals provides valuable insights into the neural mechanisms underlying movement and force production. This section covers the main methodologies applied to MN activity to predict force, gestures, and even kinematics. These approaches are integral in advancing rehabilitation, enhancing human-machine interfacing, and contributing to augmentation technologies.

Fundamental work in electrophysiology paved the way to the creation of peripheral neural interfaces by revealing common oscillations in the smoothed MN firings (<10 Hz bandwidth) that

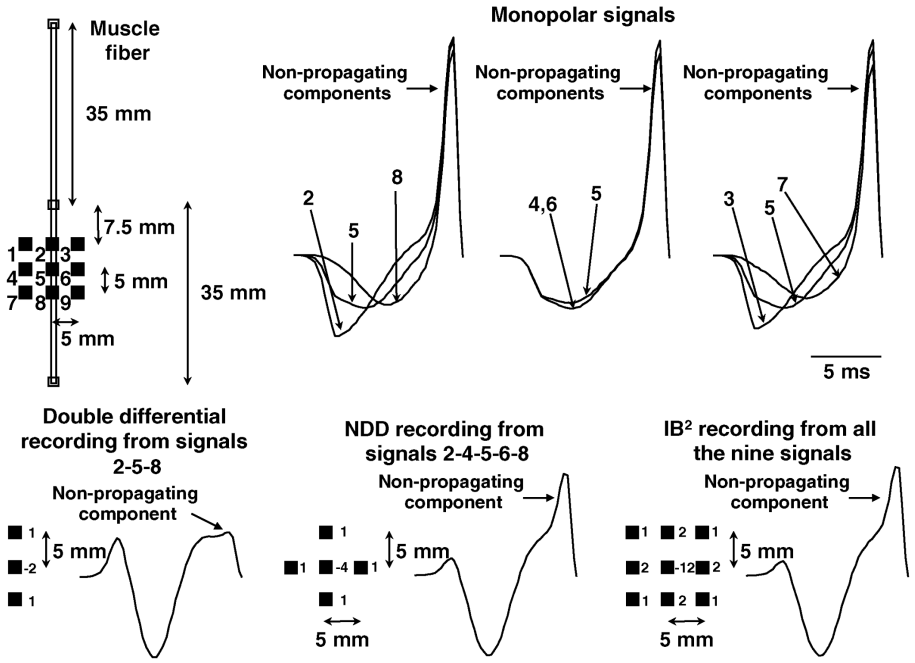

Figure 1.12: Spatial filters attenuate end-of-fibre effects. Simulated MUAPs from the montage on the top left in monopolar (top), double differential (bottom left), Laplacian (bottom middle) and second-order inverse binomial (bottom right) modes. The weights and electrodes used for each spatial filter approach are shown on the left. Note how the large end-of-fibre effects (non-propagating components) in the monopolar recordings are attenuated after spatial filtering, being almost cancelled with the double differential configuration. Reproduced from Farina et al. 2002a with permission.

were highly correlated with the exerted force (De Luca et al. 1982b; Negro et al. 2009; Thompson et al. 2018). This also indicated the presence of common synaptic inputs across the MN pool (De Luca et al. 1994; Farina et al. 2015, 2014c). Since then, a plethora of studies have used the smoothed MN firings to independently predict finger forces offline (Dai et al. 2019a; Zhang et al. 2020) and in real-time (Zheng et al. 2019). More computationally intensive approaches paired MN activity with twitch force models to refine the contribution of each MN to the exerted force (Li et al. 2022; Tang et al. 2021; Zhang et al. 2020). However, all these studies predicted the generated force in one direction by a single finger at a time, limiting the interaction potential of the interface. To compensate for this, Zheng et al. 2021 decoded MN activity during finger flexions and extension and applied a bivariate linear regression model to predict the force of a given finger in both directions. Chen et al. 2022 extended this approach by pre-assigning MNs to four wrist directions and predicting their exerted force concurrently based on MN firing features. In a similar task, Yu et al. 2021 showed that the inclusion of the MUAP representations in the force prediction along with a convolutional neural network could further improve the wrist torque prediction with respect to only MN firings. Notably, all these MN-based methods outperformed EMG in force prediction, when a large enough MN population was detected.

An alternative approach aims to decode multiple gestures from MN activity to increase the number of control commands. In this cases, decomposition is typically calibrated per gesture, and the MNs detected are merged across classes based on their MUAP waveforms. In these

settings, contractions are commonly pseudo-isometric, maintained constant over time but without force feedback, as providing it is often impractical for certain gestures. For instance, Chen et al. 2020b predicted 11 hand gestures by first pre-assigning the detected MNs to a given gesture based on their MUAP features and subsequently applying majority voting for gesture estimation, achieving over 95% accuracy. Similar results were obtained by Stachaczyk et al. 2020 when classifying individual fingers and their respective phases in the contraction based on MN firing features (namely, the spike count, standard deviation of the firing times, and inter-spike-interval per window). More recently, deep learning models such as convolutional neural networks (Zhao et al. 2022) and spiking neural networks (Tanzarella et al. 2023) have also been applied to decode finger gestures from MN activity with high accuracy ($> 95\%$). Moreover, Chen et al. 2023 demonstrated that applying stricter MN selection criteria resulted in significantly higher classification accuracy than EMG-based features, particularly when distinguishing > 20 gestures. These results were further confirmed by Yeung et al. 2023, who thoroughly evaluated multiple MN selection criteria based on the minimal redundancy maximal relevance framework to identify the optimal set of MNs for regression and classification of 18 motor tasks. Their results showed that the mutual information-based criterion paired with kernel-based regression and classification methods resulted in only $\sim 3\%$ decrease in performance when only 25% of the MN population is selected, showing the effectiveness of the selection criterion. Yet, while all these methods reported execution times under the neuromechanical delay, their accuracy was only evaluated under offline conditions, which are informative (Hinson et al. 2023a,b) but do not exactly translate to real-time interaction performance (Nawfel et al. 2021).

Few studies have also evaluated the ability of MN activity to predict the kinematics of hand gestures, despite the associated violations of the decomposition model. In their seminal work, Kapelner et al. 2018 decoded and average of 16 ± 7 MNs from the forearm of able-bodied and limb-deficient participants during slow and continuous movements of three degrees of freedom of the wrist. Yet, it is worth noting that most MNs were first detected at $62.5 \pm 26.4\%$ of the wrist range of motion, which was associated to a decomposition bias towards higher-threshold MNs with larger MUAP amplitudes. Arguably, this could also be explained by the fact that the MUAPs of these MNs would have undergone smaller changes associated to the dynamics than early recruited ones. Indeed, this reasoning was shared by the authors in a follow up study where the MN activity decoded from dynamic wrist movements was used to predict the corresponding kinematics (Kapelner et al. 2019). In this study, Kapelner et al. 2019 showed that this decomposition limitation translated in poor prediction accuracy, unless the residual EMG and a proposed physiologically-inspired dimensionality reduction approach were included in the processing pipeline. Later on, the smoothness of the predictions was improved by coupling their physiologically-inspired dimensionality reduction with a musculoskeletal model, although the same decomposition limitations were found (Kapelner et al. 2020). Surprisingly, similar performance was attained by (Chen et al. 2019) when predicting individual finger kinematics from the neural drive estimated as the first principal component of the smoothed MN firings. Here, multiple repetitions were included during the decomposition calibration that was carried out over sliding spatial windows. While this increased the number of detected MNs (25 ± 5 MNs

per trial), barely any (0-5 MNs per trial) were consistently detected across all trials, highlighting again the decomposition instability under dynamic contractions. Subsequently, Chen et al. 2021 developed a proportional and simultaneous controller of two wrist and hand degrees of freedom based on MN activity. The approach first assigned MNs to the degree of freedom they were most active, and then computed the cumulative spike train per degree of freedom to predict the position of a virtual cursor on the screen. While Chen et al. 2021 found that the MN-based controller outperformed EMG-based multiple linear regression, the position controller was linked to the contraction intensity of the EMG rather than the kinematics of the joint, making it unclear how much dynamic modulation was actually induced by the experimental protocol.

Notably, the ability to interface MNs in real-time has opened up new possibilities in augmentation technologies (Eden et al. 2022). Some notable examples include the ability to volitionally modulate high-frequency oscillations present in the ensemble of MNs firings (13–30 Hz bandwidth), without significantly altering the exerted force (Bräcklein et al. 2022a, 2021). An alternative strategy involves the skilful control of individual MNs (Basmajian 1963; Bräcklein et al. 2022b; Formento et al. 2021; Rossato et al. 2024). Yet, these findings appear to be constrained by a functional distribution of common synaptic inputs (Hug et al. 2023), where volitionally breaking recruitment is not possible within MNs belonging to the same spinal synergy. While these strategies offer the potential to expand the number of controllable degrees of freedom beyond the muscle number, the specific mechanisms governing these control approaches are still under investigation.

Yet, all these results were obtained from muscle bellies in the forearm (Chen et al. 2019, 2020b, 2021, 2023, 2022; Kapelner et al. 2018, 2020, 2019; Stachaczyk et al. 2020; Tanzarella et al. 2023; Yeung et al. 2023; Yu et al. 2021) (or covering the entire area of it, Dai et al. 2019a; Zhao et al. 2022; Zheng et al. 2019, 2021), intrinsic muscles of the hand (Basmajian 1963; Li et al. 2022; Tang et al. 2021; Tanzarella et al. 2023; Zhang et al. 2020), muscles in the lower limb (Bräcklein et al. 2022a,b, 2021; Rossato et al. 2024) or the biceps brachii (Formento et al. 2021). In contrast, interfacing MNs with electrodes around the wrist, which is the preferred location for a wearable (Cho 2019; Fang et al. 2016), has remained largely unexplored.

Taken together, these findings show the ability of MN activity to predict the exerted force and gestures, as well as potential for human augmentation technologies. Despite the promising results, some challenges remain in the prediction of dexterous and continuous movements, particularly regarding the number of accurately identified MNs during dynamics and their consistent detection across repetitions. In addition, the electrode placement of these studies is suboptimal for wearable interfaces leaving open questions regarding their translation for general consumer applications. Therefore, this thesis tackles some of these issues to improve the accuracy, reliability, and wearability of this type of neural interfaces.

1.5 Aims and thesis outline

Over the years, research in EMG has significantly expanded our understanding of MN activity and its potential for creating non-invasive neural interfaces. However, applying EMG decomposition techniques to the wrist posed certain challenges due to its distinctive signal properties. Yet, given the wrist's regard as the ideal location for wearable devices, it was essential to determine its feasibility for non-invasive neural interfacing. This step was critical for advancing the next generation of input technologies. In this context, the goal of this work was to develop an accurate, robust, non-invasive neural interface at the wrist, suitable for widespread consumer electronics. To do so, I first validated the EMG decomposition model under the end-of-fibre effects of the muscle-tendon interface at the wrist, and demonstrated their accuracy for finger gesture prediction. Thereafter, I improved the stability of this neural interface by developing an adaptive decomposition algorithm that compensated non-stationarities, such as those induced by dynamic motor tasks, in real-time. Specifically:

Chapter 2 presents a non-invasive neural interface at the wrist based on the output from the spinal cord. Here, I first validated the decomposition model for the end-of-fibre components at the wrist. Results showed that they could be accurately decoded from EMG recordings at the wrist and that their discharge properties matched the physiological range of MNs. In addition, $\sim 70\%$ of the end-of-fibre components could be retraced to the forearm above the noise level, further supporting their neural origin. Finally, I evaluated their suitability as control inputs for finger prediction in offline and real-time tasks. These tests resulted in $> 90\%$ accuracy in all scenarios, demonstrating the potential of the wrist for accurate non-invasive neural interfacing in real-time.

Yet, the aforementioned results were obtained under static conditions that are not characteristic of natural interaction paradigms. To address this limitation, **Chapter 3** introduces a decomposition adaptation algorithm that compensates non-stationarities associated with dynamic contractions in real-time. To do so, I first characterised the effect of postural changes in the MUAPs and decomposition performance. Subsequently, I leveraged properties of the signals (Kullback-Liebler divergence and kurtosis) as metrics for online learning that enabled the calibration of the adaptation hyperparameters even in the absence of ground truth. Finally, I validated the proposed algorithm in a full-spectrum dynamic neuromechanical model and experimentally recorded data from the forearm and wrist over a wide range of motion (80° flexion/extension of the wrist). Results showed $\geq 90\%$ rate of agreement, sensitivity, and precision in $\geq 80\%$ of the cases in both simulated and experimentally recorded data in a two-source validation approach. Hence, these findings demonstrate the feasibility of accurately decoding MN discharges in real-time during dynamic contractions from the forearm and wrist, improving the overall robustness of this type of neural interfacing.

Finally, **Chapter 4** provides an overview of the work in this thesis, explores its wider implications for the field, and suggests directions for future research.

Chapter 2

Decoding motor neuron activity from the wrist non-invasively

[1]

Neural interfaces need to be less obtrusive to appeal to general consumers and become socially acceptable outside rehabilitation settings. I developed a non-invasive neural interface that provides access to spinal MN activities from the wrist, which is the preferred location for a wearable. The interface decodes far-field potentials present at the tendon endings of the forearm muscles using blind source separation. First, I evaluated the reliability of the interface to detect MN firings based on far-field potentials, and thereafter I used the decoded MN activity for the prediction of finger contractions in offline and real-time conditions. The results showed that MN activity decoded from the far-field potentials at the wrist accurately predicted individual and combined finger commands and therefore allowed for highly accurate real-time task classification. These findings demonstrate the feasibility of a non-invasive, neural interface at the wrist for finger real-time control based on the output of the spinal cord.

2.1 Introduction

In our ever-growing digital world, human-machine interaction has a pivotal role not only in defining our relationship with technology but also in determining its usability and effectiveness. While current input systems such as keyboards or touchscreens are intuitive for most people, their benefits are task-specific (e.g. inputting text or selecting an item). Rising technologies such as virtual or augmented reality offer new capabilities of interaction. To ensure a genuinely immersive experience, the potential of our hands needs to be fully exploited with commands that closely mimic our natural movements in real life. Being able to perform such variety of rich gestures to interact with multiple digital systems intuitively, accurately, and quickly, will revolutionise input technologies. Evermore, bypassing the need of task-specific actuators and developing wearable solutions will make this comprehensive interaction seamless and portable.

[1]The work in this chapter has been published as "Far-field electric potentials provide access to the output from the spinal cord from wrist-mounted sensors" in the *Journal of Neural Engineering* see (Mendez Guerra et al. 2022) with authors: **Irene Mendez Guerra**[2], Deren Y. Barsakcioglu[2], Ivan Vujaklija[3], Daniel Z. Wetmore[4], Dario Farina[2]. The text has been adapted to fit the format and flow of the thesis as a cohesive single document.

[2]Department of Bioengineering, Imperial College London, London, United Kingdom

[3]Department of Electrical Engineering and Automation, Aalto University, Espoo, Finland

[4]Reality Labs, Meta, New York, United States of America

In this regard, neural interfaces can be a promising approach to complete this vision. Neural interfaces target the neural code of motor commands to drive external devices in an attempt to provide an intuitive and enhanced interaction with the environment. Although originally developed as a rehabilitation technology, the potential of neural interfaces for large-scale consumer electronics has gained momentum in the past few years. Both applications require high spatiotemporal resolution and population sampling to ensure a representative information bandwidth (Holobar et al. 2021). Yet, one key difference to appeal general consumers and meet ethical considerations is the need for non-invasive wearable devices (Yuste et al. 2017).

Traditionally, signals from the brain have been leveraged to control prostheses (Velliste et al. 2008), wheelchairs (Deng et al. 2020), and exoskeletons (Benabid et al. 2019), among other systems (Moxon et al. 2015; Shanechi 2019). Nonetheless, direct brain interfaces are currently constrained by a trade-off between their information transfer and invasiveness, with non-invasive systems providing substantially smaller information bandwidth than invasive devices (Martini et al. 2020). Furthermore, acceptance of brain interfaces for daily use outside rehabilitation applications remains uncertain. In comparison, the peripheral nervous system offers a more accessible window to motor volition (Farina et al. 2014a).

MNs in the spinal cord translate the synaptic inputs they receive from supraspinal centres and peripheral afferents into a neural output sent to their innervated muscle fibres (Farina et al. 2015). When the axonal action potentials generated by MNs reach the neuromuscular junction, they excite the fibres and produce another potential on the muscle membrane (the MUAP). They propagate from the end plates in the neuromuscular junction, along the direction of the fibres, to the tendon endings where they terminate.

Electrodes on the skin surface can detect the aggregate activity of MUAPs, filtered by the volume conductor (Farina et al. 2016b). This is the EMG signal, which has been extensively used as input for human-machine interfacing (Ahmadizadeh et al. 2021). The most common approach for decoding distal movements of the upper limb is to record EMG from forearm muscles. Still, the most convenient location for long-term adoption of wearable devices is at the wrist due to social acceptance of wristwatches (Fang et al. 2016; Raisamo et al. 2019). As forearm muscles converge into the tendons at the wrist, the muscle mass drastically reduces. Interestingly, despite the predominance of non-conductive tendon tissue at the wrist, the muscle-tendon interface shows unique electrical properties.

When MUAPs terminate at the tendons, far-field potentials emerge (Dumitru et al. 1993). To understand them, it is necessary to review the electric potential associated to a dipole current source. Briefly, in a dipole (sometimes expressed as $+-$), current flows between the positive and negative poles generating a characteristic electric field. Close to the poles, the potential changes rapidly (near-field potential region), while at relatively far distances the effect of the dipole decreases and the potential becomes constant (far-field potential region). In a bounded volume conductor, such as a limb, far-field potentials are non-propagating signal components

with fixed amplitude and morphology (Stegeman et al. 1997). A MUAP can be modelled as a quadripolar current source travelling along the muscle fibre, comprising two dipoles oriented in opposite directions ($+--+$), the so-called leading and trailing dipoles (Dumitru et al. 1993). Under this configuration, the far-field potentials of the two dipoles cancel each other and only the stereotypical propagating waveform of the MUAP is observed. However, as the dipoles sequentially disappear at the muscle-tendon interface, they only partially cancel each other's far-field potentials, generating a short non-zero net potential.

Far-field potentials have been researched for decades (Dumitru et al. 1991, 1993; Stegeman et al. 1997), but their feasibility as a source of motor control has only been evaluated indirectly. A few studies have recorded EMG signals at the wrist to decode motor intention (Botros et al. 2022; Jiang et al. 2018; Jiang et al. 2017). Using temporal EMG features, Botros et al. 2022 achieved 88% classification accuracy in offline prediction of individual finger tasks and Jiang et al. 2018 obtained 75% in a real-time control task. These accuracy values are lower than those generally reported with classic EMG recordings from the forearm (Cipriani et al. 2011; Khushaba et al. 2012). This poorer performance at the wrist has been explained by the convergence of multiple muscle tendons in a reduced space, which results in high crosstalk between the recorded signals.

To compensate for the small detection space in wrist recordings, it would be theoretically possible to decompose EMG signals into the underlying MN activity by reversing the EMG generative model. This problem is often solved by blind source separation (Barsakcioglu et al. 2021; Chen et al. 2016b; Glaser et al. 2013; Holobar et al. 2007b; Negro et al. 2016a), where the sparseness of the estimated sources is maximised under the assumption that each MUAP is unique. This is well-satisfied when recording over the muscle belly (where the propagating components of the MUAPs experience their highest amplitudes) with a sufficiently high number of sensors (i.e. in the range of tens to hundreds, Farina et al. 2008). However, at the tendons, the propagating components of the MUAPs are attenuated, being the far-field potentials the main components of the signals, as discussed above.

Here, I hypothesise that the differences in muscles fibres' conduction velocity, size, position in the volume conductor, and tendon spread would generate unique far-field potentials for each MN, with the same timing (save a constant delay of few ms, Heckman et al. 2012) as the axonal action potentials from the spinal cord. If this were true, far-field potentials could be extracted from EMG signals recorded over tendon endings, allowing for distal non-invasive neural interfaces (Figure 2.1). To test this hypothesis, I applied blind source separation methods to decompose electrical signals recorded by EMG electrodes and I validated the neural origin of the decomposed signals. Thereafter, I used the neural information obtained from the decomposed signals to predict individual and combined finger presses in offline and real-time conditions. Results showed that the decoded far-field potentials indeed correspond to individual MN discharges, and that this neural decoding enhances the information transfer to accurately predict individual and combined finger commands in offline and real-time control conditions. Therefore, here I present a new high-fidelity, non-invasive, unobtrusive, and socially acceptable neural interface at the wrist



Figure 2.1: Interfacing MNs in the spinal cord non-invasively from the wrist via volume conduction and far-field potentials at the tendon endings. MNs in the spinal cord translate the synaptic inputs they receive from supraspinal centres and peripheral afferents into a neural output sent to the muscles. When excited, they discharge axonal action potentials that reach the neuromuscular junction of the innervated muscle fibres. These MUAPs propagate from the end plates to the tendon endings where they terminate generating far-field potentials. These potentials can be detected at the tendon endings of the wrist using electrodes (in this case, arranged in a wristband) due to volume conduction. However, wrist EMG signals experience high crosstalk between each other due to the convergence of multiple tendons in the reduced space of the wrist. To enhance the information transfer needed for precise decoding of motor volition, the generative model of the wrist EMG signals can theoretically be reversed to estimate the activity of the spinal MNs as long as the induced far-field potentials at the tendons are unique for each MN.

as a viable alternative to invasive neural recordings and traditional muscle interfaces.

2.2 Methods

2.2.1 Offline experiment

2.2.1.1 Experimental setup

Nine healthy participants (four females, five males, ages: 23–31) volunteered in the study. Both informed consent forms and experimental protocols were approved by the local ethics committee in accordance with the Declaration of Helsinki.

Two flexible EMG electrode grids (64 channels arranged in 5 × 13 with 8 mm distance, GR08MM1305, OT Bioelettronica) were placed along the circumference of the wrist right below

the head of the ulna by visual inspection and physical palpation. The fixed length of the commercial electrode grids resulted in few overlapping electrodes depending on the wrist diameter. These channels were noted for each subject and discarded in the postprocessing steps along with noisy ones. On average, 102 ± 12 channels were kept at the wrist for further analysis. In addition, EMG signals were concurrently recorded from the circumference of the thickest part of the forearm using three electrode grids (64 channels arranged in 8×8 with 10 mm distance, GR10MM0808, OT Bioelettronica). Both signals were simultaneously acquired in monopolar mode (reference and ground bands were placed around the elbow) by a multi-channel amplifier (Quattrocento, OT Bioelettronica), bandpass filtered between 10 and 500 Hz, and sampled at 2048 Hz with 16-bit ADC precision. Individual finger flexion forces were recorded concurrently at 10 Hz with five micro load cells (0–5 kg CZL635, Phidget), located in an ergonomic and adjustable platform. The latter was designed to keep the hand supported while in a relaxed position. A custom acquisition framework (Matlab 2019b, The MathWorks, Inc) was implemented to synchronously acquire all the signals.

Participants were seated on a chair with their arm supported and the fingers placed in a comfortable position on top of each force sensor. They were facing a computer screen where cues and visual feedback of their fingers' flexion forces were provided. The maximum voluntary contraction (MVC) level across each finger was calibrated for each participant at the beginning of the experiment. Thereafter, they were instructed to follow the displayed trapezoidal cues (2 s rest, 2 s ramp up, 5 s steady contraction, 2 s ramp down and 2 s rest) at 15% and 30% MVC for each individual finger and the combinations of thumb-index, thumb-middle, index-middle and thumb-index-middle in a randomised order (18 trials in total). The aforementioned submaximal MVC levels were selected to cover the range of activation used in previous finger flexion studies to identify MN firings (Stachaczyk et al. 2020; Tanzarella et al. 2020). The included finger combinations activate the fingers involved in precision (thumb-index) and tripod (thumb-index-middle) pinching, which offer potential for multi-finger gestures in human-machine interaction.

After acquisition, EMG signals were digitally bandpass filtered between 20 and 500 Hz (Butterworth).

2.2.1.2 Decomposition of far-field potentials

Far-field potentials were extracted from wrist EMG signals using convolutive blind source separation as described in Section 1.2.2, with contrast function $g = x^3/6$ and extension factor equal to 1000 divided by the number of channels as proposed by Negro et al. 2016a. Generally, at the muscle belly, EMG signals constitute the sum of the underlying MUAPs. The latter can be modelled as the convolution of a series of delta trains (representing the MNs' firings) and the corresponding potential affected by the volume conductor. However, at the wrist, the propagating components of the MUAPs are attenuated, far-field potentials being the main signal source. Furthermore, most muscle belly recordings target a specific muscle. In contrast, at the wrist, most muscle fibres converge into a series of densely packed tendons, and therefore the

recorded potentials are generated by multiple pools of spinal MNs. The high-frequency nature of the far-field components at the tendons corresponds to short temporal durations compared to the propagating components of the MUAPs (Dimitrova et al. 2002; Farina et al. 2002b), which translates in relatively low values for L in Equation 1.2. In this way, the far-field potentials (**H** in Equation 1.2) are a better approximation of the source delta functions than the propagating components of the MUAPs. This property equivalently implies greater temporal sparseness for the train of action potentials of each source.

After running the fully automatic decomposition, the output for the offline analysis was checked in a semi-supervised approach that enables the modification of the thresholds of the local peak detection algorithm to update the filters of poorly detected sources and recalculate the MN firings (Del Vecchio et al. 2020a). Repeatedly detected MNs within each contraction (with >30% shared spike timings, Holobar et al. 2010) were removed at this stage.

2.2.1.3 Physiological analysis

The decomposition output was evaluated in terms of the number of identified MNs at the wrist and the percentage of those that corresponded to MUAPs occurring concurrently at the forearm. To do so, forearm signals were spike-triggered averaged in 50 ms windows using the discharge times identified from the wrist as triggers. The average potentials obtained in this way were considered detectable if their peak amplitude was higher than four times the baseline noise (Quiroga et al. 2004)—computed as the standard deviation over the first and last 15 ms of the spike triggered average. If one or more channels in the array met this condition, it was concluded that the corresponding source identified from the wrist corresponded to a detectable MUAP at the forearm and thus to the discharges of a spinal MN.

The accuracy of the decoding was further assessed based on the pulse-to-noise ratio (PNR) of the estimated spike train (mean of the detected spiking activity divided by the mean baseline of the estimated source expressed in dB, Holobar et al. 2014). In addition, the coefficient of variation of the inter spike intervals (ratio between the standard deviation and mean of the inter spike intervals expressed as a percentage) and MNs' discharge rate (ratio between the number of action potentials fired by a MN and their active period measured in seconds) were computed to evaluate their physiological properties.

2.2.1.4 Finger command classification

For the control analysis, MNs across contractions were tracked based on the 2D correlation coefficient between their far-field potentials. These were calculated by spike-triggered averaging over 25 ms windows all the wrist EMG signals from the electrode array, centred at the timings of the MNs' spikes (Keenan et al. 2005). The analysis was carried out only for those channels with significant peak amplitude (i.e. higher than two times the standard deviation of that MN's peak amplitudes among all channels). MNs were considered the same if their normalised

cross-correlation coefficient exceeded 0.70 (Del Vecchio et al. 2020b).

Thereafter, the steady contraction part (5 s) of each finger flexion was selected and concatenated along with 5 s of rest for feature extraction. MNs' firings were windowed in intervals of 120 ms with 40 ms step to compute the spike count of each MN. Wrist EMG signals were windowed alike to extract four time-domain features (Phinyomark et al. 2012) (root mean square, slope sign changes, zero crossings and waveform length) for each channel. Although multiple features have been proposed to decode movement intentions from electric signals (Botros et al. 2022), the selected feature set is the most common in pattern recognition tasks (Samuel et al. 2019).

A multilayer perceptron with one hidden layer and ten hidden neurons (Ariyanto et al. 2015) was used to classify the wrist EMG and decoded MN features separately into ten classes (nine finger flexions plus rest). The multilayer perceptron was trained using the gradient descent with momentum and adaptive learning rate backpropagation algorithm. Performance was evaluated in terms of classification accuracy applying ten-fold cross-validation. In addition, classification accuracy was calculated for two scenarios: training and testing with contractions from one force level only, and from both levels combined. In both cases, 2 s of each class were used for training and the remaining data (3 s for the single force dataset, and 8 s for the combined) for testing.

In a preliminary evaluation, principal component analysis (PCA)) was applied to reduce the dimensionality of the MNs and wrist EMG feature sets preserving 95% of their variance. However, this did not increase the performance based on MN decoding while it significantly decreased the classification accuracy of wrist EMG features (<60%) with respect to the baseline (no PCA), in all scenarios. For this reason, no dimensionality reduction was applied in further analyses.

2.2.1.5 Statistical analyses

Statistical analyses were carried out to assess the effect of force levels, finger contractions, and data type (wrist EMG vs MNs) in the physiological and task classification metrics. Statistical significance was set to $p < 0.05$. If two factors were involved, a two-way repeated measures analysis of variance (ANOVA) was performed. Normal distribution of the data was determined by the Shapiro-Wilk test of normality. Few exceptions were found in (a) the number of MNs in the little finger at 15% MVC ($p = 0.019$), (b) the PNR of the thumb at 15% ($p = 0.037$) and index at 30% ($p = 0.005$), and (c) coefficient of variation of the little at 15% ($p = 0.006$), thumb-index at 15% ($p = 0.029$) and thumb at 30% ($p = 0.001$). However, this low proportion of non-normal levels was considered acceptable for the two-way repeated measures ANOVA. The assumption of sphericity was checked by Mauchley's test and if not satisfied, the Greenhouse-Geisser correction was applied to the degrees of freedom. If two-way interaction between the factors was found, the simple main effects were analysed with focused one-way repeated measures ANOVA fixing the levels of the interacting factors.

Otherwise, the main effects were analysed by one-way repeated measures ANOVAs over the pooled data. Bonferroni correction was applied for pair-wise comparisons. When only one factor was involved, one-way repeated measures ANOVA was carried out. All statistical analyses were performed in IBM SPSS Statistics 26.

2.2.2 Real-time experiment

Four healthy participants (two females, two males, ages: 25–32) participated in the online experiment (approved by the local ethics committee in accordance with the Declaration of Helsinki) after signing informed consent forms.

In this case, only EMG signals from the wrist were acquired following the same setup previously described. Participants were comfortably seated in front of a computer screen, with their right hand resting in a neutral position on top of a table. During training, they were asked to perform isometric finger contractions against the table at up to a comfortable level following trapezoidal cues (2 s rest, 2 s ramp up, 5 s steady contraction, 2 s ramp down and 2 s rest). Three repetitions each individual finger, the combinations of thumb-index, thumb-middle, index-middle, and thumb-index-middle, as well as rest, were recorded in a randomised order (30 trials in total).

To extract MNs' firings in real-time, I implemented a dual phase blind source separation (Barsakcioglu et al. 2021). In the first calibrating phase, the algorithm followed the same procedure described above to identify the latent MNs firings by compensating the far-field potentials. Then, the obtained inverse of the far-field potential filters was applied to new wrist EMG signals epochs to decompose the activity of the previously identified MNs, and detect new far-field potentials using the stored spike and noise centroids of each source (Barsakcioglu et al. 2021). In this case the training set was used to calibrate the decomposition parameters for its later implementation in real-time during the control task. The algorithm was incorporated into the previously described acquisition framework (Matlab 2019b, The MathWorks, Inc) with a system update rate of 40 ms for processing and visualisation. After calibration, the identification of new firings took an average of 2.6 ± 0.4 ms for 128 wrist EMG signals in batches of 64 samples per channel (equivalent to 31.2 ms acquisition latency), as computed on an Intel Core i7 2.8 GHz, 16 GB RAM. This still allowed 37.4 ms for further processing, such as for feature extraction, classification, and visualisation. Therefore, the maximum latency for acquisition and processing of the overall system was 71.2 ms, well below the 100 ms optimal delay in myoelectric control (Farrell et al. 2007).

To maximise the number of detected MNs, each contraction was decomposed separately during calibration. Thereafter, those MNs with more than 20% of shared spikes were considered equal and only the one with highest PNR was preserved to avoid redundant activity. As in the previous experiment, the spike count of each MN was calculated over sliding windows of 120 ms with 40 ms step (coinciding with the update rate of the system). On the other hand, the root mean square, slope sign changes, zero crossings and waveform length were extracted for the wrist

EMG signals using the same windowing process.

Two multilayer perceptrons with one hidden layer and ten hidden neurons (Ariyanto et al. 2015) were used to classify the MNs firings and wrist EMG features separately into ten classes (nine finger flexions and rest). They were trained using gradient descent with momentum and adaptive learning rate backpropagation over the steady part of the contraction. Both multilayer perceptrons were tested separately in a real-time task with four targets of each class (40 targets in total). Participants were given 5 s to attempt each target, with a required hold time of 500 ms to consider the target successfully reached. Performance was measured in terms of completion rate (number of successful targets divided by the total number of targets, expressed as a percentage) and completion time (time needed to successfully achieve a target).

2.3 Results

To validate the wrist neural interface, I investigated the physiological properties of the decoded far-field potentials, and then assessed their performance in offline and real-time prediction of finger tasks.

2.3.1 Physiological analysis

Figures 2.2.a-b show the EMG acquisition setup at the wrist with the individual finger forces, and the cues to the subjects. Wrist EMG signals were decomposed into a series of discharge timings (decoded wrist EMG signals) by convolutive blind source separation. A representative contraction with the force profile, wrist EMG signal, and the corresponding decoded activity are depicted in Figure 2.2.c. Representative 2D amplitude maps of wrist EMG signals and three examples of the far-field potentials associated to single MNs are shown in Figure 2.2.d. The distributions of electric potentials recovered from the wrist are unique for each MN, with high synchronisation in their peak amplitude times within neurons due to the far-field nature of these electrical activities.

On average, 6 ± 3 MNs were identified per finger contraction at each force level. To ensure that this decomposed activity indeed represented the neural output from the spinal cord, the discharge timings of the decoded wrist EMG signals were used to trigger an average of the EMG signals concurrently recorded at the forearm (Figure 2.3). From the total population of 970 detected MNs at the wrist, 703 (72.47%) resulted in detectable action potentials at the forearm above the estimated noise level. This is an extremely high proportion, considering that MNs detected at the wrist may innervate muscle fibres deep into the muscle which therefore would not produce sufficiently large action potentials at the forearm skin surface. This result indicated that the timings of activation of the decoded far-field potentials indeed correspond to neural activity from the output layer of the spinal cord. This demonstrates that a peripheral recording from the skin overlying tendon tissue can be decoded into the ultimate neural code of movement.

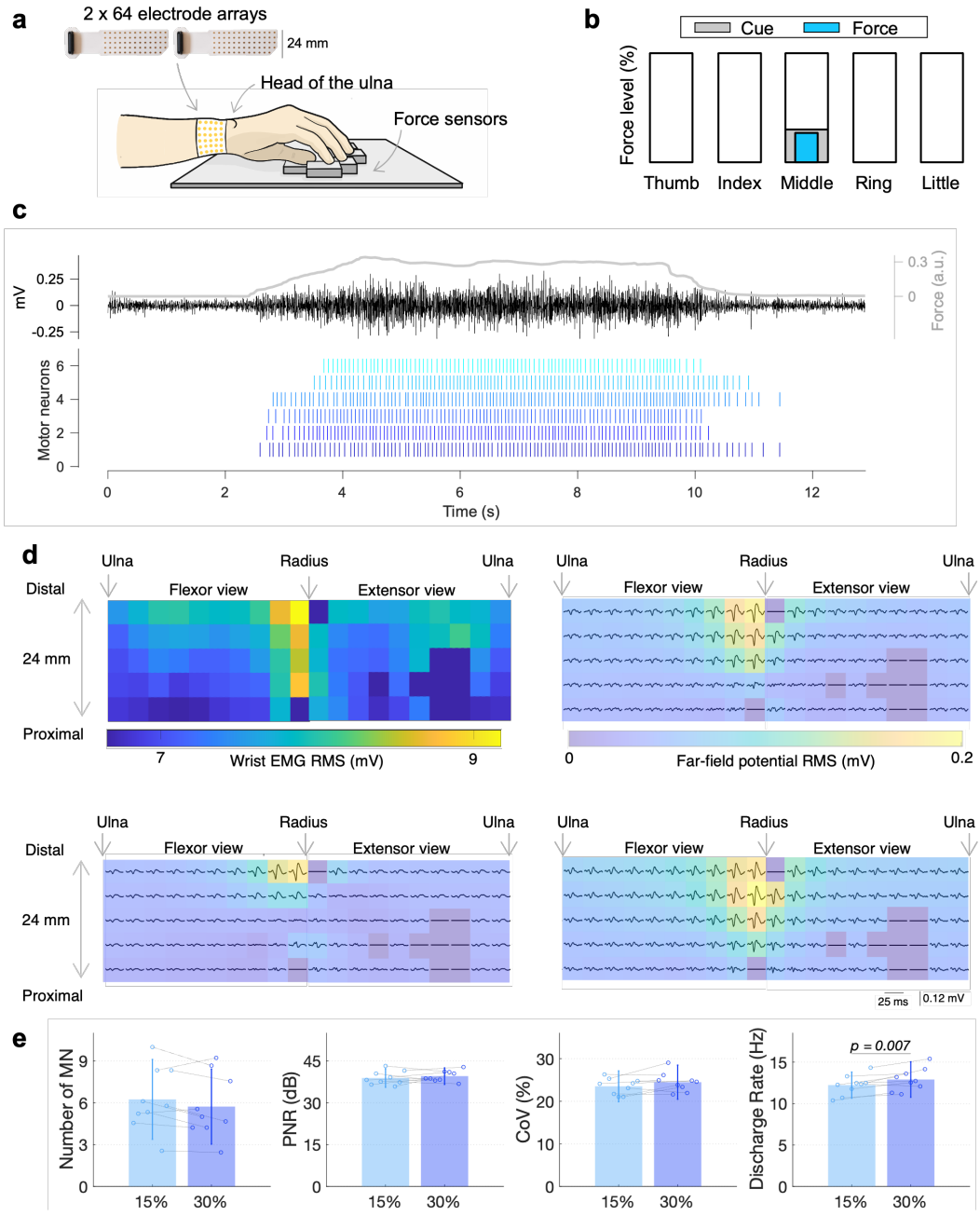

Figure 2.2: Decoded far-field potentials from the wrist interface. (a) Experimental setup for the concurrent acquisition of the wrist EMG signals and individual finger flexion forces. (b) Participant's visual feedback with the contraction cues in grey and the exerted forces in blue. (c) A representative contraction from one participant with the force profile in grey, one wrist EMG signal in black, and the decomposed spike trains (MN firings). (d) (top left) 2D spatial distribution of the root mean square (RMS) of each channel of the wrist EMG signals from one representative contraction, (top right and bottom) three examples of the reconstructed far-field potentials of three decoded MNs from the same contraction after spike-triggered averaging along with their corresponding RMS spatial maps. The channels in dark blue were discarded due to noise interference. (e) Physiological analysis of the decoded MNs' firings from the wrist for 15% (light blue) and 30% (dark blue) force efforts in terms of the number of detected MNs (MN), pulse to noise tatio (PNR), coefficient of variation (CoV) of the inter spike intervals, and MN discharge rate averaged across finger movements and subjects. The results indicate that the decoded far-field potentials from the wrist are accurate (PNR $>$ 30 dB and CoV $<$ 30%) and comply with MN's physiological behaviour (discharge rate, DR, between 5 and 25 Hz). The reported significance levels are based on two-way repeated measures ANOVA.

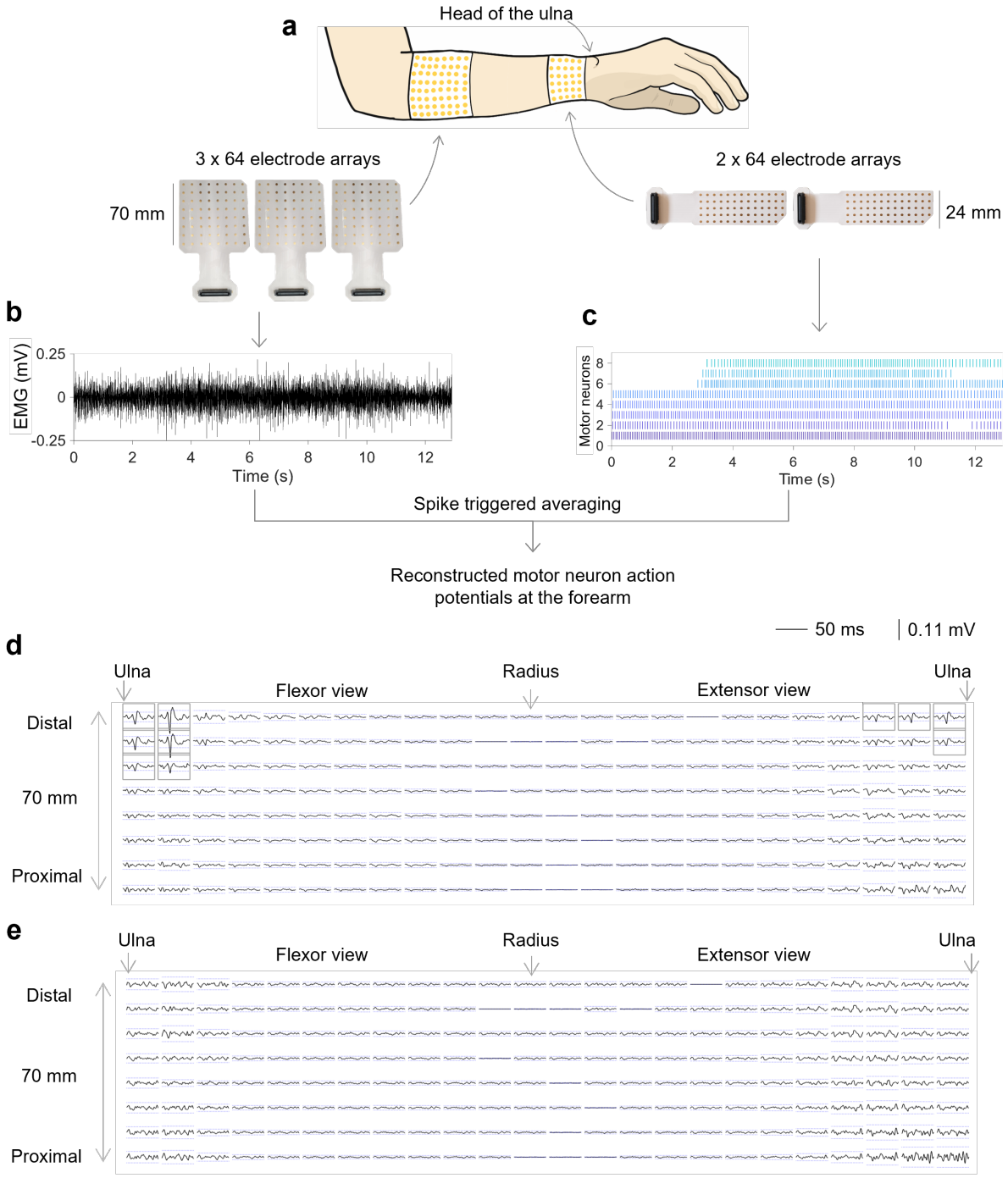

Figure 2.3: Retracing MUAPs at the forearm from the far-field potentials decoded at the wrist via spike triggered averaging. This analysis showed that 703 out of 970 far-field potentials decoded from the wrist were retraceable to the forearm, which supports the neural origin of the decoded far-field potentials. (a) Acquisition setup for concurrent recording of EMG signals at the forearm and the wrist. (b) Representative EMG signal from a single contraction at the forearm. (c) Decoded MN discharge timings from the far-field potentials at the wrist for the same contraction. (d) Representative example of a reconstructed MUAPs at the forearm from the far-field potentials at the wrist after spike trigger averaging. Grey boxes indicate those channels whose peak amplitude exceeded four times the baseline (calculated as the standard deviation of the first and last 15 ms). (e) Representative example of a spike triggered average that yielded in no retraceable MUAP.

I then used the PNR to assess the quality of the decoded MN firings. At both force levels, the PNR was greater than 30 dB and generally higher than usually observed when decoding classic EMG recordings from the forearm (Chen et al. 2019, 2020a,b; Tanzarella et al. 2019) (38.9 ± 2.3 dB and 39.6 ± 3.0 dB for 15% and 30% MVC, respectively) (Figure 2.2.e). These levels of PNR correspond to an accuracy in detection of spikes in the estimated sources with >90% sensitivity and <2% false alarm rate (Holobar et al. 2014).

After validating the decoding procedures, I further analysed the properties of the decoded discharge patterns to verify whether they were consistent with known physiological properties. I extracted the average discharge rate of each identified MN as well as the coefficient of variation of the estimated inter-spike intervals. The estimated MN discharge rates were within the physiological range of 5–25 Hz (Andreassen et al. 1980; Monster et al. 1977) at both force levels (12.23 ± 1.58 Hz and 12.90 ± 2.14 Hz at 15% and 30% MVC, respectively) (Figure 2.2.e), being significantly higher at 30% than at 15% MVC ($F_{1,8} = 12.879, p = 0.007$, one-way repeated measures ANOVA, observed power = 0.880 with $\alpha = 0.05$ and partial $\eta^2 = 0.617$), in agreement with MN's rate coding in force production (Enoka et al. 2016). The coefficient of variation of the estimated inter spike intervals was 23.51 ± 3.63% and 24.47 ± 4.01%, for 15% and 30% MVC, respectively (Figure 2.2.e), which is within known physiological values (Holobar et al. 2010).

The analysis of accuracy via spike-triggered average and PNR, as well as the physiological analysis of MN behaviour demonstrated the validity and accuracy of the proposed decoding technique. Overall, these results show the accurate identification of the activity of individual spinal MNs through non-invasive recordings overlying the tendon endings at the wrist. After confirming the validity and accuracy, I established a human-machine interface based on the proposed neural decoding approach.

2.3.2 Finger command prediction (offline)

The decoded MN activity was used to classify the corresponding finger command (individual and combined finger contractions plus rest, 10 classes in total) for each force effort separately and when contractions from both force efforts were combined into a single dataset. As a reference, I compared the classification from MNs with that obtained using the wrist EMG signals.

Figure 2.4.a shows the resulting finger classification accuracy. Statistically significant two-way interaction was found between force levels and data type ($F_{1,8} = 13.807, p = 0.006$; two-way repeated measures ANOVA, observed power = 0.607 with $\alpha = 0.05$ and partial $\eta^2 = 0.447$), so the simple main effects were analysed. When the two force levels were used independently, the decoded MNs yielded in significantly higher finger classification accuracy than wrist EMG signals at both 15% (96.93 ± 2.09% vs 81.23 ± 10.04 %; $F_{1,8} = 23.379, p = 0.001$, one-way repeated measures ANOVA, observed power = 0.987 with $\alpha = 0.05$ and partial $\eta^2 = 0.745$) and 30 MVC (97.60 ± 1.75% vs 85.62 ± 6.86 %; $F_{1,8} = 31.036, p = 0.001$, one-way repeated measures ANOVA,

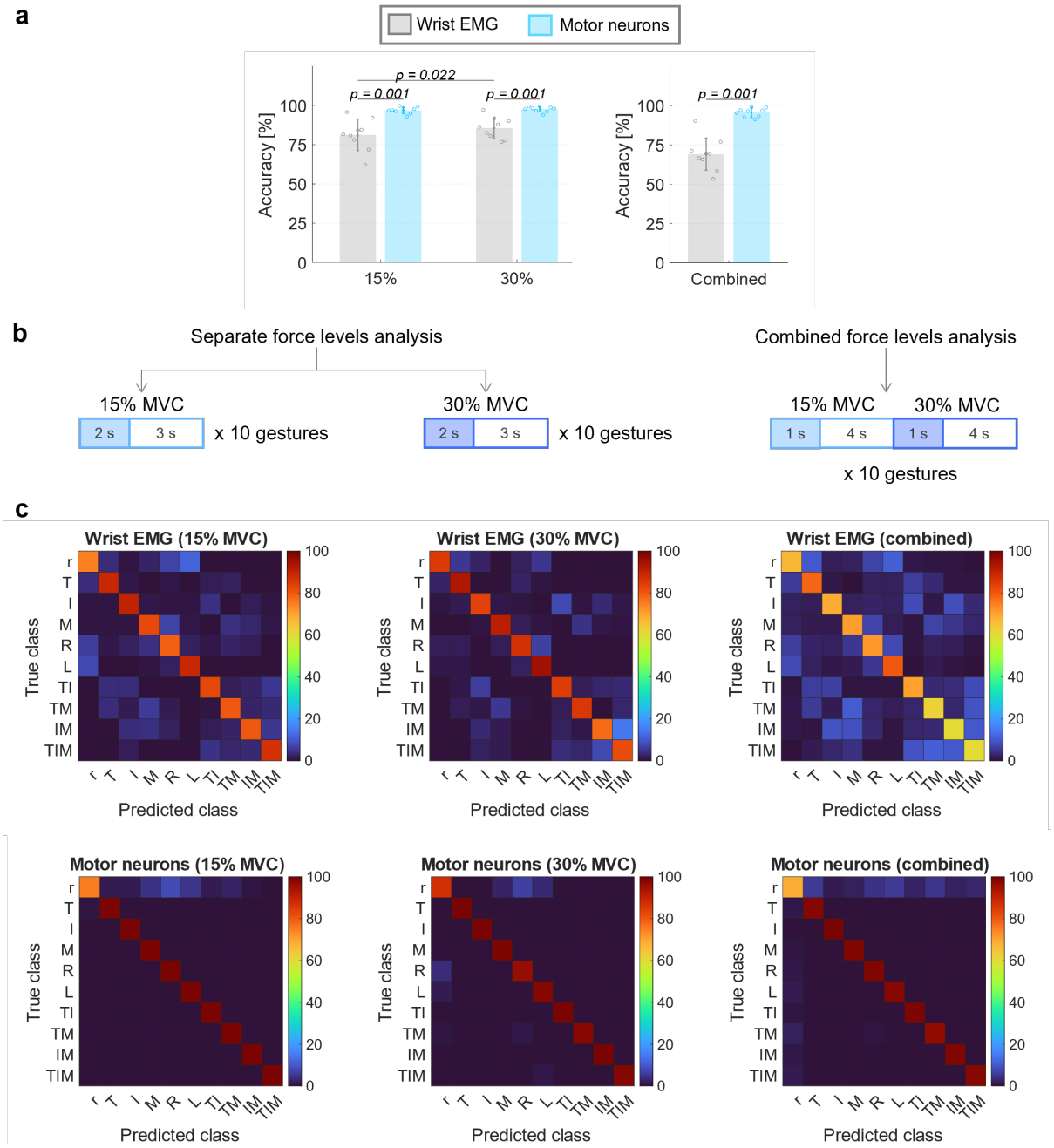

Figure 2.4: Offline finger classification performance. (a) Mean finger classification accuracy (nine finger flexions plus rest, ten classes in total) for the wrist EMG signals (in grey) and decoded MNs' firings from the wrist (in blue) from each force effort (separate analysis) and when both were combined into a single dataset. Plot significances are based on two-way (left) and one-way (right) repeated measures ANOVAs. (b) Blocks representing the ratio between training (shaded) and testing (clear) sets for each class during the ten-fold cross-validation. (c) Confusion matrices with the overall classification accuracy (colour-coded) for each class (r: rest, T: thumb, I: index, M: middle, R: ring, L: little, TI: thumb-index, TM: thumb-middle, IM: index-middle, and TIM: thumb-index-middle) for wrist EMG signals (top) and the decoded MNs (bottom) in each force condition. The obtained classification accuracies show that the decoded MN activity is a better predictor of underlying finger flexion than the wrist EMG signals, with high accuracy (high diagonal components in (c) with few off-diagonal elements), irrespective of the force level.

observed power = 0.998 with $\alpha = 0.05$ and partial $\eta^2 = 0.795$). In addition, the effect of force was only significant for the wrist EMG signals, yielding in higher classification accuracy at the highest force effort ($F_{1,8} = 8.026, p = 0.022$, one-way repeated measures ANOVA, observed power = 0.700 with $\alpha = 0.05$ and partial $\eta^2 = 0.501$).

To simulate more realistic control conditions with variable force levels, the classification accuracy was also calculated after training and testing with finger contractions from both force levels combined. Figure 2.4.b shows how both force efforts were combined into the training and testing sets for each class during cross-validation. The gain in finger classification accuracy when decoding the MN firings from the far-field potentials was even greater in this condition (95.65 $\pm$ 2.76% vs 69.04 $\pm$ 10.61% for MNs and wrist EMG signals, $F_{1,8} = 64.606, p < 0.001$, one-way repeated measures ANOVA, observed power = 1.000 with $\alpha = 0.05$ and partial $\eta^2 = 0.890$).

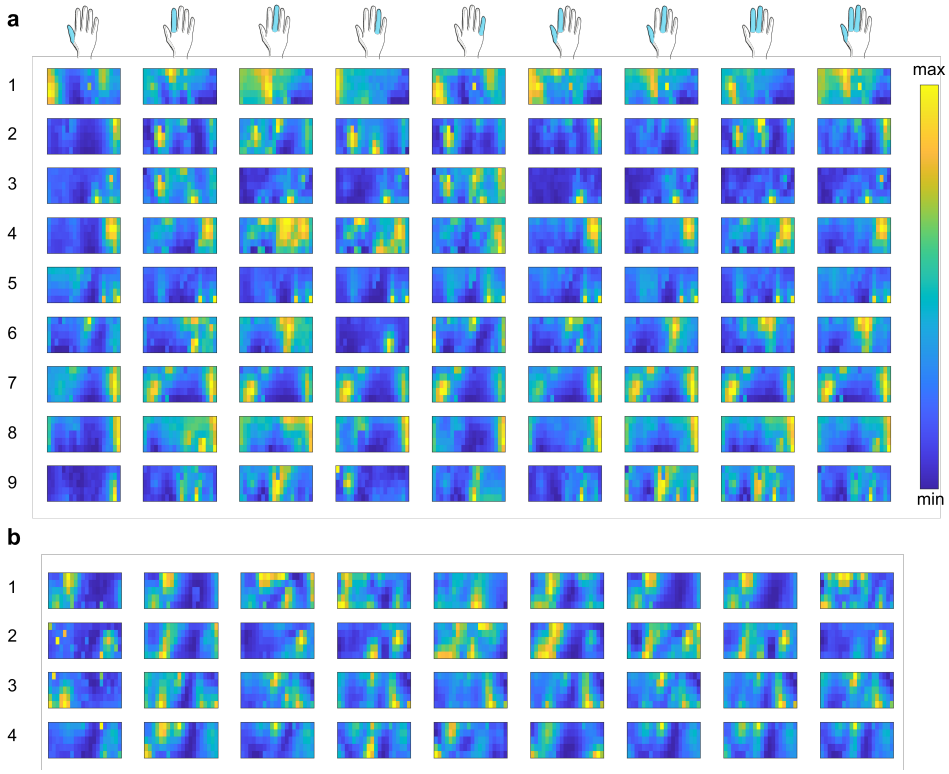

Figure 2.5: 2D spatial distribution of the normalised amplitude of the EMG signals at the wrist. Each subplot depicts the normalised root mean square of the EMG for each channel (pixel) in the electrode array at the wrist (view: bottom = proximal, top = distal, left = ulna flexors, right = ulna extensors). The values for few discarded channels due to noise have been estimated by 2D linear interpolation. The figure shows a high overlap in the activity area of the different finger contractions (columns) within each subject (rows). (a) mean across the maps at 15% and 30% of force efforts from the offline dataset. (b) mean across the maps of the three repetitions of the training set for the online prediction task.

Figure 2.4.c depicts the confusion matrices averaged across all subjects for the individual and combined force conditions, for both wrist EMG signals (top) and the decoded MN firings (bottom). The lower classification accuracy of EMG signals using temporal features can be explained by the similar activation patterns during different gestures as assessed by the spatial

distribution of their normalised EMG amplitude (Figure 2.5).

Overall, the MN activation patterns identified from the wrist provided a highly accurate prediction of finger commands.

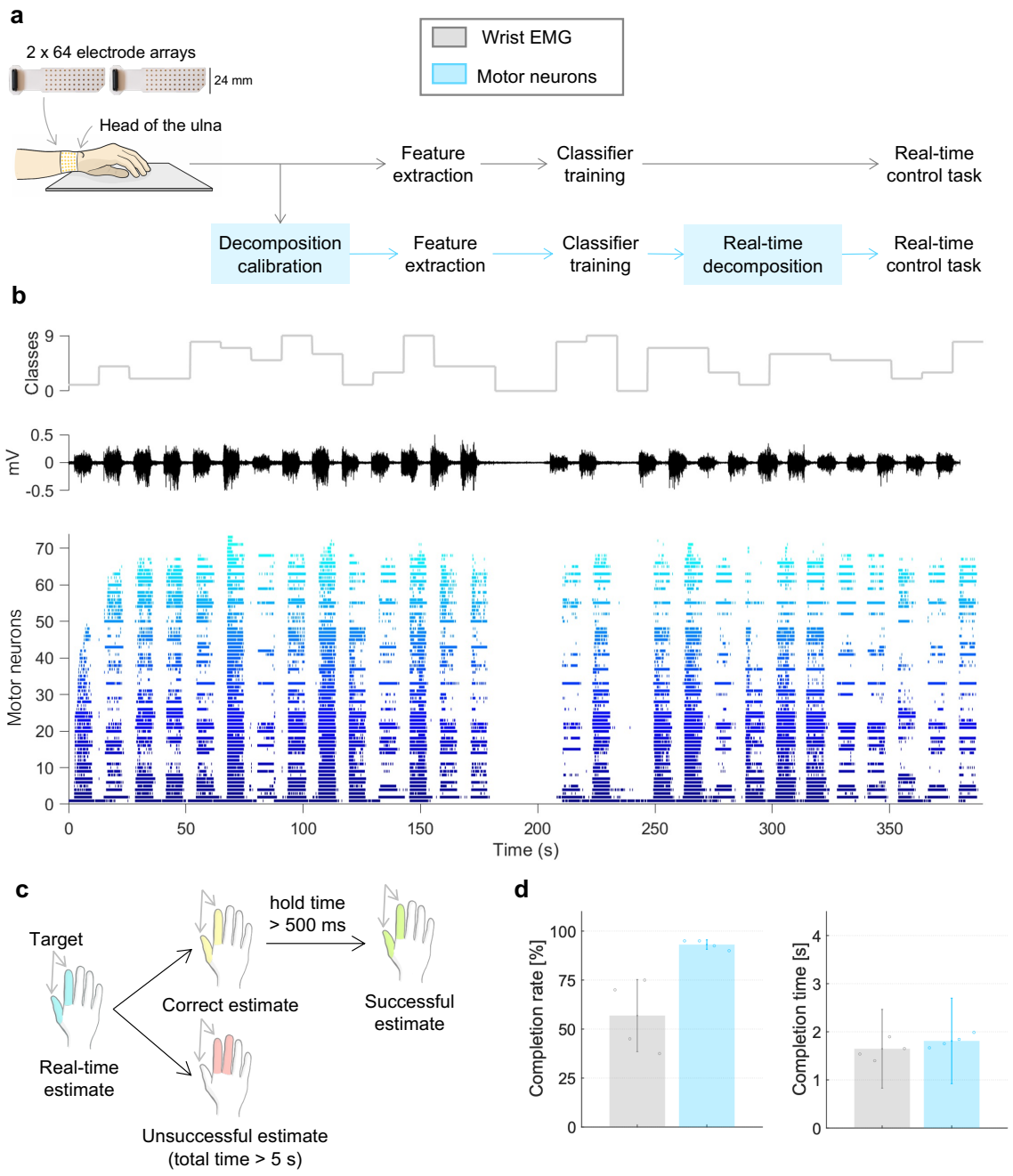

Figure 2.6: Real-time control. (a) Acquisition setup for the online testing with the processing pipelines for the wrist EMG signals (grey) and decoded MNs firings (blue). The additional steps specific of the decomposition algorithm are highlighted in blue. (b) Training set from one representative participant with the class cues on top (each individual finger plus all the combinations of thumb, index, and middle), one wrist EMG signal in the middle, and the decoded MN activity during the decomposition calibration at the bottom. (c) Success and fail conditions for the real-time control task (d) Online control performance for wrist EMG signals (grey) and decoded MN activity (blue) in terms of completion rate and completion time.

2.3.3 Real-time control

A representative example of the decoded motor firings after calibrating the neural interface (Figure 2.6.a) is shown in Figure 2.6.b. On average, 78 ± 8 MNs were identified across all tasks for each participant. The mean completion rate resulted significantly higher for the MN (93.12 ± 2.39 %) than for the wrist EMG signals (56.87 ± 18.41%), while maintaining similar completion times (1.81 ± 0.89 s vs 1.65 ± 0.82 s) (Figure 2.6.d).

The lower online control capacity when using wrist EMG signals without neural decoding is in agreement with previous work (Jiang et al. 2018). Conversely, the control using separated MN activation patterns was more accurate and provided large information transfer (ten classes, ∼93% successful task completions). This effect can be observed in the better separation between gestures in the MNs feature space projected to the first three principal components than in the EMG one (Figure 2.7).

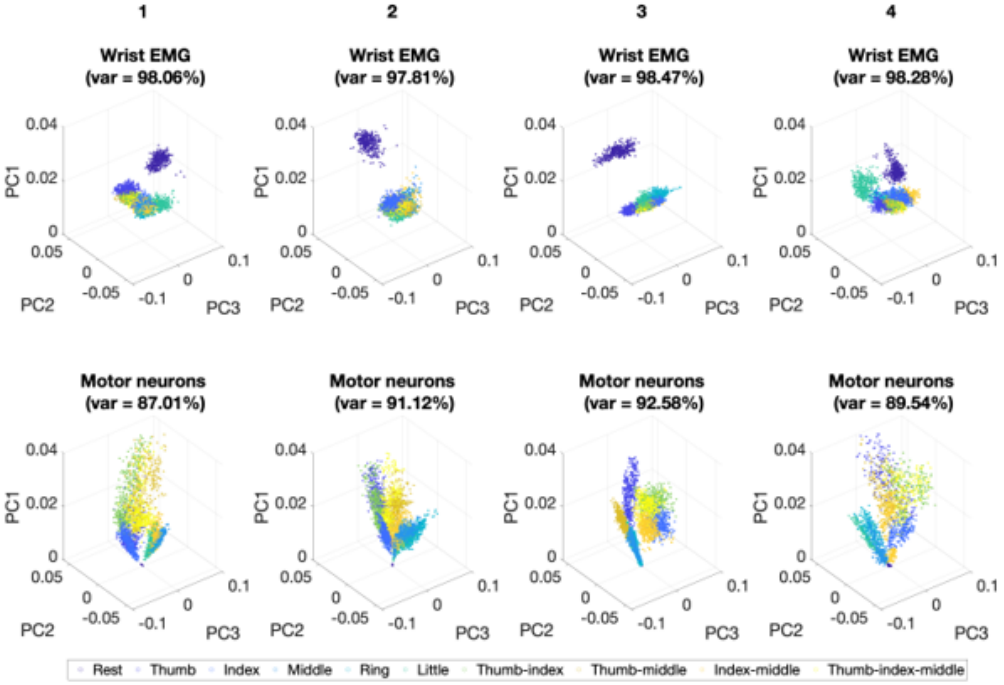

Figure 2.7: Feature space for the wrist EMG signals and decomposed motor neuron firings from the online task training. Visualisation of the features for the wrist EMG signals (top) comprising the root mean square, slope sign changes, waveform length, and zero crossings for each channel, and the spike count of the decoded motor neurons (bottom) over the first three principal components with the total explained variance between brackets. Each column represents one participant and finger contractions are colour coded. The figure shows higher separability between finger contractions in the motor neuron feature space than in the EMG one.

2.4 Discussion

I have shown that the neural information sent from the spinal cord to muscles can be accurately decoded at the single MN level from the far-field potentials generated at the muscle-tendon

interface at the wrist. This neural interface provided a high information transfer rate with the accurate real-time control (∼72 ms total delay) of ten commands elicited by finger tasks. Therefore, the presented results are in line with the vision of future portable, battery-operated systems worn at the wrist as unobtrusive and viable neural interfaces to use in daily living.

Each axonal action potential of a MN determines the generation of action potentials in the innervated muscle fibres. Once excited, the muscle fibres undergo depolarisation in a confined portion of their membrane. The depolarisation zone, which has a length of 5–10 mm, propagates along the muscle fibres from the end plate to the tendons. At the tendons, the depolarisation zone extinguishes, generating a so-called far-field potentials. These are non-propagating components produced by the unbalanced dipole moments of the leading and trailing dipoles during their extinction at the muscle-tendon interface. Far-field potentials are short and have temporal high-frequency components that are less attenuated by the volume conductor than muscle propagating potentials (Dimitrova et al. 2002). In theory, differences in muscle fibre conduction velocity, size, position in the volume conductor, and tendon spread would generate unique far-field potentials for each MN enabling their decomposition from EMG signals recorded over tendon regions.

I validated this hypothesis by retracing the far-field potentials to their corresponding potentials at the forearm from concurrent recordings via spike-triggered averaging (Figure 2.3). This approach showed that most of the sources identified at the wrist coincided with potentials at the forearm that were well above the baseline noise. This result demonstrates the neural origin of the decoded far-field potentials. Indeed, if the decoded activity were not generated by MNs, spike-triggered averaging on muscle electrical signals would yield only noise as it would be equivalent to average uncorrelated EMG signals at the forearm. The observation that approximately 30% of the decoded MNs did not result in averaged potentials above the noise level is explained by the location of the muscle fibres innervated by the detected MNs. For instance, the flexor digitorum superficialis, the flexor digitorum profundus, and the flexor pollicis longus are located deep in the forearm and therefore their innervating MNs generate action potentials detectable at the wrist that may not be at the forearm. This constitutes an advantage of wrist recordings, where muscles present at multiple depths in the forearm converge into more superficial tendons at the wrist, facilitating their detection.

While a more robust tracking approach would have compared the rate of agreement (RoA) between the firings detected at the forearm and the wrist taking into account the effect of conduction velocity, initial comparisons did not result in any common units (RoA $>$ 30%, Holobar et al. 2010). However, the lack of tracked units with this approach can be explained by the decomposition bias towards higher amplitude MNs that innervate a large number of fibres and/or whose territories are more superficial (Holobar et al. 2009). Given the different anatomies at the forearm and the wrist (Figure 1.5) and the relatively small number of detected MNs with respect to the active ones, it is not unreasonable that the decomposition detected different sets of MNs in each location. For this reason, the spike-triggered averaging approach was used instead as it can account for detectability independently of the decomposition algorithm. For

this purpose, a common spike-sorting detection threshold was set at four times the baseline noise (Quiroga et al. 2004). Unlike single probe recordings, the use of high-density electrode grids provides a 2D representation of the detected potentials. In this case, I considered a MN tracked if at least one channel met this condition. This decision was driven by the lack of reporting in previous studies, of the average number of channels where a MUAP is observed. Indeed, this gap in the field inspired the proposed channel selection approach based on the distribution of peak amplitudes for the far-field potential comparisons. Yet again, the different anatomies and electrode arrangements at the forearm and the wrist challenged the transfer of the number of selected channels to the tracking approach. Therefore, the obtained results can be regarded as an upper bound on our ability to trace back potentials form the wrist to the forearm, with possibilities for further improvement by tuning the spatial and temporal parameters for the given type of potentials.

In addition to proving the neural origin of the decoded activity by spike-triggered averaging, I also computed the PNR (known estimate of the mean square error, Holobar et al. 2014), coefficient of variation of the inter spike intervals (associated to the likelihood of erroneously detected action potentials, Holobar et al. 2010), and action potential discharge rate (used as a physiological indicator, Andreassen et al. 1980; Monster et al. 1977). All metrics were well within the expected accuracy and physiological standards, showing that the decoded far-field potentials at the wrist were reliably extracted and corresponded to the neural output from the spinal cord (Figure 2.1).

The number of identified MNs (six MNs per finger contraction at both force efforts) was consistent with the results by Stachaczyk et al. 2020 who identified between 5 and 8 MNs per finger contraction when recording signals from the forearm flexor muscles at similar force effort. Interestingly, however, the PNR levels observed at the wrist in this study were greater than those usually reported for forearm recordings, which was attributed to the different signal characteristics at the wrist with respect to those at the belly of the muscle. The potentials recorded at the wrist are far-field components (Dumitru et al. 1993), which are non-propagating potentials highly synchronised across channels within each MN (as shown in Figure 2.2.d) and shorter in time than the propagating signals recorded from muscles. These characteristics result in greater temporal sparsity at the tendons because of the shorter duration of the individual potentials. Therefore, the EMG signals recorded over tendons can be modelled as convolutive mixtures in which the filters applied to the sources have relatively short duration. Short duration filters are easier to compensate since they better approximate delta functions that represent the sources.

While this also results in sparser observations, it is important to note that far-field potentials are also subjected to the effect of the acquisition system. For instance, Farina et al. 2002a showed that monopolar recordings best capture these far-field potentials with respect to other spatial filtering modalities. In this study, commercial electrode grids were used to cover the wrist (2xGR08MM1305, OT Bioelettronica) and forearm (3xGR10MM0808, OT Bioelettronica

for the forearm). Given the commercially available options this arrangement was considered the best option to cover both locations using a single multi-channel amplifier (Quattrocento, OT Bioelettronica) in monopolar mode. Yet, this resulted in a large number of overlapping electrodes at the wrist (one array covers 2/3 of the circumference of the wrist) which had to be discarded. In addition faulty electrodes and/or those in poor contact with the skin also had to be discarded. On average, 102 ± 12 channels were kept for further analyses but the differences in selected channels affect the spatial sampling for the decomposition and its extension factor for temporal support, potentially influencing the number of reliably identified MNs. In addition, it is conceivable that subjects with smaller wrists (and thus fewer channels) present a larger signal averaging effect of the underlying potentials due to the diameter and inter-electrode distance with respect to the size of their anatomy (Farina et al. 2016b). However, this limitation is common in the field as the fabrication of custom electrodes per participant is impractical.

From the decoded far-field potentials, I performed an offline classification with the aim of using the wrist interface for control applications. While the evaluation of control paradigms is context specific and requires an effective equilibrium between functionality and usability (Karray et al. 2008), in traditional myoelectric control studies, high offline accuracies are regarded as those above 90% (Campbell et al. 2020). Results showed that the decoded far-field potentials accurately predicted finger tasks for up to ten classes with significantly higher accuracy than that of wrist EMG signals. Still, the classification accuracy of wrist EMG signals (∼83%) was slightly higher than the one obtained by Jiang et al. 2017 in a real-time gesture prediction task (∼75%). Although only four sensors were used in that previous study, their location was consistent with our electrode placement below the head of the ulna. In contrast, Botros et al. 2022 reported higher accuracies (∼88%) for offline single and combined finger prediction using the same feature set, but their electrodes targeted the muscle fibres in the proximal and medial part of the wrist instead of the tendons. The main limitation of the wrist EMG signals is their high crosstalk due to the convergence of the muscle tendons in a reduced space. This contributes to the high overlap between the classes in the spatial activity maps (Figure 2.5) and feature space (Figure 2.7) of the EMG signals, which resulted in an overall lower performance than the decoded far-field potentials. In contrast, previous studies by Dai and Hu showed that myoelectric activity spatial maps from the forearm can indeed differentiate between individual finger flexions (Dai et al. 2019b) and extensions (Dai et al. 2020) when a large muscle area is covered. More notably, myoelectric signals from the entire area of the forearm can separate over 30 finger and wrist gestures in offline conditions when a large dataset is provided (>200 contractions)(Jiang et al. 2021).

To increase the information transfer and enhance the separability between finger classes despite the limited area, the wrist EMG signals need to be decoded into the neural output of the spinal cord. However, no other study has previously addressed the potential of the wrist for non-invasive neural interfacing, thus the only comparative results are from the forearm. In a finger prediction task, Stachaczyk et al. 2020 obtained similar classification accuracy for the neural output of the spinal cord at the forearm (98%) to the presented here at the wrist (∼97%), although only for individual finger tasks (the four digits, excluding the thumb, while here I tested

classification over ten tasks comprising individual and combined finger gestures). Therefore, the reported accuracy in finger task classification when decoding MNs from the wrist is even superior to that of MNs decoded from muscle tissue. Stachaczyk et al. 2020 also found that the neural output was robust to variations in the force level, unlike myoelectric signals from the forearm when predicting finger flexions. Indeed, the increased classification error of wrist EMG signals when both force levels were combined was in agreement with previous literature on the effect of dynamic contractions in myoelectric pattern recognition (Campbell et al. 2020; Phinyomark et al. 2020). These findings suggest that MNs discriminative power between fingers does not rely on spatial information, nor on force encoding. This is supported by the feature map of the decoded wrist EMG signals presented in Figure 2.7 where the different classes exhibit higher separability than in the wrist EMG feature space, despite targeting the same area and corresponding to multiple force levels.

Yet, previous studies have shown that offline performance is not always representative of the actual usability performance in real-time (Nawfel et al. 2021; Vujaklija et al. 2017). Indeed, the limited data included in the offline analysis (segments of a single repetition per gesture) questions the reproducibility and consistency of the results. For this reason, a proof-of-concept real-time experiment was carried out with multiple repetitions to validate and extend the offline results to real-life interfacing scenarios. This analysis showed that the far-field potentials of the tendon endings at the wrist can be accurately detected and enabled real-time interfacing ($\sim$3 ms) with over 70 MNs. Moreover, this neural decoding led to high reproducibility and separability between finger contractions, as evidenced by the high task completion rate (>93%) in relatively short time ($\sim$1.81 s per task). While it is conceivable that participants used different strategies to complete the tasks, this was not fully accounted for in the experimental design. Arguably, the use of a classifier algorithm reduces the ability of subjects to develop different strategies to complete the task, as feedback of a given output (correct or not) does not provide any information of how close the subject is from another desirable outcome as is the case in a continuous controllable space. Yet, different strategies or exploratory time to perform a given task would have translated into high between subject variability in terms of completion time. Given the consistent representations in the feature space (Figure 2.7) paired with the low variability in the average completion time for both modalities across subjects (Figure 2.6), the results seem to indicate that rather than different strategies, the variability in performance and execution time seems to be driven by the classifiers' ability to correctly identify the performed gestures. However, long-term effects that might affect the overall performance of the interface such as learning were not measured since the experiment was designed as a brief proof-of-concept study. Yet, at the time of writing and to the best of my knowledge, no other study has previously implemented a pattern recognition approach with neural decoding in real-time.

Nonetheless, these results were obtained during isometric contractions where the position of the arm and hand were fixed. These conditions facilitate the decoding of the MN firings since the decomposition filters are not subjected to the effect of muscle fibre shortening/lengthening, which is typical of dynamic contractions. Yet, this constitutes a highly controlled setup, unlikely

to happen in real-life scenarios. Hence, future work should address how these factors affect the robustness and long-term performance of the non-invasive wrist neural interface.

Chapter 3

Decoding motor neuron activity during dynamic contractions

[1]

Robustness to non-stationary conditions is essential to develop stable and accurate wearable neural interfaces. I propose a novel adaptive EMG decomposition algorithm that builds on blind source separation methods by leveraging the Kullback-Liebler divergence and kurtosis of the signals as metrics for online learning. The proposed approach provides a theoretical framework to tune the adaptation hyperparameters and compensate for non-stationarities in the mixing matrix, such as due to dynamic contractions, and to identify the underlying MN discharges. The adaptation is performed in real-time (∼22 ms of computational time per 100-ms batches). The proposed adaptation algorithm significantly improved all decomposition performance metrics with respect to the absence of adaptation in a wide range of motion of the wrist (80°). The rate of agreement, sensitivity, and precision were $\geq 90\%$ in $\geq 80\%$ of the cases in both simulated and experimentally recorded data, according to a two-source validation approach. The findings demonstrate the feasibility of accurately decoding MN discharges in real-time during dynamic

[1]The work in this chapter has been published as "Real-Time Identification of Motor Neuron Discharges in Dynamic Motor Tasks" as a preprint in *biorxiv* see (Mendez Guerra et al. 2024) with authors: **Irene Mendez Guerra**[2], Deren Y. Barsakcioglu[2], Dario Farina[2]. The text has been adapted to fit the format and flow of the thesis as a single cohesive document.

[2]Department of Bioengineering, Imperial College London, London, United Kingdom

The neuromechanical model used in this chapter to simulate dynamic contractions to validate the proposed adaptive decomposition pipeline is supported from:

"A myoelectric digital twin for fast and realistic modelling in deep learning" published in *Nature Communications* see (Maksymenko et al. 2023) with authors: Kostiantyn Maksymenko[3], Alexander Kenneth Clarke[4], **Irene Mendez Guerra**[4], Samuel Deslauriers-Gauthier[3,5], and Dario Farina [4].

[3]Neurodec, Sophia Antipolis, France

[4]Department of Bioengineering, Imperial College London, London, UK

[5]Centre Inria d'Université Côte d'Azur

"NeuroMotion: Open-Source Simulator to Generate Highly-Accurate EMG Signals during Voluntary Movement" see (Ma et al. 2023b) with authors: Shihan Ma[6,7], **Irene Mendez Guerra**[6], Arnault H. Caillet[6], Jiamin Zhao[7], Alexander Kenneth Clarke[6], Kostiantyn Maksymenko[8], Samuel Deslauriers-Gauthier[8,9], Xinjun Sheng[7,10], Xiangyang Zhu[7,10] and Dario Farina[6].

[6]Department of Bioengineering, Imperial College London, London, UK

[7]State Key Laboratory of Mechanical System and Vibration, Shanghai Jiao Tong University, Shanghai, China

[8] Neurodec, Sophia Antipolis, France

[9]Inria Centre at Universit e C^ote d'Azur, Nice, France

[10]Meta Robotics Institute, Shanghai Jiao Tong University, Shanghai, China

contractions from wearable systems mounted at the wrist and forearm. Moreover, the study proposes an experimental validation method for EMG decomposition in dynamic tasks.

3.1 Introduction

The vision for neural interfaces is to tap the motor system to develop new control paradigms for rehabilitation, computer interaction, and augmentation by decoding user intentions from neural codes. One promising approach interfaces the pools of spinal MNs – the last layer of the nervous system. By leveraging the electrical potential amplification of muscle fibres, MN activity can be decoded non-invasively from surface EMG using blind source separation (Chen et al. 2016b; Holobar et al. 2007b; Negro et al. 2016a) or deep learning techniques (Clarke et al. 2021; Wen et al. 2021). In today's rapidly evolving wearable landscape, the possibility to harness such MN activity for home rehabilitation or wide-range consumer electronics is closer than ever. Yet, a key remaining challenge for this vision, is the long-term stability of the EMG decomposition during non-stationary conditions.

While EMG decomposition algorithms have undergone rigorous validation, most approaches assume a mixing matrix that is constant over time. This simplification is valid during non-fatiguing isometric static contractions, where the joint position is fixed and the force is kept constant. In these highly controlled conditions, the firings of each active MNs are cyclostationary (Farina et al. 2016a). Each MN firing determines the generation of motor unit action potentials (MUAPs) at the neuromuscular junction. MUAPs then propagate along the membrane of the muscle fibres towards the tendon endings, producing a characteristic spatiotemporal electric potential. Decomposition algorithms seek to pseudo-invert these patterns to retrieve the underlying MN firings. To do so, blind source separation approaches first uncorrelate (whiten) the EMG signals and then iteratively find the separation vectors that maximise the sparsity of the MN spike trains (Chen et al. 2016b; Holobar et al. 2007b; Negro et al. 2016a). Since the process is computationally intensive, decomposition parameters are usually calibrated in advance, prior to their real-time application in interactive settings (Barsakcioglu et al. 2021). Crucially, the effectiveness of such approach relies on the operational conditions remaining consistent with those present during the calibration phase. However, during natural movements, such stationary constraints are violated. When joints move, muscle fibres shorten and lengthen, changing not only the shape of the muscle but also pulling the surrounding tissue. These changes in the volume conductor alter the stereotypical profile of the MUAP waveforms, producing a dynamic mixing model.

At the wrist level, most forearm muscle fibres converge into tendons exhibiting unique electrical properties. When MUAPs reach the muscle-tendon interface, far-field potentials emerge as non-propagating components in the recorded signal before their complete extinction (Dumitru et al. 1991, 1993; Stegeman et al. 1997). Similarly to the propagating components of the MUAPs, far-field potentials are also influenced by changes in fibre length and volume conductor properties (Schulte et al. 2004).

Understanding the interplay between anatomical factors and dynamic modulation will con-

tribute to the development of more robust EMG decomposition algorithms. Furthermore, these insights will enhance the design of wearable technologies, given that the wrist is the preferred location for users. Yet, only few studies have tried to characterised the modulation MUAPs undergo under dynamic contractions (Glaser et al. 2019; Kramberger et al. 2021; Yokoyama et al. 2021). Most significantly, Kramberger et al. 2021 evaluated MUAP changes from the biceps brachii across the entire elbow range of motion, showing a piece-wise linear trend with segments corresponding to 20 % of the total elbow joint angle. These local linearities elucidate the reported ability to identify few MNs during dynamic contractions over relatively small ranges of motion under highly controlled experimental conditions (Oliveira et al. 2021; Yokoyama et al. 2021) and set the foundation for continuous updates.

Prior research has aimed to address the challenges of non-stationarities in the EMG mixing model by implementing recursive updates of the decomposition parameters based on new batches of data (Chen et al. 2020a; Glaser et al. 2019, 2013; Kramberger et al. 2021; Yeung et al. 2024). While these approaches have shown significant improvements in the accuracy of the detected spikes, the selection of some of the model hyperparameters is often ad-hoc based on the available dataset, providing a limited theoretical framework to deal with non-stationarities. In addition, validation so far has mainly relied on oversimplified simulated data (Chen et al. 2020a) or hybrid data approaches (Glaser et al. 2019; Kramberger et al. 2021) due to the lack of better means. Only Yeung et al. 2024 used the gold-standard of matched intramuscular recordings for validations. However identifying common MNs in intramuscular and surface recordings remains challenging and limits the validation to few sources.

Recent advances in neuromuscular modelling offer new tools to address the validation problem. One notable example is NeuroMotion (Ma et al. 2023b), which is a full-spectrum dynamic neuromechanical model that leverages physiological parameters from a myoelectric digital-twin (Maksymenko et al. 2023), a musculoskeletal model (McFarland et al. 2023) and deep learning (Ma et al. 2023a) to generate dynamic contractions with MN ground truth. While models like this one may provide previously unavailable insights on the modulation induced by dynamic contractions, it is still crucial to validate their outcomes experimentally.

Therefore, to develop a reliable and robust neural interface for long-term human-machine interaction, I first characterised how muscle fibre shortening and lengthening affect electric potentials using the NeuroMotion model (Ma et al. 2023b) and experimentally recorded data from the forearm and the wrist. To analyse the experimental data, I propose a novel MUAP tracking approach for dynamic contractions that takes into account spatial, temporal, and amplitude features. Subsequently, I present an adaptive decomposition approach that recursively updates the decomposition parameters minimising the difference between the operational conditions and those during calibration. To do so, the algorithm leverages differentiable metrics such as the Kullback-Liebler divergence and kurtosis to guide the adaptation by minimising the median squared error with respect to the values at calibration. In this way, the proposed algorithm solely relies on signal properties providing a theoretical basis for the parameter optimisation.

Here I show that the proposed adaptation can restore the accuracy of the decomposition under dynamic conditions in both simulated and experimental datasets after MUAP tracking in a double-source validation approach. Results show $\geq 90\%$ RoA, sensitivity, and precision in $\geq 80\%$ of the cases in both simulations and experimental data (median $> 98\%$ across all metrics and scenarios). Moreover, the execution time of the entire adaptation pipeline was lower than the average neuromechanical delay ($\sim$ 200 ms, Del Vecchio et al. 2018) making it suitable for real-time human-machine interaction applications.

3.2 Methods

3.2.1 Neuromuscular model simulations

Shortening and lengthening contractions at constant force were simulated using a full-spectrum dynamic neuromechanical model (NeuroMotion, Ma et al. 2023b). The open-source model combines a neural model (Fuglevand et al. 1993) that simulates MNs' recruitment and force production; an AI-based volume conductor model (BioMime, Ma et al. 2023a) that generates and/or morphs MUAPs based on dynamic physiological parameters; and an OpenSim upper limb musculoskeletal model to infer the dynamic parameters.

Briefly, the neuromuscular model simulates dynamic contractions by first emulating the desired movement in an upper limb musculoskeletal model (McFarland et al. 2023). The resulting muscle fibre length changes are fed into BioMime, an AI-based volume conductor model (Ma et al. 2023a), along with the number of fibres innervated by each MN, their depth, angular position, innervation zone, and conduction velocity. The parameters related to muscles' geometries and position are based on a myoelectric digital-twin (Maksymenko et al. 2023) that generates accurate anatomical representations from magnetic resonance imaging. Notably, the model uses the changes in muscle fibre length to compute the corresponding changes in depth and conduction velocity under the assumption that muscles' volumes are constant during dynamic contractions (Mesin et al. 2006). BioMime uses these parameters to generate the corresponding MUAPs and morph them across the simulated postural changes. Finally, EMG signals are generated by convolving the MN spike trains, simulated according to a MN recruitment and firing model (Fuglevand et al. 1993), with their respective MUAPs at the corresponding posture. The obtained signals correspond to an electrode band arranged in 10 x 32 electrodes, that is placed around the proximal third of the forearm corresponding to the muscles' bellies.

The simulated contractions involved an isometric index flexion while performing wrist flexion/extension to emulate the effect of postural changes of the hand. A pool of 100 MNs was simulated for the flexor digitorum superficialis muscle (FDS). The innervated fibres were randomly and uniformly distributed within the muscle volume, with innervation zones modelled as normally distributed around 50 $\pm$ 10 % (mean $\pm$ std) of the total fibre length. The MN's recruitment thresholds and number of innervated muscle fibres were represented by an exponential function, which had a higher number of small low-threshold MNs compared to large high-threshold ones. Conduction velocities were drawn from a normal distribution (4.0 $\pm$ 0.5 m/s, mean $\pm$ std), and

sorted according to the number of innervated fibres (Andreassen et al. 1987; Farina et al. 2000). When excitation surpassed a MN's recruitment threshold, the MN began firing at a rate of 8 pps (Fuglevand et al. 1993). As the excitation increased, the discharge rate rose linearly by 3 pps for every 10 % increase in excitation (Fuglevand et al. 1993; Keenan et al. 2006). The first MN recruited had its top discharge rate at 35 pps (Fuglevand et al. 1993). This rate reduced linearly with higher recruitment thresholds, up to 25 pps (Fuglevand et al. 1993). The last MN was recruited at 30 % of the maximum excitation. Discharge rates followed a random Gaussian-distributed process, with a 0.2 coefficient of variation (Fuglevand et al. 1993; Keenan et al. 2006).

To assess the effect of muscle shortening and lengthening, a FDS MUAP library was generated for each wrist joint angle degree (1 MUAP/°), ranging from -40°(flexion) to 40°(extension), corresponding to the range needed for most activities of daily living (Gates et al. 2016). This process was repeated for 10 bootstrapping iterations, maintaining the same parameter distributions described above. Thereafter, two dynamic contractions of the wrist were simulated under 15% constant MN excitation. In them, the wrist joint angle followed a staircase pattern with constant phases every 10° from 0° to -40° for flexion or 40° for extension. The constant and transition phases lasted 30 s and 10 s, respectively. EMG signals were generated for each contraction at 2048 Hz sampling frequency and 30 dB signal to noise ratio. Therefore, the simulated dataset comprised 20 contractions (10 bootstrapping sets, 2 conditions: flexion and extension). The constant phases of these patterns were used to calibrate a CBSS (Negro et al. 2016a) decomposition model (at 0°) and to evaluate the accuracy of the decomposition adaptation.

3.2.2 Experimental data

Nine healthy participants (four females, five males, ages: 24-30) took part in the study after signing informed consent forms. The experimental protocol was approved by the local ethics committee of Imperial College London (reference number 18IC4685) and was conducted in accordance with the Declaration of Helsinki.

EMG signals were concurrently recorded from the wrist (two electrode grids GR08MM1305, OT Bioelettronica, of 64 electrodes, arranged as 5 × 13, with 8 mm distance) and the forearm (three electrode grids GR10MM0808, OT Bioelettronica, of 64 channels arranged in 8 × 8 with 10 mm distance). First, the recording areas were shaved and treated with alcohol and abrasive gel. Thereafter, electrodes were placed along the circumference of the wrist right below the head of the ulna by visual inspection and physical palpation. Similarly, the electrodes at the forearm were placed around the circumference of the proximal third of the forearm corresponding to the muscles' belly. EMG signals were acquired in monopolar mode (reference and ground bands were placed around the elbow) by a multi-channel amplifier (Quattrocento, OT Bioelettronica), bandpass filtered between 10 and 900 Hz, and sampled at 2048 Hz with 16-bit ADC precision. After acquisition, EMG signals were digitally bandpass filtered between 20 and 500 Hz (second-order Butterworth).

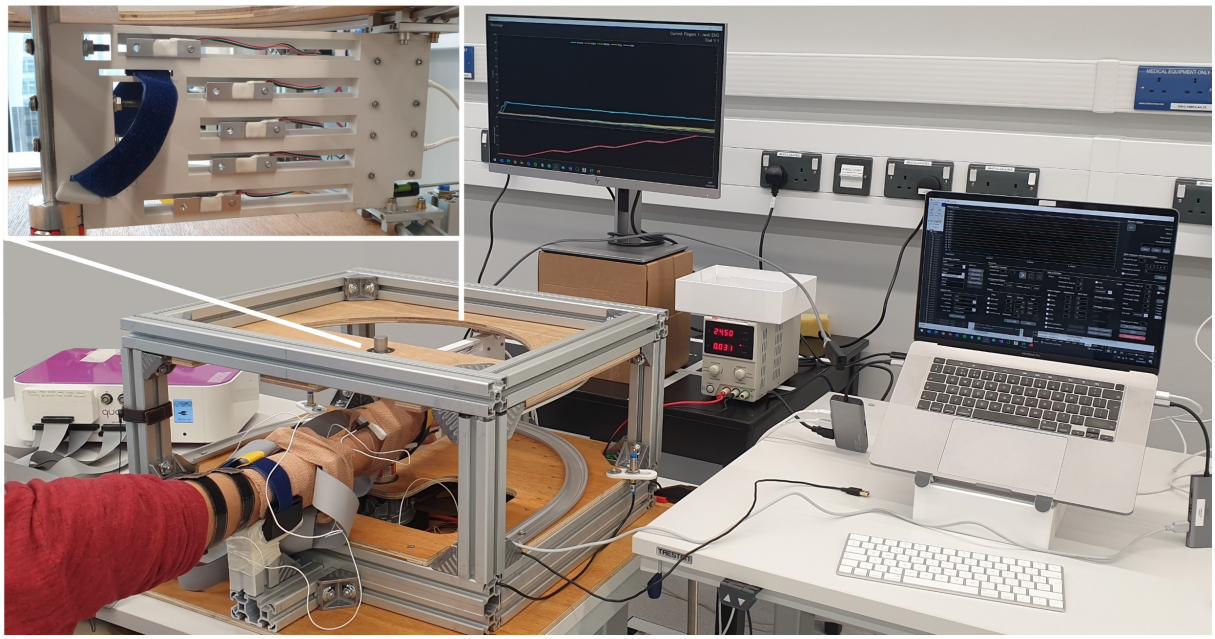

Figure 3.1: Experimental setup. EMG signals were concurrently recorded from the wrist and the forearm during isokinetic contractions where participants received feedback of their individual finger forces while a motorised platform controlled their wrist joint angle over flexion/extension. A zoomed in version of the motorised platform with the finger load cells is displayed on the top left corner.

Participants were asked to place their right arm on a custom isokinetic system for wrist flexion and extension (see Figure 3.1 and Appendix A1). The isokinetic system included an elbow support, a motorised moving platform with hand support, and five adjustable micro load cells (0–5 kg CZL635, Phidget, 25 Hz sampling frequency) to record individual digit flexion and thumb abduction forces. While participants controlled the exerted finger forces, the angle of the hand platform was controlled by the motor (DOGA brushed geared, 24 V DC, 9 Nm, 45 rpm). The motor had integrated hall sensors that tracked the speed, direction and position of the motor, which were recorded at 100 Hz sampling frequency. To avoid any injuries, the motor operating range was limited with two inductive proximity sensors (LJ12A3-4-Z/BX, Heschen) between -50° and 50°, which was well below the maximum reported range of the wrist of ∼80° and ∼70° for flexion and extension, respectively (Alford 2021). Furthermore, during the experiment, an emergency stop button was held by the operator at all times. A custom Matlab (Mathworks Inc.) program was developed to synchronise all signal recordings and to provide participants with feedback of the cues and exerted finger forces, as well as the motor cue and current position.

At the beginning of the session, the hand was positioned so that the distal palmar crease was aligned with the rotating axis of the platform at the reference neutral position. At that point, the hand was securely strapped to the platform and the position of the force sensors was adjusted to ensure comfortable reach. Thereafter, the force sensor baselines and maximum voluntary contraction (MVC) forces were calibrated for each finger. Participants performed isometric digit flexions and thumb abduction at 15% MVC (individual fingers and all possible combinations of thumb, index, and middle) while the motor changed their wrist joint angle following a staircase pattern (from 0° to -40° flexion or 40° extension every 10° steps). To avoid participants' fatigue,

the constant and transition phases of the staircase angle pattern lasted 5 s and 10 s, respectively. Two repetitions of each contraction were recorded, resulting in 36 contractions in total (9 finger gestures, 2 conditions: flexion and extension, and 2 repetitions).

3.2.3 Decomposition adaptation

As discussed in Section 1.2, EMG signals are generated by the spatiotemporal summation of the trains of potentials of the active MNs, which are mathematically formulated as the convolution between the MN spike trains and their corresponding MUAP waveforms (Farina et al. 2016a). EMG decomposition algorithms compute the pseudo-inverse of the MUAPs, under the assumption that MN spike trains are sparse (i.e. supergaussian distributions with positive kurtosis) and that each MUAP is unique for each MN, which has been also validated for the non-propagating far-field potential components at the wrist (Mendez Guerra et al. 2022). In human-machine interfacing applications, EMG decomposition parameters are first calibrated from a sample contraction offline to ensure convergence. Thereafter, the whitening matrix, separation vectors, and spike detection parameters are applied in real-time on new testing data (Barsakcioglu et al. 2021; Chen et al. 2020c). This approach requires that the mixing matrices of both calibration and testing data remain identical and constant over time. While this assumption holds in isometric contractions, it is violated under postural changes or dynamic contractions. Hence, I present a new adaptation paradigm that updates the previously calibrated whitening matrix, separation

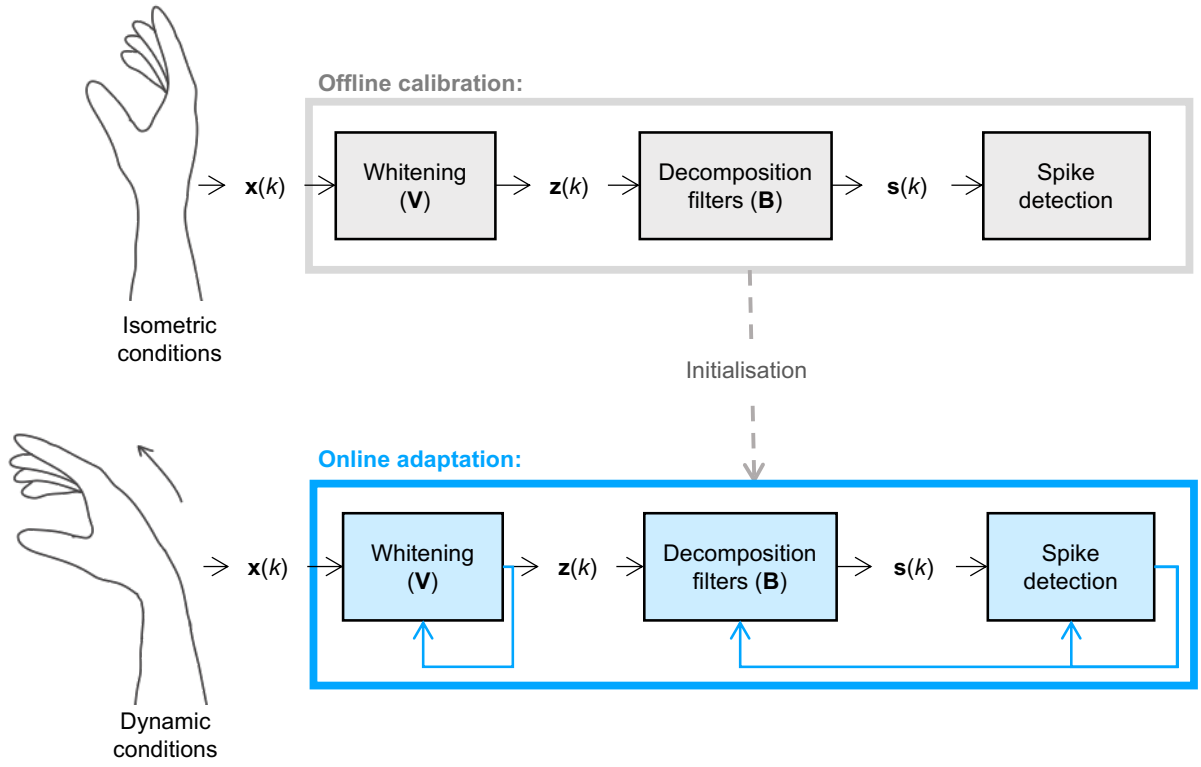

Figure 3.2: Proposed dynamic decomposition adaptation pipeline. A model previously calibrated during isometric conditions (top) is used to initialise the decomposition during dynamic contractions (bottom). In this case, the whitening, separation vectors, and spike detection parameters are updated in batches based on gradient descent.

vectors, and spike detection parameters by minimising the median squared error between the Kullback-Liebler divergence and kurtosis with respect to the calibration values for new batches of data (100 ms) to compensate for non-stationarities due to dynamic contractions or postural changes. The decomposition pipeline is shown in Figure 3.2.

The rationale of this approach relies on signal properties or contrast functions that determine the effectiveness of each step of the decomposition. For instance, the Kullback-Liebler divergence measures the deviation of the covariance of the extended EMG signals during the operational conditions from the identity matrix indicating the effectiveness of the whitening matrix. Similarly, the kurtosis of the projected sources is a measure of non-gaussianity, and hence its maximisation makes the identified sources sparser, which is the condition used to compute the separation vectors during calibration. However, an unconstrained optimisation might result in perfectly uncorrelated noise or maximum sparsity such as a single overfitted firing. To avoid this, the median squared errors between the operational and calibration metrics are minimised. This approach takes advantage of the calibration conditions to infer the right values of the Kullback-Liebler divergence and kurtosis metrics to adapt the whitening and separation vectors accordingly. Importantly, this provides a clear optimisation goal based only on the properties of the signals, allowing the calibration of the adaptation hyperparameters without relying on ground truth data. This way, the proposed approach can be viewed as a method to compensate modulations in the decomposition model that divert from the calibration conditions when MN firings were reliably identified.

3.2.3.1 Whitening adaptation

The whitening matrix is often computed via eigenvalue decomposition (Negro et al. 2016a) or singular value decomposition (Barsakcioglu et al. 2021). However, these processes are not adaptive and computationally expensive to be run in real-time. To compensate for this, I propose a new adaptive approach based on the Kullback-Leibler divergence between two zero-mean normal distributions with covariance equal to $\boldsymbol{R}_z$ and $\boldsymbol{I}$ (Cardoso et al. 1996). The Kullback-Leibler is computed as:

$$K\left(\boldsymbol{R}_z\right) = \frac{1}{2}\left(\text{Trace}\left(\boldsymbol{R}_z\right) - \log\det\left(\boldsymbol{R}_z\right) - n\right) \tag{3.1}$$

and serves as a measure of uncorrelation since it is equal to zero if $\boldsymbol{R}_z = \boldsymbol{I}$ and positive, otherwise. Therefore, the whitening matrix $\boldsymbol{V}$ is a minimiser of the following cost function ϕ_1:

$$\phi_1(\boldsymbol{V}) = K\left(\boldsymbol{R}_z\right) = K\left(\boldsymbol{V}\boldsymbol{R}_x\boldsymbol{V}^\top\right) \tag{3.2}$$

Taking the natural or relative gradient (see Appendix A in Cardoso et al. 1996) with respect to $\boldsymbol{V}$ yields:

$$\nabla\phi_1(\boldsymbol{V}) = \boldsymbol{R}_z - \boldsymbol{I} \tag{3.3}$$

that results in the following whitening update rules:

$$\boldsymbol{z}_t = \boldsymbol{V}_{t-1}\boldsymbol{x}_t \tag{3.4}$$

$$\boldsymbol{R}_{z_t} = E\left\{\boldsymbol{z}_t\boldsymbol{z}_t^\top\right\} \tag{3.5}$$

$$\boldsymbol{V}_t = \boldsymbol{V}_{t-1} - \eta_1\left[\boldsymbol{R}_{z_t} - \boldsymbol{I}\right]\boldsymbol{V}_{t-1} \tag{3.6}$$

where t represents the batch number, and η_1 is the learning rate that modulates the weight given to the new batch information. Its value is optimised as the minimiser of the median cost across all batches:

$$\eta_1 = \operatorname{argmin}\left[\underset{t}{\operatorname{med}}(\phi_1(\boldsymbol{V}))\right] = \operatorname{argmin}\left[\underset{t}{\operatorname{med}}(K(\boldsymbol{R}_z))\right] \tag{3.7}$$

While it was found that this approach works well in simulations, for experimental data the minimum median squared error between the operational and calibration conditions had to be minimised due to differences in the topology of cost functions (Figure 3.3), resulting in the updated cost function ϕ_2:

$$\phi_2(\boldsymbol{V}) = \underset{t}{\operatorname{med}}[K\left(\boldsymbol{R}_z\right) - K\left(\boldsymbol{R}_{calib}\right)]^2 \tag{3.8}$$

where $\boldsymbol{R}_{calib}$ corresponds to the covariance of the whitened signals during the calibration phase.

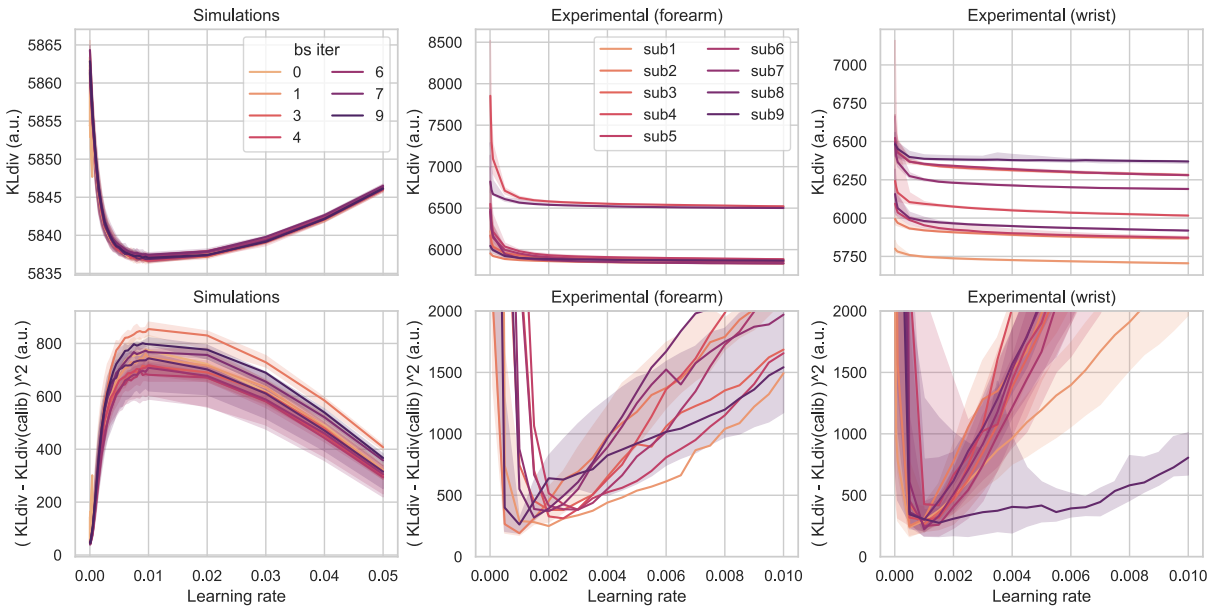

Figure 3.3: Whitening learning rate optimisation for simulated and experimental data. Top row: median (solid line) and interquartile range (shaded area) of the Kullback-Liebler divergence as a function of the learning rate for each bootstrapping iteration (colour) of the simulated data (left), each subject (colour) at the forearm (middle) and wrist (right). Bottom row: Respective median (solid line) and interquartile range (shaded area) of the median squared error of the Kullback-Liebler divergence between the operational and calibration conditions (here considered at 0°) as a function of the learning rate. While in simulations a global minimum was found for the divergence, the experimental data required the minimisation of the median squared error. Since the error was assumed constant across the contraction, both approaches share the same adaptation rule, albeit a different hyperparameter selection criteria.

Similarly as in the previous case, taking the natural gradient results in the following update rules per batch:

$$\boldsymbol{z}_t = \boldsymbol{V}_{t-1}\boldsymbol{x}_t \tag{3.9}$$

$$\boldsymbol{R}_{z_t} = E\left\{\boldsymbol{z}_t\boldsymbol{z}_t^\top\right\} \tag{3.10}$$

$$\boldsymbol{V}_t = \boldsymbol{V}_{t-1} - \eta_1[K\left(\boldsymbol{R}_{z_t}\right) - K\left(\boldsymbol{R}_{calib}\right)]\left[\boldsymbol{R}_{z_t} - \boldsymbol{I}\right]\boldsymbol{V}_{t-1} \tag{3.11}$$

Since both the learning rate η_1 and divergence error term are scalars, one can rewrite the previous Equation 3.11 as:

$$\boldsymbol{V}_t = \boldsymbol{V}_{t-1} - \eta_2\left[\boldsymbol{R}_{z_t} - \boldsymbol{I}\right]\boldsymbol{V}_{t-1} \tag{3.12}$$

where $\eta_2 = \eta_1[K\left(\boldsymbol{R}_z\right) - K\left(\boldsymbol{R}_{calib}\right)]$. By assuming a constant error rate, Equations 3.6 and Equations 3.12 become analogous, and therefore the adaptation rule for both simulated and experimental data sets was the same, except for the choice of the hyperparameter (η_1 for simulations, η_2 for experimental conditions). In this case, η_2 was optimised as the median squared error of Kullback-Liebler divergence across all batches with respect to the calibration:

$$\eta_2 = \text{argmin}\left[\underset{t}{\text{med}}(\phi_2(\boldsymbol{V}))\right] = \text{argmin}\left[\underset{t}{\text{med}}\left[K(\boldsymbol{R}_z) - K(\boldsymbol{R}_{calib})\right]^2\right] \tag{3.13}$$

An initial grid-search optimisation resulted in the following hyperparameter values: $\eta_1 = 7e^{-3}$ for the all the simulated dataset, $\eta_2 = 1e^{-3}$ for the all the experimental wrist data, and $\eta_2 = 2e^{-3}$ for the all the experimental forearm data (see Figure 3.3). After the optimal whitening hyperparameters were found, Equations 3.6 and Equations 3.12 were used to update the whitening matrix in simulations and experimental data, respectively.

3.2.3.2 Adaptation of separation vectors adaptation

To adapt to nonstationarities in the separation vectors I propose the minimisation of the median squared error of the kurtosis of the sources with respect to their value at calibration. The kurtosis corresponds to the fourth-order cumulant of a random variable and is zero for gaussian distributions. Therefore, the kurtosis can be used as measure of nongaussianity, with higher values for more sparse sources (Hyvärinen et al. 2001b). Indeed, its squared value is commonly used as approximation of the negentropy, although its nonpolynomial approximation is often preferred (Hyvärinen et al. 2001b). Following this rationale, here I approximate the kurtosis (κ) per source ($\boldsymbol{s}$) as:

$$\kappa(\boldsymbol{s}) \propto E\left\{g(\boldsymbol{s})\right\} - E\left\{g(\boldsymbol{\nu})\right\} \tag{3.14}$$

where $g(x) = \text{logcosh}(x)$ represents a nonquadratic contrast function; and $\boldsymbol{\nu}$ is a standardised gaussian variable. Given that $\boldsymbol{s} = \boldsymbol{b}^\top\boldsymbol{z}$, one can rewrite the previous expression in terms of the separation vectors resulting in:

$$\kappa(\boldsymbol{s}) = \kappa(\boldsymbol{b}^\top\boldsymbol{z}) \propto E\left\{g(\boldsymbol{b}^\top\boldsymbol{z})\right\} - E\left\{g(\boldsymbol{\nu})\right\} \tag{3.15}$$

Therefore, the median squared error of the estimate of the kurtosis with respect to the

calibration values can be expressed as:

$$\psi(\boldsymbol{b}) = \underset{t}{\text{med}}[\kappa(\boldsymbol{b}^\top \boldsymbol{z}) - \kappa(\boldsymbol{b}^\top \boldsymbol{z})_{calib}]^2 \tag{3.16}$$

where $\kappa(\boldsymbol{b}^\top \boldsymbol{z})_{calib}$ represents the kurtosis of the sources detected during the calibration period. The following update rule is obtained by taking the gradient relative to $\boldsymbol{b}$:

$$\boldsymbol{b}_{j,t} = \boldsymbol{b}_{j,t-1} - \gamma[\kappa(\boldsymbol{b}^\top \boldsymbol{z}) - \kappa(\boldsymbol{b}^\top \boldsymbol{z})_{calib})]E\left\{\boldsymbol{z}g'\left(\boldsymbol{b}^\top \boldsymbol{z}\right)\right\} \tag{3.17}$$

where $g'(x) = \tanh(x)$ is the first derivative of the contrast function $g(x)$, and γ is the learning rate. By assuming a constant error rate as in the proposed whitening update, the previous equation can be rewritten into:

$$\boldsymbol{b}_{j,t} = \boldsymbol{b}_{j,t-1} - \lambda E\left\{\boldsymbol{z}_t g'\left(\boldsymbol{b}_{j,t-1}^\top \boldsymbol{z}_t\right)\right\} \tag{3.18}$$

where $\lambda = \gamma[\kappa(\boldsymbol{b}^\top \boldsymbol{z}) - \kappa(\boldsymbol{b}^\top \boldsymbol{z})_{calib})]$. Furthermore, since this update rule is applied separately to each source, one can also reduce the computational time by updating each separation vector at the times where a new spike is detected, leading to:

$$\boldsymbol{b}_{j,t} = \boldsymbol{b}_{j,t-1} - \lambda E\left\{\boldsymbol{z}(k_{j,t})g'\left(\boldsymbol{b}_{j,t-1}^\top \boldsymbol{z}(k_{j,t})\right)\right\} \tag{3.19}$$

where $k_{j,t}$ represents the newly detected spike times of the jth source at the tth batch. As in the proposed whitening adaptation, the hyperparameter (λ) was optimised as:

$$\lambda = \text{argmin}\left[\underset{t}{\text{med}}(\psi(\boldsymbol{b}))\right] = \text{argmin}\left[\underset{t}{\text{med}}\left[\kappa(\boldsymbol{b}^\top \boldsymbol{z}) - \kappa(\boldsymbol{b}^\top \boldsymbol{z})_{calib}\right]^2\right] \tag{3.20}$$

This optimisation resulted in $\lambda = -3e^{-3}$ for the simulated dataset and $\lambda = -5e^{-4}$ for both wrist and forearm experimental data. The change in sign of the hyperparameters makes Equation 3.19 equivalent to a maximisation of the estimated kurtosis regularised by the value of the initial conditions.

Importantly, after each batch update of Equation 3.19, the separation vectors were orthonormalised using Equations 1.33 and 1.34.

3.2.3.3 Adaptation of spike detection

Since the separation vector approaches rely on the timings of the new spikes, an adaptive k-means algorithm, proposed in (Chen et al. 2020a), was implemented for spike detection. This algorithm is briefly summarised by the following relation:

$$c_{j,i} = \frac{w_1 c_{j,i} + w_2 c_{j,i,t}}{w_1 + w_2} \tag{3.21}$$

where $c_{j,i}$ represent the k-means baseline ($i = 0$) and spikes ($i = 1$) centroids for the jth MN; $c_{j,i,t}$, are the newly computed centroids within the tth batch exclusively; and w_1 and w_2 are weights

empirically set to 5 and the number of newly detected spikes in the tth batch, respectively. In this way, the adaptive k-means algorithm constitutes a weighted average of the previous and new centroids.

3.2.4 MUAP tracking

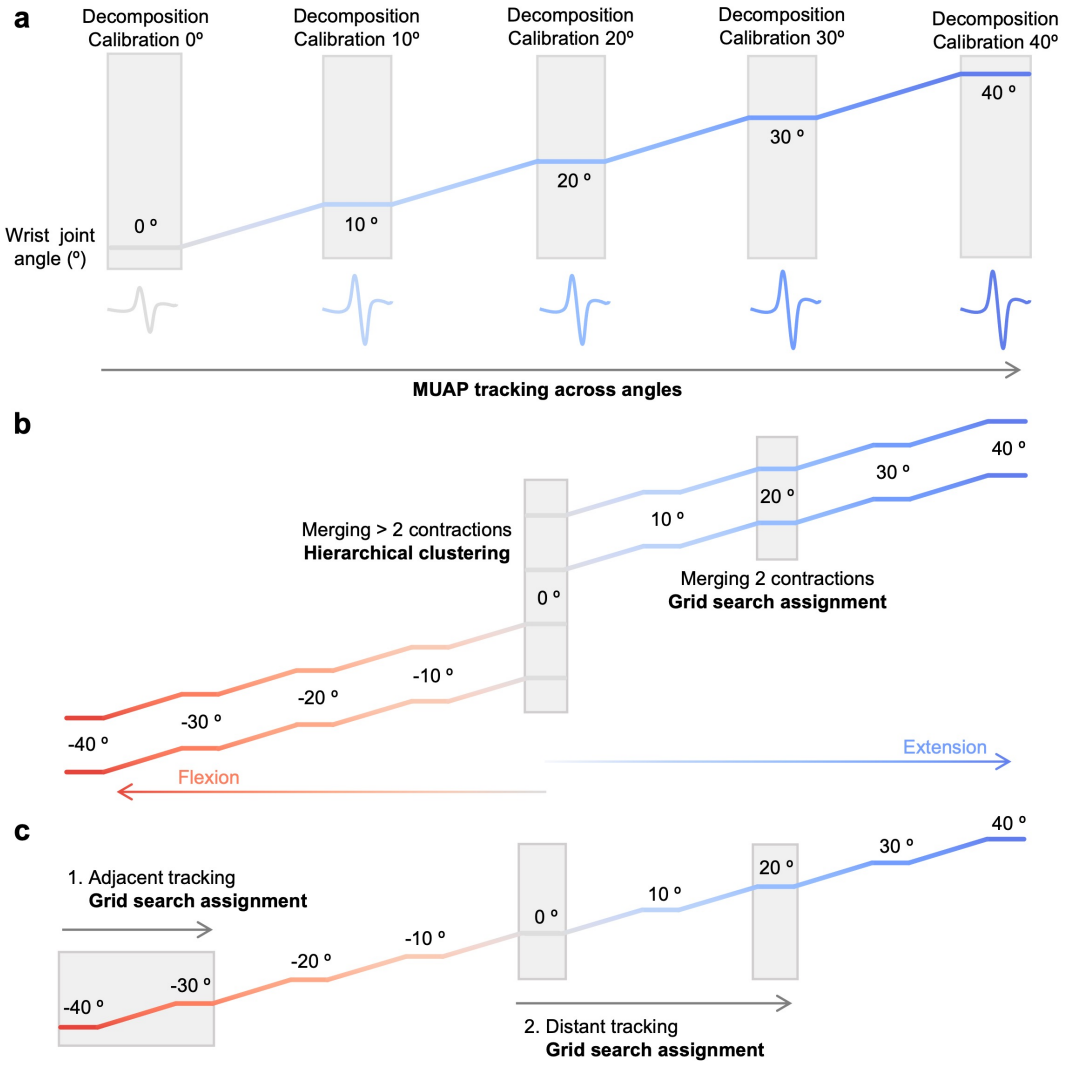

Figure 3.4: Experimental MUAP tracking approach. (a) Schematic of the motor unit action potentials (MUAPs) tracking approach after their computation at each wrist joint angle (colour coded) by independently calibrating a decomposition model at each plateau phase (shaded areas). (b) Merging of MUAPs across repetitions per angle (colour coded with flexion in red and extension in blue) based on their normalised mean squared error (NMSE) as metric for dissimilarity. Ward hierarchical clustering (new cluster formation at NMSE> 0.2) was applied when more than two contractions were being merged (at 0 °). When only two conditions were compared (rest of the angles), the proposed grid search assignment algorithm was applied instead (MUAPs were matched if NMSE< 0.2). The resulting library of unique MUAPs per angle was used for tracking across angles. (c) Tracking approach across angles using the proposed grid search assignment algorithm. (c.1) The approach sequentially compared adjacent angles to progressively track MUAP changes with the wrist joint angle (colour coded, same as in (b)). (c.2) A second loop compared distant angles to merge potentially disjoint tracking groups. In this case, only the MUAPs that had not been matched to their corresponding adjacent angle were included in the analysis. The matching threshold per comparison across angles was the same as in (b) for all cases.

From the experimental data, I first labelled all MUAPs across angles with a tracking approach to reach a gold-standard for dynamics decomposition. For this purpose, first, each plateau phase of the staircase wrist joint angle was independently decomposed without adaptation using convolutive blind source separation (Negro et al. 2016a). Only reliable MNs with pulse to noise tatio (PNR) above or equal to 30 dB, discharge rate (DR) between 5-35 Hz (both included), and coefficient of variation (CoV) of the interspike intervals below or equal to 30 (%) were kept for each segment. The selected PNR threshold is equivalent to a >90% sensitivity and <2% false alarm rate in the decomposition accuracy (Holobar et al. 2014). Similarly, the accepted DR and CoV ranges relate to physiological values (Freund 1983; Fuglevand et al. 1993; Holobar et al. 2010). In addition, duplicated MNs within the same decomposition output ($RoA \geq 0.3$) were also identified, and only the one with the highest PNR was kept. The corresponding MUAPs were computed by spike trigger averaging on 25-ms windows. Thereafter, the MUAPs found at each angle were tracked to generate ground truth for the decomposition adaptation (Figure 3.4.a).

When comparing MUAP pairs, these were first aligned by maximising their cross-correlation over the union of channels with peak MUAP amplitude greater than:

$$thr = Q3 + 1.5 \cdot IQR \tag{3.22}$$

where $Q3$ represents the third quartile (75th percentile), and IQR is the interquartile range (25th to the 75th percentile of the data). This selection effectively identifies the channels with outlying peak MUAP amplitude across the entire high-density electrode array, providing spatial selectivity to the comparison. Thereafter, the normalised mean squared error (NMSE) (Farina et al. 2008) was computed over the union of both sets of selected channels as:

$$NMSE = \frac{2\|MUAP_1 - MUAP_2\|^2}{\|MUAP_1\|^2 + \|MUAP_2\|^2} \tag{3.23}$$

Note that NMSE is a dissimilarity metric with range [0, 2], where the equivalent similarity is expressed as $1 - \text{NMSE}$. Importantly, the NMSE, unlike the correlation, can account for amplitude differences between the pairs of MUAPs, making it more suitable for dynamic contractions.

Thereafter a grid-search tracking algorithm was used to identify common MUAPs between two contractions. First, the NMSE matrix (D) with all pairwise comparisons between two MUAP sets of sizes L and M is computed. Then, the algorithm retrieves the set of values (D_{set}) below a predefined NMSE threshold (d_{thr}, which was set to $d_{thr} = 0.2$ in this study):

$$D_{set} = \{d_{l,m} | d_{l,m} < d_{thr}, l \in L, m \in M\} \tag{3.24}$$

Every value in D_{set} is evaluated in ascending order, and a link between MUAPs l and m is formed if all the following conditions are met:

$$d_{l,m} = \text{argmin}_l(D) \tag{3.25}$$

$$d_{l,m} = \text{argmin}_m(D) \tag{3.26}$$

This approach was applied to merge MUAPs across repetitions for all angles except at 0 °, where four contractions were merged with Ward hierarchical clustering based on the NMSE with 0.2 threshold for cluster formation (Figure 3.4.b). When duplicated MUAPs were found, their spikes were inspected and the one with higher number of spikes, lower CoV and higher PNR was selected for further analyses. Once a library of unique MUAPs per angle was obtained, MUAPs were tracked across angles using the grid-search tracking algorithm sequentially. First, units were linked across consecutive angles; then the algorithm was applied across non-consecutive angles to merge disjoint groups of tracked MUAPs (Figure 3.4.c). In the disjoint angle comparison, only the MUAPs that had not been matched to their respective consecutive angle were included in the analysis. The corresponding group labels were propagated to all of the the previously identified duplicates across repetitions. In this manner, the sequential search approach enabled the effective tracking of MUAP modulations exceeding the NMSE threshold, and provided a validation set of spike trains for the experimental decomposition adaptation.

3.2.5 Decomposition adaptation evaluation

The decomposition adaptation pipeline was initialised with the whitening, separation vectors, and spike detection parameters computed from the first isometric phase of the simulated and experimentally recorded staircase contractions at 0°. Thereafter, the optimal adaptation hyper-parameters were computed as described in Section 3.2.3. Once optimised, the decomposition adaptation was applied to the entire contraction. For the experimental recordings, only reliable and unique MNs (see section 3.2.4) were used to evaluate the decomposition adaptation. Similarly, for the simulated contractions, duplicated MNs within the same decomposition output ($RoA \geq 0.3$) were also identified, and the one with the highest PNR was kept. Among those, only the decomposed MNs with $RoA \geq 0.9$ with the simulated ones were used in further analyses.

To evaluate the accuracy of each adaptive pipeline, the rate of agreement, sensitivity, and precision were calculated as follows:

$$RoA = \frac{TP}{TP + FP + FN} \tag{3.27}$$

$$Sensitivity = \frac{TP}{TP + FN} \tag{3.28}$$

$$Precision = \frac{TP}{TP + FP} \tag{3.29}$$

where TP represents the number of true positive spikes of a given MN (i.e. the spiked identified both in the adapted and in the tracked/simulated trains with a tolerance of ± 0.5 ms); FP, the false positives or the number of spikes detected in the adapted train only, and FN, the false negatives or the number of spikes detected in the tracked/simulated trains only. The PNR was also calculated to assess the effect of decomposition adaptation on the surrogate metric for decomposition accuracy in the absence of ground truth (Holobar et al. 2014). Finally, the NMSE was computed to evaluate the effect of the decomposition accuracy on the MUAP (dis)similarity.

All data was processed on an Intel Core i9, 2.4 GHz 8-Core, with 64 GB laptop, except the

hyperparameter grid-search that was performed in parallel for each contraction in a CX3 cluster with 4 CPU processing nodes and 4 GB RAM. Since the queuing system of the cluster could pause jobs in the middle of their execution to optimise the resources allocated to the entire queue, the execution time was measured after the optimal hyperparameters were found in the aforementioned laptop.

3.2.6 Statistics

Statistical analyses were performed in SPSS 29.0 (IBM) with $p < 0.05$ level of significance. Nonparametric statistical tests were used when the data was not normally distributed as assessed by the Shapiro-Wilk test ($p < 0.05$). The effect of adaptation in the decomposition performance metrics of the simulated dataset was assessed by the Wilcoxon signed rank test. Mann-Whitney U tests were used to evaluate differences in the number of detected MNs between locations (wrist vs forearm), as well as differences in their respective PNR, DR, and CoV. A generalised linear mixed model with repeated measures was used to evaluate the differences in NMSE across potentially matching MUAPs (matched vs second best alternative vs mean across all alternatives for a given angle pair; within-factor effect) and location (wrist vs forearm; between-factor effect). Similarly, individual generalised linear mixed models with repeated measures were used to analyse the effect of adaptation (within-factor effect) across locations (between-factor effect) for each decomposition performance metric in experimental conditions.

3.3 Results

3.3.1 Decomposition adaptation in simulations

Ten bootstrapping iterations of wrist flexion and extension from -40° to 40° were simulated using NeuroMotion. Figure 3.5.a shows snapshots of the musculoskeletal model across the simulated wrist joint angles with the corresponding changes in muscle fibre length, depth, and conduction velocity (Figure 3.5.b-d, respectively). These non-stationary physiological parameters resulted in changes in the MUAP waveforms detected from the forearm with the wrist joint angle (Figure 3.5.e). Figure 3.5.f shows that these dynamics resulted in higher median NMSE during maximum flexion than extension (median (interquartile range): 0.17 (0.13-0.22) n.u vs. 0.09 (0.07-0.11) n.u., respectively). Importantly, these differences did not affect the identifiability of the simulated MNs as the NMSE across MUAPs of different MNs remained constant across angles (Figure 3.5.g).

Out of the 100 simulated MNs per contraction, a median of 13 (11-14) MNs were identified during the decomposition calibration phase at 0° per contraction, with 100.00 (99.63-100.00) % median RoA with the simulated ones and 38.11 (35.85-40.59) dB median PNR, 9.26 (8.71-10.03) pps median DR, and 19.98 (19.15-20.91) % median CoV (Figure 3.5.h). Figure 3.6.a depicts the overall simulated wrist joint angle pattern for a representative wrist flexion contraction along with the MNs excitation level. The innervated pulse trains before and after adaptation for three MNs over the shaded region in Figure 3.6.a are depicted in Figure 3.6.b-d, along with the simulated and detected firings (top), and corresponding RoA across the entire contraction.

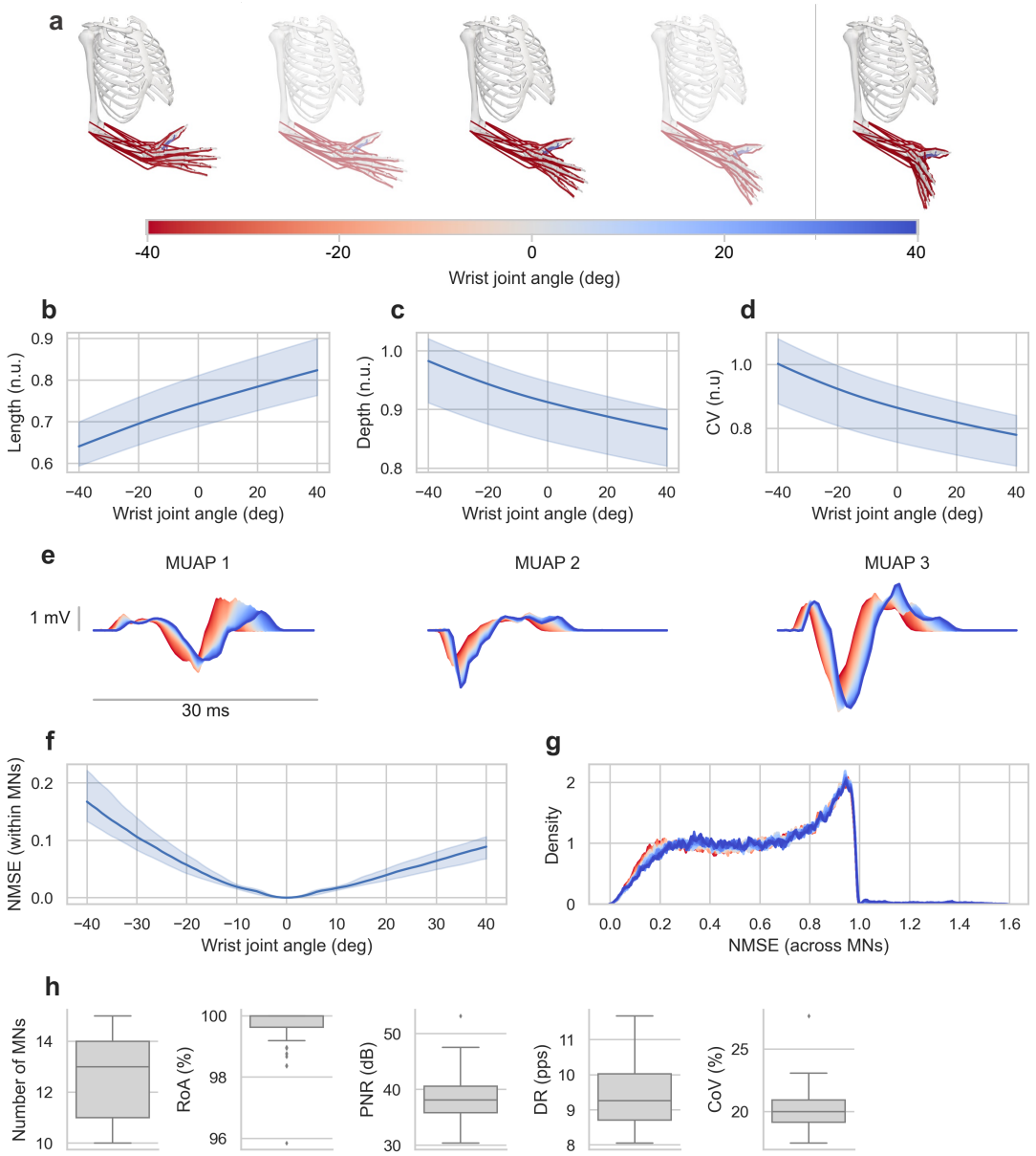

Figure 3.5: Dynamic neuromechanical simulations. (a) Snapshots of the musculoskeletal model while performing a wrist flexion from -40°to neutral (0°) to extension up to 40°. Mean (solid line) and standard deviation (shaded area) of the induced modulations in muscle fibre length in normalised units (b) as informed by the musculoskeletal model, and the corresponding changes in muscle fibre depth (c) and conduction velocity (CV) (d) in normalised units under the assumption of constant muscle volume during dynamics for all contractions. (e) One electrode visualisation of three generated motor unit action potentials (MUAPs) at the forearm with the above parameters for each wrist joint angle (colour). (f) Mean (solid line) and standard deviation (shaded area) of the normalised mean squared error (NMSE) within each motor neuron (MN) across wrist joint angles with respect to the neutral position (0°) for all the simulated MNs. (g) Distribution of the NMSE across MNs for each wrist joint angle (colours). (h) Number of identified MNs identified during the calibration phase per contraction, along with their rate of agreement (RoA) with the simulated ones, pulse to noise tatio (PNR), discharge rate (DR), and coefficient of variation of the interspike intervals (CoV).

Figure 3.6 illustrates the decrease in decomposition accuracy during dynamic contractions, where MN firings become undetectable after ∼10° without adaptation. The overall RoA, sensitivity, precision, NMSE, and PNR for all MNs across angles are displayed in Figure 3.7. In general,

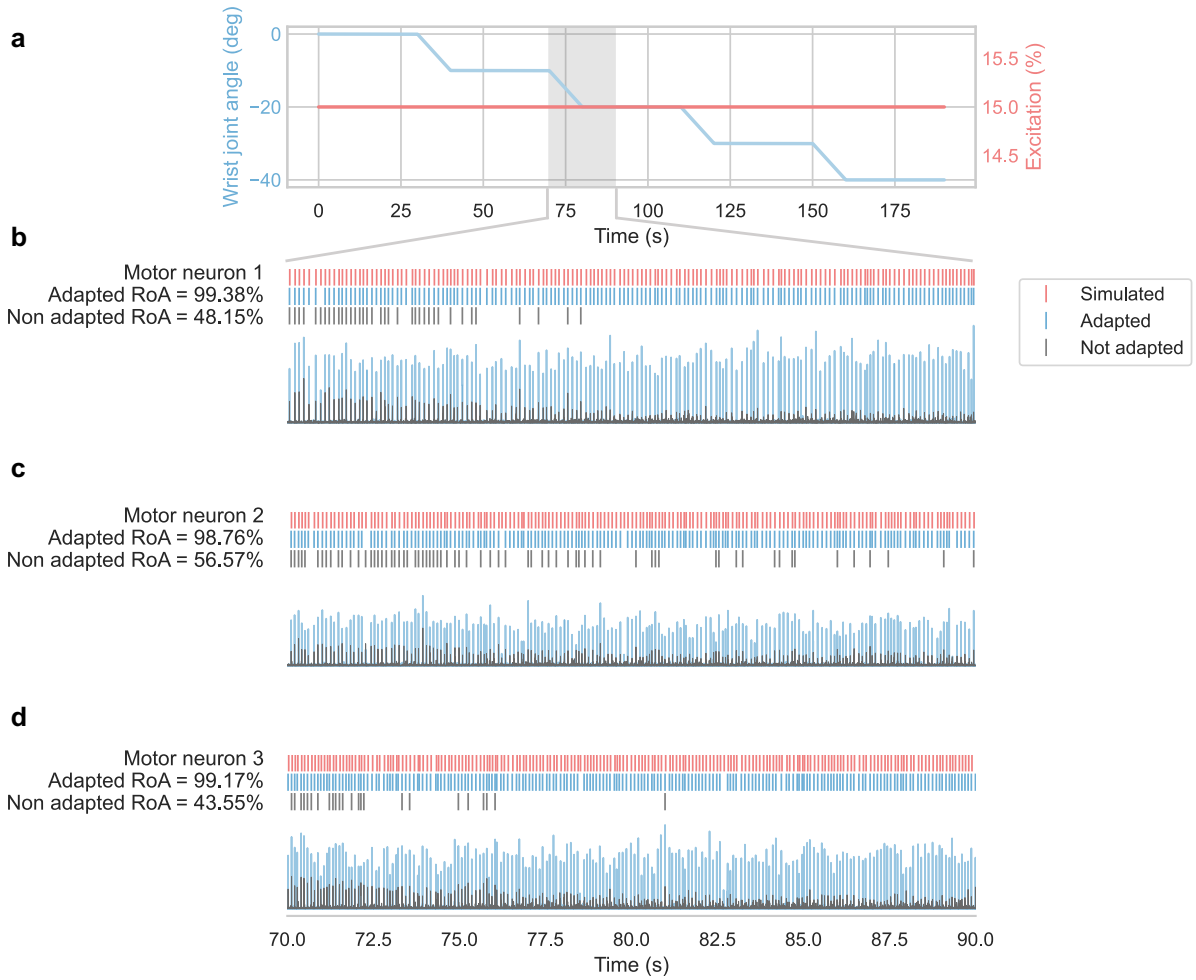

Figure 3.6: Detection of motor neuron (MN) firings during simulated dynamics. (a) Simulated wrist joint flexion angle (blue) and MN excitation level (red) for a representative contraction. (b-d) detected MN firings before adaptation (grey) and after adaptation (blue) with the simulated ones for reference (red) for three representative MN over the shaded part of the contraction in (a). The respective rates of agreement (RoA) are shown on the left, and the innervation pulse trains are depicted below before adaptation (grey) and after adaptation (blue) for each unit. Panels b-d demonstrate the need for decomposition adaptation as MN firings become undetectable after $\sim 10^{\circ}$ without adaptation.

decomposition accuracy was completely lost after 20° in both flexion and extension when decomposition parameters were fixed. Notably, decomposition adaptation compensated this effect across all angles and metrics with significant improvements in the RoA (98.10 (94.42-99.16) % vs 35.86 (22.77-53.61) % for adaptation and no adaptation, respectively, $p < 0.001$), sensitivity (98.21 (95.25-99.20) % vs 36.46 (23.64-56.03) % for adaptation and no adaptation, respectively, $p < 0.001$), precision (99.92 (99.52-100.00) % vs 62.61 (48.17-80.00) % for adaptation and no adaptation, respectively, $p < 0.001$), NMSE (0.04 (0.03-0.06) n.u. vs 0.17 (0.06-0.32) n.u. for adaptation and no adaptation, respectively, $p < 0.001$), and PNR (39.08 (37.13-41.28) dB vs 30.68 (28.21-33.90) dB for adaptation and no adaptation, respectively, $p < 0.001$).

The median execution time of the decomposition adaptation pipeline was 21.69 (20.65-22.60) ms per 100 ms batches for 320 electrodes (extension factor = 3) and 13 (11-14) MNs in a Intel

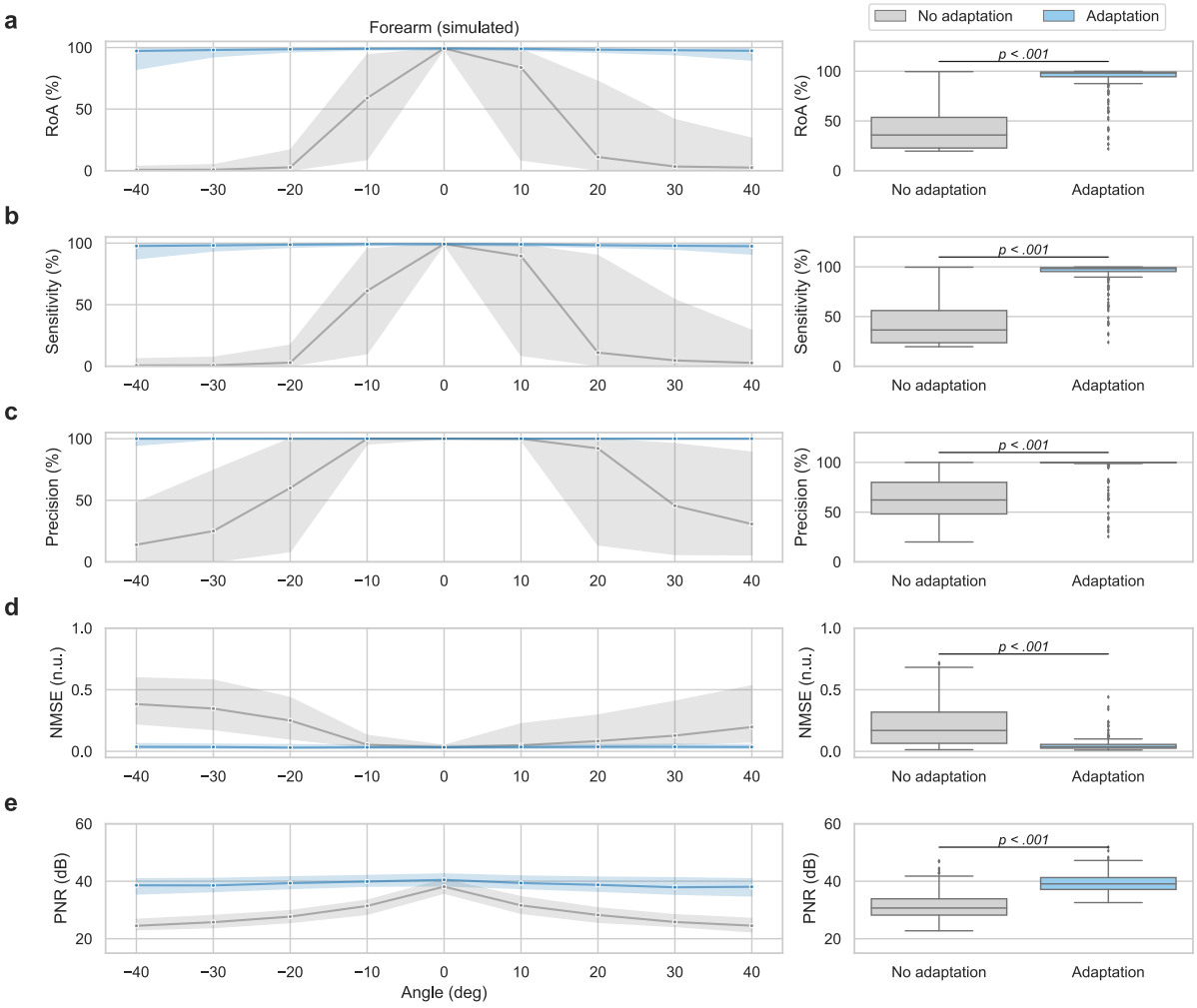

Figure 3.7: Decomposition adaptation performance in simulations. On the left, median (solid line) and interquartile range (shaded region) before (grey) and after (blue) decomposition adaptation across all simulated units for each angle for (a) rate of agreement (RoA), (b) sensitivity, (c) precision, (d) normalised mean squared error (NMSE), and (e) pulse to noise tatio (PNR). The right panels show the median and quartiles distribution of the metrics across all the simulated motor neuron (MN). Note the different scale on the y-axis between left and right for visualisation purposes. Significant p-values are show in the plots as assessed by related-samples Wilcoxon signed rank tests. Decomposition adaptation significantly improved all performance metrics ($p < 0.001$).

Core i9, 2.4 GHz 8-Core, with 64 GB machine.

Taken together, these results show that the proposed decomposition adaptation algorithm could compensate the non-stationary changes induced by the simulated dynamic contractions in real-time.

3.3.2 Experimental MUAP tracking

Figure 3.8 shows two representative examples of the tracked MUAPs at the wrist and at the forearm with the grid-search algorithm, along with the tracking paths of MNs detected at different angles. In both cases, MUAP differences across angles can be appreciated in the non-propagating components of the wrist MUAPs, and around the innervation point of the forearm ones driven

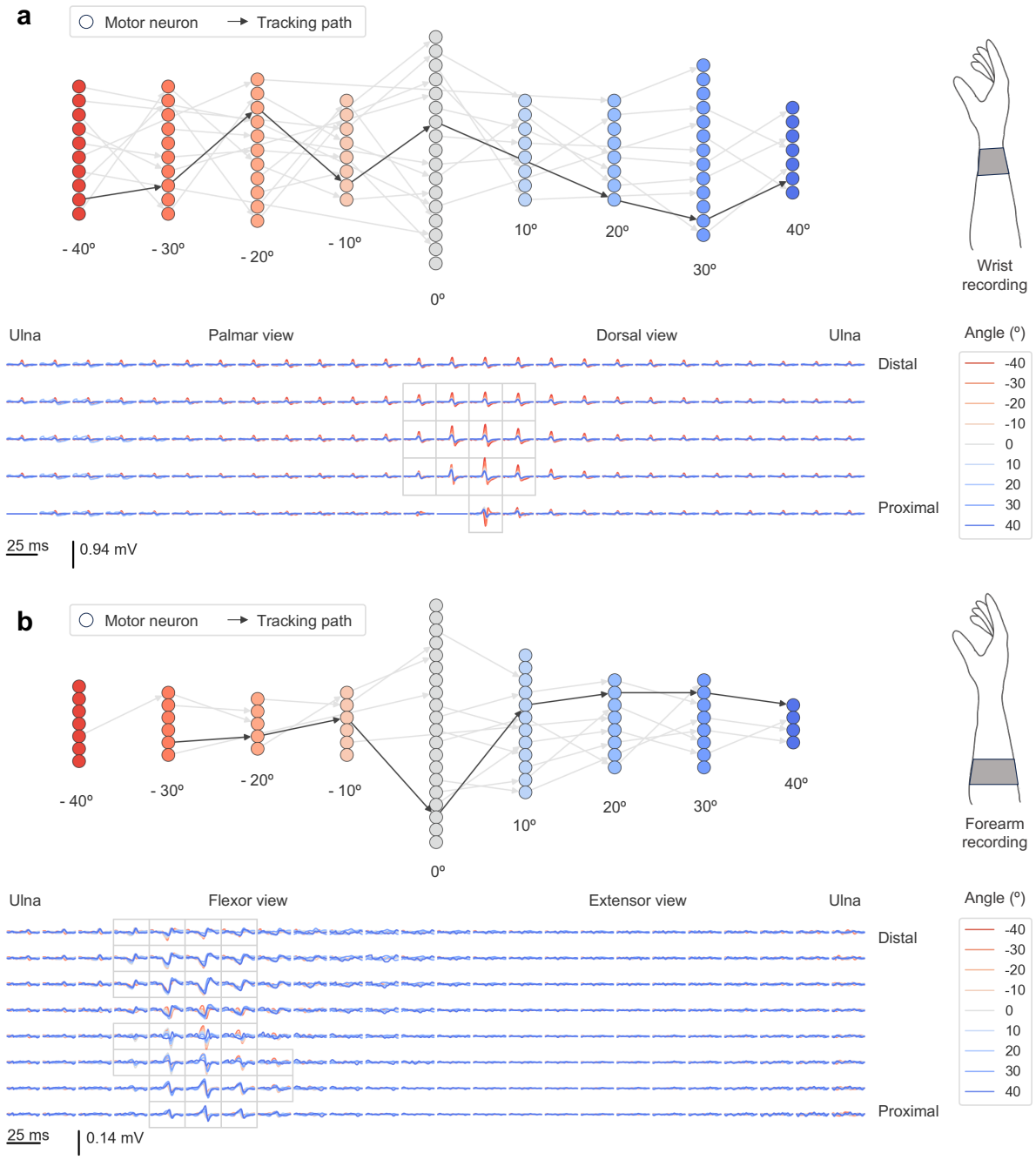

Figure 3.8: Tracked experimental motor unit action potentials (MUAPs) across angles from the wrist (a) and forearm (b). Each panel includes the detected motor neurons (MNs, circles) at each angle (colour coded in red for wrist flexion, and blue for wrist extension) for a representative finger press and subject. The grey arrows indicate the tracking paths between MUAPs across angles, with the highlighted one (in black) corresponding to the MUAPs displayed below for the wrist and forearm, respectively. The grey frames indicate the channels that were used for the MUAP comparison based on the normalised mean squared error. In both cases, MUAP differences across angles can be appreciated in the non-propagating components of the wrist MUAPs, and around the innervation point of the forearm ones driven by the change in muscle morphology during dynamic contractions.

by the change in muscle morphology during dynamic contractions.

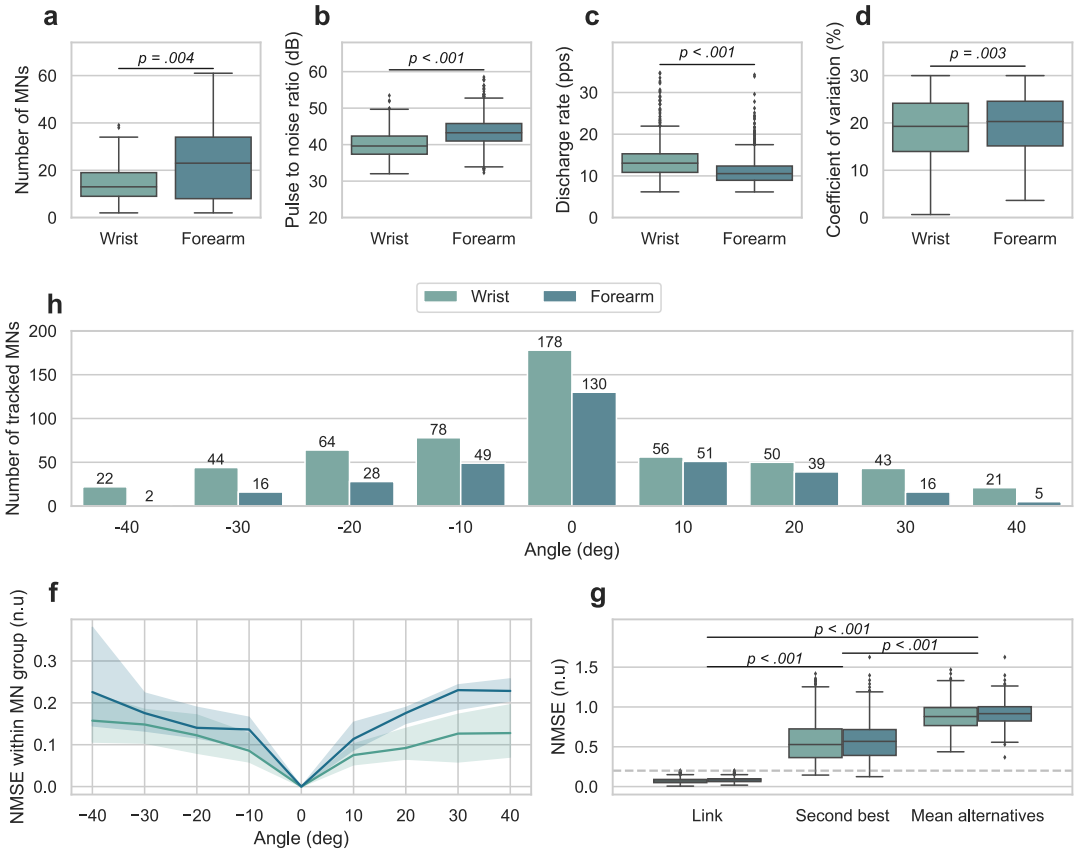

Figure 3.9: Decomposition calibration for motor unit action potential (MUAP) tracking across angles and properties. (a-d) Properties of the experimental motor neuron (MN) dataset used for MUAP tracking after merging repetitions (see Figure 3.4). Median and quartile distributions of the number of reliably and uniquely detected MNs per subject and finger after tracking across trials and angles for the wrist (green) and forearm (blue) (a), along with their corresponding pulse to noise tatio (PNR) (b), discharge rate (DR) (c), and coefficient of variation (CoV) (d). Significant p-values between the properties at the forearm and the wrist are shown in (a-d) as assessed by the Mann-Whitney U test. After applying the grid-search tracking algorithm, only the MNs that appeared at the reference position (0 °) and at least another angle were kept for further analyses. (h) Depicts the resulting number of tracked MNs for the wrist (green) and forearm (blue) (values at 0°) and the number of MNs present at each angle. This constitutes the dataset for decomposition adaptation validation. (f) Normalised mean squared error (NMSE) between the tracked MUAPs within MN group with respect to the one at 0° for the wrist (green) and forearm (blue), showing an increase in dissimilarity with the change in joint angle. (g) NMSE values between the links across MUAPs at different angles, the second closest MUAP per comparison, and the mean across all possible candidates per comparison for the wrist (green) and forearm (blue). The dashed grey line indicates the assignment threshold for the grid-search tracking algorithm. Significant p-values between the three link types are indicated in the plot as assessed by a generalised linear model with repeated measures with location as between-group factor and link types as within-group factor with subsequent pairwise comparisons with Bonferroni correction. The linked MUAPs across angles were significantly more similar (lower NMSE, $p < 0.001$) than the rest of the potential candidates supporting their assignment to the same MN group.

To validate the decomposition adaptation results with experimental data, MNs were tracked across the constant phases of the staircase wrist joint angle pattern based on the detected MUAPs after calibrating a decomposition model at each phase angle (Figure 3.4). In general, more MNs were detected at the forearm than at the wrist (13 (9-19) MNs vs 23 (8-34) MNs, respectively, $p = 0.004$) per subject and finger after tracking MNs across repetitions and angles (Figure 3.9.a).

MNs at the forearm exhibited lower firing rates than those at the wrist (8.94 (6.16-10.55) pps vs 13.06 (10.84-15.30) pps, respectively, $p < 0.001$, Figure 3.9.b). Decomposition quality was higher at the forearm than at the wrist in terms of PNR (43.25 (40.99-45.79) dB vs 39.62 (37.38-42.35) dB, respectively, $p < 0.001$, Figure 3.9.c), although the overall CoV was also higher at the forearm than at the wrist (20.30 (15.14-24.58) % vs 19.28 (13.97-24.58) %, respectively, $p = 0.003$, Figure 3.9.d).

This population of MNs were tracked across angles using the proposed grid-search algorithm based on their MUAPs NMSE. Only the MNs that were tracked for at least two angles (one being 0°as it was the calibration angle for the decomposition adaptation) were kept for further analyses. In total, 178 MNs met these conditions at the wrist and 130 MNs met them at the forearm. Figure 3.9.h shows the overall number of MNs present at each angle for the wrist and forearm. While more MNs were initially detected at the forearm, MNs at the wrist were tracked over more angles overall (3 (2-3) tracked angles vs 3 (2-4) tracked angles for the forearm and wrist, respectively, $p < 0.001$). This can be explained by the lower MUAP NMSE across angles with respect to 0° at the wrist than at the forearm (Figure 3.9.f). This effect was also independently observed as a lower median squared error of the Kullback-Liebler divergence between the operational and calibration conditions at the wrist than at the forearm in the absence of adaptation, particularly, as the deviation angle increased (Figure 3.10).

While the grid-search algorithm did not have a validation set, the NMSE values of the linked MUAPs were significantly lower than those of the second best possible candidates (0.07 (0.05-0.09) n.u vs 0.54 (0.37-0.72) n.u., respectively, $p < 0.001$) and the mean of all possible

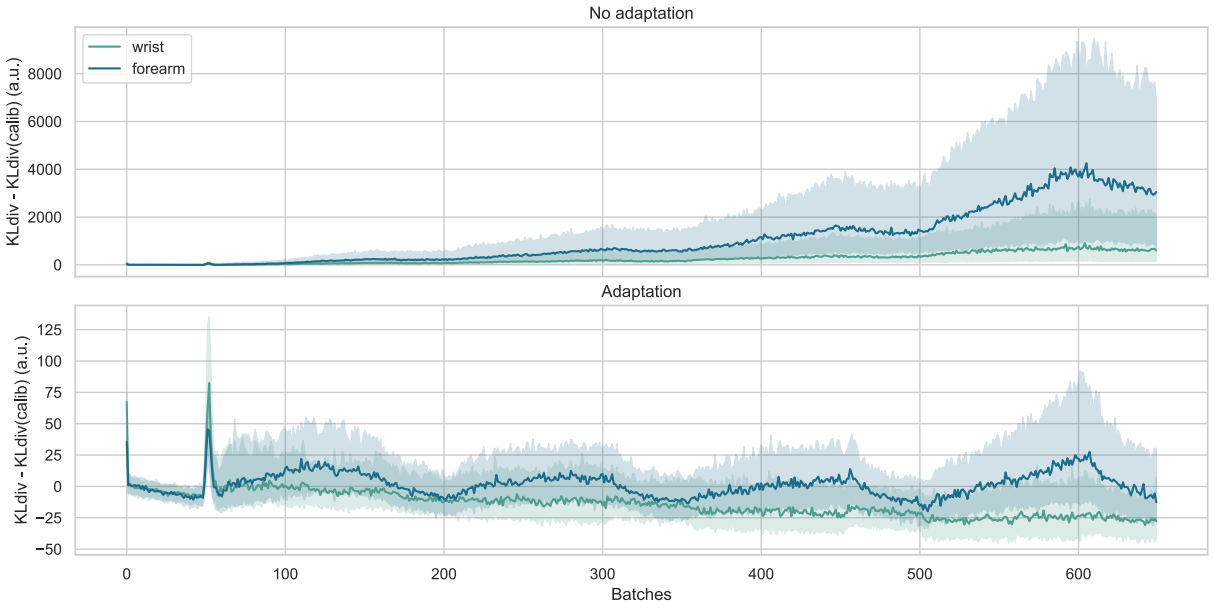

Figure 3.10: Kullback-Liebler divergence error. Top: Median (solid line) and interquartile range (shaded area) of the Kullback-Liebler divergence error with respect to the calibration before adaptation across all experimental contractions for the wrist (green) and forearm (blue). Bottom: Same as at the top, but after applying the proposed whitening adaptation. Note the change in scale on the y-axis for visualisation purposes. The two peaks at the beginning of the plot correspond to the effect of the decomposition extension factor and an artifact produced by the motor at the initialisation of the motion, respectively.

candidates (0.07 (0.05-0.09) n.u vs 0.89 (0.78-1.00), respectively, $p < 0.001$), showcasing that the selected tracking paths were outliers in the MNs' (dis)similarity distributions. Furthermore, no significant differences were found between the tracking NMSE between the forearm and the wrist ($p > 0.05$).

3.3.3 Decomposition adaptation in experimental data

The tracked MN firings of the previous section (see Figure 3.9.h) were used to validate the performance of the decomposition adaptation in experimental contractions. Figure 3.11.a shows the wrist joint angle for a representative contraction with the corresponding individual finger forces. Figure 3.11.b depicts the smoothed discharge rates of two of the detected MNs before (grey) and after (blue) adaptation at the wrist along with the tracked ones (red). The detected spike trains over the shadowed part of the contraction in Figure 3.11.a-b are shown in Figure 3.11.c for the tracked, adapted, and not adapted decompositions. The figure shows a decrease in decomposition accuracy during dynamic contractions (particularly after 20° in this case) and how decomposition adaptation increased the RoA with the tracked ones.

The overall RoA, sensitivity, precision, NMSE, and PNR for all experimental MNs across angles are displayed in Figure 3.12 for the wrist (left) and forearm (middle). The median and quartile distributions of the average performance metrics per MNs for both locations before and after adaptation are depicted on the right. Generalised linear models with repeated measures were used to assess the effect of adaptation (within-group factor) and location (between-groups factor), with subsequent pairwise comparisons with Bonferroni correction. Decomposition adaptation significantly improved all performance metrics ($p < 0.001$), with no significant difference between locations ($p > 0.05$). Overall decomposition adaptation increased the median RoA by 15.05% at the forearm (83.94 (63.21-97.75) % vs 98.99 (97.22-100.00) % before and after adaptation respectively, $p < 0.001$) and by 10.67% at the wrist (88.01 (66.26-97.15) % vs 98.68 (95.82-99.40) % before and after adaptation respectively, $p < 0.001$). While an initial statistically significant interaction was found between adaptation and location ($p = 0.024$) no statistically significant differences were found between the effects' pairwise comparisons after Bonferroni correction ($p > 0.05$ for all cases). A similar effect was observed for the sensitivity, for which decomposition adaptation increased the median sensitivity by 11.28 % at the forearm (88.18 (64.43-98.87) vs 99.46 (98.59-100) % before and after adaptation, respectively, $p < 0.001$) and by 4.98 % at the wrist (94.29 (73.23-98.69) % vs 99.27 (98.32-100.00) % before and after adaptation, respectively, $p < 0.001$). While the interaction between adaptation and location was initially significant ($p = 0.003$), no statistically significant differences were found between the effects' pairwise comparisons after Bonferroni correction ($p > 0.05$ for all cases).

Overall, decomposition with fixed parameters from the calibration maintained a high median precision at both forearm (100 (87.50-100.00) %) and wrist (98.73 (82.82-100) %). Still, significant differences in the distribution were found before and after adaptation at both the forearm (100 (98.60-100) %, $p < 0.001$) and the wrist (99.48 (96.57-100) %, $p < 0.001$). In this case, no

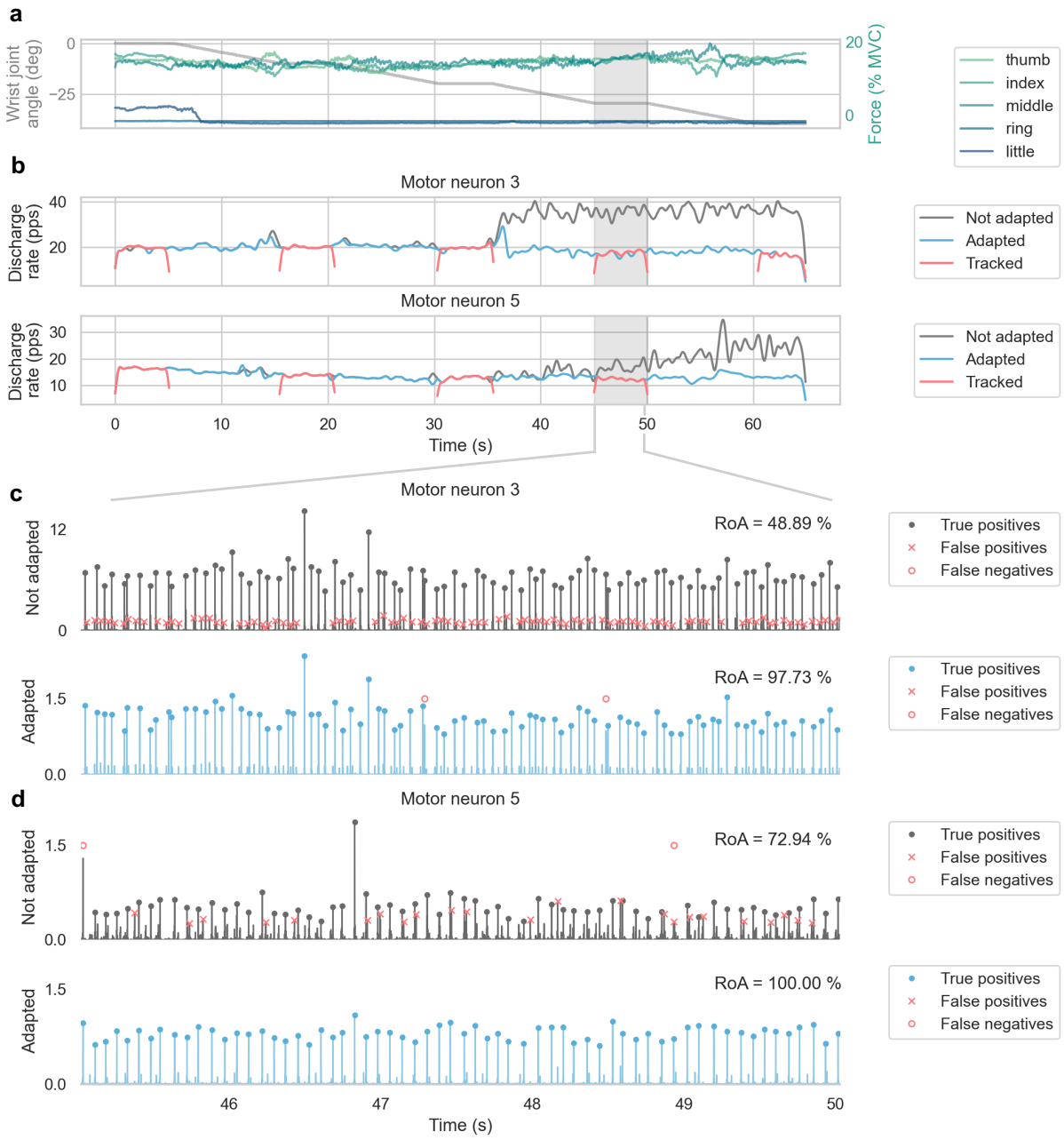

Figure 3.11: Detection of motor neuron (MN) firings during experimental dynamic contractions from the wrist. (a) Recorded wrist joint angle from the motor encoder (grey) and individual finger forces (colour) for a representative contraction. (b) Smoothed discharge rate of two MN before (grey) and after adaptation (blue) detected at the wrist, along with the smoothed discharge rate of the correspondingly tracked MN based on their MUAP waveforms (red).(c-d) Normalised innervated pulse trains before (grey) and after adaptation (blue) with respect to the maximum spike amplitude at 0°, with their correctly identified spikes with respect to the tracked ones (true positive, filled dots), falsely identified spikes (false false positive, crosses), and missed spikes (false negative, empty circles), over the shaded part of the contraction in (a-b). The respective rates of agreement (RoA) for each unit and decomposition approach are shown on the right. Note the change in y-axis in (c) for visualisation purposes. The figure illustrates the decrease in decomposition accuracy during dynamic contractions, in this case beyond $\sim 20°$, and how decomposition adaptation can restore it.

statistically significant interaction was found between adaptation and location ($p > 0.05$). A similar trend was observed for the NMSE where a significant difference between the distributions

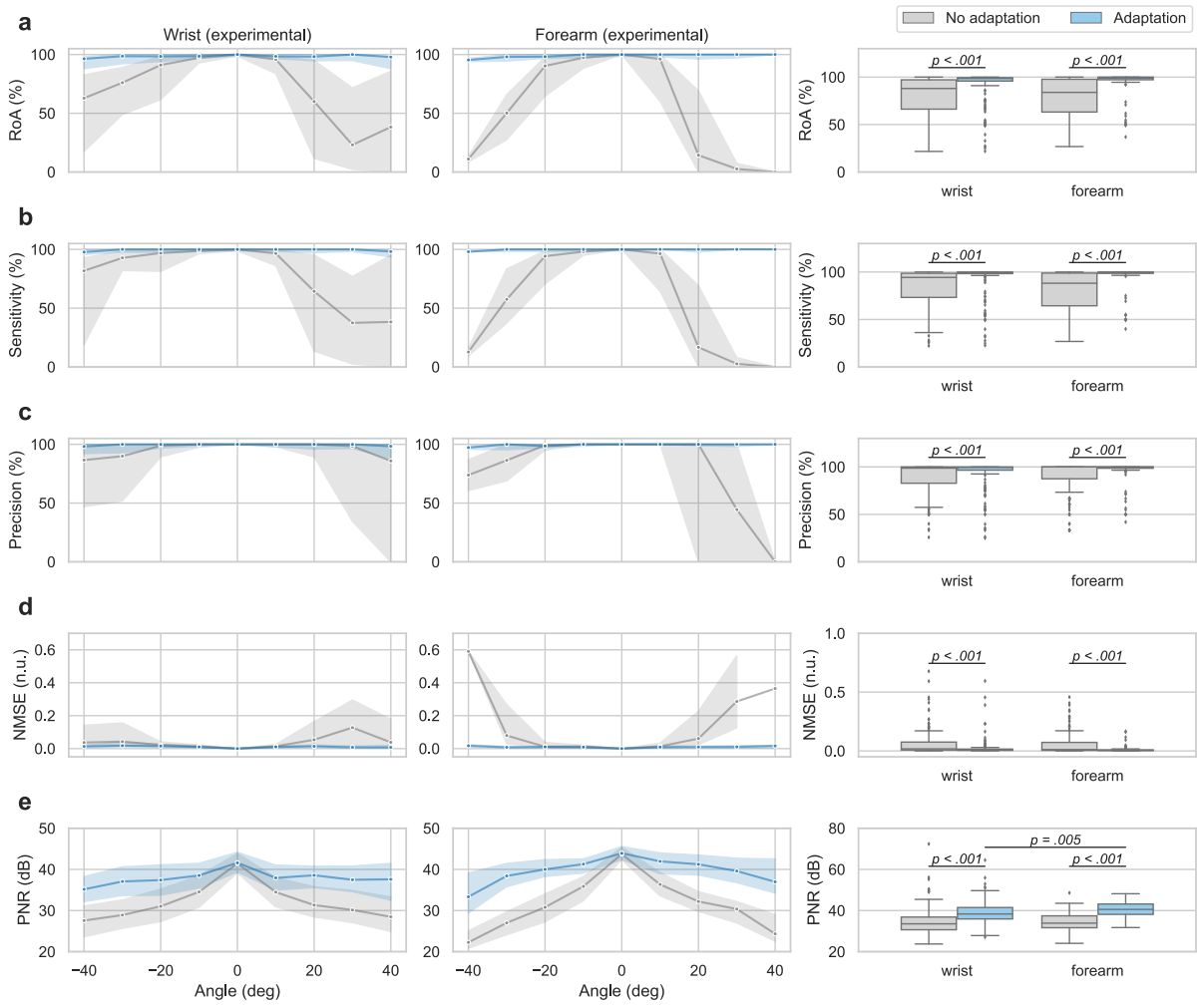

Figure 3.12: Decomposition adaptation performance in experimental data across the tracked motor neuron (MN). First two columns: median (solid line) and interquartile range (shaded region) before (grey) and after (blue) decomposition adaptation across all tracked MN for each angle for (a) rate of agreement (RoA), (b) sensitivity, (c) precision, (d) normalised mean squared error (NMSE), and (e) pulse to noise tatio (PNR) at the forearm and wrist, respectively. The right panels show the median and quartiles distribution of the metrics across all the tracked MN at the wrist and forearm, respectively. Note the different scale on the y-axis between the line and boxplots for visualisation purposes. Significant p-values are show in the plots as assessed by generalised linear models with repeated measures to assess the impact of adaptation (within-group effect) and location (between-groups effect), with subsequent pairwise comparisons with Bonferroni correction. Decomposition adaptation significantly improved all performance metrics ($p < 0.001$), with no significant difference between locations ($p > 0.05$).

was found both at the forearm (0.01 (0.01-0.07) n.u. vs 0.01 (0.00-0.01) n.u. before and after adaptation, respectively, $p < 0.001$) and at the wrist (0.02 (0.01-0.08) n.u. vs 0.01 (0.01-0.02) n.u. before and after adaptation, respectively, $p < 0.001$). As for precision, no statistically significant interaction was found between adaptation and location ($p > 0.05$). Finally, decomposition adaptation increased the median PNR by 6.67 dB at the forearm (33.88 (31.65-37.43) dB vs 40.55 (38.13-43.17) dB before and after adaptation, respectively, $p < 0.001$) and by 4.79 dB at the wrist (33.54 (30.67-36.83) dB vs 38.33 (35.92-41.48) dB before and after adaptation respectively, $p < 0.001$). A statistically significant interaction was found between adaptation and location ($p = 0.002$), which led to a significant difference in the distributions of the forearm and the wrist

after adaptation ($p = 0.005$, pairwise comparison with Bonferroni correction).

Taken together, these results show that the proposed decomposition adaptation algorithm significantly improved the decomposition performance in experimental data across all metrics, regardless of the location. Importantly, the convergence of the MUAP tracking and decomposition adaptation algorithms, which are independent from each other, constitute a type of two-source validation.

3.4 Discussion

Identifying MN activities under non-stationary conditions from EMG is essential to complete the vision of wearable non-invasive neural interfaces. Here, I have presented a decomposition adaptation algorithm that leverages the Kullback-Liebler divergence and kurtosis of the signals as metrics for online learning, providing a theoretical framework to optimise the algorithm's hyperparameters and adapt to non-stationarities by minimising the median squared error with respect to the calibration values. The proposed adaptation algorithm was able to compensate the effect of dynamic contractions resulting in $\geq 90\%$ RoA, sensitivity, and precision (median $> 98\%$) in $\geq 80\%$ of the cases in both simulations and experimental data after MN tracking in a two-source validation approach. Below I discuss the relevance of these results for MN detection and interfacing applications over dynamic contractions.

When muscle fibres shorten and lengthen, their morphology changes, deforming their surrounding tissue, and resulting in varying potentials that dynamically mix the underlying MN firings. In this study, I quantified this effect as changes in the MUAP waveforms with the wrist joint angle in both simulated and experimental conditions (Figure 3.5 and Figure 3.8, respectively). While, the NMSE increased with the wrist joint angle deviation from the reference position at 0° in both cases, different nonlinear trends were observed between the simulated and experimental data. This discrepancy can be explained by 1) the effect of spike triggered averaging in the detection of the experimental MUAPs, 2) slightly different joint placements across participants in the isokinetic system, and 3) the activation of more than one muscle in experimental conditions whose rate of change may not necessarily be the same. Even though the placement of the wrist joint was standardised by aligning the distal palmar crease with the rotating axis of the platform at the reference neutral position, the exact joint placement cannot be guaranteed across participants. For instance, the level of radial/ulnar deviation or pronation/supination was not measured, although is expected to be similar across participants due to the mechanical design of the platform. Yet, variations in the joint position could affect the initial conditions, potentially activating muscles not only involved in finger flexion such as the FDS during simulations, and hence resulting in the combination of multiple muscles' modulations in Figure 3.9.f. However, isolating the contributions of individual muscles from surface recordings is challenging due to the presence of cross-talk (Farina et al. 2002b). In addition, such postural variability across subjects could affect their mechanical outputs due to the asymmetric muscle force-length relationship. Yet, these small postural differences across participants are not expected to have a major impact on the obtained experimental decomposition

and tracking results considering that 1) the force level was referenced with respect to those initial conditions, 2) the decomposition algorithm was allowed to converge under each condition, and 3) that MUAP tracking was performed within subject. Furthermore, while the effect of spike triggered averaging could have been reduced by recording longer contractions at more wrist joint angles, a trade-off was necessary to avoid participants' fatigue. Importantly, the maximum median NMSE (~ 0.2 n.u.) was similar in both simulated and recorded MUAPs, supporting the suitability of NeuroMotion (Ma et al. 2023b) as a tool to model dynamic contractions for dynamic decomposition models. In fact, the simulated/detected MUAP changes were qualitatively similar to those reported by Holobar and collaborators (Glaser et al. 2019; Kramberger et al. 2021) for the biceps brachi. However, a direct quantitative comparison is complicated due to the different targeted muscles and metrics used (cross-correlation coefficient vs NMSE).

While the cross-correlation coefficient is arguably a more common metric for MUAP tracking in isometric contractions (Del Vecchio et al. 2019a; Goodlich et al. 2023; Martinez-Valdes et al. 2017), its use during dynamics should be treated with caution due to its insensitivity to amplitude changes. While Oliveira et al. 2021 pioneered its used to track MUAPs from the tibialis anterior between dynamic ankle dorsiflexions, their success may be explained by the limited range of motion explored ($\sim 20°$). In fact, a recent study has shown that decomposition performance for the tibialis anterior over dynamic contractions with up to 20° was equivalent to that of isometric contractions in hybrid data (Yokoyama et al. 2021). Since in this study I explored a substantially larger range of motion (80°) over smaller muscles at the forearm, here I used the NMSE instead. Notably, NMSE can reflect amplitude changes and was previously proposed as a metric to detect the unique representation of MUAPs in surface recordings (Farina et al. 2008). This sensitivity was important to 1) characterise the overall MUAP changes during the simulated/experimental contractions to provide benchmarks for the dynamic modulation compensated by the decomposition adaptation, and 2) to ensure that the uniqueness of different MUAPs simulated by NeuroMotion did not collapse when inducing the dynamic modulation (Figure 3.5.a-g). Therefore, when coupling the NMSE with the proposed channel selection approach that identifies the channels with outlying peak amplitude, the resulting metric condenses temporal, spatial, and amplitude features to measure (dis)similarities. It is worth noting that channel selection is essential over high-density recordings to avoid deceivingly large similarities due to a large amount of common silent channels as those present in Figure 3.8.

Experimental MUAP tracking showed that the modulation induced by muscle fibre shortening/lengthening was higher at the forearm than at the wrist as assessed by the NMSE across angles. This is attributable to the convergence of most muscle fibres into tendons at the wrist, who exhibit different contractile properties. Importantly, the MUAPs at the wrist are dominated by non-propagating far-field potentials (Figure 3.8.a) that emerge during the progressive extinction of the action potential at the muscle-tendon interface (Dumitru et al. 1991, 1993; Stegeman et al. 1997). Therefore, these MUAPs are arguably more susceptible to relative displacements of the muscle-tendon interface than to the contractile properties of the muscle. Conversely, at the forearm, these changes alter the propagating MUAP components and relative location of the

innervation zone (Figure 3.8.b) resulting in larger NMSE values with respect to the reference position. The higher sensitivity of recordings over the muscle belly to dynamic contractions may explain why although more MNs were decomposed at the forearm than at the wrist, the latter ones were tracked along more angles. Yet, these results rely on the performance of the tracking algorithm. While the tracking approach did not have a validation set per se, the linked MUAPs exhibited a NMSE significantly lower than that of their corresponding second best alternative, supporting the hypothesis that the representation of MUAPs belonging to the same MNs are more similar within themselves than across different MNs. It is also worth noting that by sequentially linking the most similar MUAPs across angles, the tracking algorithm only assumes local continuity in the (dis)similarity distribution and can potentially track larger changes than the predefined threshold with respect to the reference position (in this case at 0°, see Figure 3.9.f). Here I set the NMSE linking threshold to 0.2 n.u. as an equivalent dissimilarity value of the correlation coefficient threshold previously used in the literature (0.8, Oliveira et al. 2021). While arguably the selection of this threshold may condition the results, with potential for further improvement, the fact that decomposition adaptation resulted in $\geq$ 90% RoA, sensitivity, and precision with respect to the firings of the experimentally tracked MUAPs in $\geq$ 80% of the cases, supports the accuracy of the grid search tracking approach in a form of two-source validation since both methodologies are completely independent from each other.

However, it should be noted that the lower number of MNs tracked at each angle with respect to the total detected at 0° does not necessarily reflect a decreased recruitment of MNs during dynamics. In fact, the findings of Oliveira et al. 2021 suggest that MN rate coding (as opposed to MN recruitment) is the main driver of muscle shortening and lengthening during small dynamic ankle dorsiflexions at different speeds and constant load. Instead, the lower number of MNs tracked at each angle echo the fact that decomposition algorithms tend to identify only a portion of the active MNs. Moreover, here I only used the reliably detected MNs for tracking with PNR $\geq$ 30 dB, 5 $\leq$ DR $\leq$ 35 pps, and CoV $\leq$ 30 %. The selected PNR threshold has been shown to be equivalent to a >90% sensitivity and <2% false alarm rate in the decomposition accuracy (Holobar et al. 2014). Similarly, the aforementioned DR and CoV ranges correspond to the physiological behaviour of MN firings (Freund 1983; Fuglevand et al. 1993) and their accurate identification (Holobar et al. 2010). However, the imposition of such constraints likely decreased the overall number of detected MNs that may otherwise have been kept if manual validation was applied (Del Vecchio et al. 2020a), reducing our ability to track them across angles. Nonetheless, manual decomposition editing is not possible in human-machine interaction applications, and the overall number MNs selected for the validation of the decomposition adaptation (308 MNs in total, 178 at the wrist, and 130 at the forearm) was higher than the one reported in previous studies with hybrid data sets (252 MNs in Glaser et al. 2019; Kramberger et al. 2021) and experimental data (18 MNs in Yeung et al. 2024).

3.4.1 Effect of dynamics in the decomposition model

The larger modulation at the forearm during dynamics was also independently observed as a higher median squared error of the Kullback-Liebler divergence between operational and

calibration conditions at the forearm than at the wrist (Figure 3.10). As expected, larger MUAP differences with respect to the calibration conditions affected the signals' covariance, increasing the divergence error. In fact, such discrepancies resulted in an optimal learning rate twice as high during the whitening adaptation ($\eta_2 = 2e^{-3}$ vs $\eta_2 = 1e^{-3}$ for the forearm and wrist, respectively). Notably, once the whitening adaptation was applied to compensate the effect of the dynamics, the same optimal learning rate for the separation vectors was found in both locations ($\lambda = -5e^{-4}$). This supports the efficacy of the proposed adaptation algorithm, since the minimisation of the median squared error of the sources' kurtosis with respect to the calibration relates to the sources' higher order statistics rather than the dynamics of the volume conductor.

Still, few considerations need to be taken into account. First, the optimisation of the whitening hyperparameters was slightly different in simulations than in experimental data. The Kullback-Liebler divergence was minimised in simulated conditions as opposed to the minimisation of the median squared error with respect to the calibration values applied to the experimental data. This discrepancy can be explained by the different optimisation topology between the simulated and the experimental data (Figure 3.3). These differences could be attributable to the activation of a single muscle in simulations, the injection of artificial noise, or the dynamics of the volume conductor model, which are all factors that can alter the covariance matrix. However, it is worth noting that here I assumed a constant error rate during both the whitening and separation vector optimisation, i.e. the optimised parameters correspond to the product of the learning rates and the error, either the divergence or kurtosis, and therefore the adaptation rules for both the simulated and experimental data are the same, except for the choice of the whitening hyperparameter. This was a simplification assumption, yet the inclusion of the actual error term in the adaptation may provide further benefits such as faster learning or the ability to tune each MN separation vector differently due to varying error rates in the kurtosis of the sources within a given contraction. However, the consistency of the minimisation of the median squared error across subjects and locations was remarkable (Figure 3.3), supporting the validity of such assumption for the current task.

3.4.2 MN identification performance during dynamics

Decomposition performance results showed that without adaptation, the median RoA starts decreasing after 10°deviations in both extension and flexion for simulations and experimental data. To the best of my knowledge, this is the first study to characterise the effect of muscle shortening and lengthening (here determined as the wrist joint angle during flexion and extension) in the performance of the decomposition (without adaptation) for both simulated and experimental data across a wide range of motion (80°). While some MN firings were accurately detected over larger deviations during wrist flexion, from 30° performance was lost overall, particularly at the forearm. This is consistent with the larger MUAP changes observed at the forearm than at the wrist with the angle deviation. The found tolerance of the decomposition model to changes in posture is akin to the one observed in previous studies for the tibialis anterior (Oliveira et al. 2021; Yokoyama et al. 2021) and MUAP similarity in the biceps brachii (Kramberger et al. 2021). Here I included angle plateau phases in the dynamic contraction to enable the generation of

ground truth via MUAP tracking from independently calibrated decomposition models at each plateau angle. However, these results support the validation of future decomposition adaptation approaches over purely dynamic contractions as long as the decomposition model is calibrated over segments within the decomposition postural tolerance ($\sim$10°).

The proposed adaptation significantly improved all performance metrics (RoA, sensitivity, precision, NMSE, and PNR), resulting in $\geq$ 90% RoA, sensitivity, and precision in $\geq$ 80% of the cases in both simulations and experimental data (median >98% for the three metrics across data sets). Importantly, no statistically significant differences between the wrist and the forearm were found for all metrics, showcasing the ability of the algorithm to compensate different modulations related to the anatomical factors described before. In addition, the performance of the proposed decomposition adaptation was equivalent if not higher than previously proposed adaptation approaches based on recursive updates of the decomposition parameters. For instance, the approach proposed by Chen et al. 2020a resulted in average $\sim$ 80% sensitivity and precision when compensating MUAP modulations at different speeds simulated in a cylindrical volume conductor. More recently, Yeung et al. 2024 reported an average $\sim$ 84% RoA in experimental data over a moderate range of motion (up to 25% wrist extension, equivalent to $\sim$17° based on the $\sim$ 70° maximum range of motion of the wrist during extension, Alford 2021) after adaptation. While direct comparison is difficult due to the different conditions analysed, the achieved performance over the extensive range of motion evaluated here (-40° flexion to 40° extension, corresponding to the range needed for activities of the daily living, Gates et al. 2016) arguably represents more challenging conditions for the decomposition. Importantly, the aforementioned approaches included ad-hoc values for the learning rates and recursive support, which are conceivably hard to transfer and tune to different data sets without ground truth. Here instead, I proposed two online learning metrics based on the Kullback-Liebler divergence and kurtosis of the signals to overcome this limitation.

3.4.3 Translational potential, limitations, and future directions

The overarching motivation of the proposed decomposition adaptation was to reliably detect previously identified MNs (in this case, under isometric contractions) during non-stationary conditions such as postural changes or dynamic contractions. The ultimate goal was to develop an adaptation method that would be suitable for human-machine interaction applications with the potential to improve the overall robustness of the neural interface. Importantly, the enhanced stability of the MN identification could also result in benefits during motor control by promoting learning (Formento et al. 2021). To ensure this compatibility, the proposed decomposition adaptation had not only to be accurate but also execute under the neuromechanical delay ($\sim$ 200 ms, Del Vecchio et al. 2018). In this case, once the optimal learning rates were identified, the total execution time of the entire adaptation pipeline was $\sim$22 ms per 100 ms batches (approximately half of the previously proposed approaches, Chen et al. 2020a; Yeung et al. 2024), showcasing the suitability of the proposed adaptation for real-time human-machine interaction applications.

Crucially, the proposed approach provides two online learning metrics based on the Kullback-

Liebler divergence and kurtosis of the signals to tune the algorithm's hyperparametes. Importantly, these metrics are agnostic to the ground truth and their optimisation in this study has resulted in $\geq 90\%$ RoA, sensitivity, and precision in $\geq 80\%$ of the cases in both simulations and experimental data, demonstrating the ability of these metrics to capture the modulation induced by the dynamic contractions. The success of these metrics is rooted in the assumptions of the blind source separation model that first uncorrelates the mixed signals and subsequently finds the orthogonal transformation that guarantees their independence (Hyvärinen et al. 1997) (or sparsity in the decomposition model, Negro et al. 2016a). Therefore, the proposed metrics can be considered proxies of decomposition performance where a high Kullback-Liebler divergence indicates lower uncorrelation of the EMG signals; and low kurtosis (estimated here by the logcosh contrast function) reflects a poorer separation of the underlying sources similar to the PNR (Holobar et al. 2014).

In this study, the hyperparameter optimisation was carried out sequentially first for the whitening and then for the kurtosis. However, the weight of each specific adaptation stage was not measured. In this regard, Yeung et al. 2024 showed that adaptive spike detection alone can improve decomposition performance, but significantly better performance is achieved when updating the entire pipeline during changes in posture ($\sim 8\%$ improvement). From their results it can be inferred that the ideal pipeline should adjust all stages in the decomposition model from whitening and separation vectors to the spike detection parameters. Indeed, Figure 3.10 shows how the median squared error of the Kullback-Liebler divergence with respect to the calibration increases with the deviation angle, indicating the failure of the whitening and therefore, the presence of correlated components in the projected sources. In turn, this would translate in a noisier baseline that could induce FP in the adaptive spike detection (Figure 3.11.d). In addition, changes in the variance of the projected sources could alter the amplitude of the spikes with respect to the spike detection parameters, also increasing the likelihood of FP (see extreme case in Figure 3.11.c where the amplitude of the spikes increases over ten-fold with respect of the calibration, resulting in a high number of FP). Similarly, without updating the separation vectors, the amplitude of the detected spikes could decrease with the modulation, making their detection prone to FP if their amplitude is similar to the noise in the baseline or FN if their amplitude falls below the detection threshold (Figure 3.11.d). Given the efficient execution of the proposed adaptation pipeline (22 ms per 100-ms batches) it was deemed worth it to update all decomposition stages, providing a significant boost in performance and showing its suitablility for human-machine interaction.

While the evaluated decomposition performance was carried out after hyperparameter optimisation, which is arguably a form of model precalibration that requires initial data, the fact that the obtained hyperparameters generalised across subjects and locations shows promising potential for its application to different tasks where ground truth is not available. However, in this study I only evaluated slow staircase contraction patterns for wrist flexion and extension, and so the interplay between online learning and dynamic modulation speed still needs to be assessed. Nonetheless, these results open the door to a two double calibration scenario where

the decomposition model is initialised first during an isometric contraction, and the underlying dynamic modulation is learnt later in a second tuning phase. Future work should address which approach is more effective and robust for human-machine interfacing.

3.5 Conclusions

Identifying MN activity reliably from EMG under non-stationary conditions is essential to develop robust wearable non-invasive neural interfaces. Here, I introduced a novel decomposition adaptation algorithm that leverages the Kullback-Liebler divergence and kurtosis of the signals as metrics for online learning. The proposed approach provides a ground-truth agnostic theoretical framework to tune the algorithm's hyperparameters and adapt to non-stationarities, such as dynamic contractions, by minimising the median squared error of the metrics with respect to the calibration values in real-time ($\sim$ 22 ms execution time per 100 ms batches). The proposed adaptation algorithm significantly improved all decomposition performance metrics with respect to no adaptation in a wide range of motion of the wrist during flexion and extension (80°). Results showed $\geq$ 90% RoA, sensitivity, and precision in $\geq$ 80% of the cases in both simulations and experimental data from the wrist and forearm after tracking MNs across wrist joint angles based on their MUAP waveforms in a two-source validation approach. These findings show promising potential for the application of the proposed decomposition adaptation approach to different tasks where ground truth is not available, and real-time human-machine interfacing.

Chapter 4

Conclusions and future work

4.1 Summary

How we interact with technology continually evolves, constantly seeking for more intuitive and immersive experiences. Neural interfaces offer a unique window into motion intention to deliver such seamless interactions with technology. Furthermore, advances in motor control, decoding algorithms, and wearable systems bring the prospects of harnessing neural activity for a wide range of consumer electronics closer than ever. Yet, while the wrist offers an unobtrusive and widely acceptable location for a wearable, its unique electrophysiological properties posed unresolved questions regarding the non-invasive detection of neural activity, its potential for human-machine interfacing, and its stability under changing conditions. Hence, this thesis aimed to address these questions to develop an accurate, robust, non-invasive neural interface at the wrist, suitable for wearable devices.

In **Chapter 2**, I showed that MN firings can be accurately decoded from the far-field potentials detected from surface EMG signals at the wrist. Apart from meeting decomposition performance standards and the physiological behaviour of MNs under isometric contractions, I showed that most MNs detected at the wrist could be traced back to the forearm above the noise level, further supporting the neural origin of these far-field potentials. Subsequently, I demonstrated that the decoded MN firings predicted with $> 95\%$ accuracy the corresponding finger gestures in an offline analysis, which was significantly better than that achieved with EMG-based features from the wrist. These findings were confirmed in a real-time control task, where subjects successfully completed 93% of the tasks when decoding MN firings from the wrist.

After these encouraging results, in **Chapter 3**, I focused on improving the stability of the interface to non-stationarities such as the modulation induced by postural changes and dynamic contractions. To do so, I proposed two metrics for online learning based on the decomposition model, whose hyperparameters are tuned by minimising the median squared error with respect to the calibration conditions, without relying on ground truth. This approach resulted in hyperparameters that generalised across subjects (at least within task) and reflected anatomical property differences between the forearm and the wrist. In addition, the proposed adaptation approach significantly improved all performance metrics in both simulations and experimental

conditions (average rate of agreement, precision, and sensitivity across angles was $\geq 90\%$ in $\geq 80\%$ of the cases) with respect to the fixed decomposition. Finally, the execution time was well below the neuromechanical delay (22 ms per 100 ms batch), making it suitable for real-time interfacing applications.

Taken together, these findings expand our knowledge on non-invasive neural interfaces at the most distal end of the neuromuscular system, bringing us closer to realising our vision of seamless human-computer interaction using wearable systems.

4.2 Strengths and limitations

The ideal neural interface for general consumer applications should be stable and able to capture rich spatiotemporal information from a large population of neurons to accurately predict user intentions with minimal training (Holobar et al. 2021). The work in this thesis tackled some of these challenges, particularly the detection of MNs from the wrist non-invasively, their information content, and the robustness of this interface to nonstationarities. Despite the progress, I acknowledge limitations in the methods and the scope of the studies. In this section, I discuss the strengths and limitations of the overall work.

4.2.1 Detection of MN non-invasively from the wrist

In this thesis I showed that it is possible to reliably decompose MNs from the wrist non-invasively meeting decomposition accuracy standards (CoV $\leq 30\%$ and PNR ≥ 30 dB, Holobar et al. 2014, 2010) and the the physiological range of firing rates during isometric contractions (5-35 pps, Freund et al. 1975; Fuglevand et al. 1993). These results support the notion that variability in conduction velocity, tendon spread, and tendon location provide enough discrimination power to identify the underlying MN firings despite the complex anatomy at the wrist (see transverse section in Figure 1.5), where the tendons of the forearm muscles converge in a reduced space. While the findings in Chapter 2 were obtained from a small dataset (single contraction for 9 finger gestures and 9 participants), results were replicated in Chapter 3 for a different set of 9 participants over 9 finger gestures, 9 wrist joint angles, and 2 repetitions, showcasing the reliability and the reproducibility of the results.

However, it is imperative to acknowledge the limitations in the validation of the neural origin performed in Chapter 2. First, MNs detected at the wrist were traced back at the forearm by spike-triggered averaging the forearm EMG signals from the firings at the wrist. This resulted in a 2D representation of the corresponding potentials at the forearm. Then, a MN from the wrist was considered detectable at the forearm if at least one channel exhibited peak amplitude above four times the baseline noise. While this criterion was based on intracortical spike sorting techniques (Quiroga et al. 2004), its direct application to muscle recordings may be suboptimal as well as providing an indirect matching. A more robust tracking approach would have compared the RoA between the firings detected at the forearm and the wrist taking into account the

effect of conduction velocity. However, initial comparisons showed no common units between the two locations (RoA $>$ 30%, Holobar et al. 2010). While discouraging at first glance, these results can be explained by the different anatomies at the forearm and the wrist (Figure 1.5), the decomposition bias towards higher amplitude MNs that innervate a large number of fibres and/or whose territories are more superficial (Holobar et al. 2009), and the relatively small number of detected MNs with respect to the active ones. Taken together, these factors indicate that it is feasible to detect different sets of MNs at the forearm and the wrist, despite targeting similar muscles such as the flexor digitorum superficialis. Therefore, the reported ability to trace back $\sim 72\%$ of the detected MN at the forearm to the wrist of can be considered as an upper bound, due to the rather permissive spatial and amplitude parameters of the spike-triggered averaging approach. Due to these difficulties, the firings of the MNs detected at the forearm and the wrist were not compared in Chapter 3.

In addition, this thesis did not provide means to characterise the stationary far-field potentials with respect to the propagating components of the MUAPs. Some of these metrics could have included the waveform duration (Dumitru et al. 1999), phase, as well as an estimate of the conduction velocity (Farina et al. 2000, 2001b). Yet, to perform this comparison linear arrays oriented along the muscle fibres' and tendons' directions should have been used, rather than the band arrangement used in this work due to its similarity with wearable systems (Mendez et al. 2017; Reality Labs et al. 2024). In addition, these metrics could have also informed the optimal values for the length of the MUAP filter (L) and extension factor (R) in Equation 1.11 for the far-field components at the wrist. In turn, this could have provided a quantitative characterisation of the higher sparsity of the far-field potentials at the wrist. However, it is worth noting that by assuming a larger L and thus, R in the model, more temporal support is added to the separation vectors in the decomposition, arguably increasing its ability to reconstruct the MN firings. Finally, such metrics could have measured the quality of the reconstructed far-field potentials by spike-triggered averaging which should be addressed in future work (see more on this in Section 4.3).

4.2.2 Control based on MN activity

In this thesis, the information content of the detected MN activity for the prediction of the underlying movement was assessed in a pattern recognition approach as described in Chapter 2. While, the offline analysis showed $> 95\%$ classification accuracy (high according to myoelectric control standards of $> 90\%$ accuracy), these results were based on a cross-validation approach over a single contraction per finger, which is a limited dataset. Notably, this configuration may have favoured the classification performance based on MNs due to their regular firings within an isometric contraction, in contrast to the variable burst seen in EMG signals. To address this limitation, I carried out an online control experiment (10 gestures) with multiple repetitions (3 per gesture during training, and 4 during testing) to validate the offline results. To the best of my knowledge, this was the first real-time classification task with the subject in the loop using MNs. In this case, offline results were replicated with an average of $\sim 93\%$ real-time classification accuracy. However, the recruitment of only 4 participants for the task makes it a proof-of-concept

study.

Yet, these results were obtained from isometric contractions rather than the natural movements common of human interaction. To address this, in Chapter 3, I developed a decomposition adaptation algorithm to compensate the modulation in muscle fibre length and volume conductor to accurately detect MN firings under non-stationary conditions. Although the recorded dataset could have been used for gesture prediction, Chapter 3 focused instead on the validation of the algorithm in terms of decomposition accuracy. Hence, the benefits of decomposition adaptation in gesture prediction during dynamics were not assessed. Future work should evaluate this interplay also considering the control paradigm (see more on this in Section 4.3).

4.2.3 Decomposition during dynamic contractions

Apart from proposing a new decomposition adaptation approach to compensate non-stationarities in the model, in the work of Chapter 3, I characterised the failure mode of the static decomposition algorithm and the MUAP changes with the wrist joint angle. In terms of decomposition performance, I showed that the static model (i.e. without adaptation) has a tolerance of 10° per wrist flexion and extension direction, which is in agreement to previous studies in the tibialis anterior (Oliveira et al. 2021; Yokoyama et al. 2021). Indeed, this tolerance to small postural changes may have facilitated the identification of MN firings during the pseudo-isometric conditions of the real-time control task described in Chapter 2.

Another strength of this work is the characterisation of the MUAP changes across the wrist joint angle to determine the level of induced modulation. This was possible thanks to the proposed spatiotemporal MUAP tracking approach based on the NMSE. In Chapter 2, I introduced a channel selection approach, which then I refined in Chapter 3 to select the channels with outlying peak amplitude as defined in Equation 3.22. This approach provided spatial selectivity to the comparison, which was needed to discard the large number of silent channels present in a band arrangement. In addition, to track MUAP across angles, I used the NMSE defined in Equation 3.23 (Farina et al. 2008) to make the comparison sensitive to changes in amplitude as opposed to the more common cross-correlation coefficient used in Chapter 2. Taken together, these metrics enhance the sensitivity of the approach to detect changes across dynamics. While the tracking approach did not have a ground truth per se, the convergence of both tracking and decomposition adaptation to the same solution constitutes a form of two-source validation since both methodologies are completely independent from each other. Notably, this strategy was particularly suitable for the wrist, where the muscle endings are surrounded by a high density of blood vessels, nerves, and tendons, making unfeasible the insertion of intramuscular electrodes for the gold-standard validation. Yet, factors such as the contraction duration to compute the MUAPs or the dis/similarity threshold required to match MUAP remain arguably arbitrary in the field and their optimal values should be addressed in future work (see more in Section 4.3).

Finally, in the literature, two main strategies have been proposed to deal with non-stationarities in the decomposition model by: 1) offline iterative methods that identify MN firings adapting to

modulations over multiple runs (Glaser et al. 2019; Kramberger et al. 2021), and 2) real-time recursive approaches that compensate the induced modulation over short batches of data (Chen et al. 2020a; Glaser et al. 2013; Yeung et al. 2024). Notably, the online methods, unlike the offline approaches, require an initialisation step, typically during isometric contractions. In Chapter 3, I advanced these real-time approaches by proposing two online learning metrics based on the required signal properties for decomposition (namely, their uncorrelation and non-gaussianity). Importantly, their hyperparameters can be tuned in the absence of ground truth by minimising the median squared error with respect to the calibration conditions. In Chapter 3, I showed that the minimisation of the difference with respect to the calibration conditions, provides a good balance between the optimisation of the signal properties and the risk of overfitting the model, resulting in $\geq 90\%$ rate of agreement, sensitivity, and precision in $\geq 80\%$ of the cases, with hyperparameters that generalised across subjects (at least within task), and reflected physiological differences between the forearm and the wrist. This represents a major advantage with respect to the ad-hoc values found in previous studies (Chen et al. 2020a; Glaser et al. 2013; Yeung et al. 2024), promoting its deployment to different experimental settings. Furthermore, the execution time of the proposed approach (22 ms per 100-ms batches) is approximately twice as fast as the previously proposed methods (Chen et al. 2020a; Glaser et al. 2013; Yeung et al. 2024). Yet, the current pipeline was evaluated on a single task where the wrist joint angle following a staircase pattern. This task was needed to include isometric phases to generate the validation set based on spatiotemporal MUAP tracking across angles to match the firings of independent decomposition calibrations at each angle. However, the ability of the proposed approach to compensate to multiple dynamic modulation speeds and magnitudes was not measured. Future work should address or bypass this as proposed in Section 4.3 and evaluate the performance in real-time. Furthermore, as a consequence of the selected task, the error term of the update was considered constant throughout the contraction. While this simplification assumption worked well for the tested conditions, the inclusion of the actual error term in the decomposition adaptation may offer further improvements in the accurate detection of MN firings.

4.3 Future perspectives

From the aforementioned results, strengths, and limitations, future work directions emerge to expand the development and implementation of non-invasive neural interfaces for general consumer applications.

Firstly, in this thesis I did not pursue the optimisation of the control paradigm for MN-based neural interfaces. Instead, in Chapter 2, I focused on validating the suitability of MN firings detected from the wrist as functional inputs for human-machine interfacing. In addition, I tapped into their usability for multi-action interaction by accurately predicting the corresponding finger gestures in a real-time control task. Yet, this work did not explore which is the optimal control paradigm (understood as mapping between MN activity and digital outputs - discrete actions vs continuous signals) nor its associated processing pipeline. Notably, the evaluation of these control paradigms is context specific and requires an effective equilibrium between functionality and usability (Karray et al. 2008). The review presented in Section 1.4 showed these strategies

could include the mapping to the exerted force (Thompson et al. 2018), gesture (Stachaczyk et al. 2020; Tanzarella et al. 2023), or kinematics (Chen et al. 2019; Yeung et al. 2023); as well as the use of MN activity as a source for motor augmentation (Bräcklein et al. 2022b, 2021; Formento et al. 2021). Hence, future work in this direction could further improve the control performance obtained from MNs decoded from the wrist.

A common trend in all these approaches is the longing for a larger number of reliably decomposed MNs. Recently, Grison et al. 2023 proposed a particle swarm optimisation of contrast functions that enhances the sensitivity of the decomposition, resulting in a higher yield of MNs than the gold-standard method. While the aforementioned results were obtained for intramuscular EMG, they offer promising insights to increase the number of decomposed MNs from surface recordings. However, merely detecting additional sources may not necessarily lead to improved interaction performance. Future research should explore metrics to better assess the quality of the MN population sampling in terms of detection and information content.

Currently, the PNR (Holobar et al. 2014), SIL (Negro et al. 2016a), and CoV (Holobar et al. 2010) are the most commonly used proxies for decomposition accuracy. Combining them is recommended to filter out noisy spiking activity that may meet the PNR and SIL thresholds but not the acceptable CoV level. However, the regularity of the firings measured by the CoV is only applicable under isometric contractions, and thus, new quality metrics should be developed for dynamic ones. In addition, in operational conditions such as real-time tasks, it may be advisable to compute the PNR and SIL over batches of data to monitor possible detection degradation. In fact, this approach was previously suggested by Glaser et al. 2019, who continuously calculated the PNR over short windows to refine their MN estimates during dynamic contractions. Similarly, in Chapter 3, I used differentiable metrics such as the Kullback–Leibler divergence and kurtosis to drive the adaptation, showing their suitability to measure deviations from the initial calibration. Follow-up studies should explore the most effective MN quality metrics/approaches for nonstationary conditions.

Simultaneously, the human-computer interaction capabilities of the detected MN population should also be assessed. In this regard, multiple methods have been proposed depending on the approach. For instance, Bräcklein et al. 2022b used recruitment thresholds as criteria for MN selection. Alternatively, Formento et al. 2021 selected MNs belonging to different spinal neural synergies (Hug et al. 2023). While these methods keep one MN per controllable direction, information theory metrics such as those proposed by Stachaczyk et al. 2020 or Yeung et al. 2023 provide valuable insights to effectively reduce the redundancy within a MN population. For instance, Yeung et al. 2023 showed that the minimal redundancy maximal relevance framework with mutual information-based criterion enabled the effective selection of 25% of the MN population with only $\sim 3\%$ decrease in performance in both offline classification and regression tasks. Notably, these approaches allow the concentration of resources on the subset of MNs that are most informative for human-machine interaction, facilitating the integration of real-time adaptation pipelines for continuous refinement. Therefore, subsequent studies combining more

robust detection quality metrics along with selection approaches may additionally enhance the stability and performance of this kind of neural interface.

Another important factor for the reliability of these interfaces is the consistent detection of MNs across postures and sessions, which is influenced by the MUAP tracking approach. While shorter contraction times reduce the effect of fatigue, they also imply lower number of spikes for MUAP computation, resulting in a less effective filtration of uncorrelated components in the MUAPs. In addition, in recordings with electrodes arranged in a band, the large number of silent channels produces deceivingly high similarities without channel selection. To mitigate this, in Chapters 2-3, I proposed peak amplitude outlier detection approaches that select the channels with highest amplitudes for comparison. In Chapter 3, I paired this with two tracking approaches for 1) constant conditions (e.g. repetitions of the same task) based on hierarchical clustering and 2) dynamic conditions based on progressive sequential tracking using a grid-search assignment algorithm. Furthermore, I used the NMSE (Farina et al. 2008) as (dis)similarity metric to account for possible amplitude changes in MUAPs, particularly with the wrist joint angle. However, previous studies have used the cross-correlation coefficient that is insensitive to these amplitude changes (Del Vecchio et al. 2019b; Goodlich et al. 2023; Martinez-Valdes et al. 2017). Hence, future research on this topic should identify the optimal method for channel selection, similarity metric and threshold value, while accounting for confounding factors such as silent channels, number of spikes used for the MUAP calculation, and changes during dynamics. In addition the exploration of MUAP quality metrics could also benefit this process, offering new contrasts for tracking and AI-based volume conductor models such as BioMime (Ma et al. 2023a). The consistency and consensus in these tracking approaches will also influence the ability to progressively follow MNs across dynamics (as introduced in Chapter 3), which provides a non-invasive decomposition validation approach across multiple postures. Furthermore, the refinement of MUAP tracking strategies could also facilitate the identification of MNs across sessions (Del Vecchio et al. 2019b; Goodlich et al. 2023; Martinez-Valdes et al. 2017), promoting the long-term stability of the interface and user learning (Formento et al. 2021).

Yet, the most crucial aspect to ensure a robust and reliable MN interface is the ability of the decomposition algorithm to adapt to nonstationarities. In Chapter 3, I proposed two online learning metrics whose hyperparameters can be tuned in the absence of ground truth by minimising the median squared error with respect to the calibration conditions. This optimisation resulted in $\geq 90\%$ rate of agreement, sensitivity, and precision in $\geq 80\%$ of the cases, with common hyperparameters across subjects (at least for the evaluated task) and specific to each location (wrist vs. forearm). Despite the encouraging results, this approach has focused on compensating the nonstationarities in the output (i.e. MN firings) rather than learning the modulating function induced by the dynamics. Consequently, one may wonder if the performance of this type of methods is constrained by the speed and magnitude of the dynamic contraction, as well as the repetitions included in the learning set of the offline approaches. Indeed, previous studies that have simulated multiple speeds of muscle shortening/lengthening have adjusted the number of repetitions to ensure the same recording length across conditions (Chen et al.

2020a; Glaser et al. 2019; Kramberger et al. 2021), compensating the trade-off between samples and speed. On the other hand, the online learning algorithms may not be able to compensate fast movements, particularly, if their change in joint angle with respect to the initialisation conditions is larger than the decomposition tolerance ($\sim$10°). Nonetheless, this limitation could be compensated with a double calibration scenario where the decomposition model is first initialised during an isometric contraction, and then, the underlying dynamic modulation is subsequently learnt over a slow dynamic contraction. This approach could potentially deal better with the nonlinear relationships between force, speed, muscle length, and MN behaviour in terms of recruitment and rate coding (see Section 1.1.4). Especially considering that movement speed increases the discharge rate under constant loads (Oliveira et al. 2021), raising the likelihood of overlapping spikes, and thereby complicating the separation problem even in the absence of dynamic modulations in the anatomical volume. Therefore, future research should investigate whether adapting the decomposition output or learning the underlying dynamic modulation is the most effective and robust approach for deployment during real-time dynamic contractions. In this regard, full-spectrum neuromechanical models such as NeuroMotion (Ma et al. 2023b) offer new possibilities to study these effects.

Finally, to achieve the objective of non-invasive neural interfacing for mainstream consumer electronics, the integration of decomposition and control models into a wearable system becomes imperative. In Chapter 2, I showcased the feasibility of real-time implementation of these pipelines, along with the efficient execution of the adaptation method introduced in Chapter 3. Nonetheless, incorporating these methods into an embedded system requires a careful evaluation of the optimal trade-offs between performance and the number of electrodes, their montages, and the systems' physical resources (including energy consumption, memory usage, and heat generation). Subsequent work should ultimately assess the interplay between these hardware variables.

4.4 Final remarks

In conclusion, in this thesis, I have extended the non-invasive detection of MN activity to the wrist, demonstrated their potential for human-machine interaction, and devised methods to adapt to nonstationarities. Furthermore, I have outlined strengths, limitations, and future research directions concerning the control paradigm, long-term stability of the interface, decomposition outlook for dynamic contractions, and integration with wearable systems. Collectively, these findings and perspectives advance us towards a future where seamless interaction with technology is at the reach of our wrists.

Appendices

A1 Isokinetic wrist platform

This section describes the specifications and features of the isokinetic platform (IsoKin-Wrist) that I designed and built for the experimental data collection described in Chapter 3.

A1.1 Design

IsoKin-Wrist is a motorised platform that assists the movement of wrist flexion and extension while recording individual digit flexion and thumb abduction forces. The system is intended to be used for research purposes only. Figure A1.1 shows all platform components and the external devices setup. Figures A1.2, A1.3, and A1.4 show the dimensions of the bottom part, top enclosure, and hand platform, respectively.

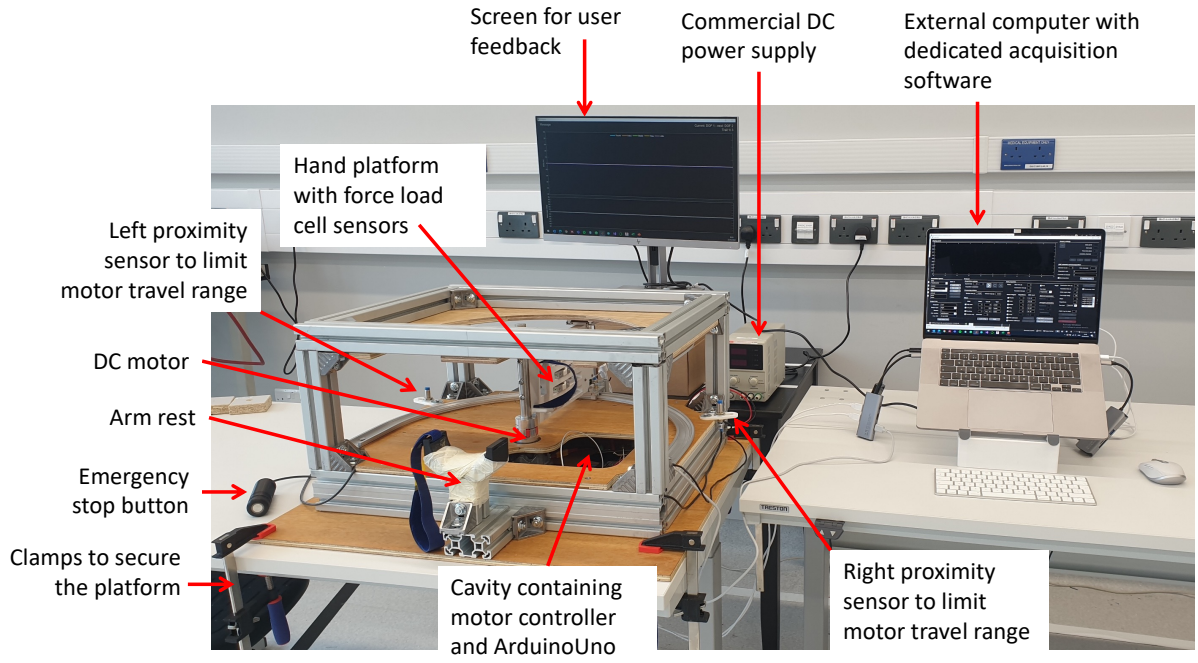

Figure A1.1: IsoKin-Wrist device with all labelled components including the motor, motor controller and ArduinoUno board to handle communication, arm and hand rest, force load cell sensors, and security features such as the inductive proximity sensors and the emergency stop button. The setup also includes an external commercially available DC power supply, a computer with the dedicated software for data acquisition, and an additional screen for user feedback.

IsoKin-Wrist platform requires a commercial DC power supply, an external computer to trigger the actuation of the platform, and screen to display feedback to the subjects. Prior any

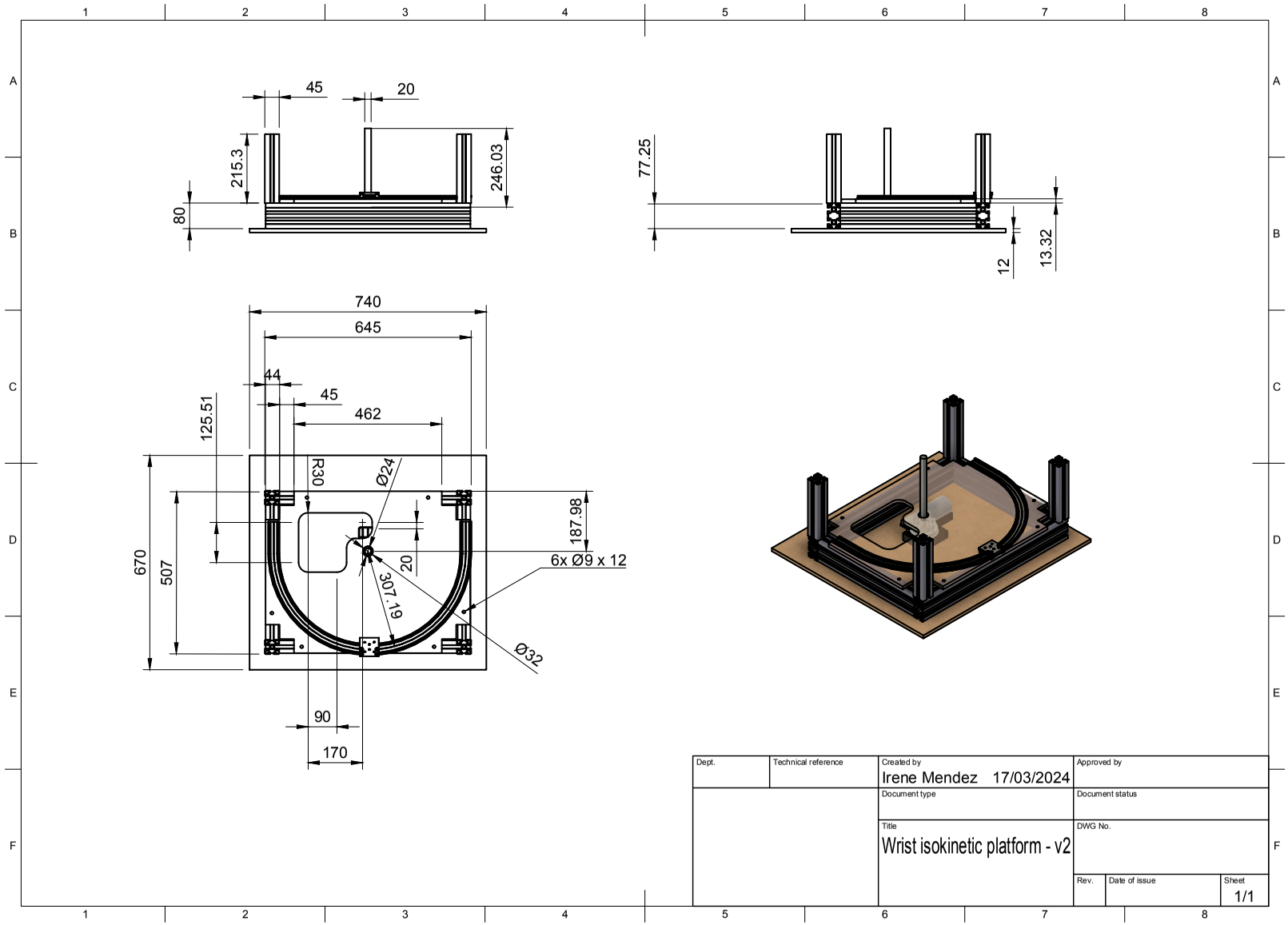

Figure A1.2: Dimensions of the isokinetic wrist system (bottom part). The railings (WSB-06-30-RK300HS, 300 mm radius) and carriages (WWB-06-30-06-R300) were bought from Igus.

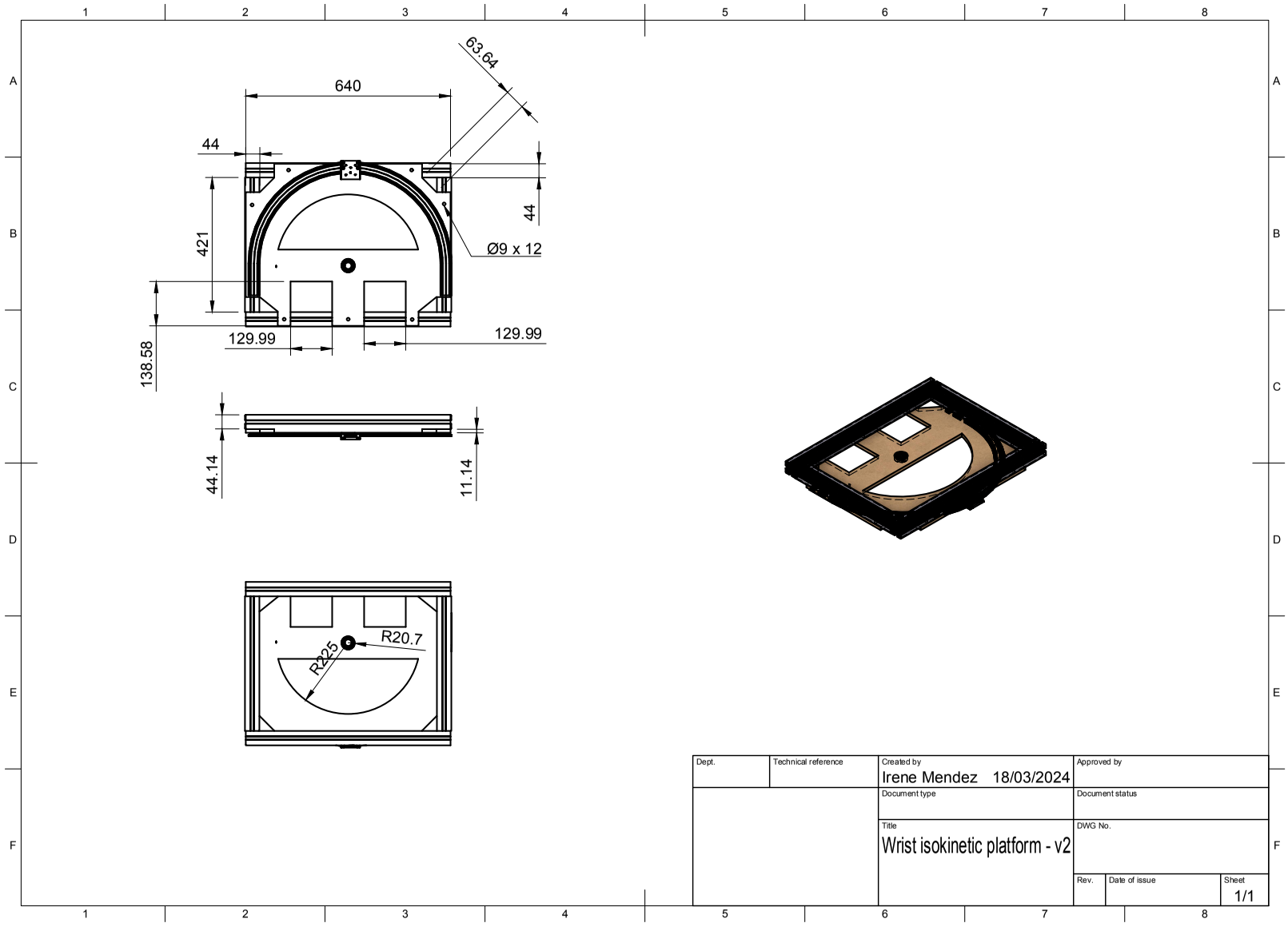

Figure A1.3: Dimensions of the isokinetic wrist system (top part). The railings (WSB-06-30-RK300HS, 300 mm radius) and carriages (WWB-06-30-06-R300) were bought from Igus.

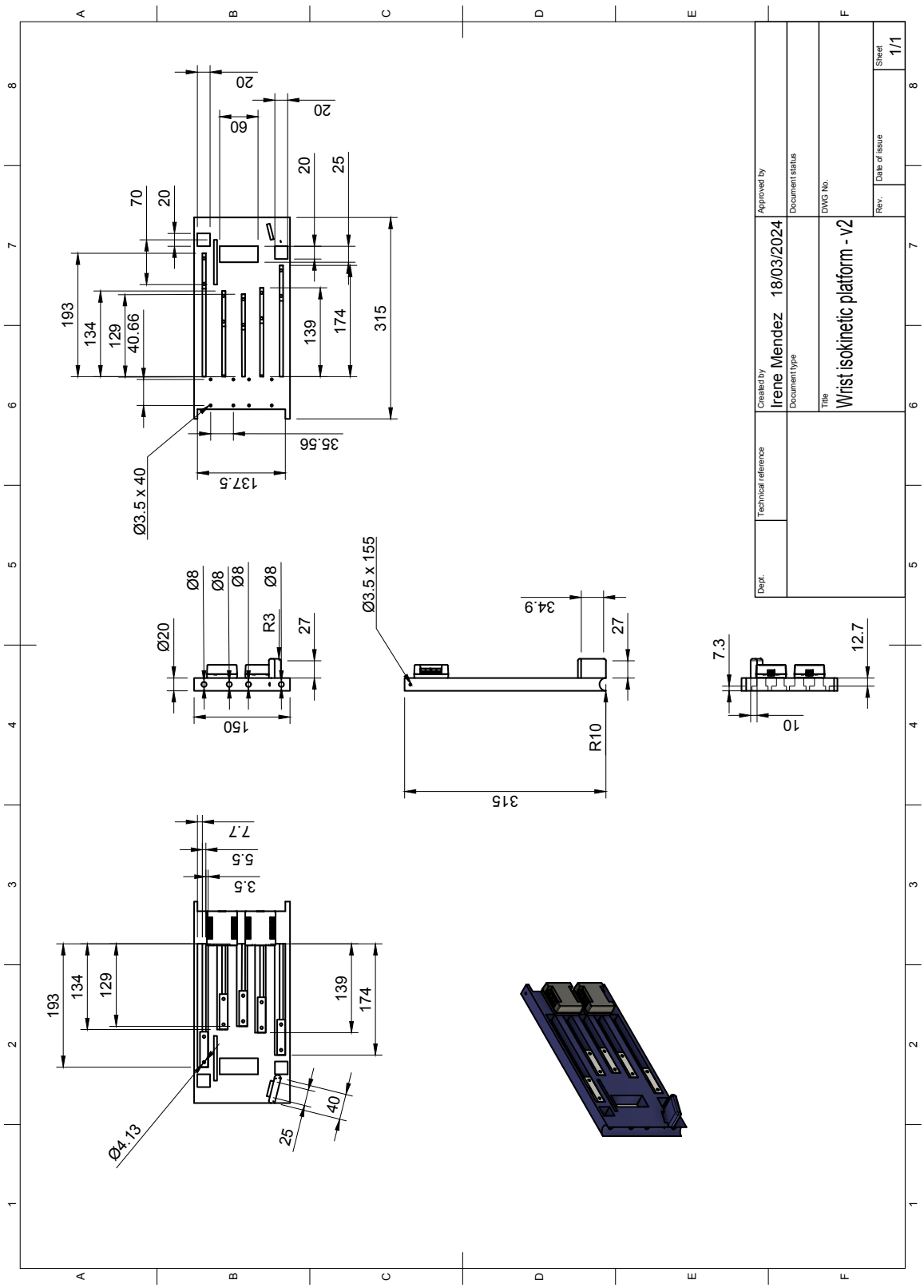

Figure A1.4: Dimensions of the isokinetic wrist system (hand platform)

experiments, the motor needs to be calibrated using commercial software (BasicMicro Motion Studio, see Section A1.3.2). A custom dedicated software that I developed (see Section A1.3) needs to run on the external computer to acquire, synchronise, and record EMG signals, individual forces, as well as the motor's position and speed. The software also handles participant's feedback, and triggers motor predefined cues. The motor calibration and data acquisition programs require a Windows 10 or 11 machine.

A1.2 Electrical components

This subsection describes the hardware component specifications of IsoKin-Wrist. Figure A1.5 shows all components and their connections.

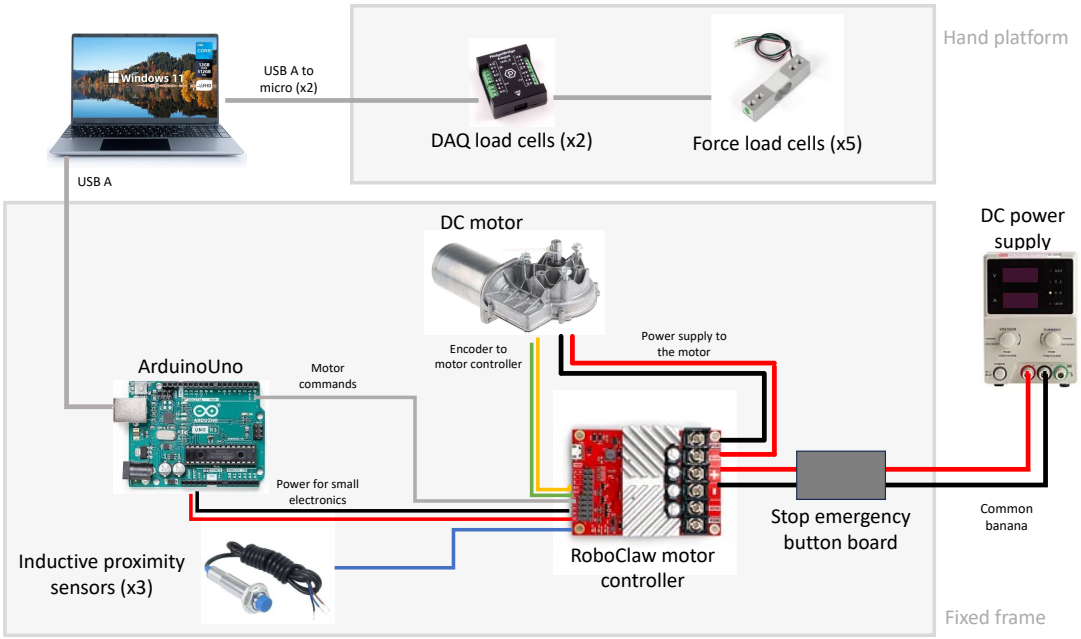

Figure A1.5: IsoKin-Wrist connection setup. The system is comprised by a DC motor, which is controlled by a commercial motor controller board and powered by an external and commercial DC power supply. An emergency stop button board is placed between the DC power supply and the motor controller to safely disengage power to the motor in case of emergency. The motor controller also reads the data from the motor encoder and inductive proximity sensors that limit the motor's travelling range within the natural range of wrist flexion and extension. An external computer is required for data acquisition, feedback display, and to trigger motor cues. The communication between the computer and the motor controller is handled by an ArduinoUno board. In addition, five force load cells are integrated within the hand moving platform with their dedicated commercial DAQ board that is connected to the computer. For the experiment the operator only needs to connect the cables outside the shaded areas: 2 USB A cables coming from the load cell DAQ boards, 1 USB A cable from the ArduinoUno, 2 standard banana cables to the DC power supply color coded for the positive and negative ends.

A1.2.1 Computer

Windows 10 or 11 machine with an i7-7700HQ (4 cores @ 2.80GHz up to 3.80GHz) or later processor, at least 8 Gb of RAM, and the ability to connect 3 USB A male cables (directly or with an adaptor).

A1.2.2 External screen

Additional screen to provide feedback to users of their finger flexion forces and the position and speed of the motor.

A1.2.3 DC motor

A commercial DOGA Brushed Geared DC motor (319.4862.30.00) is used to move the hand resting platform. The motor is RoHS compliant and adheres to the administrative and technical requirements of the ANSI/ESD S20.20:2014 and BS EN 61340-5-1:2007 Electrostatic Control Standards. Table A1.1 lists DOGA Brushed Geared DC motor (319.4862.30.00) specifications.

Table A1.1: DOGA Brushed Geared DC motor (319.4862.30.00) specifications

Attribute	Value
DC motor type	Brushed gearhead
Gearhead type	Worm
Supply voltage	24 V (DC)
Nominal current	3 A
Nominal speed	45 rpm
Nominal output torque	9 Nm
Shaft diameter	12 mm
Dimensions	206.5 x 60 x 122.7 mm
Core construction	Iron core
Feedback	Hall sensor for speed, direction and position of the motor

A1.2.4 DC motor controller

Commercial DC motor controller (BasicMicro RoboClaw 2x15A) designed to control two brushed DC motors at 15 Amps continuous with up to 30 Amps peak per channel. In this case only one is in used. It is controlled from an ArduinoUno board and incorporates inputs for limit and home switches. The motor controller enables position control, and PID autotuning via BasicMicro Motion Studio software. Table A1.2 lists BasicMicro RoboClaw 2x15A motor controller specifications.

A1.2.5 DC power supply

A commercial DC power supply able to deliver 24 V and up to 3 A current, with standard banana connectors.

A1.2.6 Emergency stop button board

Emergency stop button custom board from the MIT Open Source Leg (Azocar et al. 2020), containing a safety mechanism used to cut power to any DC power input system it is connected to in the case of an emergency. For more details see the e-stop user manual The board does not need a dedicated power source as it is designed to share the same DC power source as the

Table A1.2: DC motor controller (BasicMicro RoboClaw 2x15A) specifications

Features	
Motor Channels	2
Bridge Channels	No
Peak Current per Channel	30 A
Continuous Current per Channel	15 A
Max Voltage	34 V (DC)
BEC	5 VDC @ 1 Amp
3.3V Safe Outputs	Yes
5V Tolerant Inputs	Yes
Quadrature Encoders	Yes
Absolute Encoders	Yes
Encoder Auto Tune	Yes
Thermal Protection	Yes
Current Sense	Yes
User Selectable Peak Current	Yes
Battery Protection	Yes
Regenerative Braking	Yes
Over Voltage Protection	Yes
Under Voltage Protection	Yes
Self Diagnostics	Yes

Control	
USB	Yes
Analog	Yes
RS232	Yes
RC Pulse	Yes
Position Control Mode	Yes
Velocity Control Mode	Yes
Motor Type	Brushed DC

Mechanical	
Dimensions	L: 74mm x W: 52mm x H: 17mm
Weight	61 grams
Enclosed	Optional
Heat Sink	Top mounted Fins
Cooling	Convection

system it is connected to. The board can handle any combination of DC power source voltage and current ranges described in Table A1.3

Table A1.3: Emergency stop button voltage and current ranges

Parameter	Range
DC power source voltage	11V to 50 V
Current	0 A to 15 A

A1.2.7 Inductive proximity sensors

Two commercial inductive proximity sensors (LJ12A3-4-Z/BX, Heschen) are placed between -50°(flexion) and 50°(extension) to limit the travelling range of the motor for safety. This is well below the maximum functional range of the wrist between ∼80° and ∼70° for flexion and extension, respectively (Alford 2021). An additional inductive proximity sensor is positioned at 0°to indicate the home position for the motor. Table A1.4 list the specifications of the inductive proximity sensors.

Table A1.4: Inductive proximity sensors (LJ12A3-4-Z/BX, Heschen) specifications

Parameter	Value
Mounting hole diameter	12mm
Detecting distance	4mm
Working voltage	10-30 VDC
Current output	200mA
Output type	NPN/PNP NO(Normally Open)
Set distance	0-3.6mm
Detect Object	Magnetic Metal

A1.2.8 ArduinoUno board

An ArduinoUno board is connected to the external computer (section A1.2.1) and the motor controller (section A1.2.4) to deliver motor commands. The board contains Arduino code using BasicMicro's interface (for more details, read Packet Serial section in BasicMicro RoboClaw 2x15A User Manual) to define motor commands between -40°and 40°wrist joint angles (range needed for most activities of the daily living, Gates et al. 2016) at a maximum speed of 40°/s. The board is connected to the external computer via a USB-B to USB-A male to male cable.

A1.2.9 Force load cells and dedicated DAQs

The hand resting platform contains five commercial load cells (Phidgets, 5Kg, ID: 3133_0) to measure individual finger flexion forces. They are connected to their compatible dedicated DAQ boards (Phidgets, PhidgetBridge 4-Input ID: 1046_0B), which are connected to the external computer (section A1.2.1) via a mini-USB to USB A male to male cable. Table A1.5 and Table A1.6 contain the specifications of the Phidget 5kg load cells and PhidgetBridge 4-Input DAQ, respectively.

Table A1.5: Phidgets 5Kg load cells specifications

Sensor Properties	
Controlled By	Bridge Input
Sensor Type	Single Point Load Cell
Load Cell Accuracy Grade	Consumer Grade
Weight Capacity Max	5 kg
Maximum Overload	6 kg
Creep	5 g/hr
Zero Balance	± 75 g
Cell Repeatability Error Max	± 2.5 g
Cell Non-Linearity Max	2.5 g
Cell Hysteresis Max	2.5 g
Temperature Effect on Span	250 mg/°C
Temperature Effect on Zero	500 mg/°C
Electrical Properties	
Rated Output	1 mV/V
Rated Output Error Max	± 150 µV/V
Output Impedance	1 kΩ
Supply Voltage Max	5 V DC
Physical Properties	
Compensated Temperature Min	-10 °C
Compensated Temperature Max	40 °C
Operating Temperature Min	-20 °C
Operating Temperature Max	55 °C
Cable Length	550 mm
Cable Gauge	30 AWG
Material	Aluminium Alloy (LY12CZ)
Screw Thread Size	M5x0.8

Table A1.6: PhidgetBridge 4-Input DAQ specifications

Board	
Controlled By	USB (Mini-USB)
API Object Name	Bridge
Number of Bridge Inputs	4
Bridge Data Interval Min	* 8 ms
Bridge Data Interval Max	1000 ms
Bridge Input Current Max	± 3 nA
Differential Voltage Resolution	24 bit
Data Rate Max	125 Hz
Electrical Properties	
USB Voltage Min	4.5 V DC
USB Voltage Max	5.3 V DC
USB Speed	Full Speed
Current Consumption Min	35 mA
Current Consumption Max	500 mA
Available External Current	465 mA
Input Voltage Limit Min	Ground + 0.25V DC
Input Voltage Limit Max	5V Supply - 0.25V DC
Physical Properties	
Recommended Wire Size	16 - 26 AWG
Operating Temperature Min	0 °C
Operating Temperature Max	70 °C

A1.3 Software

A custom Matlab program "IsoKin-Wrist v.1 Lite" was developed for data acquisition, synchronisation, recording, and feedback in real-time.

A1.3.1 Software prerequisites

To operate IsoKin-Wrist the following software is required:

1. Phidgets21 library and Windows installation drivers to be able to read the load cell data in Matlab.
2. For the motor controller:
   - Roboclaw Windows USB Driver
   - Roboclaw Arduino Library
   - Roboclaw Motion Studio to calibrate the PID of the motor
   - Robot Operating System Driver also required for the calibration of the PID of the motor
3. Matlab R2021a or superior

A1.3.2 Motor calibration

Before using IsoKin-Wrist for wrist joint position control, its motor should be calibrated. This process is only required once and it has already been done. It is only described here for future reference. Importantly, the calibration of the PID controller should be done in the absence of a participant.

The PID is calibrated by the BasicMicro Motion Studio commercial software. To do so, disconnect the ArduinoUno and inductive proximity sensors from the motor controller, and connect a USB-micro to USB-A male to male cable from the motor controller to the external Windows computer running Motion Studio. Follow the step-by-step guide described in the BasicMicro user manual for RoboClaw series brushed DC motor controllers (Position settings section, p. 23) and this BasicMicro video tutorial. Once the PID has been calibrated, the ArduinoUno and inductive proximity sensors must be connected back.

A1.3.3 Data Acquisition Procedure

To launch "IsoKin-Wrist v1 Lite", open Matlab and execute the following commands in the command line:

```
[obj,app] = IsoKin-Wrist();
```

This will open two GUIs, one with the controls for the operator (hereto referred as mainGUI, see Figure A1.6), and the other one for user feedback (hereto referred as subGUI, see Figure A1.7)

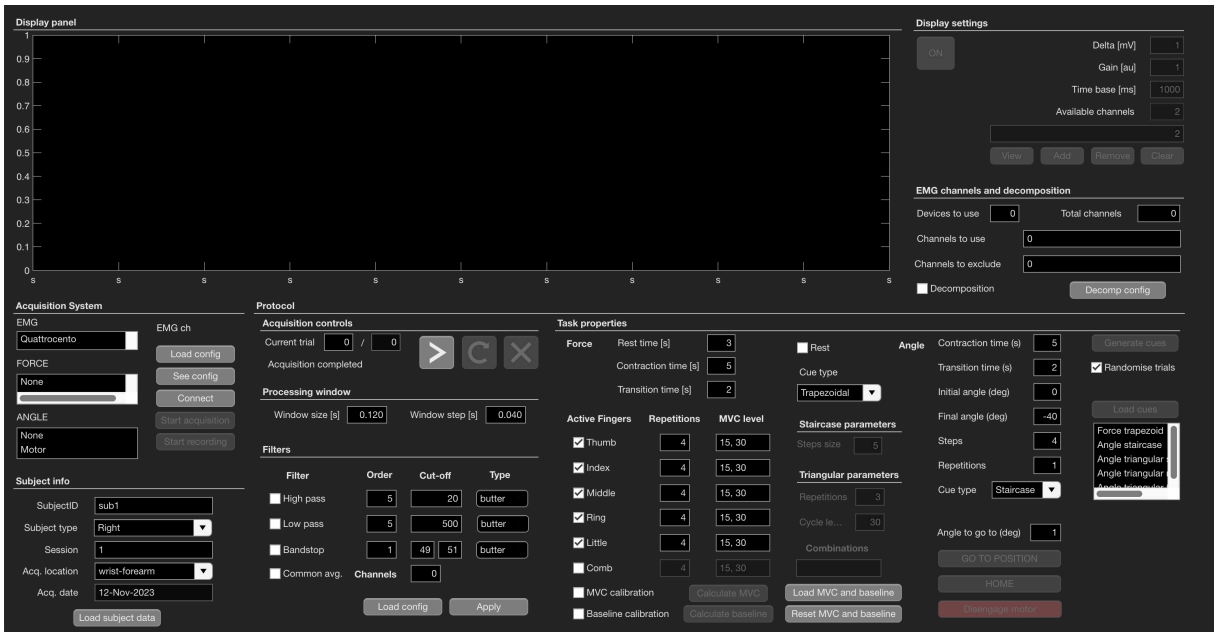

Figure A1.6: mainGUI of IsoKin-Wrist v1 Lite with the controllers for the operator.



Figure A1.7: subGUI of IsoKin-Wrist v1 Lite to display user feedback of their finger forces, wrist joint angle, and speed.

A1.3.4 Calibrate force sensors

To calibrate the force load cells to remove the baseline and normalise the force to the participant's maximum voluntary contraction (MVC) force, follow these steps:

1. In the mainGUI:
    - Navigate to the Acquisition Systems panel.
    - Select ForcePhidget_platform for FORCE, and None for ANGLE.
    - Click the Connect button.
2. In the Display Settings panel, turn ON the display.
3. Start the acquisition by clicking the Start Acquisition button.
4. In the Protocol section:
    - Select the baseline calibration checkbox.
    - Generate cues by clicking the corresponding button.
    - Proceed to the acquisition controls by clicking 'Next' (>).
5. The recording will start automatically. Wait for the message "Recording has ended, and Data has been saved successfully" in the command line. Ensure no action until this message appears.
6. Stop the acquisition by clicking the respective button in the Acquisition Systems panel.

7. Calculate baseline values by clicking the Calculate baseline button in the Task Properties.

For the MVC calibration, repeat steps 4-8, checking the MVC calibration checkbox in step 5 and performing Calculate MVC in step 8. Once both MVC and baseline have been successfully computed, ensure to uncheck the corresponding check boxes in the Task Properties.

A1.3.5 Recordings with force only

To perform force recordings only, follow these steps:

1. Start the acquisition by clicking the Start Acquisition button.
2. In the Protocol section:
    - Select Force trapezoid from the cue list.
    - Click Load cues.
    - Generate cues by clicking the corresponding button.
    - Proceed to the acquisition controls by clicking 'Next' (>). Recording will start and stop automatically
3. Once the data has been stored correctly, repeat step 2 to load, generate, and record the next trial.

A1.3.6 Recordings with the motor

This section focuses on connecting and configuring the motor for data acquisition:

1. In the mainGUI:
    - Select ForcePhidget_platform for FORCE, and Motor for ANGLE.
    - Click the Connect button.
2. After these settings, you'll be connected to both systems.
3. Turn ON the display in the Display Settings panel.
4. Initiate the acquisition by clicking the Start Acquisition button in the Acquisition Systems panel.
5. Load the corresponding cues for the motor and force, which include the definition of the angle range, motor speed and target force. To do so, perform the following steps:
    - Select the appropriate cue in the Task Properties.
    - Click the Load cues button in the Task Properties.
6. Click 'generate cues' and then 'Next' to proceed in the acquisition controls.Recording will start and stop automatically.
7. Once the data has been stored correctly, repeat step 5-6 to load, generate, and record the next trial.

A1.4 Emergency stop procedure

1. Press emergency button to cut power supply immediately to the motor. Once pressed the motor will not move until the system is reset.
2. Remove the subject's hand from the platform immediately. Check the status of the participant.
3. Inspect all connections and maks sure everything is connected as in Figure A1.5.
4. In Matlab, stop the trial acquisition, and disconnect motor from the software.
5. Disconnect the USB cable from the ArduinoUno to the computer.
6. Click the reset button on the Arduino board.
7. Connect the USB-micro to USB-A male to male cable from the motor controller to the computer.
8. Open BasicMicro Motion Studio software.
9. Release the emergency button. At this point the software will take over the control of the motor.
10. Once you see a device in Attached Devices, click Connect to selected unit.
11. Go to position settings.
12. Move the M1 position slider very slowly to reset the motor position to 0 degrees as marked by the home limit sensor.
13. Once at the home position, click on the three dots button next to M1 encoder at the top of the window to reset the encoder.
14. Click on Disconnect selected units.
15. Close Motion control app.

At this point the motor should have reset if there is no hardware malfunction. However, it is advised to proceed with extreme caution an run few test recordings without the participant to make sure everything is working correctly. Do not proceed further if motor control is not restored and contact the corresponding lab manager.

A2 Copyright licenses and permissions

Chapters 2 and 3 were published in a peer-reviewed journal and open-source repository, respectively, under **CC-BY 4.0** and **CC-BY-NC 4.0** licenses (Creative Commons Attribution 4.0 International License), respectively. The CC-BY 4.0 license allows the reproduction of the material provided the original work is properly cited. The same applies for the CC-BY-NC 4.0 for non-commercial applications. Permission was requested for the figures in the Introduction that were not published under the CC-BY license. Table A2.1 provides a summary of the source and copyright license for each reused item. Figures A2.1 and A2.2 show copies of publishers' permissions for the required figures. Figures A2.3 and A2.4 show copies of the confirmation of licensing and publication rights for Figures 1.1 and 1.2 created with BioRender.com.

Figure / Chapter	**Journal**	**Publisher**	**Copyright License**	**Proofs**
Figure 1.3	N/A (Book)	McGraw-Hill	N/A	Figure A2.1
Figure 1.4	N/A (Book)	OpenStax	CC-BY 4.0 Deed	N/A
Figure 1.5	N/A (Book)	Wolters Kluwer	N/A	Figure A2.2.a
Figure 1.6	N/A (Book)	Wiley	N/A	Figure A2.2.b
Figure 1.7	Advances in Physiology Education	American Physiological Society	N/A	Figure A2.2.c
Figure 1.8	Muscle & Nerve	Wiley	N/A	Figure A2.2.d
Figure 1.10.a	Advances in Physiology Education	American Physiological Society	N/A	Figure A2.2.c
Figure 1.10.b-d	N/A (Book)	Wiley	N/A	Figure A2.2.e
Figure 1.11.a	N/A (Book)	Wiley	N/A	Figure A2.2.f
Figure 1.11.b	Journal of Electromyography and Kinesiology	Science Direct	CC-BY 4.0	N/A
Figure 1.12	Biological Cybernetics	Springer Nature	N/A	Figure A2.2.e
Chapter 2	Journal of Neural Engineering	IOP science	CC-BY 4.0	N/A
Chapter 3	biorxiv	Cold Spring Harbor Laboratory	CC-BY-NC 4.0	N/A

Table A2.1: A summary of the sources and copyright license of items included in the thesis.



This is a License Agreement between Irene Mendez Guerra ("User") and Copyright Clearance Center, Inc. ("CCC") on behalf of the Rightsholder identified in the order details below. The license consists of the order details, the Marketplace Permissions General Terms and Conditions below, and any Rightsholder Terms and Conditions which are included below.

All payments must be made in full to CCC in accordance with the Marketplace Permissions General Terms and Conditions below.

Order Date	05-Feb-2024	**Type of Use**	Republish in a thesis/dissertation
Order License ID	1446866-1	**Publisher**	MCGRAW-HILL
ISBN-13	9780071390118	**Portion**	Chart/graph/table/figure

LICENSED CONTENT

Publication Title	Principles of neural science	**Language**	English
Author/Editor	KANDEL, ERIC R.	**Rightsholder**	McGraw Hill LLC
Date	01/01/2013	**Publication Type**	Book

REQUEST DETAILS

Portion Type	Chart/graph/table/figure	**Distribution**	Worldwide
Number of Charts / Graphs / Tables / Figures Requested	1	**Translation**	Original language of publication
		Copies for the Disabled?	No
Format (select all that apply)	Print, Electronic	**Minor Editing Privileges?**	No
Who Will Republish the Content?	Academic institution	**Incidental Promotional Use?**	No
Duration of Use	Life of current and all future editions	**Currency**	GBP
Lifetime Unit Quantity	More than 2,000,000		
Rights Requested	Main product		

NEW WORK DETAILS

Title	Non-invasive neural interfacing for wearable electromyographic systems	**Institution Name**	Imperial College London
		Expected Presentation Date	2024-02-07
Instructor Name	Irene Mendez Guerra		

ADDITIONAL DETAILS

Order Reference Number	N/A	**The Requesting Person / Organization to Appear on the License**	Irene Mendez Guerra

REQUESTED CONTENT DETAILS

Title, Description or Numeric Reference of the Portion(s)	Figure 34-9	**Title of the Article / Chapter the Portion Is From**	The motor unit and muscle action
Editor of Portion(s)	Eric R. Kandel, James H. Schwartz, Thomas M. Jessell, Steven A. Siegelbaum, A. J. Hudspeth	**Author of Portion(s)**	Roger M. Enoka, Keir G. Pearson
		Issue, if Republishing an Article From a Serial	N/A
Volume / Edition	5th	**Publication Date of Portion**	2013-01-01
Page or Page Range of Portion	780		

Figure A2.1: Proof of permission for Figure 1.3

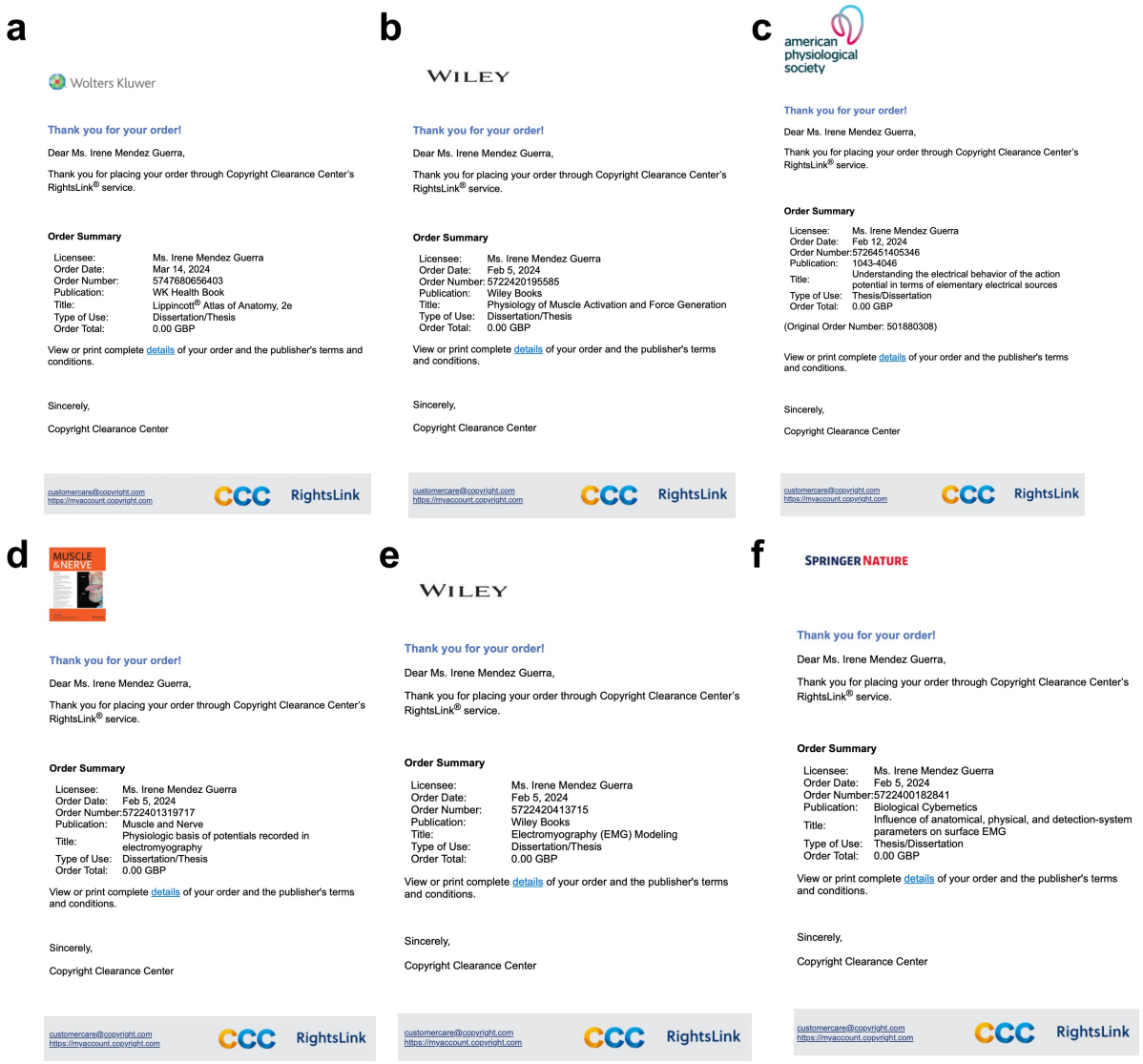

Figure A2.2: Proof of permissions for (a) Figure 1.5, (b) Figure 1.6, (c) Figure 1.7 and Figure 1.10.a, (d) Figure 1.8, (e) Figure 1.10.b-d and Figure 1.11.a, (f) Figure 1.12

49 Spadina Ave. Suite 200
Toronto ON M5V 2J1 Canada
www.biorender.com

Confirmation of Publication and Licensing Rights

March 4th, 2024
Science Suite Inc.

Subscription:	*Individual*
Agreement number:	*MV26JB1NSU*
Journal name:	*PhD thesis*

To whom this may concern,

This document is to confirm that Irene Mendez has been granted a license to use the BioRender content, including icons, templates and other original artwork, appearing in the attached completed graphic pursuant to BioRender's Academic License Terms. This license permits BioRender content to be sublicensed for use in journal publications.

All rights and ownership of BioRender content are reserved by BioRender. All completed graphics must be accompanied by the following citation: "Created with BioRender.com".

BioRender content included in the completed graphic is not licensed for any commercial uses beyond publication in a journal. For any commercial use of this figure, users may, if allowed, recreate it in BioRender under an Industry BioRender Plan.

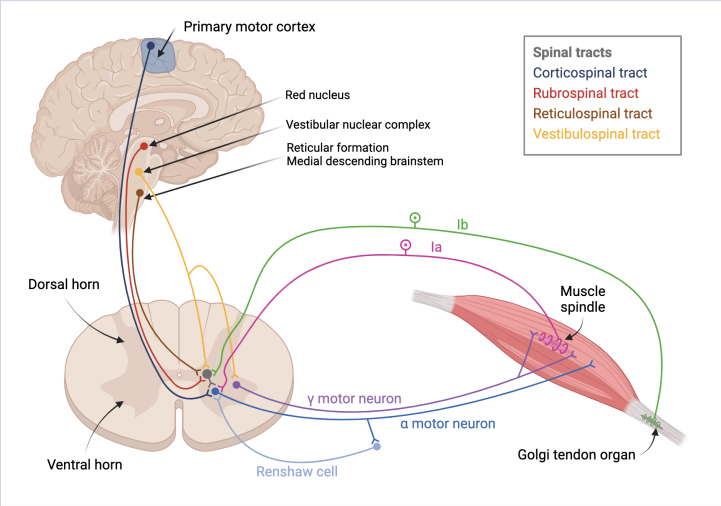

For any questions regarding this document, or other questions about publishing with BioRender refer to our BioRender Publication Guide, or contact BioRender Support at support@biorender.com.

Figure A2.3: Confirmation of publication and licensing rights for Figure 1.1 created with BioRender.com

49 Spadina Ave. Suite 200
Toronto ON M5V 2J1 Canada
www.biorender.com

Confirmation of Publication and Licensing Rights

March 4th, 2024
Science Suite Inc.

Subscription:	*Individual*
Agreement number:	*YS26JB23BO*
Journal name:	*PhD thesis:*

To whom this may concern,

This document is to confirm that Irene Mendez has been granted a license to use the BioRender content, including icons, templates and other original artwork, appearing in the attached completed graphic pursuant to BioRender's Academic License Terms. This license permits BioRender content to be sublicensed for use in journal publications.

All rights and ownership of BioRender content are reserved by BioRender. All completed graphics must be accompanied by the following citation: "Created with BioRender.com".

BioRender content included in the completed graphic is not licensed for any commercial uses beyond publication in a journal. For any commercial use of this figure, users may, if allowed, recreate it in BioRender under an Industry BioRender Plan.

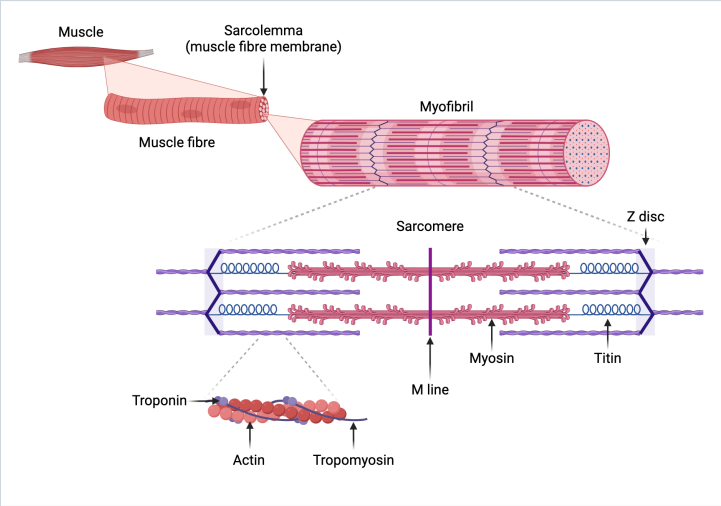

For any questions regarding this document, or other questions about publishing with BioRender refer to our BioRender Publication Guide, or contact BioRender Support at support@biorender.com.

Figure A2.4: Confirmation of publication and licensing rights for Figure 1.2 created with BioRender.com

Bibliography

Adrian, E. D. and Bronk, D. W. (Mar. 1929). The discharge of impulses in motor nerve fibres. Part II. The frequency of discharge in reflex and voluntary contractions. *The Journal of Physiology* 67:i3–151.

Ahmadizadeh, C., Khoshnam, M., and Menon, C. (July 2021). Human Machine Interfaces in Upper-Limb Prosthesis Control: A Survey of Techniques for Preprocessing and Processing of Biosignals. en. *IEEE Signal Processing Magazine* 38:12–22.

Alford, S. L. (Oct. 2021). Remote self-measurement of wrist range of motion performed on normal wrists by a minimally trained individual using the iPhone level application only demonstrated good reliability in measuring wrist flexion and extension. *Journal of Hand Therapy* 34:549–554.

Andreassen, S and Arendt-Nielsen, L (1987). Muscle fibre conduction velocity in motor units of the human anterior tibial muscle: a new size principle parameter. en. *The Journal of Physiology* 391. _eprint: https://onlinelibrary.wiley.com/doi/pdf/10.1113/jphysiol.1987.sp016756:561–571.

Andreassen, S and Rosenfalck, A (Oct. 1980). Regulation of the firing pattern of single motor units. *Journal of Neurology, Neurosurgery, and Psychiatry* 43:897–906.

Ariyanto, M., Caesarendra, W., Mustaqim, K. A., Irfan, M., Pakpahan, J. A., Setiawan, J. D., and Winoto, A. R. (Oct. 2015). Finger movement pattern recognition method using artificial neural network based on electromyography (EMG) sensor. en. *2015 International Conference on Automation, Cognitive Science, Optics, Micro Electro-Mechanical System, and Information Technology (ICACOMIT)*. Bandung, Indonesia: IEEE, 12–17.

Azocar, A. F., Mooney, L. M., Duval, J.-F., Simon, A. M., Hargrove, L. J., and Rouse, E. J. (Oct. 2020). Design and clinical implementation of an open-source bionic leg. en. *Nature Biomedical Engineering* 4. Publisher: Nature Publishing Group:941–953.

Barsakcioglu, D. Y., Bräcklein, M., Holobar, A., and Farina, D. (Mar. 2021). Control of Spinal Motoneurons by Feedback From a Non-Invasive Real-Time Interface. *IEEE Transactions on Biomedical Engineering* 68:926–935.

Barsakcioglu, D. Y. and Farina, D. (Oct. 2018). A real-time surface EMG decomposition system for non-invasive human-machine interfaces. en. *2018 IEEE Biomedical Circuits and Systems Conference (BioCAS)*. Cleveland, OH: IEEE, 1–4.

Basmajian, J. V. (Aug. 1963). Control and Training of Individual Motor Units. *Science* 141. Publisher: American Association for the Advancement of Science:440–441.

Basmajian, J. V. and Stecko, G. (Sept. 1962). A new bipolar electrode for electromyography. *Journal of Applied Physiology* 17. Publisher: American Physiological Society:849–849.

Bawa, P. and Murnaghan, C. (Oct. 2009). Motor Unit Rotation in a Variety of Human Muscles. *Journal of Neurophysiology* 102. Publisher: American Physiological Society:2265–2272.

Bean, B. P. and Koester, J. D. (May 2021). Propagated signaling: the action potential. *Principles of Neural Science*. 6th ed. McGraw-Hill, 254–272.

Belouchrani, A., Abed-Meraim, K., Cardoso, J.-F., and Moulines, E. (Feb. 1997). A blind source separation technique using second-order statistics. en. *IEEE Transactions on Signal Processing* 45:434–444.

Benabid, A. L., Costecalde, T., Eliseyev, A., Charvet, G., Verney, A., Karakas, S., Foerster, M., Lambert, A., Morinière, B., Abroug, N., Schaeffer, M.-C., Moly, A., Sauter-Starace, F., Ratel, D., Moro, C., Torres-Martinez, N., Langar, L., Oddoux, M., Polosan, M., Pezzani, S., Auboiroux, V., Aksenova, T., Mestais, C., and Chabardes, S. (Dec. 2019). An exoskeleton controlled by an epidural wireless brain–machine interface in a tetraplegic patient: a proof-of-concept demonstration. *The Lancet Neurology* 18:1112–1122.

Betts, J. G., Desaix, P., Johnson, E., Johnson, J. E., Korol, O., Kruse, D. H., Poe, B., Wise, J. A., Womble, M., and Young, K. A. (Apr. 2022). Muscles of the Pectoral Girdle and Upper Limbs. English. *Anatomy and Physiology*. 2nd ed. OpenStax.

Botros, F. S., Phinyomark, A., and Scheme, E. J. (Jan. 2022). Electromyography-Based Gesture Recognition: Is It Time to Change Focus From the Forearm to the Wrist? en. *IEEE Transactions on Industrial Informatics* 18:174–184.

Bouton, C. E., Shaikhouni, A., Annetta, N. V., Bockbrader, M. A., Friedenberg, D. A., Nielson, D. M., Sharma, G., Sederberg, P. B., Glenn, B. C., Mysiw, W. J., Morgan, A. G., Deogaonkar,

M., and Rezai, A. R. (May 2016). Restoring cortical control of functional movement in a human with quadriplegia. en. *Nature* 533:247–250.

Bräcklein, M., Barsakcioglu, D. Y., Vecchio, A. D., Ibáñez, J., and Farina, D. (Apr. 2022a). Reading and Modulating Cortical β Bursts from Motor Unit Spiking Activity. en. *Journal of Neuroscience* 42:3611–3621.

Bräcklein, M., Barsakcioglu, D. Y., Ibáñez, J., Eden, J., Burdet, E., Mehring, C., and Farina, D. (June 2022b). The control and training of single motor units in isometric tasks are constrained by a common input signal. *eLife* 11. Ed. by J. A. Pruszynski, T. Moore, and A. Fuglevand:e72871.

Bräcklein, M., Ibáñez, J., Barsakcioglu, D. Y., and Farina, D. (Feb. 2021). Towards human motor augmentation by voluntary decoupling beta activity in the neural drive to muscle and force production. en. *Journal of Neural Engineering* 18:016001.

Caillet, A. H., Avrillon, S., Kundu, A., Yu, T., Phillips, A. T. M., Modenese, L., and Farina, D. (Aug. 2023). *Larger and denser: an optimal design for surface grids of EMG electrodes to identify greater and more representative samples of motor units*. en. Pages: 2023.02.18.529050 Section: New Results.

Caillet, A. H., Phillips, A. T. M., Farina, D., and Modenese, L. (Sept. 2022a). Estimation of the firing behaviour of a complete motoneuron pool by combining electromyography signal decomposition and realistic motoneuron modelling. en. *PLOS Computational Biology* 18:e1010556.

Caillet, A. H., Phillips, A. T., Farina, D., and Modenese, L. (July 2022b). Mathematical relationships between spinal motoneuron properties. *eLife* 11. Ed. by H. Merchant, B. G. Shinn-Cunningham, R. K. Powers, and L. Abdala Elias:e76489.

Campbell, E., Phinyomark, A., and Scheme, E. (Jan. 2020). Current Trends and Confounding Factors in Myoelectric Control: Limb Position and Contraction Intensity. en. *Sensors* 20. Number: 6 Publisher: Multidisciplinary Digital Publishing Institute:1613.

Cardoso, J.-F. and Laheld, B. (Dec. 1996). Equivariant adaptive source separation. *IEEE Transactions on Signal Processing* 44:3017–3030.

Carpentier, A., Duchateau, J., and Hainaut, K. (2001). Motor unit behaviour and contractile changes during fatigue in the human first dorsal interosseus. en. *The Journal of Physiology* 534:903–912.

Chen, C., Chai, G., Guo, W., Sheng, X., Farina, D., and Zhu, X. (Jan. 2019). Prediction of finger kinematics from discharge timings of motor units: implications for intuitive control of myoelectric prostheses. en. *Journal of Neural Engineering* 16. Publisher: IOP Publishing:026005.

Chen, C., Ma, S., Sheng, X., Farina, D., and Zhu, X. (Dec. 2020a). Adaptive Real-Time Identification of Motor Unit Discharges From Non-Stationary High-Density Surface Electromyographic Signals. *IEEE Transactions on Biomedical Engineering* 67:3501–3509.

Chen, C., Yu, Y., Ma, S., Sheng, X., Lin, C., Farina, D., and Zhu, X. (Jan. 2020b). Hand gesture recognition based on motor unit spike trains decoded from high-density electromyography. en. *Biomedical Signal Processing and Control* 55:101637.

Chen, C., Yu, Y., Sheng, X., Farina, D., and Zhu, X. (Apr. 2021). Simultaneous and proportional control of wrist and hand movements by decoding motor unit discharges in real time. en. *Journal of Neural Engineering* 18. Publisher: IOP Publishing:056010.

Chen, C., Yu, Y., Sheng, X., Meng, J., and Zhu, X. (July 2023). Real-Time Hand Gesture Recognition by Decoding Motor Unit Discharges Across Multiple Motor Tasks From Surface Electromyography. *IEEE Transactions on Biomedical Engineering* 70. Conference Name: IEEE Transactions on Biomedical Engineering:2058–2068.

Chen, C., Yu, Y., Sheng, X., and Zhu, X. (July 2020c). Analysis of motor unit activities during multiple motor tasks by real-time EMG decomposition: perspective for myoelectric control. en. *2020 42nd Annual International Conference of the IEEE Engineering in Medicine & Biology Society (EMBC)*. Montreal, QC, Canada: IEEE, 4791–4794.

Chen, C., Yu, Y., Sheng, X., and Zhu, X. (May 2022). Non-Invasive Analysis of Motor Unit Activation During Simultaneous and Continuous Wrist Movements. *IEEE Journal of Biomedical and Health Informatics* 26. Conference Name: IEEE Journal of Biomedical and Health Informatics:2106–2115.

Chen, M., Holobar, A., Zhang, X., and Zhou, P. (2016a). Progressive FastICA Peel-Off and Convolution Kernel Compensation Demonstrate High Agreement for High Density Surface EMG Decomposition. *Neural Plasticity* 2016:3489540.

Chen, M., Zhang, X., Chen, X., and Zhou, P. (Jan. 2018). Automatic Implementation of Progressive FastICA Peel-Off for High Density Surface EMG Decomposition. en. *IEEE Transactions on Neural Systems and Rehabilitation Engineering* 26:144–152.

Chen, M. and Zhou, P. (Jan. 2016b). A Novel Framework Based on FastICA for High Density Surface EMG Decomposition. en. *IEEE Transactions on Neural Systems and Rehabilitation Engineering* 24:117–127.

Cho, J. (June 2019). Current Status and Prospects of Health-Related Sensing Technology in Wearable Devices. en. *Journal of Healthcare Engineering* 2019:e3924508.

Cipriani, C., Antfolk, C., Controzzi, M., Lundborg, G., Rosen, B., Carrozza, M. C., and Sebelius, F. (June 2011). Online Myoelectric Control of a Dexterous Hand Prosthesis by Transradial Amputees. en. *IEEE Transactions on Neural Systems and Rehabilitation Engineering* 19:260–270.

Clarac, F. and Barbara, J.-G. (Aug. 2011). The emergence of the "motoneuron concept": From the early 19th C to the beginning of the 20th C. *Brain Research*. Paths of Discovery in Motoneuron Neurobiology 1409:23–41.

Clarke, A. K., Atashzar, S. F., Vecchio, A. D., Barsakcioglu, D., Muceli, S., Bentley, P., Urh, F., Holobar, A., and Farina, D. (Feb. 2021). Deep Learning for Robust Decomposition of High-Density Surface EMG Signals. en. *IEEE Transactions on Biomedical Engineering* 68:526–534.

Collinger, J. L., Wodlinger, B., Downey, J. E., Wang, W., Tyler-Kabara, E. C., Weber, D. J., McMorland, A. J., Velliste, M., Boninger, M. L., and Schwartz, A. B. (Feb. 2013). High-performance neuroprosthetic control by an individual with tetraplegia. en. *The Lancet* 381:557–564.

Dai, C., Cao, Y., and Hu, X. (June 2019a). Prediction of Individual Finger Forces Based on Decoded Motoneuron Activities. en. *Annals of Biomedical Engineering* 47:1357–1368.

Dai, C. and Hu, X. (Feb. 2019b). Extracting and Classifying Spatial Muscle Activation Patterns in Forearm Flexor Muscles Using High-Density Electromyogram Recordings. eng. *International Journal of Neural Systems* 29:1850025.

Dai, C. and Hu, X. (Mar. 2020). Finger Joint Angle Estimation Based on Motoneuron Discharge Activities. en. *IEEE Journal of Biomedical and Health Informatics* 24:760–767.

De Luca, C. J., LeFever, R. S., McCue, M. P., and Xenakis, A. P. (1982a). Behaviour of human motor units in different muscles during linearly varying contractions. en. *The Journal of Physiology* 329:113–128.

De Luca, C. J., LeFever, R. S., McCue, M. P., and Xenakis, A. P. (1982b). Control scheme governing concurrently active human motor units during voluntary contractions. en. *The Journal of Physiology* 329:129–142.

De Luca, C. J. (June 1979). Physiology and Mathematics of Myoelectric Signals. *IEEE Transactions on Biomedical Engineering* BME-26:313–325.

De Luca, C. J., Adam, A., Wotiz, R., Gilmore, L. D., and Nawab, S. H. (Sept. 2006). Decomposition of Surface EMG Signals. *Journal of Neurophysiology* 96:1646–1657.

De Luca, C. J. and Erim, Z (1994). Common drive of motor units in regulation of muscle force. en. *Trends in Neurosciences* 17:299–305.

Del Vecchio, A. and Farina, D. (Dec. 2019a). Interfacing the neural output of the spinal cord: robust and reliable longitudinal identification of motor neurons in humans. en. *Journal of Neural Engineering* 17:016003.

Del Vecchio, A., Germer, C. M., Elias, L. A., Fu, Q., Fine, J., Santello, M., and Farina, D. (2019b). The human central nervous system transmits common synaptic inputs to distinct motor neuron pools during non-synergistic digit actions. en. *The Journal of Physiology* 597:5935–5948.

Del Vecchio, A., Holobar, A., Falla, D., Felici, F., Enoka, R. M., and Farina, D. (Aug. 2020a). Tutorial: Analysis of motor unit discharge characteristics from high-density surface EMG signals. *Journal of Electromyography and Kinesiology* 53:102426.

Del Vecchio, A., Sylos-Labini, F., Mondì, V., Paolillo, P., Ivanenko, Y., Lacquaniti, F., and Farina, D. (2020b). Spinal motoneurons of the human newborn are highly synchronized during leg movements. *Science Advances* 6:1–10.

Del Vecchio, A., Úbeda, A., Sartori, M., Azorín, J. M., Felici, F., and Farina, D. (Nov. 2018). Central nervous system modulates the neuromechanical delay in a broad range for the control of muscle force. *Journal of Applied Physiology* 125:1404–1410.

Deng, X., Yu, Z. L., Lin, C., Gu, Z., and Li, Y. (Jan. 2020). A Bayesian Shared Control Approach for Wheelchair Robot With Brain Machine Interface. en. *IEEE Transactions on Neural Systems and Rehabilitation Engineering* 28:328–338.

Desmedt, J. E. and Gidaux, E. (Nov. 1981). Spinal Motoneuron Recruitment in Man: Rank Deordering with Direction But Not with Speed of Voluntary Movement. en. *Science* 214:933–936.

Desmedt, J. E. and Godaux, E. (1979). Voluntary motor commands in human ballistic movements. en. *Annals of Neurology* 5:415–421.

Desmedt, J. E. and Godaux, E. (1978). Ballistic contractions in fast or slow human muscles; discharge patterns of single motor units. en. *The Journal of Physiology* 285:185–196.

Dimitrova, N. A. and Dimitrov, G. V. (Feb. 2003). Interpretation of EMG changes with fatigue: facts, pitfalls, and fallacies. *Journal of Electromyography and Kinesiology* 13:13–36.

Dimitrova, N. A., Dimitrov, G. V., and Nikitin, O. A. (Aug. 2002). Neither high-pass filtering nor mathematical differentiation of the EMG signals can considerably reduce cross-talk. *Journal of Electromyography and Kinesiology* 12:235–246.

Dimitrova, N. and Dimitrov, G. (Apr. 2006). Electromyography (EMG) Modeling. *Wiley Encyclopedia of Biomedical Engineering*.

Duchateau, J. and Enoka, R. M. (2008). Neural control of shortening and lengthening contractions: influence of task constraints. en. *The Journal of Physiology* 586:5853–5864.

Duchateau, J. and Enoka, R. M. (Jan. 2022). Distribution of motor unit properties across human muscles. *Journal of Applied Physiology* 132:1–13.

Dumitru, D. (2000). Physiologic basis of potentials recorded in electromyography. en. *Muscle & Nerve* 23:1667–1685.

Dumitru, D. and King, J. C. (1991). Far-field potentials in muscle. en. *Muscle & Nerve* 14:981–989.

Dumitru, D. and King, J. C. (Sept. 1993). Far-field potential production by quadrupole generators in cylindrical volume conductors. *Electroencephalography and Clinical Neurophysiology/Evoked Potentials Section* 88:421–431.

Dumitru, D., King, J. C., and Rogers, W. E. (1999). Motor unit action potential components and physiologic duration. en. *Muscle & Nerve* 22:733–741.

Eden, J., Bräcklein, M., Ibáñez, J., Barsakcioglu, D. Y., Di Pino, G., Farina, D., Burdet, E., and Mehring, C. (Mar. 2022). Principles of human movement augmentation and the challenges in making it a reality. en. *Nature Communications* 13. Number: 1 Publisher: Nature Publishing Group:1345.

Enoka, R. M. and Duchateau, J. (Apr. 2016). Physiology of Muscle Activation and Force Generation. en. *Surface Electromyography : Physiology, Engineering, and Applications*. Ed. by R. Merletti and D. Farina. 1st ed. Chapter 1. Wiley, 1–29.

Enoka, R. M. (June 2019). Physiological validation of the decomposition of surface EMG signals. *Journal of Electromyography and Kinesiology* 46:70–83.

Enoka, R. M. and Pearson, K. G. (2012). The Motor Unit and Muscle Action. *Principles of Neural Science*. 5th ed. McGraw-Hill, 768–789.

Enoka, R. M., Trayanova, N., Laouris, Y., Bevan, L., Reinking, R. M., and Stuart, D. G. (1992). Fatigue-related changes in motor unit action potentials of adult cats. en. *Muscle & Nerve* 15:138–150.

Fang, Y.-M. and Chang, C.-C. (Mar. 2016). Users' psychological perception and perceived readability of wearable devices for elderly people. *Behaviour & Information Technology* 35:225–232.

Farina, D., Fortunato, E., and Merletti, R. (Mar. 2000). Noninvasive estimation of motor unit conduction velocity distribution using linear electrode arrays. en. *IEEE Transactions on Biomedical Engineering* 47:380–388.

Farina, D. and Merletti, R. (June 2001a). A novel approach for precise simulation of the EMG signal detected by surface electrodes. *IEEE Transactions on Biomedical Engineering* 48. Conference Name: IEEE Transactions on Biomedical Engineering:637–646.

Farina, D., Mesin, L., Martina, S., and Merletti, R. (Mar. 2004). A Surface EMG Generation Model With Multilayer Cylindrical Description of the Volume Conductor. en. *IEEE Transactions on Biomedical Engineering* 51:415–426.

Farina, D., Muhammad, W., Fortunato, E., Meste, O., Merletti, R., and Rix, H. (Mar. 2001b). Estimation of single motor unit conduction velocity from surface electromyogram signals detected with linear electrode arrays. en. *Medical and Biological Engineering and Computing* 39:225–236.

Farina, D. and Aszmann, O. (2014a). Bionic Limbs: Clinical Reality and Academic Promises. *Science Translational Medicine* 6:257ps12–257ps12.

Farina, D., Cescon, C., and Merletti, R. (June 2002a). Influence of anatomical, physical, and detection-system parameters on surface EMG. en. *Biological Cybernetics* 86:445–456.

Farina, D. and Holobar, A. (Feb. 2016a). Characterization of Human Motor Units From Surface EMG Decomposition. en. *Proceedings of the IEEE* 104:353–373.

Farina, D., Jiang, N., Rehbaum, H., Holobar, A., Graimann, B., Dietl, H., and Aszmann, O. C. (July 2014b). The Extraction of Neural Information from the Surface EMG for the Control of Upper-Limb Prostheses: Emerging Avenues and Challenges. en. *IEEE Transactions on Neural Systems and Rehabilitation Engineering* 22:797–809.

Farina, D., Merletti, R., Indino, B., Nazzaro, M., and Pozzo, M. (2002b). Surface EMG crosstalk between knee extensor muscles: Experimental and model results. en. *Muscle & Nerve* 26:681–695.

Farina, D. and Negro, F. (Jan. 2015). Common Synaptic Input to Motor Neurons, Motor Unit Synchronization, and Force Control. en-US. *Exercise and Sport Sciences Reviews* 43:23.

Farina, D., Negro, F., and Dideriksen, J. L. (2014c). The effective neural drive to muscles is the common synaptic input to motor neurons. en. *The Journal of Physiology* 592:3427–3441.

Farina, D., Negro, F., Gazzoni, M., and Enoka, R. M. (Sept. 2008). Detecting the Unique Representation of Motor-Unit Action Potentials in the Surface Electromyogram. *Journal of Neurophysiology* 100:1223–1233.

Farina, D. and Rainoldi, A. (July 1999). Compensation of the effect of sub-cutaneous tissue layers on surface EMG: a simulation study. *Medical Engineering & Physics* 21:487–497.

Farina, D., Stegeman, D. F., and Merletti, R. (Apr. 2016b). Biophysics of the Generation of EMG Signals. en. *Surface Electromyography : Physiology, Engineering, and Applications*. Ed. by R. Merletti and D. Farina. 1st ed. Wiley, 1–24.

Farina, D., Vujaklija, I., Brånemark, R., Bull, A. M. J., Dietl, H., Graimann, B., Hargrove, L. J., Hoffmann, K.-P., Huang, H., Ingvarsson, T., Janusson, H. B., Kristjánsson, K., Kuiken, T., Micera, S., Stieglitz, T., Sturma, A., Tyler, D., Weir, R. F. F., and Aszmann, O. C. (Apr. 2023). Toward higher-performance bionic limbs for wider clinical use. en. *Nature Biomedical Engineering* 7:473–485.

Farrell, T. R. and Weir, R. F. (Mar. 2007). The Optimal Controller Delay for Myoelectric Prostheses. en. *IEEE Transactions on Neural Systems and Rehabilitation Engineering* 15:111–118.

Fischbach, G. D. and Siegelbaum, S. A. (May 2021). Directly gated transmission: the nerve-muscle synapse. *Principles of Neural Science*. 6th ed. McGraw-Hill, 254–272.

Formento, E., Botros, P., and Carmena, J. M. (Nov. 2021). Skilled independent control of individual motor units via a non-invasive neuromuscular–machine interface. en. *Journal of Neural Engineering* 18:066019.

Francic, A. and Holobar, A. (2021). On the Reuse of Motor Unit Filters in High Density Surface Electromyograms Recorded at Different Contraction Levels. en. *IEEE Access* 9:115227–115236.

Freund, H. J. (Apr. 1983). Motor unit and muscle activity in voluntary motor control. *Physiological Reviews* 63:387–436.

Freund, H. J., Budingen, H. J., and Dietz, V. (July 1975). Activity of single motor units from human forearm muscles during voluntary isometric contractions. *Journal of Neurophysiology* 38. Publisher: American Physiological Society:933–946.

Fuglevand, A. J., Winter, D. A., and Patla, A. E. (Dec. 1993). Models of recruitment and rate coding organization in motor-unit pools. *Journal of Neurophysiology* 70:2470–2488.

Fukashiro, S., Hay, D. C., and Nagano, A. (May 2006). Biomechanical Behavior of Muscle-Tendon Complex during Dynamic Human Movements. en. *Journal of Applied Biomechanics* 22:131–147.

Gates, D. H., Walters, L. S., Cowley, J., Wilken, J. M., and Resnik, L. (2016). Range of Motion Requirements for Upper-Limb Activities of Daily Living. *American Journal of Occupational Therapy* 70:7001350010p1–7001350010p10.

Gest, T. R. (Jan. 2020). The Upper Limb. en. *Lippincott Atlas of Anatomy*. 2nd ed. Wolters Kluwer.

Glaser, V. and Holobar, A. (Jan. 2019). Motor Unit Identification From High-Density Surface Electromyograms in Repeated Dynamic Muscle Contractions. en. *IEEE Transactions on Neural Systems and Rehabilitation Engineering* 27:66–75.

Glaser, V., Holobar, A., and Zazula, D. (Nov. 2013). Real-Time Motor Unit Identification From High-Density Surface EMG. en. *IEEE Transactions on Neural Systems and Rehabilitation Engineering* 21:949–958.

Goislard de Monsabert, B., Hauraix, H., Caumes, M., Herbaut, A., Berton, E., and Vigouroux, L. (Oct. 2020). Modelling force-length-activation relationships of wrist and finger extensor muscles. en. *Medical & Biological Engineering & Computing* 58:2531–2549.

Goodlich, B. I., Del Vecchio, A., and Kavanagh, J. J. (Aug. 2023). Motor unit tracking using blind source separation filters and waveform cross-correlations: reliability under physiological and pharmacological conditions. *Journal of Applied Physiology* 135:362–374.

Griffiths, R. I. (1991). Shortening of muscle fibres during stretch of the active cat medial gastrocnemius muscle: the role of tendon compliance. en. *The Journal of Physiology* 436:219–236.

Grison, A., Clarke, A. K., Muceli, S., Ibanez Pereda, J., Kundu, A., and Farina, D. (Nov. 2023). *A Particle Swarm Optimised Independence Estimator for Blind Source Separation of Neurophysiological Time Series*. en.

Hauraix, H., de Monsabert, B. G., Herbaut, A., Berton, E., and Vigouroux, L. (2018). Force-Length Relationship Modeling of Wrist and Finger Flexor Muscles. *Medicine and Science in Sports and Exercise* 50. Publisher: American College of Sports Medicine (ACSM):2311–2321.

Heckman, C. and Enoka, R. M. (2004). Physiology of the motor neuron and the motor unit. en. *Handbook of Clinical Neurophysiology*. Vol. 4. Elsevier, 119–147.

Heckman, C. and Enoka, R. M. (2012). Motor unit. *Comprehensive physiology*. Publisher: John Wiley & Sons, Inc.:2629–2682.

Helmholtz, H. (Jan. 1853). Ueber einige Gesetze der Vertheilung elektrischer Ströme in körperlichen Leitern, mit Anwendung auf die thierisch-elektrischen Versuche (Schluss.) en. *Annalen der Physik* 165:353–377.

Henneman, E. (Mar. 1985). The size-principle: a deterministic output emerges from a set of probabilistic connections. *Journal of Experimental Biology* 115:105–112.

Henneman, E. (Dec. 1957). Relation between Size of Neurons and Their Susceptibility to Discharge. en. *Science* 126:1345–1347.

Hinson, R. M., Berman, J., Filer, W., Kamper, D., Hu, X., and Huang, H. (2023a). Offline Evaluation Matters: Investigation of the Influence of Offline Performance on Real-Time Operation of Electromyography-Based Neural-Machine Interfaces. en. *IEEE Transactions on Neural Systems and Rehabilitation Engineering* 31:680–689.

Hinson, R. M., Berman, J., Lee, I.-C., Filer, W. G., and Huang, H. (2023b). Offline Evaluation Matters: Investigation of the Influence of Offline Performance of EMG-Based Neural-Machine Interfaces on User Adaptation, Cognitive Load, and Physical Efforts in a Real-Time Applica-

tion. *IEEE Transactions on Neural Systems and Rehabilitation Engineering* 31. Conference Name: IEEE Transactions on Neural Systems and Rehabilitation Engineering:3055–3063.

Hochberg, L. R., Serruya, M. D., Friehs, G. M., Mukand, J. A., Saleh, M., Caplan, A. H., Branner, A., Chen, D., Penn, R. D., and Donoghue, J. P. (July 2006). Neuronal ensemble control of prosthetic devices by a human with tetraplegia. en. *Nature* 442. Number: 7099 Publisher: Nature Publishing Group:164–171.

Hof, A. L., Geelen, B. A., and Van den Berg, J. (Jan. 1983). Calf muscle moment, work and efficiency in level walking; Role of series elasticity. *Journal of Biomechanics* 16:523–537.

Holobar, A. and Farina, D. (July 2021). Noninvasive Neural Interfacing With Wearable Muscle Sensors: Combining Convolutive Blind Source Separation Methods and Deep Learning Techniques for Neural Decoding. *IEEE Signal Processing Magazine* 38. Conference Name: IEEE Signal Processing Magazine:103–118.

Holobar, A., Farina, D., Gazzoni, M., Merletti, R., and Zazula, D. (Mar. 2009). Estimating motor unit discharge patterns from high-density surface electromyogram. *Clinical Neurophysiology* 120:551–562.

Holobar, A., Minetto, M. A., and Farina, D. (Jan. 2014). Accurate identification of motor unit discharge patterns from high-density surface EMG and validation with a novel signal-based performance metric. en. *Journal of Neural Engineering* 11:016008.

Holobar, A., Minetto, M. A., Botter, A., Negro, F., and Farina, D. (June 2010). Experimental Analysis of Accuracy in the Identification of Motor Unit Spike Trains From High-Density Surface EMG. *IEEE Transactions on Neural Systems and Rehabilitation Engineering* 18:221–229.

Holobar, A. and Zazula, D. (July 2004). Correlation-based decomposition of surface electromyograms at low contraction forces. en. *Medical and Biological Engineering and Computing* 42:487–495.

Holobar, A. and Zazula, D. (2007a). Gradient Convolution Kernel Compensation Applied to Surface Electromyograms. en. *Independent Component Analysis and Signal Separation*. Ed. by M. E. Davies, C. J. James, S. A. Abdallah, and M. D. Plumbley. Lecture Notes in Computer Science. Berlin, Heidelberg: Springer, 617–624.

Holobar, A. and Zazula, D. (Sept. 2007b). Multichannel Blind Source Separation Using Convolution Kernel Compensation. *IEEE Transactions on Signal Processing* 55:4487–4496.

Hounsgaard, J. (Mar. 2017). Motor Neurons. en. *Comprehensive Physiology*. Ed. by R. Terjung. 1st ed. Wiley, 463–484.

Hug, F., Avrillon, S., Del Vecchio, A., Casolo, A., Ibanez, J., Nuccio, S., Rossato, J., Holobar, A., and Farina, D. (June 2021). Analysis of motor unit spike trains estimated from high-density surface electromyography is highly reliable across operators. *Journal of Electromyography and Kinesiology* 58:102548.

Hug, F., Avrillon, S., Ibáñez, J., and Farina, D. (2023). Common synaptic input, synergies and size principle: Control of spinal motor neurons for movement generation. en. *The Journal of Physiology* 601:11–20.

Huxley, A. F. and Niedergerke, R. (May 1954). Structural Changes in Muscle During Contraction: Interference Microscopy of Living Muscle Fibres. en. *Nature* 173. Number: 4412 Publisher: Nature Publishing Group:971–973.

Hyvarinen, A. (May 1999). Fast and robust fixed-point algorithms for independent component analysis. *IEEE Transactions on Neural Networks* 10. Conference Name: IEEE Transactions on Neural Networks:626–634.

Hyvärinen, A., Karhunen, J., and Oja, E. (2001a). Convolutive Mixtures and Blind Deconvolution. en. *Independent Component Analysis*. Section: 19. John Wiley & Sons, Ltd, 355–370.

Hyvärinen, A., Karhunen, J., and Oja, E. (2001b). ICA by Maximization of Nongaussianity. en. *Independent Component Analysis*. Section: 8. John Wiley & Sons, Ltd, 165–202.

Hyvärinen, A., Karhunen, J., and Oja, E. (2001c). ICA by Maximum Likelihood Estimation. en. *Independent Component Analysis*. Section: 9. John Wiley & Sons, Ltd, 203–219.

Hyvärinen, A., Karhunen, J., and Oja, E. (2001d). ICA by Minimization of Mutual Information. en. *Independent Component Analysis*. Section: 10. John Wiley & Sons, Ltd, 221–227.

Hyvärinen, A., Karhunen, J., and Oja, E. (2001e). What is Independent Component Analysis? en. *Independent Component Analysis*. Section: 7. John Wiley & Sons, Ltd, 145–164.

Hyvärinen, A. and Oja, E. (July 1997). A Fast Fixed-Point Algorithm for Independent Component Analysis. *Neural Computation* 9:1483–1492.

Ito, M., Kawakami, Y., Ichinose, Y., Fukashiro, S., and Fukunaga, T. (Oct. 1998). Nonisometric behavior of fascicles during isometric contractions of a human muscle. *Journal of Applied Physiology* 85. Publisher: American Physiological Society:1230–1235.

Jackson, A. and Zimmermann, J. B. (Dec. 2012). Neural interfaces for the brain and spinal cord—restoring motor function. en. *Nature Reviews Neurology* 8:690–699.

Jiang, S., Lv, B., Guo, W., Zhang, C., Wang, H., Sheng, X., and Shull, P. B. (Aug. 2018). Feasibility of Wrist-Worn, Real-Time Hand, and Surface Gesture Recognition via sEMG and IMU Sensing. en. *IEEE Transactions on Industrial Informatics* 14:3376–3385.

Jiang, X., Merhi, L.-K., Xiao, Z. G., and Menon, C. (Mar. 2017). Exploration of Force Myography and surface Electromyography in hand gesture classification. *Medical Engineering & Physics* 41:63–73.

Jiang, X., Liu, X., Fan, J., Ye, X., Dai, C., Clancy, E. A., Akay, M., and Chen, W. (2021). Open Access Dataset, Toolbox and Benchmark Processing Results of High-Density Surface Electromyogram Recordings. en. *IEEE Transactions on Neural Systems and Rehabilitation Engineering* 29:1035–1046.

Kapelner, T., Negro, F., Aszmann, O. C., and Farina, D. (Jan. 2018). Decoding Motor Unit Activity From Forearm Muscles: Perspectives for Myoelectric Control. en. *IEEE Transactions on Neural Systems and Rehabilitation Engineering* 26:244–251.

Kapelner, T., Sartori, M., Negro, F., and Farina, D. (Apr. 2020). Neuro-Musculoskeletal Mapping for Man-Machine Interfacing. en. *Scientific Reports* 10. Number: 1 Publisher: Nature Publishing Group:5834.

Kapelner, T., Vujaklija, I., Jiang, N., Negro, F., Aszmann, O. C., Principe, J., and Farina, D. (Apr. 2019). Predicting wrist kinematics from motor unit discharge timings for the control of active prostheses. *Journal of NeuroEngineering and Rehabilitation* 16:47.

Karray, F., Alemzadeh, M., Saleh, J. A., and Arab, M. N. (Jan. 2008). Human-Computer Interaction: Overview on State of the Art. en. *International Journal on Smart Sensing and Intelligent Systems* 1:137–159.

Katz, B. and Miledi, R. (Jan. 1997). The measurement of synaptic delay, and the time course of acetylcholine release at the neuromuscular junction. *Proceedings of the Royal Society of London. Series B. Biological Sciences* 161. Publisher: Royal Society:483–495.

Kawakami, Y. and Fukunaga, T. (Jan. 2006). New Insights into In Vivo Human Skeletal Muscle Function: en. *Exercise and Sport Sciences Reviews* 34:16–21.

Kawakami, Y., Ichinose, Y., and Fukunaga, T. (Aug. 1998). Architectural and functional features of human triceps surae muscles during contraction. *Journal of Applied Physiology* 85. Publisher: American Physiological Society:398–404.

Keenan, K. G., Farina, D., Maluf, K. S., Merletti, R., and Enoka, R. M. (Jan. 2005). Influence of amplitude cancellation on the simulated surface electromyogram. *Journal of Applied Physiology* 98. Publisher: American Physiological Society:120–131.

Keenan, K. G., Farina, D., Merletti, R., and Enoka, R. M. (June 2006). Amplitude cancellation reduces the size of motor unit potentials averaged from the surface EMG. *Journal of Applied Physiology* 100:1928–1937.

Khushaba, R. N., Kodagoda, S., Takruri, M., and Dissanayake, G. (Sept. 2012). Toward improved control of prosthetic fingers using surface electromyogram (EMG) signals. *Expert Systems with Applications* 39:10731–10738.

Koester, J. D. and Siegelbaum, S. A. (May 2021). Membrane potential and the passive electrical properties of the neuron. *Principles of Neural Science*. 6th ed. McGraw-Hill, 273–300.

Komi, P. V. (2003). Stretch-Shortening Cycle. en. *Strength and Power in Sport*. Section: 10 _eprint: https://onlinelibrary.wiley.com/doi/pdf/10.1002/9780470757215.ch10. John Wiley & Sons, Ltd, 184–202.

Kramberger, M. and Holobar, A. (2021). On the Prediction of Motor Unit Filter Changes in Blind Source Separation of High-Density Surface Electromyograms During Dynamic Muscle Contractions. en. *IEEE Access* 9:103533–103540.

Li, X., Zhang, X., Tang, X., Chen, M., Chen, X., Chen, X., and Liu, A. (Feb. 2022). Decoding muscle force from individual motor unit activities using a twitch force model and hybrid neural networks. en. *Biomedical Signal Processing and Control* 72:103297.

Liddell, E. G. and Sherrington, C. S. (Jan. 1925). Recruitment and some other features of reflex inhibition. en. *Proceedings of the Royal Society of London. Series B. Biological Sciences* 97:488–518.

Lorach, H., Galvez, A., Spagnolo, V., Martel, F., Karakas, S., Intering, N., Vat, M., Faivre, O., Harte, C., Komi, S., Ravier, J., Collin, T., Coquoz, L., Sakr, I., Baaklini, E., Hernandez-Charpak, S. D., Dumont, G., Buschman, R., Buse, N., Denison, T., Van Nes, I., Asboth, L., Watrin, A., Struber, L., Sauter-Starace, F., Langar, L., Auboiroux, V., Carda, S., Chabardes, S., Aksenova, T., Demesmaeker, R., Charvet, G., Bloch, J., and Courtine, G. (June 2023).

Walking naturally after spinal cord injury using a brain–spine interface. en. *Nature* 618:126–133.

Ma, S., Clarke, A. K., Maksymenko, K., Deslauriers-Gauthier, S., Sheng, X., Zhu, X., and Farina, D. (Oct. 2023a). *Conditional Generative Models for Simulation of EMG During Naturalistic Movements*.

Ma, S., Mendez Guerra, I., Caillet, A. H., Zhao, J., Clarke, A. K., Maksymenko, K., Deslauriers-Gauthier, S., Sheng, X., Zhu, X., and Farina, D. (Oct. 2023b). *NeuroMotion: Open-source Simulator with Neuromechanical and Deep Network Models to Generate Surface EMG signals during Voluntary Movement*. en. preprint.

Maksymenko, K., Clarke, A. K., Mendez Guerra, I., Deslauriers-Gauthier, S., and Farina, D. (Mar. 2023). A myoelectric digital twin for fast and realistic modelling in deep learning. en. *Nature Communications* 14:1600.

Martinez-Valdes, E., Laine, C., Falla, D., Mayer, F., and Farina, D. (June 2016). High-density surface electromyography provides reliable estimates of motor unit behavior. en. *Clinical Neurophysiology* 127:2534–2541.

Martinez-Valdes, E., Negro, F., Laine, C. M., Falla, D., Mayer, F., and Farina, D. (2017). Tracking motor units longitudinally across experimental sessions with high-density surface electromyography. en. *Journal of Physiology* 595:1479–1496.

Martinez-Valdes, E., Enoka, R. M., Holobar, A., McGill, K., Farina, D., Besomi, M., Hug, F., Falla, D., Carson, R. G., Clancy, E. A., Disselhorst-Klug, C., Van Dieën, J. H., Tucker, K., Gandevia, S., Lowery, M., Søgaard, K., Besier, T., Merletti, R., Kiernan, M. C., Rothwell, J. C., Perreault, E., and Hodges, P. W. (Feb. 2023). Consensus for experimental design in electromyography (CEDE) project: Single motor unit matrix. en. *Journal of Electromyography and Kinesiology* 68:102726.

Martini, M. L., Oermann, E. K., Opie, N. L., Panov, F., Oxley, T., and Yaeger, K. (Feb. 2020). Sensor Modalities for Brain-Computer Interface Technology: A Comprehensive Literature Review. en-US. *Neurosurgery* 86:E108.

McFarland, D. C., Binder-Markey, B. I., Nichols, J. A., Wohlman, S. J., De Bruin, M., and Murray, W. M. (May 2023). A Musculoskeletal Model of the Hand and Wrist Capable of Simulating Functional Tasks. en. *IEEE Transactions on Biomedical Engineering* 70:1424–1435.

Mendez, I., Hansen, B. W., Grabow, C. M., Smedegaard, E. J. L., Skogberg, N. B., Uth, X. J., Bruhn, A., Geng, B., and Kamavuako, E. N. (July 2017). Evaluation of the Myo armband for the classification of hand motions. *2017 International Conference on Rehabilitation Robotics (ICORR)*. ISSN: 1945-7901, 1211–1214.

Mendez Guerra, I., Barsakcioglu, D. Y., Vujaklija, I., Wetmore, D. Z., and Farina, D. (Apr. 2022). Far-field electric potentials provide access to the output from the spinal cord from wrist-mounted sensors. en. *Journal of Neural Engineering* 19:026031.

Mendez Guerra, I., Barsakcioglu, D. Y., and Farina, D. (Feb. 2024). *Wearable Neural Interfaces: Real-Time Identification of Motor Neuron Discharges in Dynamic Motor Tasks*. en. Pages: 2024.02.05.578874 Section: New Results.

Merletti, R., Botter, A., and Barone, U. (2016). Detection and Conditioning of Surface EMG Signals. en. *Surface Electromyography : Physiology, Engineering, and Applications*. Section: 3. John Wiley & Sons, Ltd, 1–37.

Merletti, R. and Muceli, S. (Dec. 2019). Tutorial. Surface EMG detection in space and time: Best practices. *Journal of Electromyography and Kinesiology* 49:102363.

Merletti, R., Rainoldi, A., and Farina, D. (Jan. 2001). Surface Electromyography for Noninvasive Characterization of Muscle. en-US. *Exercise and Sport Sciences Reviews* 29:20.

Merletti, R. and Farina, D. (Nov. 2008). Analysis of intramuscular electromyogram signals. *Philosophical Transactions of the Royal Society A: Mathematical, Physical and Engineering Sciences* 367. Publisher: Royal Society:357–368.

Mesin, L., Joubert, M., Hanekom, T., Merletti, R., and Farina, D. (Apr. 2006). A finite element model for describing the effect of muscle shortening on surface EMG. *IEEE Transactions on Biomedical Engineering* 53. Conference Name: IEEE Transactions on Biomedical Engineering:593–600.

Monster, A. W. and Chan, H. (Nov. 1977). Isometric force production by motor units of extensor digitorum communis muscle in man. *Journal of Neurophysiology* 40. Publisher: American Physiological Society:1432–1443.

Moritani, T., Stegeman, D., and Merletti, R. (July 2004). Basic Physiology and Biophysics of EMG Signal Generation. en. *Electromyography*. Ed. by R. Merletti and P. Parker. 1st ed. Wiley, 1–25.

Moritz, C. T., Barry, B. K., Pascoe, M. A., and Enoka, R. M. (May 2005). Discharge Rate Variability Influences the Variation in Force Fluctuations Across the Working Range of a Hand Muscle. *Journal of Neurophysiology* 93. Publisher: American Physiological Society:2449–2459.

Moxon, K. and Foffani, G. (Apr. 2015). Brain-Machine Interfaces beyond Neuroprosthetics. en. *Neuron* 86:55–67.

Muceli, S., Poppendieck, W., Holobar, A., Gandevia, S., Liebetanz, D., and Farina, D. (Nov. 2022). Blind identification of the spinal cord output in humans with high-density electrode arrays implanted in muscles. *Science Advances* 8. Publisher: American Association for the Advancement of Science:eabo5040.

Nawab, S. H., Chang, S.-S., and De Luca, C. J. (Oct. 2010). High-yield decomposition of surface EMG signals. *Clinical Neurophysiology* 121:1602–1615.

Nawfel, J. L., Englehart, K. B., and Scheme, E. J. (2021). A Multi-Variate Approach to Predicting Myoelectric Control Usability. en. *IEEE Transactions on Neural Systems and Rehabilitation Engineering* 29:1312–1327.

Negro, F., Holobar, A., and Farina, D. (2009). Fluctuations in isometric muscle force can be described by one linear projection of low-frequency components of motor unit discharge rates. en. *The Journal of Physiology* 587:5925–5938.

Negro, F., Muceli, S., Castronovo, A. M., Holobar, A., and Farina, D. (Feb. 2016a). Multi-channel intramuscular and surface EMG decomposition by convolutive blind source separation. en. *Journal of Neural Engineering* 13:026027.

Negro, F., Yavuz, U., and Farina, D. (2016b). The human motor neuron pools receive a dominant slow-varying common synaptic input. en. *The Journal of Physiology* 594:5491–5505.

Nunez, P. L. and Srinivasan, R. (2006). *Electric fields of the brain: the neurophysics of EEG*. en. Second edition. New York Oxford: Oxford University Press.

Oliveira, A. S. and Negro, F. (June 2021). Neural control of matched motor units during muscle shortening and lengthening at increasing velocities. *Journal of Applied Physiology* 130. Publisher: American Physiological Society:1798–1813.

Oya, T., Riek, S., and Cresswell, A. G. (2009). Recruitment and rate coding organisation for soleus motor units across entire range of voluntary isometric plantar flexions. en. *The Journal of Physiology* 587:4737–4748.

Pasquet, B., Carpentier, A., and Duchateau, J. (2006). Specific modulation of motor unit discharge for a similar change in fascicle length during shortening and lengthening contractions in humans. en. *The Journal of Physiology* 577:753–765.

Person, R. S and Kudina, L. P (May 1972). Discharge frequency and discharge pattern of human motor units during voluntary contraction of muscle. *Electroencephalography and Clinical Neurophysiology* 32:471–483.

Phinyomark, A., Campbell, E., and Scheme, E. (2020). Surface Electromyography (EMG) Signal Processing, Classification, and Practical Considerations. en. *Biomedical Signal Processing: Advances in Theory, Algorithms and Applications*. Ed. by G. Naik. Series in BioEngineering. Singapore: Springer, 3–29.

Phinyomark, A., Phukpattaranont, P., and Limsakul, C. (June 2012). Feature reduction and selection for EMG signal classification. *Expert Systems with Applications* 39:7420–7431.

Powers, J. D., Malingen, S. A., Regnier, M., and Daniel, T. L. (May 2021). The Sliding Filament Theory Since Andrew Huxley: Multiscale and Multidisciplinary Muscle Research. en. *Annual Review of Biophysics* 50:373–400.

Quiroga, R. Q., Nadasdy, Z., and Ben-Shaul, Y. (Aug. 2004). Unsupervised Spike Detection and Sorting with Wavelets and Superparamagnetic Clustering. *Neural Computation* 16:1661–1687.

Raisamo, R., Rakkolainen, I., Majaranta, P., Salminen, K., Rantala, J., and Farooq, A. (Nov. 2019). Human augmentation: Past, present and future. *International Journal of Human-Computer Studies*. 50 years of the International Journal of Human-Computer Studies. Reflections on the past, present and future of human-centred technologies 131:131–143.

Reality Labs, C.-l., Sussillo, D., Kaifosh, P., and Reardon, T. (Feb. 2024). *A generic noninvasive neuromotor interface for human-computer interaction*. en. Pages: 2024.02.23.581779 Section: New Results.

Rodriguez-Falces, J. (Mar. 2015). Understanding the electrical behavior of the action potential in terms of elementary electrical sources. *Advances in Physiology Education* 39. Publisher: American Physiological Society:15–26.

Rodriguez-Falces, J., Malanda, A., and Navallas, J. (Feb. 2022). Effects of muscle shortening on single-fiber, motor unit, and compound muscle action potentials. en. *Medical & Biological Engineering & Computing* 60:349–364.

Roeleveld, K, Blok, J. H, Stegeman, D. F, and van Oosterom, A (Dec. 1997). Volume conduction models for surface EMG; confrontation with measurements1Roeleveld, Blok and Stegeman participate in the National Institute for Fundamental and Clinical Human Movement Sciences of Nijmegen University and the Vrije Universiteit Amsterdam.1. *Journal of Electromyography and Kinesiology* 7:221–232.

Rossato, J., Avrillon, S., Tucker, K., Farina, D., and Hug, F. (Jan. 2024). *The volitional control of individual motor units is constrained within low-dimensional manifolds by common inputs*. en. Pages: 2024.01.05.573816 Section: New Results.

Ruff, R. L. (2003). Neurophysiology of the Neuromuscular Junction: Overview. en. *Annals of the New York Academy of Sciences* 998:1–10.

Samuel, O. W., Asogbon, M. G., Geng, Y., Al-Timemy, A. H., Pirbhulal, S., Ji, N., Chen, S., Fang, P., and Li, G. (2019). Intelligent EMG Pattern Recognition Control Method for Upper-Limb Multifunctional Prostheses: Advances, Current Challenges, and Future Prospects. en. *IEEE Access* 7:10150–10165.

Schulte, E., Farina, D., Merletti, R., Rau, G., and Disselhorst-Klug, C. (July 2004). Influence of muscle fibre shortening on estimates of conduction velocity and spectral frequencies from surface electromyographic signals. eng. *Medical & Biological Engineering & Computing* 42:477–486.

Schwartz, A. B., Cui, X. T., Weber, D., and Moran, D. W. (Oct. 2006). Brain-Controlled Interfaces: Movement Restoration with Neural Prosthetics. en. *Neuron* 52:205–220.

Shanechi, M. M. (Oct. 2019). Brain–machine interfaces from motor to mood. en. *Nature Neuroscience* 22. Number: 10 Publisher: Nature Publishing Group:1554–1564.

Sherrington, C. S. (Jan. 1925). Remarks on some aspects of reflex inhibition. *Proceedings of the Royal Society of London. Series B, Containing Papers of a Biological Character* 97. Publisher: Royal Society:519–545.

Sorrell, E., Rule, M. E., and O'Leary, T. (May 2021). Brain–Machine Interfaces: Closed-Loop Control in an Adaptive System. en. *Annual Review of Control, Robotics, and Autonomous Systems* 4:167–189.

Stachaczyk, M., Atashzar, S. F., Dupan, S., Vujaklija, I., and Farina, D. (2020). Toward Universal Neural Interfaces for Daily Use: Decoding the Neural Drive to Muscles Generalises Highly Accurate Finger Task Identification Across Humans. en. *IEEE Access* 8:149025–149035.

Stegeman, F., Van Oosterom, A., and Colon, E. J. (Aug. 1987). Far-field evoked potential components induced by a propagating generator: computational evidence. *Electroencephalography and Clinical Neurophysiology* 67:176–187.

Stegeman, D. F., Dumitru, D., King, J. C., and Roeleveld, K. (Sept. 1997). Near- and Far-Fields: Source Characteristics and the Conducting Medium in Neurophysiology. en-US. *Journal of Clinical Neurophysiology* 14:429.

Tang, X., Zhang, X., Chen, M., Chen, X., and Chen, X. (2021). Decoding Muscle Force From Motor Unit Firings Using Encoder-Decoder Networks. *IEEE Transactions on Neural Systems and Rehabilitation Engineering* 29. Conference Name: IEEE Transactions on Neural Systems and Rehabilitation Engineering:2484–2495.

Tanzarella, S., Iacono, M., Donati, E., Farina, D., and Bartolozzi, C. (2023). Neuromorphic Decoding of Spinal Motor Neuron Behaviour During Natural Hand Movements for a New Generation of Wearable Neural Interfaces. *IEEE Transactions on Neural Systems and Rehabilitation Engineering* 31. Conference Name: IEEE Transactions on Neural Systems and Rehabilitation Engineering:3035–3046.

Tanzarella, S., Muceli, S., Del Vecchio, A., Casolo, A., and Farina, D. (July 2019). A high-density surface EMG framework for the study of motor neurons controlling the intrinsic and extrinsic muscles of the hand. en. *2019 41st Annual International Conference of the IEEE Engineering in Medicine and Biology Society (EMBC)*. Berlin, Germany: IEEE, 2307–2310.

Tanzarella, S., Muceli, S., Del Vecchio, A., Casolo, A., and Farina, D. (Aug. 2020). Non-invasive analysis of motor neurons controlling the intrinsic and extrinsic muscles of the hand. en. *Journal of Neural Engineering* 17:046033.

Thomas, J., Deville, Y., and Hosseini, S. (Apr. 2006). Time-domain fast fixed-point algorithms for convolutive ICA. en. *IEEE Signal Processing Letters* 13:228–231.

Thompson, C. K., Negro, F., Johnson, M. D., Holmes, M. R., McPherson, L. M., Powers, R. K., Farina, D., and Heckman, C. J. (2018). Robust and accurate decoding of motoneuron behaviour and prediction of the resulting force output. en. *The Journal of Physiology* 596:2643–2659.

Tonin, L. and Millán, J. D. R. (May 2021). Noninvasive Brain–Machine Interfaces for Robotic Devices. en. *Annual Review of Control, Robotics, and Autonomous Systems* 4:191–214.

Van Cutsem, M. and Duchateau, J. (2005). Preceding muscle activity influences motor unit discharge and rate of torque development during ballistic contractions in humans. en. *The Journal of Physiology* 562:635–644.

Velliste, M., Perel, S., Spalding, M. C., Whitford, A. S., and Schwartz, A. B. (June 2008). Cortical control of a prosthetic arm for self-feeding. en. *Nature* 453. Number: 7198 Publisher: Nature Publishing Group:1098–1101.

Vujaklija, I., Roche, A. D., Hasenoehrl, T., Sturma, A., Amsuess, S., Farina, D., and Aszmann, O. C. (2017). Translating Research on Myoelectric Control into Clinics—Are the Performance Assessment Methods Adequate? *Frontiers in Neurorobotics* 11.

Wen, Y., Avrillon, S., Hernandez-Pavon, J. C., Kim, S. J., Hug, F., and Pons, J. L. (Apr. 2021). A convolutional neural network to identify motor units from high-density surface electromyography signals in real time. en. *Journal of Neural Engineering* 18:056003.

Westad, C., Westgaard, R. H., and De Luca, C. J. (2003). Motor unit recruitment and derecruitment induced by brief increase in contraction amplitude of the human trapezius muscle. en. *The Journal of Physiology* 552:645–656.

Westgaard, R. H. and De Luca, C. J. (Apr. 2001). Motor Control of Low-Threshold Motor Units in the Human Trapezius Muscle. *Journal of Neurophysiology* 85. Publisher: American Physiological Society:1777–1781.

Wienecke, J., Zhang, M., and Hultborn, H. (Dec. 2009). A Prolongation of the Postspike Afterhyperpolarization Following Spike Trains Can Partly Explain the Lower Firing Rates at Derecruitment Than Those at Recruitment. *Journal of Neurophysiology* 102. Publisher: American Physiological Society:3698–3710.

Wilson, F. N., Macleod, A. G., and Barker, P. S. (Jan. 1933). The distribution of the action currents produced by heart muscle and other excitable tissues immersed in extensive conducting media. *The Journal of General Physiology* 16:423–456.

Winter, D. A., Fuglevand, A. J., and Archer, S. E. (Jan. 1994). Crosstalk in surface electromyography: Theoretical and practical estimates. *Journal of Electromyography and Kinesiology* 4:15–26.

Wood, S. J. and R. Slater, C. (July 2001). Safety factor at the neuromuscular junction. en. *Progress in Neurobiology* 64:393–429.

Yeung, D., Negro, F., and Vujaklija, I. (2023). Optimal Motor Unit Subset Selection for Accurate Motor Intention Decoding: Towards Dexterous Real-Time Interfacing. *IEEE Transactions on Neural Systems and Rehabilitation Engineering* 31. Conference Name: IEEE Transactions on Neural Systems and Rehabilitation Engineering:4225–4234.

Yeung, D., Negro, F., and Vujaklija, I. (2024). Adaptive HD-sEMG decomposition: towards robust real-time decoding of neural drive. en. *Journal of Neural Engineering*.

Yokoyama, H., Sasaki, A., Kaneko, N., Saito, A., and Nakazawa, K. (2021). Robust Identification of Motor Unit Discharges From High-Density Surface EMG in Dynamic Muscle Contractions of the Tibialis Anterior. en. *IEEE Access* 9:123901–123911.

Yu, Y., Chen, C., Sheng, X., and Zhu, X. (July 2021). Wrist Torque Estimation via Electromyographic Motor Unit Decomposition and Image Reconstruction. *IEEE Journal of Biomedical and Health Informatics* 25. Conference Name: IEEE Journal of Biomedical and Health Informatics:2557–2566.

Yuste, R., Goering, S., Arcas, B. A. y., Bi, G., Carmena, J. M., Carter, A., Fins, J. J., Friesen, P., Gallant, J., Huggins, J. E., Illes, J., Kellmeyer, P., Klein, E., Marblestone, A., Mitchell, C., Parens, E., Pham, M., Rubel, A., Sadato, N., Sullivan, L. S., Teicher, M., Wasserman, D., Wexler, A., Whittaker, M., and Wolpaw, J. (Nov. 2017). Four ethical priorities for neurotechnologies and AI. en. *Nature* 551. Number: 7679 Publisher: Nature Publishing Group:159–163.

Zhang, X., Zhu, G., Chen, M., Chen, X., Chen, X., and Zhou, P. (Dec. 2020). Muscle Force Estimation Based on Neural Drive Information From Individual Motor Units. *IEEE Transactions on Neural Systems and Rehabilitation Engineering* 28. Conference Name: IEEE Transactions on Neural Systems and Rehabilitation Engineering:3148–3157.

Zhao, Y., Zhang, X., Li, X., Zhao, H., Chen, X., Chen, X., and Gao, X. (June 2022). Decoding finger movement patterns from microscopic neural drive information based on deep learning. *Medical Engineering & Physics* 104:103797.

Zheng, Y. and Hu, X. (Oct. 2019). Real-time isometric finger extension force estimation based on motor unit discharge information. en. *Journal of Neural Engineering* 16. Publisher: IOP Publishing:066006.

Zheng, Y. and Hu, X. (May 2021). Concurrent Estimation of Finger Flexion and Extension Forces Using Motoneuron Discharge Information. *IEEE Transactions on Biomedical Engineering* 68. Conference Name: IEEE Transactions on Biomedical Engineering:1638–1645.